CORA Cork Open Research Archive
Cartlann Taighde Oscailte Chorcaí

Title	Development of a triple stage heat transformer for the recycling of low temperature heat energy
Authors	Donnellan, Philip
Publication date	2014
Original Citation	Donnellan, P. 2014. Development of a triple stage heat transformer for the recycling of low temperature heat energy. PhD Thesis, University College Cork.
Type of publication	Doctoral thesis
Rights	© 2014, Philip Donnellan. - http://creativecommons.org/licenses/by-nc-nd/3.0/
Download date	2026-11-01 03:03:20
Item downloaded from	https://hdl.handle.net/10468/2006



UCC
University College Cork, Ireland
Coláiste na hOllscoile Corcaigh

Development of a triple stage heat transformer for the recycling of low temperature heat energy

Philip Donnellan
BE
107564406

Thesis submitted for the degree of Doctor of Philosophy



NATIONAL UNIVERSITY OF IRELAND, CORK

Department of Process and Chemical Engineering

July 2014

Head of Department: Dr Jorge Oliviera

Supervisors: Dr Kevin Cronin
Dr Edmond Byrne

Research supported by the Irish Research Council

Contents

List of Figures xi
List of Tables xii
Abstract xiv
Acknowledgements xv
List of Publications xvi

1 Introduction to Absorption Heat Transformers 1
1.1 Absorption Heat transformers 2
1.1.1 AHT Fundamental Principle 7
1.2 Single Stage Heat Transformers (SSHT) 8
1.2.1 SSHT Cycle Description 8
1.2.2 AHT Performance Criteria 10
1.2.3 SSHT Parametric Studies 13
1.2.3.1 Coefficient of Performance (COP) 13
1.2.3.2 Exergetic Coefficient of Performance (ECOP) . 14
1.2.3.3 Flow Ratio (FR) 14
1.2.3.4 Exergy Destruction (E_D) 15
1.2.3.5 SSHT Simulations 16
1.2.4 Alternate Configurations 16
1.2.4.1 Alternate Internal Heat Recovery Configurations 16
1.2.4.2 Multi-component Absorber/Generator 17
1.2.4.3 Ejector Absorption Heat Transformers (EAHT) 18
1.2.4.4 Combined SSHT-Water Purification Cycles . . 19
1.3 Advanced Heat Transformers 20
1.3.1 Double Absorption Heat Transformers (DAHT) 20
1.3.1.1 DAHT Cycle Description 20
1.3.1.2 DAHT Parametric Studies 22
1.3.2 Alternate Two Stage AHT Configurations 22
1.3.2.1 Double Stage Heat Transformers (DSHT) . . . 22
1.3.2.2 Alternate DAHT Stream Configurations 23
1.3.2.3 Double Effect Heat Transformers (DEHT) . . . 24
1.3.3 Triple Absorption Heat Transformers (TAHT) 25
1.3.3.1 TAHT Cycle Description 25
1.3.3.2 TAHT Parametric Studies 26
1.4 Working Fluids Comparison 27
1.4.1 Ammonia-Water 28
1.4.2 TFE Refrigerant Fluids 28
1.4.3 Water-Carrol Mixture 29

1.4.4 Additives . . . 30
1.4.5 Salt and Water Combinations . . . 31
1.4.6 Working Fluids conclusion . . . 32
1.5 AHT Case Studies . . . 33
1.5.1 SSHT Case Studies . . . 33
1.5.2 Advanced Heat Transformer Case Studies . . . 34
1.6 Research Motivation and Thesis objective . . . 35
1.7 Thesis Structure . . . 36

Part I Whole System Analysis

2 Thermodynamic and Heat Transfer Modelling 39
2.1 Introduction . . . 40
2.2 Physical Properties . . . 43
2.3 Thermodynamic modelling of the TAHT . . . 43
2.3.1 Governing Equations . . . 45
2.3.2 Dependent Factors . . . 46
2.3.3 Heat of Absorption . . . 48
2.4 Individual Unit design and modelling . . . 49
2.4.1 Solution Heat Exchangers . . . 49
2.4.2 Absorber . . . 50
2.4.3 Condenser . . . 51
2.4.4 Excess Energy Heat Exchangers . . . 53
2.4.5 Evaporator . . . 54
2.4.6 Generator . . . 55
2.5 Heat Exchanger Sizing . . . 56

3 First and Second Law Multidimensional Analysis of a TAHT 60
3.1 Introduction . . . 61
3.2 Mathematical Modelling . . . 62
3.3 Multidimensional design of experiment . . . 62
3.3.1 TAHT Thermodynamic Limitations . . . 63
3.3.2 Level Selection . . . 64
3.3.3 Analysis of Results . . . 67
3.4 Results and Discussion . . . 68
3.4.1 System Output Analysis . . . 68
3.4.2 Manipulated Variable Analysis . . . 69
3.4.2.1 Pinch heat transfer gradient (dT_{Hx}) . . . 70
3.4.2.2 Total Gross temperature lift (GTL3) . . . 70
3.4.2.3 GTL1 and GTL2 . . . 72
3.4.2.4 Condensation Temperature (T_c) . . . 73
3.4.2.5 Temperature of the evaporator (T_e) . . . 78
3.4.3 Example case study, showing potential optimised system operation . . . 81
3.4.4 Unit Exergy Destruction . . . 84
3.5 Conclusions . . . 85

4 Internal Energy and Exergy Recovery in High Temperature Application Absorption Heat Transformers 87
4.1 Introduction . . . 88
4.2 Internal Heat Recovery in Absorption Heat Transformers . . . 93
4.3 Mathematical Modelling . . . 94
4.4 Heat exchange network modelling . . . 95
4.4.1 Selecting streams available for heat transfer and analysis 99
4.5 Results and Discussion . . . 100
4.5.1 Individual heat sink analysis . . . 100
4.5.2 Heat exchanger combination analysis . . . 102
4.5.3 Temperature influence upon Optimum designs . . . 104
4.6 Conclusions . . . 107

5 Economic Evaluation of an Industrial High Temperature Lift Heat Transformer 108
5.1 Introduction . . . 109
5.2 Case Study: An Oil Refinery . . . 111
5.3 Mathematical Modelling . . . 112
5.3.1 Thermodynamic . . . 112
5.3.2 Costing . . . 113
5.3.3 Economic Indicator . . . 114
5.4 Plant Conditions . . . 115
5.5 Results . . . 116
5.5.1 Sizing . . . 116
5.5.2 Costing . . . 117
5.5.3 Thermodynamic Performance . . . 118
5.5.4 Economic Performance . . . 119
5.6 Discussion . . . 123
5.6.1 Waste Stream Physical Properties . . . 124
5.6.2 Quantity of waste heat available . . . 128
5.6.3 System Design . . . 130
5.7 Conclusions . . . 135

Part II Bubble Absorption Analysis

6 Bubble Column Development 137
6.1 Experimental Objectives . . . 138
6.2 Bubble Column Experimental Set Up . . . 141
6.3 Properties Measurement . . . 144
6.4 Calibration . . . 148
6.5 Experimental Procedure . . . 149
6.6 Data Analysis . . . 150

7 Absorption of Steam Bubbles in Lithium Bromide Solution 152
7.1 Introduction . . . 153
7.2 Mathematical Modelling . . . 155

7.2.1 Absorption Theory 156
7.2.2 Absorption Rate 158
7.2.3 Statistical Analysis 162
7.3 Results and Discussion 163
7.3.1 Experimental Results 163
7.3.2 Modelling Results 168
7.3.3 Effect of Temperature and Concentration 173
7.3.4 Effect of Air Presence 176
7.3.5 Effect of Initial Bubble Diameter 178
7.4 Conclusions 179

8 Analysis of Collapsing Bubble Motion with Random Process Theory 182
8.1 Introduction 183
8.2 Mathematical Modelling 186
8.2.1 Bubble Shape Model 186
8.2.2 Deterministic Bubble Kinematic Model 188
8.2.3 Probabilistic Modelling 192
8.2.4 Numerical Simulation 194
8.2.5 Model Empirical Parameter Selection 196
8.3 Results and Discussion 198
8.3.1 Evolution of Bubble Shape with Time 198
8.3.2 Deterministic Analysis of Bubble Motion 202
8.3.3 Probabilistic Analysis of Bubble Motion 205
8.3.4 Comparison with Non-Condensing Bubbles 206
8.3.5 Parameter impact upon Variability 207
8.4 Conclusions 208

Part III Discussion and Conclusions

9 General Conclusions 210

Appendices

Appendix A Mathematical Function Details 232
A.1 Water-Lithium Bromide Solution Properties 233
A.1.1 Gibbs Free Energy 233
A.1.2 Diffusivity 236
A.2 Heat Transfer Coefficients 236
A.2.1 Shell Side Heat Transfer Coefficient 236

List of Figures

1.1 Schematic of a vapour compression heat pump cycle 4
1.2 Schematic of a single effect absorption heat pump 5
1.3 Conceptual operation of an absorption heat transformer 6
1.4 Schematic of the fundamental principle behind the operation of an absorption heat transformer 7
1.5 Schematic of a single stage heat transformer (SSHT) 9
1.6 Schematic of a conventional power cycle 10
1.7 Schematic of an the flows entering and leaving an absorber in a heat transformer 12
1.8 Schematic of a single stage heat transformer (SSHT) configuration in which the absorber coolant is preheated by the dilute solution leaving the absorber 17
1.9 Schematic of an ejection absorption heat transformer (EAHT) . 18
1.10 Schematic of a single stage heat transformer coupled with a water purification cycle in which the latent heat from the auxiliary condenser is recycled to both the evaporator and the generator . 19
1.11 Schematic of a double absorption heat transformer (DAHT) in which the dilute solution from the absorber acts as the concentrated solution for the absorber-evaporator 21
1.12 Schematic of a double stage heat transformer (DSHT) in which the absorber in the low temperature cycle (right hand side cycle in this figure) is coupled to the evaporator in the high temperature cycle (left hand side cycle in this figure) 23
1.13 Schematic of a double effect heat transformer (DEHT) 24
1.14 Schematic of a triple absorption heat transformer (TAHT) . . . 25

2.1 Schematic of the triple absorption heat transformer (TAHT) being simulated 40
2.2 Comparison of the specific enthalpy of absorption of steam vapour in $LiBr - H_2O$ solution at different salt concentrations at atmospheric pressure (101325Pa) 49
2.3 Schematic of the falling film absorber modelled in this heat transformer 51
2.4 Schematic of an air-cooled condenser simulated in the heat transformer 52
2.5 Schematic of the falling film evaporator modelled in this heat transformer 54

2.6 Schematic of the falling film generator modelled in this heat transformer 55

3.1 Schematic of the operational temperatures, pressures and concentrations within the main unit operations of a typical TAHT, illustrating the system's thermodynamic limitations 63
3.2 Relative influence of each factor/interaction upon the system's COP 68
3.3 Relative influence of each factor/interaction upon the system's ECOP 69
3.4 Relative influence of each factor/interaction upon the system's flow ratio (FR) 69
3.5 Relative influence of each factor/interaction upon the system's total rate of exergy destruction (E_D) 70
3.6 Average (non-interacting) effect of dT_{Hx} upon the system's dependent variables showing a 99% confidence interval 71
3.7 Interactive effect of T_c and dT_{Hx} on the system's ECOP 72
3.8 Average (non-interacting) effect of GTL3 upon the system's dependent variables showing a 99% confidence interval 73
3.9 Average (non-interacting) effect of GTL1 upon the system's dependent variables showing a 99% confidence interval 74
3.10 Average (non-interacting) effect of GTL2 upon the system's dependent variables showing a 99% confidence interval 75
3.11 Interactive effect of T_c and GTL1 on the system's FR 76
3.12 Interactive effect of T_c and GTL2 on the system's COP 76
3.13 Average (non-interacting) effect of T_c upon the system's dependent variables showing a 99% confidence interval 77
3.14 Interactive effect of T_c and GTL3 on the system's E_D 78
3.15 Average (non-interacting) effect of T_e upon the system's dependent variables showing a 99% confidence interval 79
3.16 Varying effect of T_e upon the system's ECOP, highlighting the impact of letting the condensation temperature vary or keeping it fixed. This plot assumes the following levels: T_{cond} = 1, GTL1 = 3, GTL2 = 3 and the following settings: dT_{Hx} = 10K, GTL3 = 145 °C. The minimum allowable condensation temperature is set at 40 °C in this example. 80
3.17 Schematic of the general temperature and energy adjustment achieved by the TAHT in the case study example discussed in section 3.4.3. 81
3.18 Salt concentrations within the cycle of the case study discussed in section 3.4.3 depicted against the $LiBr - H_2O$ crystallisation curve referenced from Pátek and Klomfar (2006). The absorber-evaporator-1 cycle refers to the solution cycle circulating between the generator and Absorber-evaporator-1 in Figure 1.14, while the absorber-evaporator-2 and absorber cycles refer to the salt solutions circulating between these unit operations and the generator respectively. 82

3.19 Percentage exergy destruction caused by each unit operation within the cycle 84

4.1 Schematic of an endoreversible heat transformer 90
4.2 Schematic of an the flows entering and leaving an absorber in a heat transformer 90
4.3 Variation in the absorber exergy destruction rate with an increase in the difference between the temperatures entering and leaving the absorber. This figure assumes the ratio of steam to solution entering the unit is 0.2, the inlet $LiBr - H_2O$ concentration is 0.65 (w/w) and the outlet temperature is 140 °C at atmospheric pressure. 91
4.4 Absorber exergy destruction rate with a variation in the difference between the temperatures entering and leaving the absorber and a variation in the ratio of steam to solution entering the unit (mass flowrate of steam divided by mass flowrate of solution). This figure the inlet $LiBr - H_2O$ concentration is 0.65 (w/w) and the outlet temperature is 140 °C at atmospheric pressure. 92
4.5 Schematic of the basic TAHT containing no heat exchangers . . 96
4.6 Schematic of the conventional triple absorption heat transformer (TAHT) 98
4.7 The percentage by which each of the individual heat sinks increase the basic TAHT's (Figure 4.5) COP 101
4.8 Schematic of the optimum design of the TAHT containing two heat exchangers 103
4.9 Schematic of the optimum design of the TAHT containing three heat exchangers 104
4.10 Schematic of the optimum design of the TAHT containing four heat exchangers 105
4.11 Schematic of the optimum design of the TAHT containing five heat exchangers 106
4.12 Limiting conditions of both evaporator temperature and system gross temperature lift (GTL) according to which either the conventional or HEN TAHT designs using three heat exchangers should be used. 106

5.1 Schematic of the TAHT's operation in this case study 116
5.2 Breakdown of the general trend observed for project costs in the oil refinery 118
5.3 Probability and Cumulative distribution functions (PDF and CDF) of the simple payback period (SPBP) at the current gas price (CGP) as defined in section 5.3.2 119
5.4 Probability and Cumulative distribution functions (PDF and CDF) of the discounted payback period (DPBP) at the current gas price (CGP) as defined in section 5.3.2 120

5.5 Probability and Cumulative distribution functions (PDF and CDF) of the net present value (NPV) at the current gas price (CGP) as defined in section 5.3.2 121
5.6 Cumulative distribution functions of the simple payback period (SPBP) at various potential gas prices based upon the current gas price (CGP) defined in section 5.3.2 122
5.7 Cumulative distribution functions of the discounted payback period (DPBP) at various potential gas prices based upon the current gas price (CGP) defined in section 5.3.2 123
5.8 Cumulative distribution functions of the net present value (NPV) at various potential gas prices based upon the current gas price (CGP) defined in section 5.3.2 124
5.9 Cumulative distribution function of the TAHT's simple payback period (SPBP) highlighting the importance of the waste stream's physical properties 125
5.10 Cumulative distribution function of the TAHT's discounted payback period (DPBP) highlighting the importance of the waste stream's physical properties 126
5.11 Cumulative distribution function of the TAHT's net present value (NPV) highlighting the importance of the waste stream's physical properties 127
5.12 Cumulative distribution functions of the simple payback period (SPBP) utilising different quantities of waste heat streams in the TAHT 128
5.13 Cumulative distribution functions of the discounted payback period (DPBP) utilising different quantities of waste heat streams in the TAHT 129
5.14 Cumulative distribution functions of the net present value (NPV) utilising different quantities of waste heat streams in the TAHT 130
5.15 Percentage of the total TAHT cost allocated to each type of equipment 131
5.16 Cumulative distribution functions of the simple payback period (SPBP) assuming the benefits of plate heat exchanger usage (Genssle and Stephan, 2000) 131
5.17 Cumulative distribution functions of the discounted payback period (DPBP) assuming the benefits of plate heat exchanger usage (Genssle and Stephan, 2000) 132
5.18 Cumulative distribution functions of the net present value (NPV) assuming the benefits of plate heat exchanger usage (Genssle and Stephan, 2000) 133

6.1 Schematic of the bubble absorber column developed for this study 141
6.2 Photograph of the experimental set up 142
6.3 Photograph of bubbles forming in the $LiBr - H_2O$ solution in the bubble column 143
6.4 Photograph of the steam generation system 144

6.5 Photograph of a bubble in the $LiBr - H_2O$ solution 145
6.6 Schematic of the high speed camera set up during the experimental runs 146
6.7 Photograph of the high speed camera used to track the bubble collapse 147
6.8 Photograph of the experimental lighting set up 148
6.9 Example of a bubble being tracked using the Pro Analyst Software 151
6.10 Demonstration of measuring the sparger width using a micrometer 151

7.1 Schematic of the different temperatures and concentrations which exist around a collapsing bubble 156
7.2 Typical shape deformation observed in the bubble. The bubble morphology alternates with time between spherical, oblate-spheroid and prolate-spheroid morphologies. In this figure the oscillation may be simplified as being approximately: spherical → oblate-spheroid → prolate-spheroid → oblate-spheroid → spherical 160
7.3 Experimental diameter versus time for a typical oscillating bubble showing the difference between maximum and minimum diameter at a particular time due to oscillation 161
7.4 Experimental diameter versus time at concentration level 1 and temperature level 1 163
7.5 Experimental diameter versus time at concentration level 1 and temperature level 2 164
7.6 Experimental diameter versus time at concentration level 2 and temperature level 1 164
7.7 Experimental diameter versus time at concentration level 2 and temperature level 2 165
7.8 Experimental diameter versus time at concentration level 3 and temperature level 1 165
7.9 Experimental diameter versus time at concentration level 3 and temperature level 2 166
7.10 Experimental diameter versus time at concentration level 3 and temperature level 3 166
7.11 Averaged experimental bubble diameter compared to the diameter profile predicted by the model at concentration level 1 and temperature level 1 168
7.12 Averaged experimental bubble diameter compared to the diameter profile predicted by the model at concentration level 1 and temperature level 2 169
7.13 Averaged experimental bubble diameter compared to the diameter profile predicted by the model at concentration level 2 and temperature level 1 169
7.14 Averaged experimental bubble diameter compared to the diameter profile predicted by the model at concentration level 2 and temperature level 2 170

7.15 Averaged experimental bubble diameter compared to the diameter profile predicted by the model at concentration level 3 and temperature level 1 170
7.16 Averaged experimental bubble diameter compared to the diameter profile predicted by the model at concentration level 3 and temperature level 2 171
7.17 Averaged experimental bubble diameter compared to the diameter profile predicted by the model at concentration level 3 and temperature level 3 171
7.18 Illustration of the goodness of fit between the model and the experimental data 174
7.19 Comparison of the time required for a 95% reduction in bubble volume at different concentrations and temperature gradients (i.e.: the difference between the boiling temperature of the solution and the temperature of the solution) for a 4mm initial diameter bubble 175
7.20 Variation of water volume fraction within the bubble throughout its collapse at different temperature settings for concentration level 3 177
7.21 Simulation of the diameter versus time profile for a bubble collapsing with different initial volumetric fractions of water present in the vapour phase. A 4mm initial bubble is modelled in a 50% (w/w) solution with a temperature difference of 10 °C between the solution's temperature and it boiling temperature. 178
7.22 Simulation of the bubble H_2O volumetric fraction versus time profile for a bubble collapsing with different initial volumetric fractions of water present in the vapour phase. A 4mm initial bubble is modelled in a 50% (w/w) solution with a temperature difference of 10 °C between the solution's temperature and its boiling temperature. 179
7.23 Variation of the bubble absorption time (for a 95% reduction in bubble volume) with respect to initial bubble diameter. The bubble is simulated in a 50% $LiBr - H_2O$ solution, whose temperature is 10 °C below its boiling temperature. 180
7.24 Variation of the bubble absorption time (for a 95% reduction in bubble volume) per unit bubble volume with respect to initial bubble diameter. The bubble is simulated in a 50% $LiBr - H_2O$ solution, whose temperature is 10 °C below its boiling temperature. 180

8.1 Oblate Spheroid bubble shape approximation 187
8.2 Regressed bubble semi major axis for Concentration 3 - Temperature 3 highlighting the random behaviour of this variable 188
8.3 Regressed bubble Aspect Ratio for Concentration 3 - Temperature 3 highlighting the random behaviour of this variable 189
8.4 Experimental and regressed correlograms at Concentration 1-Temperature 2 197

8.5 Probability Density Functions of the residual resulting from the linear regressions at Concentration 1-Temperature 2 197
8.6 Comparison of mean forces acting upon the collapsing bubble at Concentration 2 - Temperature 2 200
8.7 Deterministic model velocity and displacement versus time at concentration 1 200
8.8 Deterministic model velocity and displacement versus time at concentration 2 201
8.9 Deterministic model velocity and displacement versus time at concentration 3 201
8.10 Experimental and Modelled Displacement versus time at concentration 1 203
8.11 Experimental and Modelled Displacement versus time at concentration 2 204
8.12 Experimental and Modelled Displacement versus time at concentration 3 204
8.13 Experimentally observed vertical displacements versus confidence intervals predicted by the model at Concentration 1- Temperature 2 205
8.14 Comparison between absorbing and non-absorbing bubble vertical velocities at Concentration 2 206
8.15 Comparison between the vertical displacement standard deviations under different conditions of either probabilistic or deterministic semi-major axes and aspect ratios at Concentration 2 207

A.1 Specific Gibbs free energy of the $LiBr - H_2O$ solution at various different salt concentrations and temepratures at atmospheric pressure (101325Pa). 233
A.2 Mass diffusivity of water in a lithium bromide solution as a function of salt concentration 236

List of Tables

2.1 Basic design parameters selected for different shell and tube units in the TAHT 56
2.2 Basic design parameters selected for different air-cooled units in the TAHT 56

3.1 List of manipulated factors used in the multidimensional analysis 63
3.2 Definition of the experimental temperature regions for T_e, GTL3, dT_{Hx}. 66

4.1 The best system performances (based upon the cycle's COP) for each number of heat exchangers included into the TAHT. The performance of the conventional TAHT design is also included as a reference. 102

5.1 Heat transfer surface area requirements of each piece of equipment in the TAHT, when it is being used to cool the Naphtha and Residue oil waste heat streams 117

6.1 All of the concentrations and temperatures used in the experiment 149

7.1 Average solution properties at each experimental setting, where C1-T1 represents the setting Concentration 1-Temperature 1 etc. 172
7.2 Ranges of bubble absorption parameters estimated by the model 172

8.1 Solution properties at each experimental setting, where C1-T1 represents the setting Concentration 1-Temperature 1 etc. 196
8.2 Average solution dimensionless numbers at each experimental setting, where C1-T1 represents the setting Concentration 1-Temperature 1 etc. 197
8.3 Regression data for all concentration and temperature settings . 198
8.4 Regression data for all concentration and temperature settings . 199

A.1 Parameters used in the Gibbs free energy correlation used in this thesis (Yuan and Herold, 2005) 235
A.2 Parameters used in the Gibbs free energy correlation used in this thesis (Yuan and Herold, 2005) 235
A.3 Empirical Factors required for the calculation of the ideal shell side heat transfer coefficient in equations A.6 and A.7 238

I, Philip Donnellan, certify that this thesis is my own work and has not been submitted for another degree at University College Cork or elsewhere.

_____

Philip Donnellan

Abstract

Absorption heat transformers are thermodynamic systems which are capable of recycling industrial waste heat energy by increasing its temperature. Triple stage heat transformers (TAHTs) can increase the temperature of this waste heat by up to approximately 145 °C.

The principle factors influencing the thermodynamic performance of a TAHT and general points of operating optima were identified using a multivariate statistical analysis, prior to using heat exchange network modelling techniques to dissect the design of the TAHT and systematically reassemble it in order to minimise internal exergy destruction within the unit. This enabled first and second law efficiency improvements of up to 18.8% and 31.5% respectively to be achieved compared to conventional TAHT designs. The economic feasibility of such a thermodynamically optimised cycle was investigated by applying it to an oil refinery in Ireland, demonstrating that in general the capital cost of a TAHT makes it difficult to achieve acceptable rates of return.

Decreasing the TAHT's capital cost may be achieved by redesigning its individual pieces of equipment and reducing their size. The potential benefits of using a bubble column absorber were therefore investigated in this thesis. An experimental bubble column was constructed and used to track the collapse of steam bubbles being absorbed into a hotter lithium bromide salt solution. Extremely high mass transfer coefficients of approximately 0.0012m/s were observed, showing significant improvements over previously investigated absorbers. Two separate models were developed, namely a combined heat and mass transfer model describing the rate of collapse of the bubbles, and a stochastic model describing the hydrodynamic motion of the collapsing vapour bubbles taking into consideration random fluctuations observed in the experimental data. Both models showed good agreement with the collected data, and demonstrated that the difference between the solution's temperature and its boiling temperature is the primary factor influencing the absorber's performance.

Acknowledgements

I would like to thank my two co-supervisors Dr Edmond Byrne and Dr Kevin Cronin for all of their support and help throughout this project. Both were extremely receptive at all times of any ideas which I wished to pursue, and their doors were always open when I came looking for advice or guidance. It has been a pleasure to work so closely with people of such high calibre from both a professional and personal perspective.

I received much help, for which I am very grateful, from the technical staff in the department, Paul Conway, John Barrett and Tim Twomey, in particular during the construction and operation of my experimental rig. Without this help much of the project would not have been possible.

During my time here, I have sought advice and help from all of the academic and administrative staff in the department on different issues. In these situations I was always treated with the highest respect and for this I would like to thank Dr Jorge Oliveira, Dr John Fitzpatrick, Dr Maria de Sousa Gallagher, Dr Denis Ring, Julie Holland and Anne-Marie McSweeney.

The Phillips 66 Whitegate Oil Refinery provided me with much data and accommodated my project through consultations and the provision of resources. I want to extend my gratitude to the company for this. In particular I am indebted to Dermot O'Sullivan and Conor Phelan who gave up much of their valuable time to help me.

Funding for this PhD was provided by the Irish Research Council under the EMBARK initiative. This funding allowed me the freedom to define and manage the project as I felt appropriate, while offering all the financial support which I required.

To both of my parents (Jim and Christine), and to Dearbhail, I want to thank you for supporting me throughout this project and helping me through the tough times. Yours was not an enviable task. Thank you.

List of Publications

Peer Reviewed Journal Papers emanating from this work to date

- Donnellan, P., Byrne, E.P. & Cronin, K. (2013) Internal energy and exergy recovery in high temperature application absorption heat transformers, Applied Thermal Engineering, 56, 1-10.
- Donnellan, P., Byrne, E., Oliveira, J. & Cronin, K. (2014) First and second law multidimensional analysis of a triple absorption heat transformer (TAHT), Applied Energy, 113, 141-151.
- Donnellan, P., Cronin, K., Acevedo, Y. & Byrne, E. (2014) Economic evaluation of an industrial high temperature lift heat transformer, Energy, 73, 581-591.
- Donnellan, P., Duggan, S. Cronin, K. & Byrne, E. (2014) Experimental absorption of steam bubbles in a concentrated lithium bromide solution, Chemical Engineering Science, 119, 10-21.
- Donnellan, P., Cronin, K. & Byrne, E. (2014) Recycling Waste Heat Energy Using Vapour Absorption Heat Transformers: A Review, Renewable & Sustainable Energy Reviews, Under Review.
- Donnellan, P., Byrne, E. & Cronin, K.(2014) Analysis of Collapsing Bubble Motion with Random Process Theory, Chemical Engineering Science, Under Review.

International Conference Publications emanating from this work to date

- Donnellan, P., Byrne, E. & Cronin, K. (2013) Development of a high performance heat transformer for large waste heat temperature augmentations, 9th European Congress of Chemical Engineering, The Hague, The Netherlands 21-25 April 2013.
- Donnellan, P., Byrne, E., Lee, W. & Cronin, K. (2014) Experimental analysis of the rate of absorption of steam bubbles in lithium bromide solution for use in an absorption heat transformer, 10th International Conference on Heat Transfer, Fluid Mechanics and Thermodynamics, Orlando, Florida 14-16 July 2014.

- Donnellan, P., Cronin, K. & Byrne, E. (2014) Examining the economic viability of an absorption heat transformer in energy intensive industries, 10th International Conference on Heat Transfer, Fluid Mechanics and Thermodynamics, Orlando, Florida 14-16 July 2014.

Other Publications

- Donnellan, P. (2014) Recycling heat energy – Prolonging the lifetime of industry's most invaluable resource, The Boolean, 4, 18-23.

Chapter 1

Introduction to Absorption Heat Transformers

Nomenclature

AHT	Absorption Heat Transformer
COP	Coefficient of performance of the system
DAHT	Double absorption heat transformer
DEHT	Double effect heat transformer
DSHT	Double stage heat transformer
dT_{Hx}	Minimum pinch temperature (heat transfer gradient) utilised in all system heat transfer operations (°C)
E	Rate of Exergy (W)
EAHT	Ejector absorption heat transformer
ECOP	Exergetic coefficient of performance of the system
E_D	Total rate of exergy destruction within the cycle (W)
E_{dest}	Rate of exergy destruction in a unit operation (W)
FR	Flow ratio of the system
GTL	Gross Temperature Lift (°C)
h	Specific enthalpy (J/kg)
$\dot{m}$	Mass flowrate (kg/s)
Q	Heat exchanger duty (W)
s	Specific Entropy (J/kgK)
SSHT	Single Stage Heat Transformer
T	Temperature (K)
TAHT	Triple absorption heat transformer

1.1 Absorption Heat transformers

Future uncertainty regarding sources of energy supply and the increasing regulation of emissions means that reducing fuel requirements is an attractive proposition for many companies. Currently, vast quantities of heat energy are being dumped to atmosphere as waste on a daily basis. It is estimated that roughly $3x10^{13}$kWh of heat energy is being lost as dissipative waste energy every year from the US manufacturing industry alone (Hendricks and Choate, 2006). Such figures correspond to approximately 50% of the energy input to this sector leaving in the form of exhaust gases, cooling water, heated products and from surfaces of hot equipment (Johnson and Choate, 2008). Although such figures represent large quantities of a valuable resource not many systems are currently employed in industry to combat this situation.

The principle reason that this energy is being discharged is due to its low temperature, as the plant cannot further utilise it in any heating operations. In order

Nomenclature continued

Chemical Symbols

$CaCl_2$	Calcium hydroxide
CsOH	Caesium hydroxide
E181	Dimethylether tetra-ethylene glycol
EMIM	1-Ethyl-3-methylimidazolium
H_2O	Water
KOH	Potassium hydroxide
LiBr	Lithium bromide
LiCl	Lithium chloride
LiI	Lithium iodide
$LiNO_3$	Lithium nitrate
$MgCl_2$	Magnesium chloride
NaOH	Sodium hydroxide
NH_3	Ammonia
NMP	N-methy1-2-pyrrolidone
TFE	2,2,2-tri-fluoroethanol
PYR	2-pyrrolidone
$ZnCl_2$	Zinc chloride

Subscripts

a	Absorber
e	Evaporator
g	Generator
o	Ambient conditions (T = 298K, P = 101325Pa)

to allow recycling and reusing of this energy, its temperature must therefore be increased using a heat pump. The principle of a heat pump is to transfer thermal energy from a low temperature source to a high temperature sink. Many different configurations of heat pumps exist, however in general they may be divided into two main categories, namely vapour compression heat pumps and absorption heat pumps (Romero et al., 2010). Vapour compression heat pumps utilise electrical energy to simultaneously compress and heat an internally circulating vapour in a compressor as illustrated in Figure 1.1. These cycles are simple in design and can achieve large gross temperature lifts (GTLs), however their main disadvantage for use in the energy recovery sector is that they require significant quantities of valuable electrical energy.

Absorption heat pumps attempt to reduce this electrical requirement. Such systems use a working fluid pair consisting of a refrigerant and an absorbent. One of

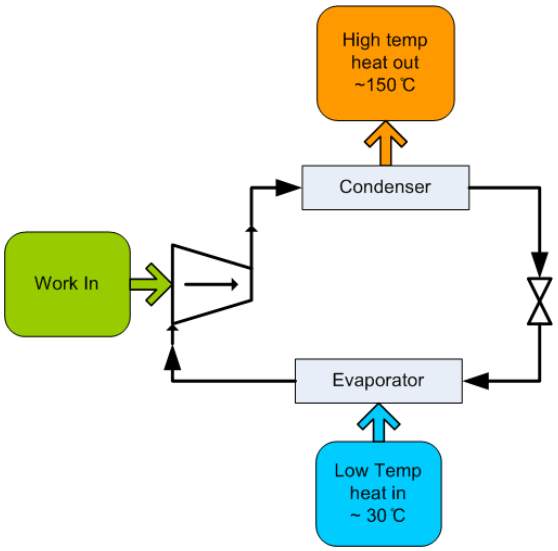


Figure 1.1: Schematic of a vapour compression heat pump cycle

the most common types of absorption refrigeration systems applied in industry today is the lithium bromide and water ($LiBr - H_2O$) system. In this cycle, the water acts as the refrigerant, and the lithium bromide as the absorbent. This system has been developed in recent years to increase its applicability in many different situations. The original configuration is called the 'single effect' system, and consists principally of one absorber, one generator, one evaporator and one condenser, as illustrated in Figure 1.2.

In Figure 1.2, the pure liquid water leaving the condenser has its pressure reduced in a throttling valve, prior to entering the evaporator. In the evaporator, low temperature waste heat energy is used to evaporate the water. The generated water vapour is absorbed into a concentrated $LiBr - H_2O$ solution in the absorber. This absorption is highly exothermic, and thus large quantities of heat energy must be removed from the absorber, which is maintained at a higher temperature than the evaporator. The water-rich solution leaving the absorber, termed the dilute solution, is then pumped to the generator which operates at a higher temperature. Here high temperature waste heat energy is used to boil off a fraction of the water from the $LiBr - H_2O$ solution. This water vapour leaves the generator and is condensed in the condenser where its latent heat of vaporization is removed by an external heat sink. The liquid which remains behind in the generator following the removal of the water vapour is termed the concentrated solution. Its pressure is reduced suitably, and is then returned to the absorber to complete the closed cycle.

It may be seen from this description that an absorption heat pump must engage

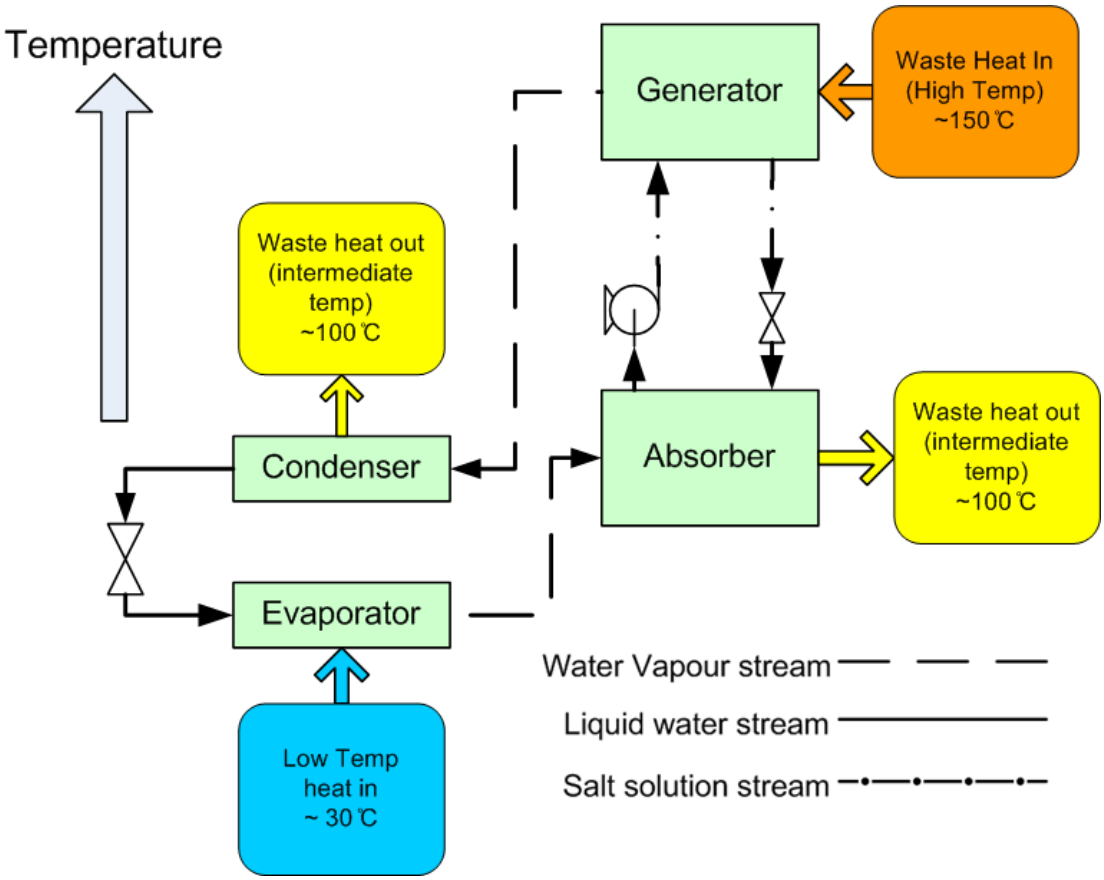


Figure 1.2: Schematic of a single effect absorption heat pump

with at least three heat energy reservoirs (heat sources/sinks), namely one at a low temperature, one at an intermediate temperature and one at a high temperature (Srikhirin et al., 2001). In a single stage absorption heat pump, the thermal loads of the absorber and generator may be up to 30% higher than the thermal loads of the condenser and evaporator respectively (Talbi and Agnew, 2000). Thus if such a system were to be implemented for the purposes of heat energy recycling it would be necessary to have large quantities of high temperature energy available for use in the generator. This requirement for high temperature heat energy and the ability of the system to absorb heat at a very low temperature in the evaporator means that absorption cycles such as the one illustrated in Figure 1.2 are generally more suited to refrigeration purposes. Thus these systems are generally termed absorption chillers, and are used generate a cooling effect at the evaporator using the waste energy supplied to the generator.

The absorber and generator's large heating and cooling loads may however be utilised advantageously when recycling heat energy if the pressure profile within the cycle is inverted. This means that the absorber and evaporator operate at a

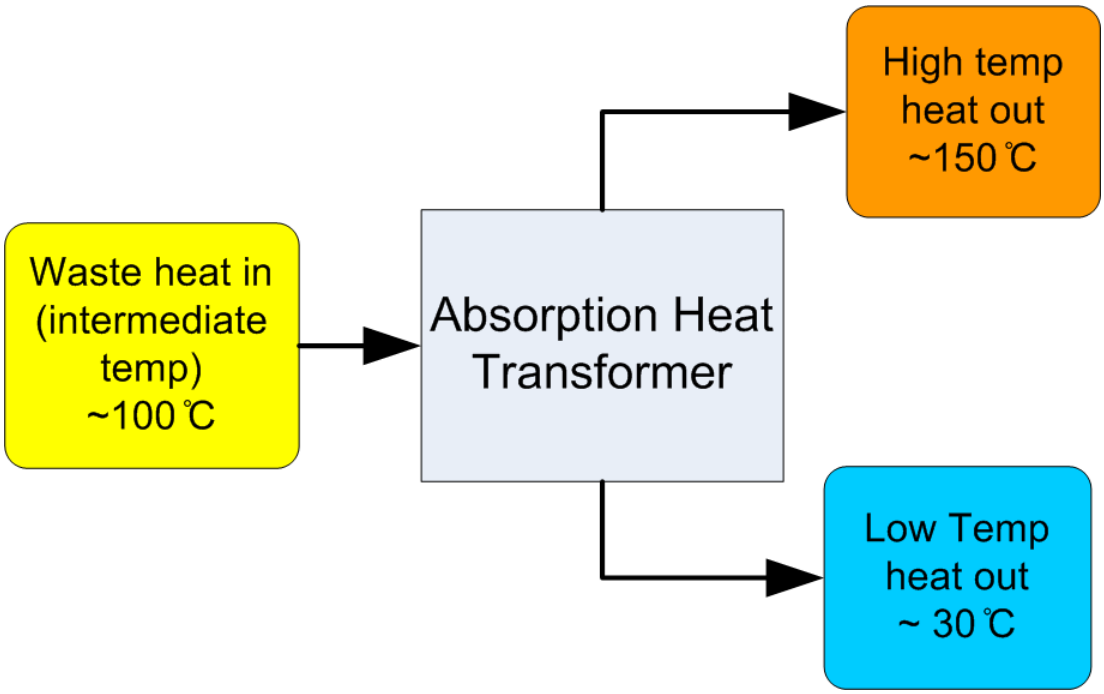


Figure 1.3: Conceptual operation of an absorption heat transformer

high pressure and the generator and condenser at a lower pressure. This is the principle behind any vapour absorption heat transformer (AHT).

An absorption heat transformer (AHT) is a closed cycle thermodynamic system which is used to convert an intermediate temperature waste heat source into a quantity of high temperature, high quality, usable energy as illustrated in Figure 1.3 (Rivera, 2000). Up to 50% of the waste heat may typically be recovered (Yin et al., 2000; Rivera, 2000; Sözen and Yücesu, 2007; Romero et al., 2010), and their operation requires only very small amounts of mechanical energy (Romero et al., 2010). The remainder of the heat energy which is not recovered is discharged to a low temperature sink (Rivera, 2000) (Figure 1.3). Although only very few of these systems are currently in industrial use (Sözen and Yücesu, 2007), it has been demonstrated that considerable energy savings and a reduction in fuel requirements may be achieved if installed in the correct facility (Abrahamsson et al., 1995). It is for these reasons that heat transformers have been termed 'future technology which will be important for energy utilization in the 21st century' by the International Energy Agency (Sözen and Yücesu, 2007).

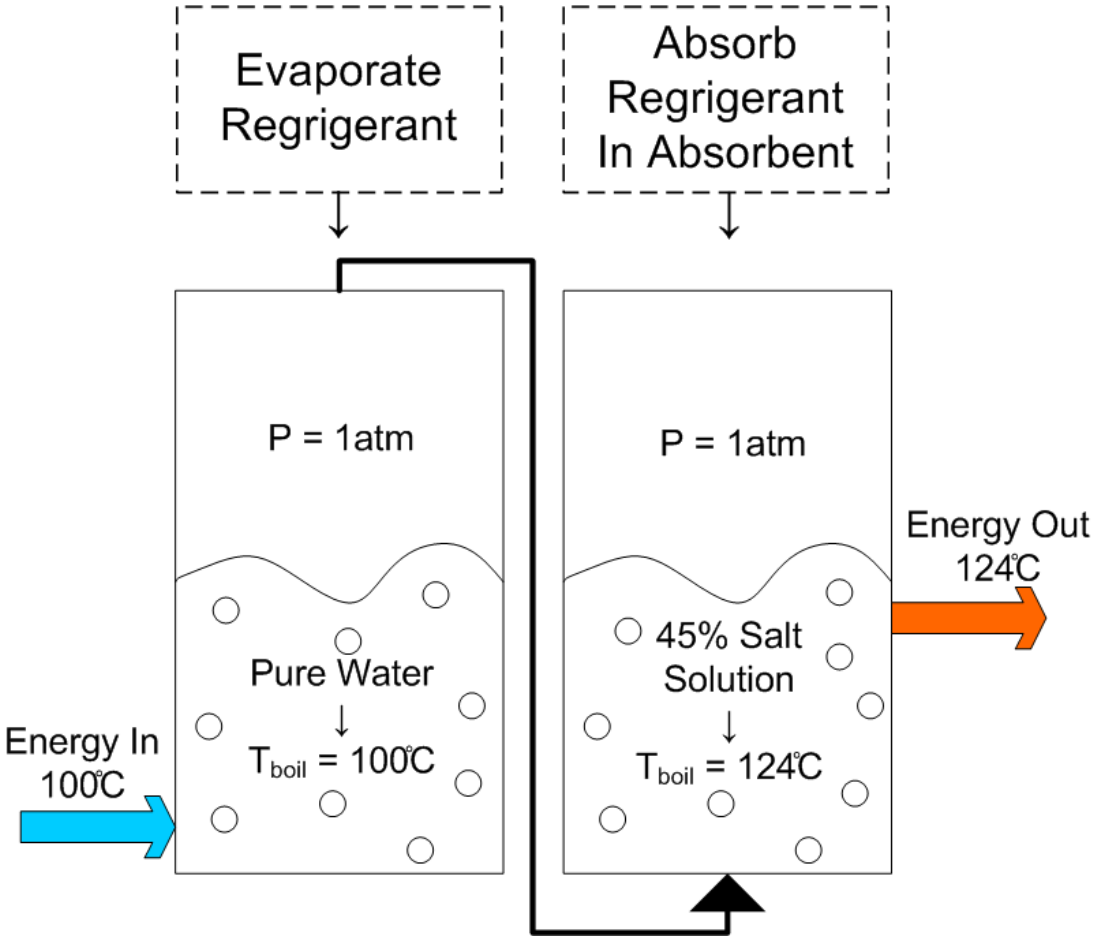


Figure 1.4: Schematic of the fundamental principle behind the operation of an absorption heat transformer

1.1.1 AHT Fundamental Principle

The fundamental principle behind the operation of an absorption heat transformer is the manipulation of boiling temperatures. In Figure 1.4 two vessels are shown, one containing a pure liquid refrigerant (in this case water) and the other an absorbent solution ($LiBr - H_2O$). Both vessels are at atmospheric pressure, and thus the boiling temperature of the refrigerant is 100 °C. The salt content in the $LiBr - H_2O$ solution increases its boiling temperature to a higher value (approximately 124 °C in this example, corresponding to a salt mass fraction of 0.45). Thermal energy may be supplied to the left vessel (containing the refrigerant) at 100 °C producing pure water vapour at 100 °C. This vapour then flows to the other vessel where it is absorbed into the salt solution. Due to the higher boiling temperature of the absorbent, this vessel may be maintained at a higher temperature (in this case 124 °C). This means that the heat of absorption

liberated when the vapour is contacted with the salt solution may be removed from the vessel at this higher temperature. Therefore while thermal heat energy is being supplied to the left hand side vessel (termed the evaporator) at 100 °C, heat energy is simultaneously being removed from the vessel on the right at 124 °C (termed the absorber), achieving a 24 °C gross temperature lift (GTL). This is the fundamental principle behind absorption heat transformers. Further unit operations (typically a condenser and a generator) are required to convert the simple process depicted in Figure 1.4 into a continuous operation (i.e.: by supplying the evaporator with fresh liquid water at 100 °C and the absorber with concentrated salt solution at 45%w/w) as described throughout the remainder of this chapter.

1.2 Single Stage Heat Transformers (SSHT)

1.2.1 SSHT Cycle Description

A single stage heat transformer (SSHT) is effectively a single effect absorption heat pump (or absorption chiller) working in reverse (Srikhirin et al., 2001), and consists primarily of one condenser, one evaporator, one absorber and one generator (Figure 1.5). The primary difference compared to the single stage absorption heat pump is that the absorber and evaporator now operate at high pressure and the condenser and generator at a lower pressure. A heat source supplied to the generator is used to separate the more volatile component, the refrigerant, from the absorbent (generally water and $LiBr - H_2O$ solution respectively) by evaporation at an intermediate temperature ($\sim$100 °C). The refrigerant vapour then flows to the condenser where it is condensed by reducing its temperature, discharging its latent heat to a low temperature heat sink (at $\sim$30-40 °C, generally to atmosphere). The condensed refrigerant is pumped to a higher pressure prior to entering the evaporator, where it is once more evaporated (at $\sim$100 °C) utilising an external heat source (generally the same heat source as used by the generator). This refrigerant vapour is then absorbed in the absorber into the concentrated absorbent solution coming from the generator. Some of the heat of absorption liberated is used to maintain the absorber at a temperature higher than that of the evaporator and generator (approximately 30-60 °C hotter), while the remainder of the liberated heat energy is removed as the high temperature heat product. The dilute absorbent solution leaving the absorber is used to pre-

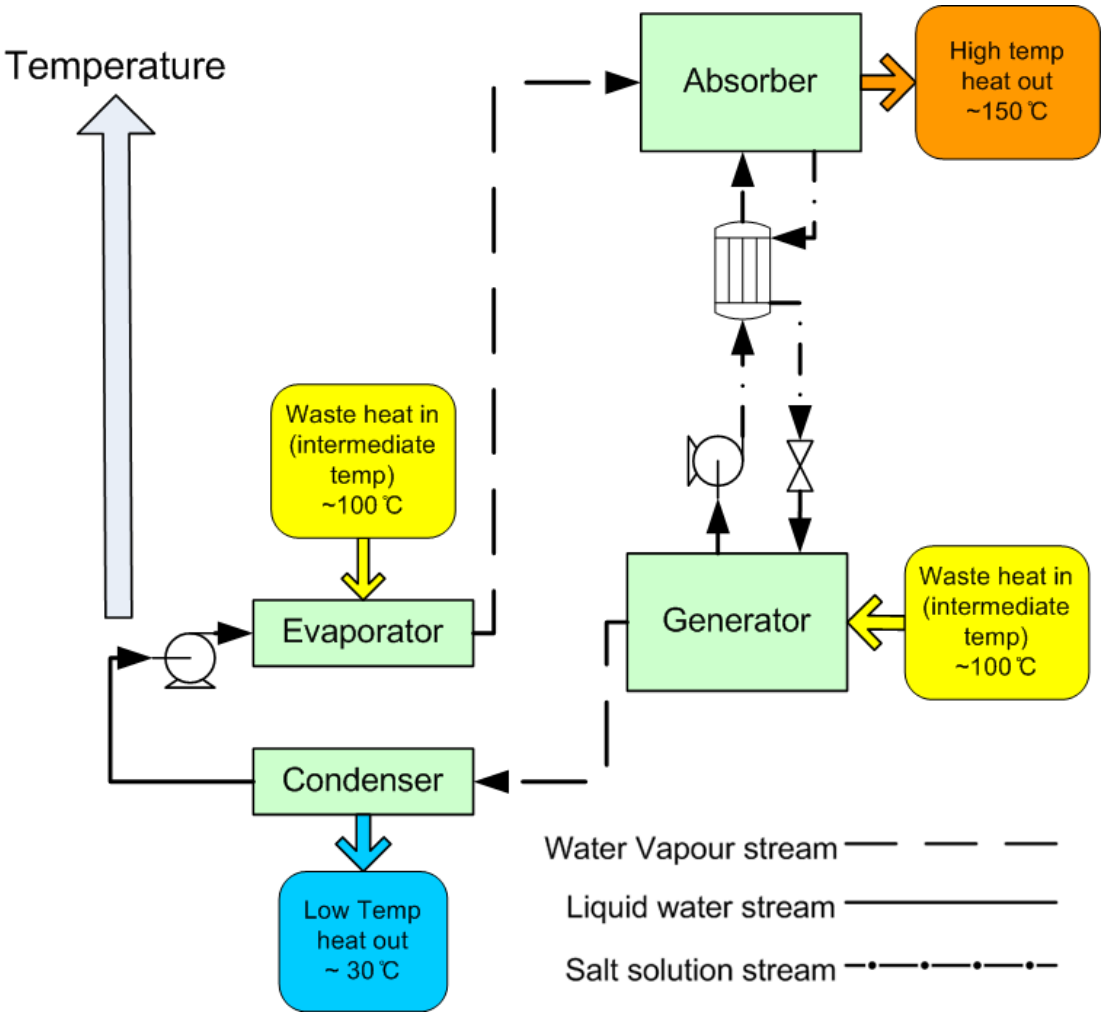


Figure 1.5: Schematic of a single stage heat transformer (SSHT)

heat the concentrated solution entering the absorber from the generator, prior to having its pressure reduced and returning to the generator.

From this description of the SSHT, it may be seen that it is effectively a conventional power cycle in which the turbine has been replaced by a physio-chemical process (i.e.: the interaction between the absorber and generator). This means that the primary difference between the power cycle and a SSHT is that while the power cycle uses the expansion of the vapour produced in the evaporator through a turbine to produce a quantity of mechanical work, a SSHT absorbs this vapour into an absorbent solution (in this case $LiBr - H_2O$) in order to produce a quantity of high temperature useful heat energy.

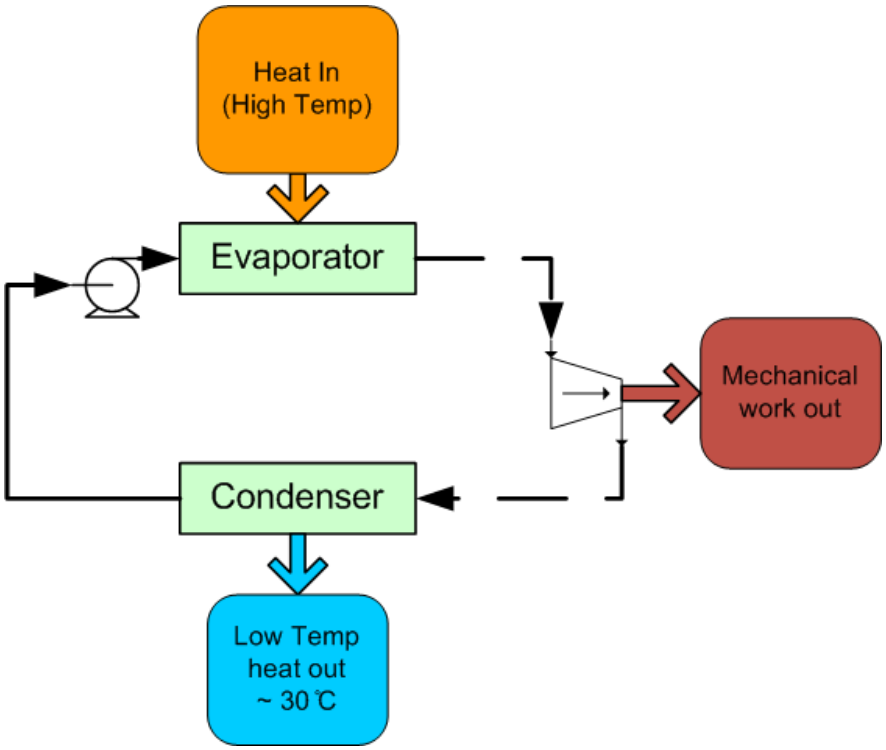


Figure 1.6: Schematic of a conventional power cycle

1.2.2 AHT Performance Criteria

The thermodynamic performance of an absorption heat transformer is quantified by several dependent variables. These dependent variables may be broken up into two categories, namely first law and second law parameters. The first law of thermodynamics states that energy must be conserved in an AHT. Thus this law merely imposes the restriction upon the cycle that the heat energy leaving the system must equal the total heat energy entering it plus any energy created. This type of analysis therefore enables the quantification of cycle attributes such as the fraction of waste heat which is recycled by the system. In order to truly understand a system's performance however, the second law must be used as this quantifies all irreversibilities and non-idealities within components (Rivera et al., 2011a). The second law of thermodynamics states that the entropy of a system never decreases. Reversible systems do not generate any entropy, whereas real systems do. Thus the quantity of entropy generated in a system, or within one component, may be used as a measure of the irreversibility or non-ideality of that system/component. This enables the identification of areas within the cycle which should be addressed in order to improve performance. The first law parameters being used in this thesis are the system's coefficient of performance (COP) and the flow ratio (FR), while the second law parameters are the exergetic

coefficient of performance (ECOP) and the total rate of exergy destruction (E_D).

The system's COP is defined as the ratio of the useful heat product leaving the system with respect to its energy inputs. It can generally be regarded as the most important parameter that quantifies the operation of the system and the objective is to have it at the maximum possible value.

$$COP = \frac{|Q_a|}{|Q_e| + |Q_g| + \sum |W_{pumps}|} \tag{1.1}$$

Exergy is defined as the maximum mechanical work which may be extracted from a heat source at its current temperature and pressure. Exergy is conserved in an ideal process, but destroyed in real processes (Martínez and Rivera, 2009). The ECOP of the system represents the efficiency of the system with respect to retaining exergy. It is defined as the ratio of the maximum useful exergy available from the system to the total exergy entering the system, and it too should be maximised.

$$ECOP = \frac{|Q_a| \left(1 - \frac{T_o}{T_a}\right)}{|Q_e| \left(1 - \frac{T_o}{T_e}\right) + |Q_g| \left(1 - \frac{T_o}{T_g}\right) + \sum |W_{pumps}|} \tag{1.2}$$

The flow ratio is a measure of the approximate size of the unit based upon flow rates. It is defined as the ratio of the total mass flow rate of dilute solution entering the generator to the mass flowrate of refrigerant vapour leaving the same unit. As the Flow Ratio gives an indication of the size of the heat transformer per unit heat output, the general aim is to minimize its value.

$$FR = \frac{\text{mass flow of salt solution entering the generator}}{\text{mass flow of vapour leaving the generator}} \tag{1.3}$$

The total rate of exergy destruction (E_D) is a quantitative measure of the lost work potential of the waste heat energy being supplied to the system, and is simply a summation of the exergy destructions in each component as given by equations 1.4 to 1.6. This parameter represents the amount of the inputted energy which may no longer be used to produce mechanical work following the heat transformation process. It is generally utilised as a means of estimating the amount of irreversibility within the system (a reversible system has no exergy destruction), and thus it should be minimised at all times.

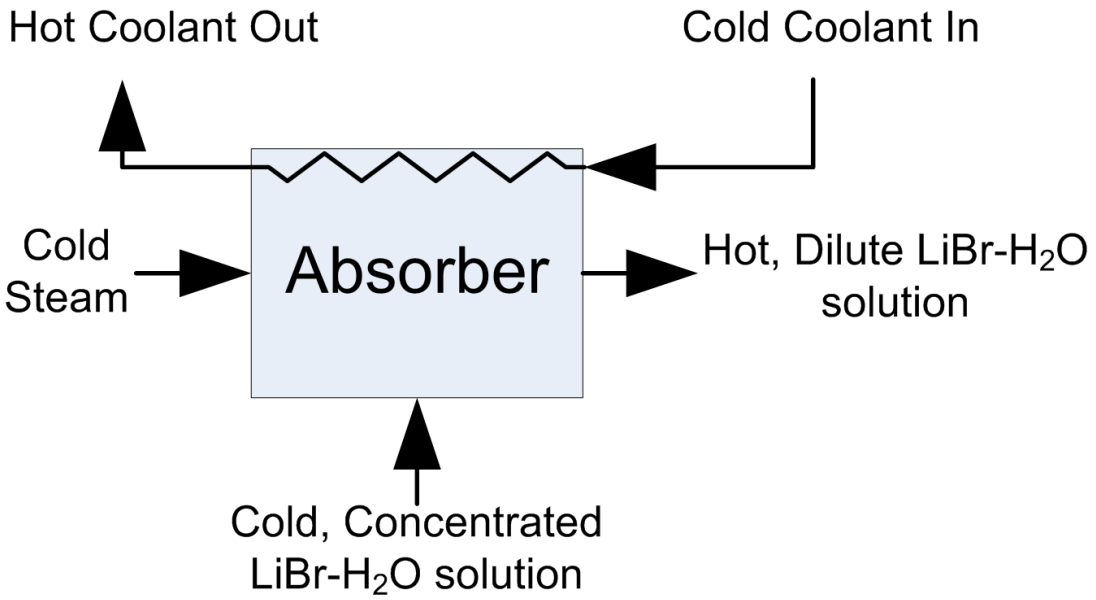


Figure 1.7: Schematic of an the flows entering and leaving an absorber in a heat transformer

$$E = \dot{m}\left[(h - h_o) - T_o\,(s - s_o)\right] \tag{1.4}$$

$$(E_{dest})_k = (E_{in} - E_{out})_k + Q_k\left(1 - \frac{T_o}{T_k}\right) - W_k \tag{1.5}$$

$$E_D = \sum_{k=1}^{\text{number of unit operations}} (E_{dest})_k \tag{1.6}$$

The purpose of a heat transformer is to upgrade the temperature of a waste heat source. Thus a variable termed the gross temperature lift (GTL) is introduced to quantify this temperature augmentation. It is defined as the difference in temperature between the solution leaving the heat transformer's absorber and the vapour leaving its evaporator (equation 1.7).

$$GTL = T_{absorber} - T_{evaporator} \tag{1.7}$$

The flows in and out of an absorber are illustrated in Figure 1.7. The cold concentrated salt solution and the cold water vapour require a certain quantity of the heat of absorption being liberated in order to increase their temperatures to the final temperature of the dilute salt solution leaving the unit. The maxi-

mum GTL which may be achieved by one absorber is calculated by conducting simultaneous mass and energy balances upon the unit, assuming it to behave adiabatically (i.e.: the heat of absorption perfectly balances the sensible heat requirements of the entering concentrated salt solution and water vapour streams). In reality, the evaporator temperature in the SSHT will have been set, and thus this will dictate the pressure in the absorber. A GTL is typically then specified (depending upon the company's requirements) which sets the temperature of the absorber. The salt concentration within the unit can then be calculated with respect to the boiling temperature of $LiBr - H_2O$ (e.g.: select the concentration in order to maintain the absorber at 5 °C below the solution's boiling temperature). Therefore all variables associated with the absorber are known and the enthalpy and mass balances can be used to find the energy transferred to the absorber's coolant, which represents the heat output from the heat transformer.

1.2.3 SSHT Parametric Studies

Several studies have been published in recent years which conduct parametric analyses upon SSHTs in order to obtain a better understanding of the effect which both internal and external settings have upon the cycle's performance variables. This section discusses some of their main findings.

1.2.3.1 Coefficient of Performance (COP)

A number of studies have demonstrated that the COP of a SSHT increases with an increase in both the generator and evaporator temperatures (Sekar and Saravanan, 2011), while decreasing with an increase in the condenser temperature (Horuz and Kurt, 2009, 2010). It may also be increased by increasing the solution heat exchanger efficiency (Chuang et al., 2004).

The increase in COP associated with increasing generator and evaporator temperatures has been shown to be initially quite rapid (Sözen and Yücesu, 2007), but to level off quickly (Rivera and Romero, 2000). Siqueiros and Romero (2007) demonstrated that by raising the evaporator temperature by 1 °C the COP of the cycle can be increased by up to 78%, while a 2 °C augmentation in the heat source temperature can result in an increase in the COP of up to 121%. To the author's best knowledge, the only SSHT publication to contradict any of the above trends was presented by Rivera et al. (2010a), who found that their ex-

perimental COP decreased with an increase in the evaporator temperature. No analysis was provided regarding possible reasons for this deviation.

Romero and Rodríguez-Martínez (2008) showed that the cycle's COP decreases slightly with an increase in absorber temperature (i.e.: the GTL), but then begins to fall off rapidly once some critical absorber temperature is reached. Increasing the evaporator and generator temperatures or else decreasing the condensation temperature is shown to increase this critical absorber temperature (Romero and Rodríguez-Martínez, 2008). A similar increase may be achieved by increasing the effectiveness of the solution heat exchanger (Ibarra-Bahena et al., 2013).

Contrasting results have been presented regarding the effect of the mass flow rate of the heat source to the generator. Guo et al. (2012) demonstrated in a numerical example (using falling film units for all major components) that the system's COP is more sensitive to changes in the heat source's mass flowrate compared to changes in the flowrate of the cooling fluid serving the condenser. This study claims that a decrease in the heat source's mass flowrate decreases the cycle's COP. In contrast, Huicochea et al. (2013a) experimentally demonstrated that increasing the mass flowrate of hot water to supply the generator decreases both the SSHT's COP and ECOP.

1.2.3.2 Exergetic Coefficient of Performance (ECOP)

The SSHT's ECOP shows similar trends to the COP, increasing (initially quite rapidly (Sözen and Yücesu, 2007)) with an increase in the evaporator and generator temperatures before beginning to decrease (Sözen, 2004; Rivera et al., 2010b), and increasing with a decrease in condensation temperature (Rivera et al., 2010b). The ECOP also decreases slightly with an increase in absorber temperature (i.e.: the GTL), before beginning to fall off rapidly once some critical absorber temperature is reached (Rivera et al., 2010b).

1.2.3.3 Flow Ratio (FR)

The flow ratio of the cycle has been experimentally demonstrated by Barragán et al. (1996, 1997) to increase with an increase in the GTL, a decrease in the concentration difference between the concentrated and dilute solutions, a decrease in the solution heat exchanger effectiveness and a decrease in COP. Subsequently Guo et al. (2012) demonstrated that the performance of a SSHT under off-design

conditions is improved by ensuring that the flow ratio remains constant even when the heating and cooling sources to the cycle vary.

1.2.3.4 Exergy Destruction (E_D)

Conflicting results have been presented when identifying which unit operations within the cycle are associated with the largest sources of exergy destruction (and hence irreversibility), even for similar cycles using the $LiBr - H_2O$ working fluid. Rivera et al. (2010a) demonstrated experimentally that the absorber accounts for half of the total irreversibility followed by the condenser and the generator whose exergetic efficiencies are shown to be similar. Rivera et al. (2010b) similarly attributed 30% of the irreversibility to the absorber, followed by the condenser. In turn, Rivera et al. (2011a) experimentally demonstrated that the condenser has the lowest exergetic efficiency, followed by the absorber. While the results presented by Gomri (2009) agree with some of the previous studies that the absorber has the highest irreversibility followed by the generator, this study claims that the condenser is the second most ideal unit within the SSHT (even more ideal than the pumps). No explanations have been offered relating to these discrepancies.

In studies using $NH_3 - H_2O$, no such contrasts have been presented, as both Sözen (2004) and Sözen and Yücesu (2007) attributed the largest exergy destruction rates to the absorber (80% and 70% respectively), with the generator having the second largest inefficiencies.

Ishida and Ji (1999) examined the exergy losses in a SSHT using the concept of energy utilisation diagrams (EUD). From these, it was shown that the majority of the exergy loss in the absorber occurs during the premixing stage, and thus multi-compartment absorption is proposed. Using this redesigned absorber, the ECOP is increased and the exergy destruction due to premixing reduced. The absorber's irreversibility may also be decreased by decreasing its temperature (Rivera et al., 2011a). Likewise the total irreversibility within the SSHT has been demonstrated to decrease with a decrease in the condensation temperature and to increase with an increase in the evaporator and generator temperatures (Rivera et al., 2010b). A method based upon the rate of change of the irreversibility within each component has subsequently been used to determine the optimum pressure ratio and concentrations within a SSHT using $LiBr - H_2O$ (Zebbar et al., 2012).

1.2.3.5 SSHT Simulations

The majority of all simulated SSHT studies predict COP values of between 0.4 and 0.5 (Chuang et al., 2004), and GTLs of approximately 50 °C (Rivera, 2000). Experimental SSHT cycles which have been tested generally do not achieve these high levels of energy recovery however. Rivera and Romero (2000) developed an experimental SSHT using the working fluids $LiBr - H_2O$ to simulate the upgrading of heat energy at 80 °C from a solar pond. A maximum COP of 0.16 was recorded, along with GTLs up to 44 °C. Similarly Best et al. (1997) found their theoretical GTL predictions using the water-Carrol mixture working fluid to be much greater than those previously recorded experimentally, while Rivera et al. (2011a) achieved experimental COPs of 0.23-0.33 in their study. The reduced performances obtained are linked to large heat losses from the equipment in each case.

Several methods have been presented which enable approximate optimum points of operation to be identified when designing a SSHT system such as empirical correlations (Şencan et al., 2007), approximations of the cycle as an endoreversible cycle (Chen, 1995, 1997a,b; Qin et al., 2004b), and general equations for optimum operating points in irreversible cycles (Chen, 1998; Qin et al., 2004a, 2008; Sun et al., 2005; Wu and Chen, 2005).

1.2.4 Alternate Configurations

The standard SSHT configuration (Figure 1.5) has been adapted by some researchers in an attempt to increase its performance. Some of these cycles shall be introduced in this section.

1.2.4.1 Alternate Internal Heat Recovery Configurations

While it has been demonstrated that the simple inclusion of additional heat exchangers within the cycle, such as in the SSHT presented by Ismail (1995) is of little benefit (Barragán et al., 1997), Horuz and Kurt (2010) and Parham et al. (2013) managed to increase the COP of the standard SSHT by approximately 10% by using the solution heat exchanger to preheat the absorber's coolant instead (Figure 1.8). It should be noted however that this configuration doubled the flow ratio (and hence increases capital costs) compared to the standard SSHT, and is

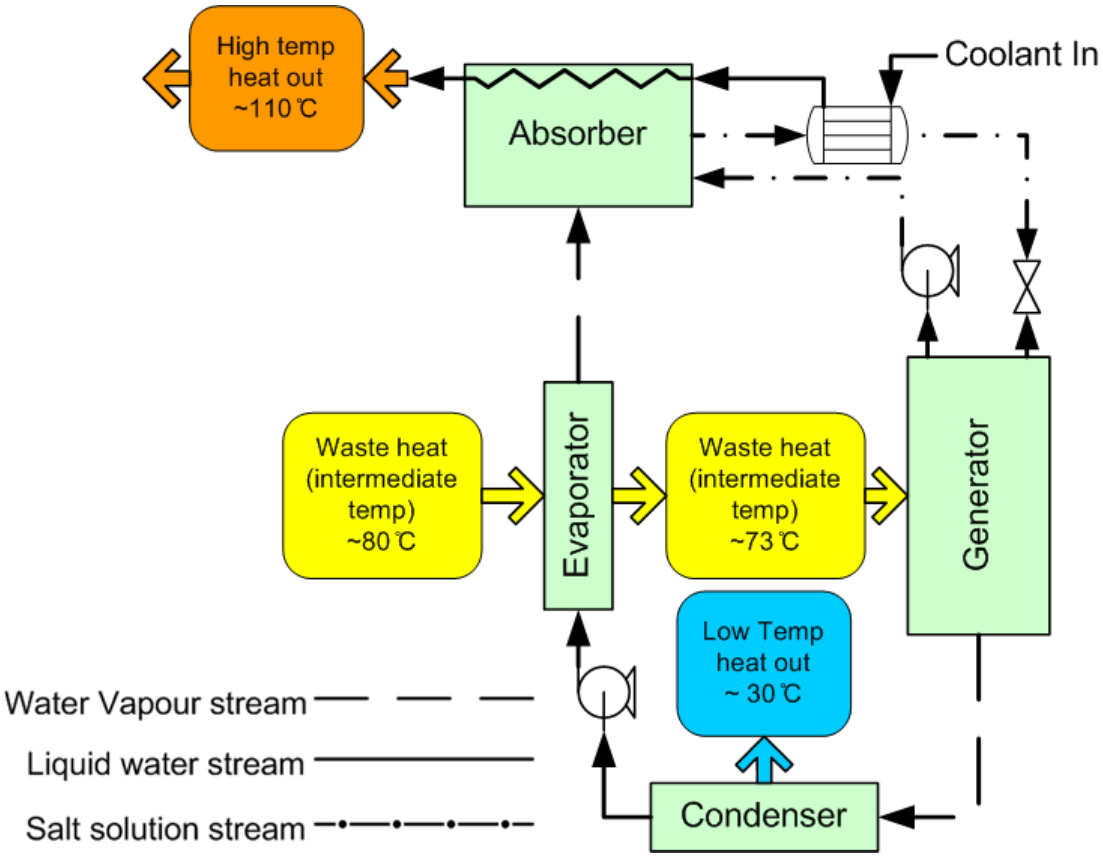


Figure 1.8: Schematic of a single stage heat transformer (SSHT) configuration in which the absorber coolant is preheated by the dilute solution leaving the absorber

completely dependent upon the entering temperature of the absorber's coolant into the system.

1.2.4.2 Multi-component Absorber/Generator

Ishida and Ji (1999, 2000) proposed the use of multi-compartment absorbers and generators (see section 1.2.3.4) in order to minimise exergy losses and hence irreversibility within heat transformers. Scott et al. (1999b,c) developed an open cycle using such a multi-compartment absorber and generator, while Shiming et al. (2001) modelled a self regenerated absorption heat transformer cycle in which the coldest compartment within the multi-compartment absorber is used to heat the multi-compartment generator's hottest compartment. No direct comparisons are made between these systems and the conventional SSHT cycle however.

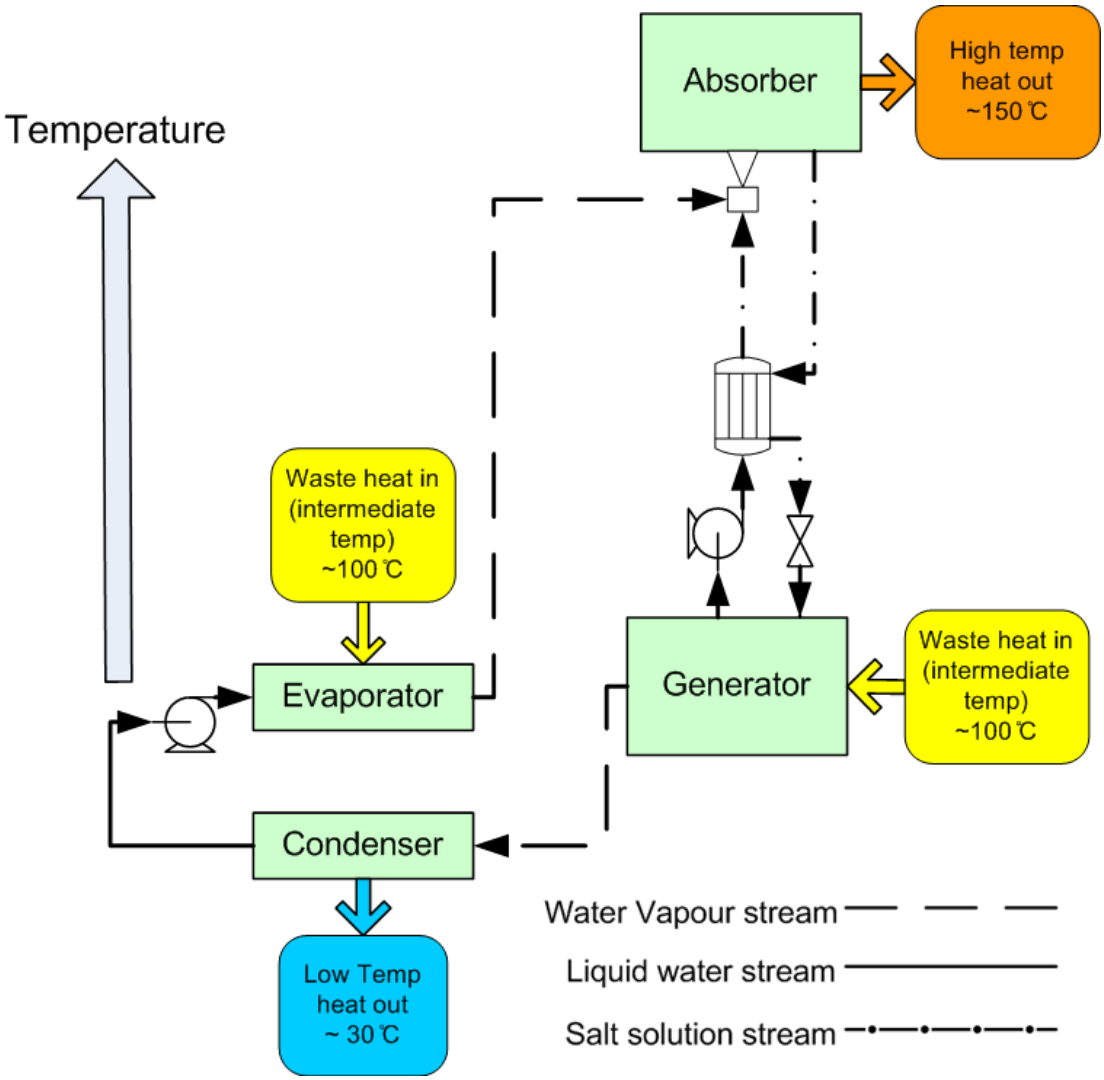


Figure 1.9: Schematic of an ejection absorption heat transformer (EAHT)

1.2.4.3 Ejector Absorption Heat Transformers (EAHT)

Shi et al. (2001) examined the benefits of installing an ejector into the SSHT cycle (called an ejector absorption heat transformer, EAHT). The ejector is placed at the entrance to the absorber as illustrated in Figure 1.9, and the concentrated $LiBr - H_2O$ solution entering the absorber is used to entrain the saturated vapour which gives rise to a higher pressure in the absorber compared to the evaporator. With a compression ratio of 1.2, the GTL increased by 5 °C, and the ECOP by 2.7%. The COP however decreased by 0.4%. Sözen and Yücesu (2007) tested a similar EAHT and determined that the COP is increased by 14%, the GTL by 6 °C, the ECOP by 30% and that the flow ratio is decreased by 57% compared to a conventional $NH_3 - H_2O$ SSHT excluding the ejector.

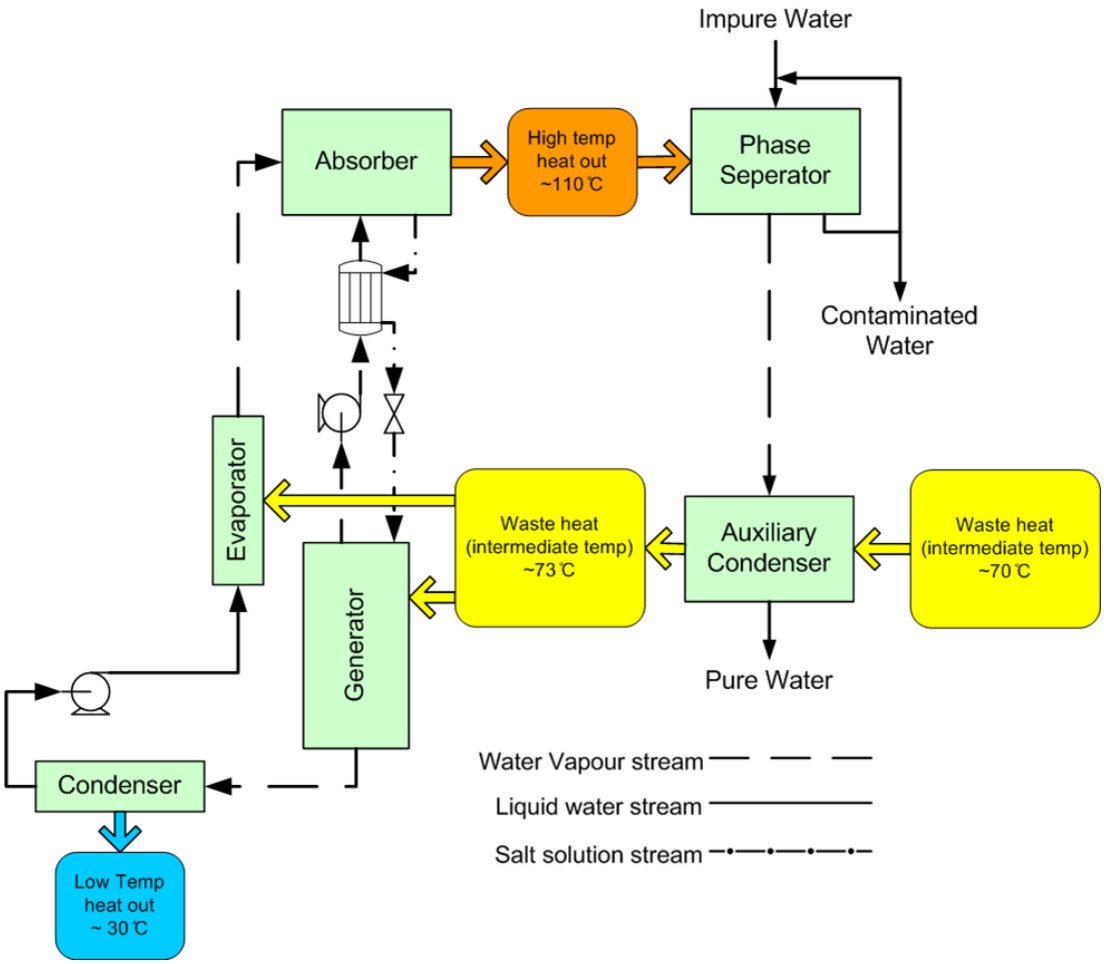


Figure 1.10: Schematic of a single stage heat transformer coupled with a water purification cycle in which the latent heat from the auxiliary condenser is recycled to both the evaporator and the generator

1.2.4.4 Combined SSHT-Water Purification Cycles

In recent years, the majority of single stage heat transformer studies have been conducted in Mexico with the aim of using low temperature heat energy for water purification or desalination purposes. The basic cycle implemented in such studies is shown in Figure 1.10 (Huicochea et al., 2004). The heat energy from the SSHT absorber is used to evaporate some of the impure water which is then subsequently condensed in the auxiliary condenser to produce the distilled water product. The temperature of the heat source to the SSHT is increased by using it to cool the auxiliary condenser. Thus the majority of the heat energy used during the water distillation process is recycled back into the SSHT (Huicochea and Siqueiros, 2010; Meza et al., 2014). The reusing of this heat energy has been demonstrated to increase the COP of this coupled cycle by more than 50%

compared to the conventional SSHT (Romero et al., 2007). COP values as high as 1.02 have also been achieved using an open cycle version of such a combined cycle (Zhang et al., 2014b).

Many studies have examined different modelling techniques to enable in-line control of SSHT cycles combined with water purification systems, such as thermodynamic models (Escobar et al., 2009, 2008), corrosion models (Escobar et al., 2009) and Artificial Neural Networks (Hernández et al., 2008, 2009a,b).

1.3 Advanced Heat Transformers

Single stage heat transformers are capable of achieving temperature augmentations up to approximately 50 °C. Such systems are thus ideally suited to situations in which only small temperature increases are required such as in water purification plants. However in order to achieve greater temperature lifts, more advanced systems, such as multiple stage heat transformers, are required (Romero et al., 2011). Two stage heat transformers are generally capable of achieving gross temperature lifts of approximately 80 °C while maintaining a COP of approximately 0.36 (Martínez and Rivera, 2009). In order to achieve even higher GTLs, triple absorption heat transformers (TAHTs) may be used to reach GTLs of up to ∼145 °C, while recycling approximately 20% of the waste energy (Zhuo and Machielsen, 1996).

1.3.1 Double Absorption Heat Transformers (DAHT)

1.3.1.1 DAHT Cycle Description

A double absorption heat transformer (DAHT) is very similar to a SSHT, except that it includes an additional absorber-evaporator (Figure 1.11). In Figure 1.11 all of the units are arranged vertically according to their temperature (as shown by the axis on the left hand side) to allow for easy interpretation. This system consists of 6 basic units, namely a condenser, a generator, an evaporator, an absorber-evaporator, a solution heat exchanger, and an absorber. A heat source supplied to the generator is used to separate the more volatile component, the refrigerant, from the absorbent (typically water and $LiBr - H_2O$ solution respectively) by evaporation at an intermediate temperature. The refrigerant vapour then flows to the condenser where it is condensed by reducing

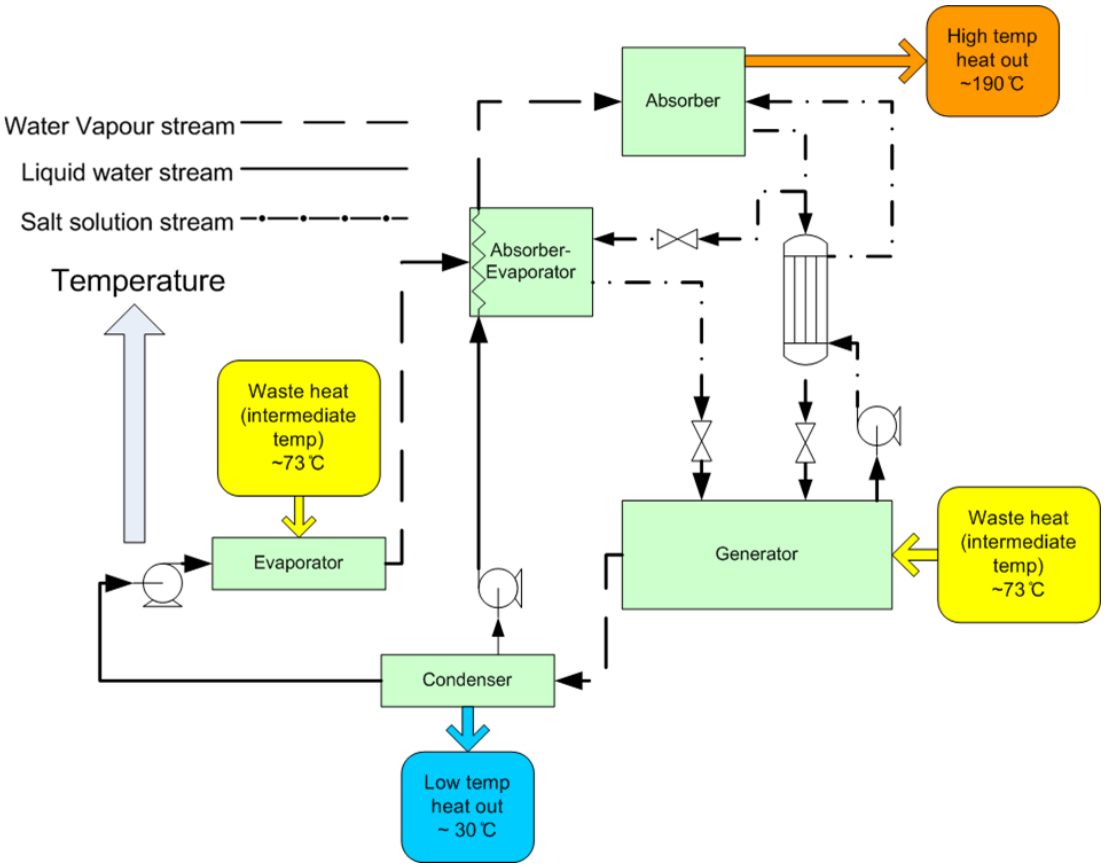


Figure 1.11: Schematic of a double absorption heat transformer (DAHT) in which the dilute solution from the absorber acts as the concentrated solution for the absorber-evaporator

its temperature, discharging its latent heat to a low temperature heat sink (generally to atmosphere). One fraction of the condensed refrigerant is pumped to a higher pressure prior to entering the evaporator, where it is once more evaporated utilising an external heat source (generally the same heat source as used by the generator). This refrigerant vapour is then absorbed in the absorber-evaporator into an absorbent solution. Some of the heat of absorption liberated is used to maintain the absorber-evaporator at a temperature higher than that of the evaporator (approximately 30-60 °C hotter). The dilute solution produced in the absorber-evaporator has its pressure reduced and returns to the generator. The second fraction of the condensed refrigerant leaving the condenser is pumped to a higher pressure (greater than the pressure in the evaporator), and is then evaporated by utilising the remaining heat of absorption being liberated by the absorber-evaporator. This refrigerant vapour is then absorbed in the absorber into the strong absorbent solution coming from the generator. Some of the heat of absorption liberated is used to maintain the absorber at a tempera-

ture higher than that of the absorber-evaporator (approximately 30-60 °C hotter), while the remainder of the liberated heat energy is removed as the high temperature heat product. Some of the absorbent solution leaving the absorber enters the absorber-evaporator and is used to absorb the refrigerant vapour being produced in the evaporator. The remainder of the solution coming from the absorber flows through a solution heat exchanger to pre-heat the concentrated solution entering the absorber prior to having its pressure reduced and returning to the generator.

1.3.1.2 DAHT Parametric Studies

Martínez and Rivera (2009) conducted a detailed exergy analysis upon such a DAHT cycle. The generator was found to be the largest source of irreversibility, accounting for 40% of the total exergy destruction (its irreversibility increasing rapidly with an increase in the generator temperature), followed by the absorber-evaporator at 21%. Its COP remains almost constant with an increase in GTL up to a critical value, before beginning to fall off rapidly.

1.3.2 Alternate Two Stage AHT Configurations

Several authors have attempted to develop various novel two stage configurations which may offer improved performances in certain scenarios. This section outlines the principle configurations which have been reported in the literature.

1.3.2.1 Double Stage Heat Transformers (DSHT)

The primary alternate two-stage configuration is called a double stage heat transformer (DSHT), which is essentially the combination of two single stage heat transformers (SSHTs) as illustrated in Figure 1.12 (Göktun and Er, 2002). The waste heat energy is supplied to one of the SSHT cycles (termed the low temperature cycle) which increases its temperature by ∼50 °C. The absorber of this low temperature cycle is then used to supply some or all of the required input energy to the other SSHT cycle (termed the high temperature cycle). This high temperature cycle further increases the temperature of the heat energy by another ∼30 °C, meaning that a total GTL of ∼80 °C is possible. Much research has been conducted examining the optimum way to couple the low and high temperature SSHT cycles within the DSHT (Rivera et al., 1994; Shi et al., 2001), however the system presented in Figure 1.12 in which the low temperature cycle absorber is

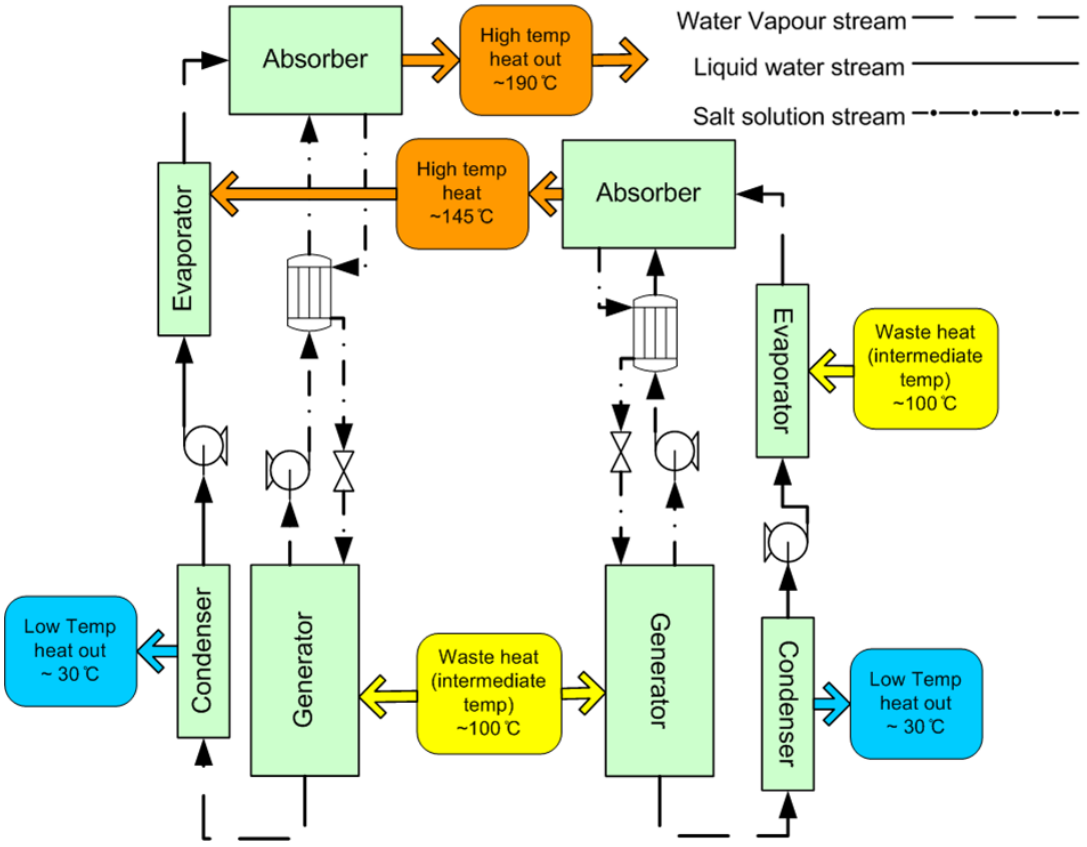


Figure 1.12: Schematic of a double stage heat transformer (DSHT) in which the absorber in the low temperature cycle (right hand side cycle in this figure) is coupled to the evaporator in the high temperature cycle (left hand side cycle in this figure)

coupled to the high temperature cycle's evaporator is generally favoured (Best et al., 1997; Rivera et al., 2001). This cycle has been shown to achieve marginally higher COPs than the DAHT discussed in section 1.3.1 (Romero et al., 2011), while its achievable GTL may be up to 20 °C higher (Best et al., 1997; Rivera et al., 2001). Ji and Ishida (1999) demonstrated that using multi-compartment absorbers and generators within this DSHT cycle further increases its ECOP and achievable GTL.

1.3.2.2 Alternate DAHT Stream Configurations

Several studies have been conducted which examine the possibility of improving the performance of the DAHT illustrated in Figure 1.11 by varying the source of lithium bromide solution entering the absorber-evaporator. Zhao et al. (2003a) and Horuz and Kurt (2009) demonstrated that higher COPs may be achieved if

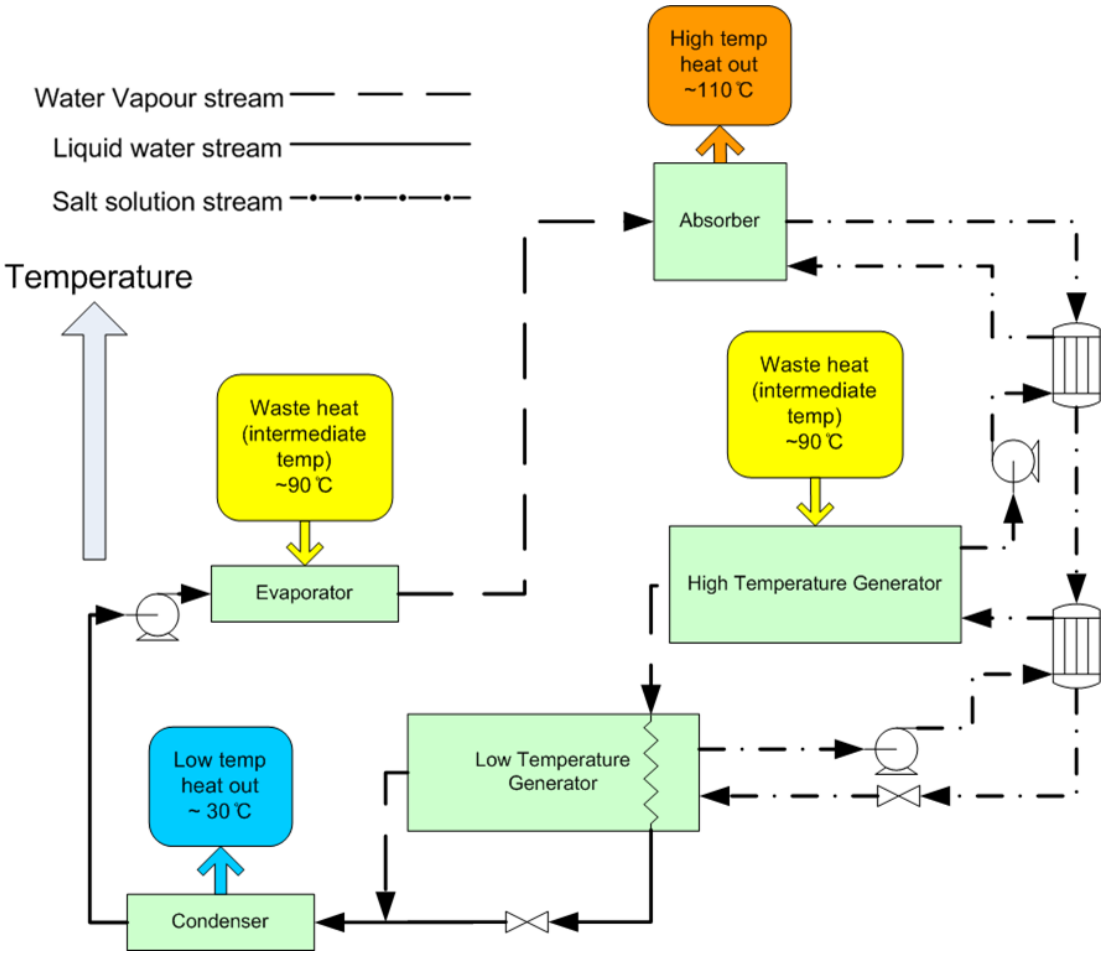


Figure 1.13: Schematic of a double effect heat transformer (DEHT)

all the dilute solution leaving the absorber in Figure 1.11 enters the absorber-evaporator (instead of a fraction of it as in Figure 1.11), while similar COPs were achieved by Zhao et al. (2003b) directly using the concentrated salt solution leaving the generator in the absorber-evaporator (5-10 °C increases in the GTL were also reported in this case). Unfortunately no attention has been focussed upon the effect such switches have upon the flow ratio of the cycle, and thus it cannot be comprehensively stated which configuration is superior.

1.3.2.3 Double Effect Heat Transformers (DEHT)

A double effect heat transformer (DEHT) is a version of the DAHT in which two generators are used instead of two absorbers (Figure 1.13). Zhao et al. (2005) demonstrated that while its COP is approximately 20% greater than that of a corresponding SSHT, such a cycle is only suitable in situations where relatively

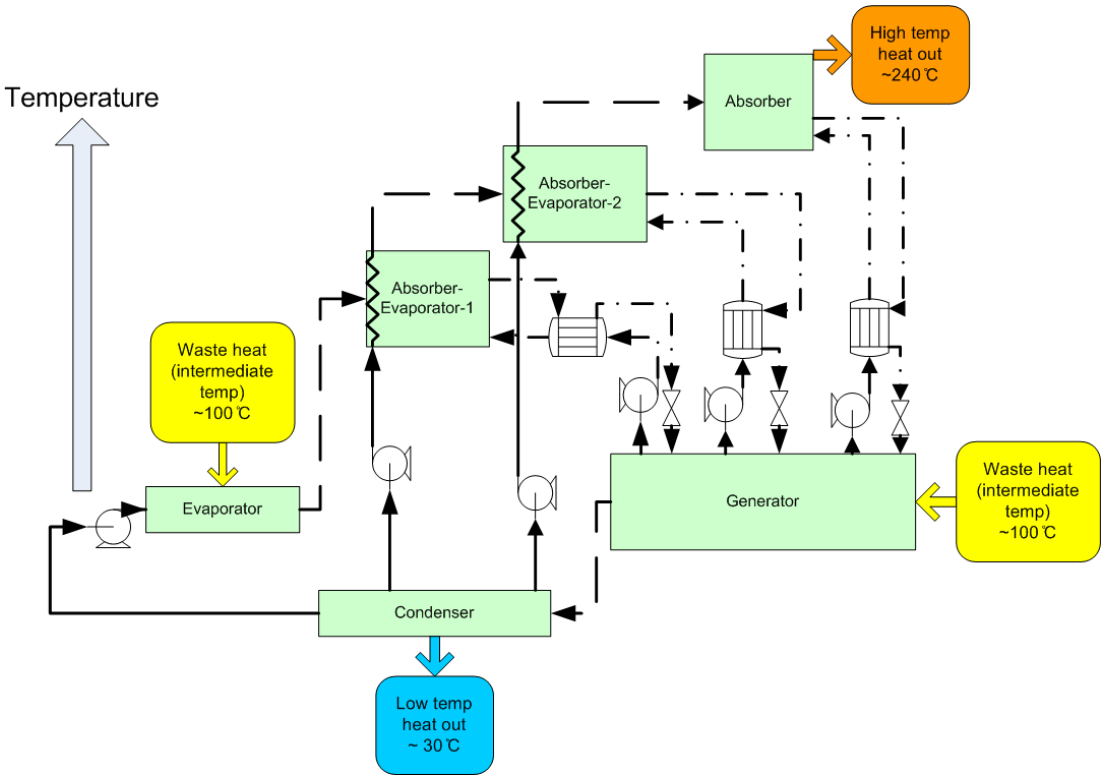


Figure 1.14: Schematic of a triple absorption heat transformer (TAHT)

high temperature heat energy is available and small GTLs are required as the COP of the DEHT is shown to fall off much more rapidly with an increase in absorber temperature than that of the SSHT. Once a certain GTL is exceeded, the SSHT is capable of recycling a greater fraction of the supplied heat energy (Gomri, 2010).

1.3.3 Triple Absorption Heat Transformers (TAHT)

In many industrial applications such as in an oil refinery, heat energy at temperatures greater than 200 °C may be necessary, a requirement which neither single stage nor two stage heat transformers are generally capable of achieving. In situations such as these, a triple stage unit may be utilised (Chuang et al., 2004).

1.3.3.1 TAHT Cycle Description

A triple absorption heat transformer (TAHT) consists of 9 basic units, namely a condenser, a generator, an evaporator, two absorber-evaporators (at different

temperatures), three heat exchangers, and an absorber as demonstrated in Figure 1.14. A heat source supplied to the generator is used to separate the more volatile component, the refrigerant, from the absorbent by evaporation at an intermediate temperature. The refrigerant vapour then flows to the condenser where it is condensed by reducing its temperature, discharging its latent heat to a low temperature heat sink (generally to atmosphere). One fraction of the condensed refrigerant is pumped to a higher pressure (P_1) prior to entering the evaporator, where it is once more evaporated utilising an external heat source (generally the same heat source as used by the generator). This refrigerant vapour is then absorbed in absorber-evaporator-1 into the concentrated absorbent solution coming from the generator. Some of the heat of absorption liberated is used to maintain absorber-evaporator-1 at a temperature higher than that of the evaporator (approximately 30-60 °C hotter). The second fraction of the condensed refrigerant leaving the condenser is pumped to a pressure P_2 (greater than P_1), and is then evaporated by utilising the remaining heat of absorption being liberated by absorber-evaporator-1. This refrigerant vapour is then absorbed in absorber-evaporator-2 into the concentrated absorbent solution coming from the generator. Some of the heat of absorption liberated is used to maintain absorber-evaporator-2 at a temperature higher than that of absorber-evaporator-1 (approximately 30-60 °C hotter). The third (and final) fraction of the condensed refrigerant leaving the condenser is pumped to an even higher pressure P_3 (greater than P_2), and is then evaporated by utilising the remaining heat of absorption being liberated by absorber-evaporator-2. This refrigerant vapour is then absorbed in the absorber into the concentrated absorbent solution coming from the generator. Some of the heat of absorption liberated is used to maintain the absorber at a temperature higher than that of absorber-evaporator-2 (again approximately 30-60 °C hotter), while the remainder of the liberated heat energy is removed as the high temperature heat product. The dilute absorbent solutions produced in absorber-evaporator-1, absorber-evaporator-2 and the absorber are used to preheat the respective concentrated solutions entering them from the generator, prior to having their pressure reduced and returning to the generator.

1.3.3.2 TAHT Parametric Studies

Only a small number of studies have been conducted to date examining the triple absorption heat transformer (TAHT). Zhuo and Machielsen (1996) demonstrated that a TAHT can achieve GTL values of 145 °C while maintaining a COP of

approximately 0.2, while Lee and Sherif (2000) conducted a basic study on the performance of a TAHT in which it is demonstrated that it achieves lower COPs and ECOPs but higher GTLs than both DAHTs and SSHTs. The TAHT's COP and ECOP were shown to increase with an increase in heat source temperature and decrease with an increase in the temperature of the condenser's coolant. It may therefore be observed that very little is known regarding the operation and design of triple stage heat transformers, effectively preventing their potential implementation.

1.4 Working Fluids Comparison

The lithium bromide and water ($LiBr - H_2O$) working fluid combination is the only working fluid combination in current commercial use (Ibarra-Bahena et al., 2013). This is due to a number of advantages such as water's high enthalpy of evaporation and low viscosity which make it an excellent refrigerant (Sekar and Saravanan, 2011). The $LiBr - H_2O$ solution has good heat and mass transfer capabilities (Yin et al., 2000) and is a safe (it is non-toxic, non flammable and non-explosive (Zhuo and Machielsen, 1996)) and environmentally friendly solution (Sekar and Saravanan, 2011). Significant capital cost savings may also be achieved as lithium bromide's negligible vapour pressure means that no rectifying apparatus is required in the cycle (Yin et al., 2000). Generally a single $LiBr - H_2O$ absorber is capable of achieving a gross temperature lifts of approximately 45-50 °C due to the large difference between the vapour pressures of pure water and the salt solution (Rivera, 2000), and also due to the very high solubility of lithium bromide in water (Rivera et al., 2011a). However the main advantage of using $LiBr - H_2O$ is the long period of application experience in manufacture and operation for absorption refrigeration machines (Zhuo and Machielsen, 1996). This experience means that $LiBr - H_2O$ is currently the working fluid standard which is used in almost all analyses and designs and against which all new tested working fluid pairs are compared.

The $LiBr - H_2O$ solution also has several well documented disadvantaged such as the requirement for sub-atmospheric working pressures which means that almost perfect sealing is required in the equipment (Zhuo and Machielsen, 1996). $LiBr - H_2O$ is highly corrosive and causes pitting corrosion especially at temperatures above 150 °C (Stephan et al., 1997). This corrosivity is turn may make equipment excessively expensive in any AHT as highly resistant materials of

construction are required (Zhuo and Machielsen, 1996). Crystallisation in the generator is a potential operational problem, and may be overcome by utilising other fluids with higher solubilities than $LiBr - H_2O$ (Rivera, 2000). The GTL of 45-50 °C achievable using $LiBr - H_2O$ may also be seen as a potential limitation of the fluid which should be addressed (Sözen and Arcaklioğlu, 2007). Non-thermodynamic issues such as the high cost of the obtaining lithium bromide salt and its low availability are additional factors which should be considered (Reyes et al., 2010). Thus much effort has been focussed upon finding alternatives which have similar (or improved) thermodynamic attributes to $LiBr - H_2O$ while eliminating some of its negative features. Many different working fluids have been tested such as $NaOH - H_2O$ (Gränfors et al., 1997; Stephan et al., 1997), E181-TFE (Genssle and Stephan, 2000) and $CaCl_2 - H_2O$ (Barragán R. et al., 1998) and their performances contrasted. This section explores the results of some of these comparisons.

1.4.1 Ammonia-Water

The $NH_3 - H_2O$ working fluid is widely used in absorption heat pumps (absorption chillers), and has lower levels of corrosivity than $LiBr - H_2O$ (Rivera and Cerezo, 2005). Kurem and Horuz (2001) compared the use of $NH_3 - H_2O$ and $LiBr - H_2O$ as working fluids in a SSHT. It was demonstrated that the $LiBr - H_2O$ system had a marginally higher COP under all tested conditions while it also had a slightly higher flow ratio. It is stated that for the $NH_3 - H_2O$ cycle to have the same thermodynamic performance as the $LiBr - H_2O$ working fluid pair, a more complex (and hence expensive) system is required, including better internal heat recovery and the use of a rectifier following the generator. The use of $NH_3 - H_2O$ is especially unsuitable for high temperature applications due to the very high pressures required (a temperature of 100 °C requires a pressure of ∼100bar in the cycle) (Zhuo and Machielsen, 1996). Thus while several heat transformer analyses have been conducted using this working fluid (Sözen et al., 2005; Colorado et al., 2011a; Sözen and Arcaklioğlu, 2007; Colorado et al., 2011b), it does not appear to match the favourable characteristics of $LiBr - H_2O$.

1.4.2 TFE Refrigerant Fluids

Several TFE (2,2,2-tri-fluoroethanol) working fluid combinations have been tested due to their favourable properties such as high thermal stability, flat vapour

pressure curve and strong deviation from Rault's Law (Yin et al., 2000).

A comparison performed by Genssle and Stephan (2000) found that the COP of a SSHT using $LiBr - H_2O$ is generally 15-20% higher than that of an equivalent cycle using E181-TFE. Similarly, Zhao et al. (2005) demonstrated that the COP of a DEHT using the working fluid combination E181-TFE is approximately 10% lower than that of the corresponding system using $LiBr - H_2O$. Zhang and Hu (2012) also tested the working pair E181-TFE, and compared its performance to similar cycles using a water-ionic liquid pair ($EMIM - H_2O$) and $LiBr - H_2O$. Neither the ionic liquid nor the E181-TFE combination could match the thermodynamic output of the $LiBr - H_2O$ working fluid.

Yin et al. (2000) contrasted the use of four different working fluid combinations in a SSHT namely

1. $LiBr - H_2O$
2. NMP (N-methy1-2-pyrrolidone) - TFE (2,2,2-tri-fluoroethanol)
3. E181(dimethylether tetra-ethylene glycol) - TFE (2,2,2-tri-fluoroethanol)
4. PYR(2-pyrrolidone) - TFE (2,2,2-tri-fluoroethanol)

The analysis showed that the $LiBr - H_2O$ combination has the highest COP, but that its GTL is in turn the lowest. The highest GTL was achieved by NMP-TFE. The authors suggest that the $LiBr - H_2O$ combination is most suitable below 150 °C, but that the other fluid combinations may be used effectively up to 200 °C. Thus Wang et al. (2002) compared the performances of three double stage heat transformers (DSHTs), namely one which uses $LiBr - H_2O$ as the working fluid in both cycles, one which uses NMP-TFE in both cycles and one which uses $LiBr - H_2O$ in the first stage and NMP-TFE in the second stage. The DSHT using only $LiBr - H_2O$ always had the highest COP however.

The high toxicity of these TFE working fluids (Yin et al., 2000) combined with their inferior thermodynamic performances, indicate that none of these fluids appear suitable to replace $LiBr - H_2O$ in a general sense.

1.4.3 Water-Carrol Mixture

Several heat transformer studies have been conducted which use the water-Carrol mixture as the working fluid. The Carrol mixture is simply a mixture of LiBr and ethylene glycol ($[CH_2OH]_2$) in the proportion 1:4.5 (Rivera et al., 2001). It

is claimed that using the water-Carrol mixture retains the same thermodynamic properties as the $LiBr - H_2O$ solution, while increasing solubility and allowing salt mass fractions of up to 0.8 to be achieved prior to crystallisation (Ibarra-Bahena et al., 2013). There is no real difference between the solutions' corrosivities, however the water-Carrol mixture does have a higher viscosity (Rivera et al., 2002).

Rivera et al. (2002, 1999) experimentally analysed SSHTs using the water-Carrol mixture as the working fluid. The water-Carrol mixture achieved slightly higher COPs (∼0.3-0.4) and also higher GTLs (approximately 10 °C) than the $LiBr - H_2O$ solution (Rivera et al., 2002). This working fluid was also demonstrated to achieve higher COPs and GTLs than $LiBr - H_2O$ in simulated DAHTs by Rivera et al. (2001).

Thus the water-Carrol mixture has been demonstrated to be a suitable replacement for the $LiBr - H_2O$ solution, as it can match and at times exceed its thermodynamic performances. By using this fluid, the risk of crystallisation in the heat transformer is reduced, however it does not appear to improve upon the severe corrosivity of the $LiBr - H_2O$ working pair and thus other options may be sought.

1.4.4 Additives

Additives may be incorporated into the $LiBr - H_2O$ solution in order to increase its heat and mass transfer capabilities. Rivera and Cerezo (2005) experimentally analysed the benefits of including the additives 1-octanol and 2-ethyl-1-hexanol to a $LiBr - H_2O$ solution operating in a SSHT. Including 400ppm of 2-ethyl-1-hexanol was demonstrated to increase the available GTL by up to 7 °C and to increase the COP by up to 40% compared to the cycle using pure $LiBr - H_2O$, while including 1-octanol in the $LiBr - H_2O$ solution was demonstrated to only increase the SSHT's performance slightly. Following on from these results, Rivera et al. (2011b) conducted a first and second law experimental analysis using the same working fluids (in a SSHT). It was again observed that a concentration of 400ppm of the additive 2-ethyl-1-hexanol had a substantial effect upon all aspects of the heat transformer's performance. In particular it was observed that an increase of up to 100% was possible in the cycle's ECOP at certain operating conditions, and that the irreversibility of the absorber is reduced due to the Marangoni effect.

From these comparisons it may be deduced that adding the additive 2-ethyl-1-hexanol may significantly increase the thermodynamic performance of the SSHT. This additive does however not address the two principle problems of the $LiBr - H_2O$ solution, namely its (relatively) low solubility and high corrosivity.

1.4.5 Salt and Water Combinations

Many of the positive thermodynamic characteristics of the $LiBr - H_2O$ working fluid pair are associated with its use of water as the refrigerant (such as high latent heat of vaporisation), while the negative characteristics are associated with the use of the salt LiBr (such as high corrosivity). Thus a number of researchers have tested different salt and water fluid combinations, in an attempt to replace lithium bromide.

The binary salt solutions $CaCl_2 - H_2O$ (Barragán et al., 1996), $MgCl_2 - H_2O$ (Barragán et al., 1997) and $LiCl - H_2O$ (Reyes et al., 2010) have all been demonstrated to have significantly inferior performances when used as working fluids in SSHTs compared to $LiBr - H_2O$. This is primarily due to the low solubilities of these salts.

Improved performances were reported by Barragán et al. (1998) who experimentally tested ternary salt working fluids. The GTL of the $LiCl - ZnCl_2 - H_2O$ combination was slightly higher than that of an equivalent $LiBr - H_2O$ cycle due to its increased solubility. Unfortunately no COP comparisons could be made due to excessive experimental heat losses from the equipment.

Building upon this success of utilising more complex salt mixtures, Bourouisa et al. (2004) tested the working fluid combination water-(LiBr+LiI+LiNO3+LiCl) in a SSHT. The multi-component salt working fluid was capable of achieving a higher COP value compared to the $LiBr - H_2O$ system under the conditions examined. Unlike the SSHT using $LiBr - H_2O$, its COP did not appear to decrease noticeably with an increase in condensation temperature or a decrease in the evaporator/generator temperature. In certain instances, the new working fluid's performance was almost equal to its maximum achievable value set by the Carnot cycle (real COP was 0.52 compared to Carnot of 0.54). This salt combination has a higher solubility than $LiBr - H_2O$ (hence reducing crystallisation risk) and is also claimed to be less corrosive.

Rivera and Romero (1998) discussed the possibility of using a working fluid con-

sisting of aqueous sodium, potassium and caesium hydroxides (NaOH, KOH, CsOH in the proportions 0.4:0.36:0.24). No direct comparisons were made with the $LiBr - H_2O$ cycle, however this working fluid has previously been shown to achieve higher COPs than $LiBr - H_2O$ in absorption heat pumps (Romero et al., 2001).

The use of an aqueous mixture of alkali-metal nitrate salts (called Alkitrate) has been demonstrated to marginally improve the performance of a SSHT (compared to $LiBr - H_2O$), however extremely low solubilities prevent this combination from becoming a feasible option (Zhuo and Machielsen, 1996).

Thus it may be concluded that the binary salts tested, such as $CaCl_2 - H_2O$ do not have the same thermodynamic capabilities as the $LiBr - H_2O$ solution, however all of the investigated multi-salt combinations showed positive attributes. In particular the working fluid water-(LiBr+LiI+LiNO3+LiCl) appears to be a viable candidate for further research due to its excellent thermodynamic performance and increased solubility.

1.4.6 Working Fluids conclusion

From the results outlined in this section, it is clear that no definitive working fluid combination has been identified which justifies the movement away from the conventional $LiBr - H_2O$ solution. Some multi-salt combinations have been demonstrated to improve both the thermodynamic performance and physical properties of the solution, however only very few references are made to reductions in the corrosivity of the working fluid. This is an issue which must be dealt with in the future, as it represents an important factor when determining the capital and maintenance costs of a heat transformer.

The suggestion has been made by Aristov (2012) that the thermodynamic properties of all absorbent pairs capable of being incorporated into absorption heat transformers should be tabulated in one common database to allow for easy access and consistency. Proposals are made in the paper as to which properties should be included and also which fluid working pairs may be suitable.

1.5 AHT Case Studies

The use of absorption heat transformers has many benefits from a thermodynamic perspective as has been highlighted in preceding sections. However in order to gauge their applicability in industrial scenarios, case studies must be conducted which examine both their thermodynamic and economic performance in different specific scenarios. The reality is that irrespective of how much energy they can recycle, unless heat transformers can generate sufficient rates of return and acceptably short payback periods, they are unlikely targets for industrial investment.

1.5.1 SSHT Case Studies

Abrahamsson et al. (1995) built a pilot self-circulating single stage heat transformer using the working fluid $NaOH - H_2O$, and incorporated it into an evaporation unit in a pulp and paper mill in Sweden. A GTL of 23 °C was achieved, and a payback period of 4.4 years is estimated by the paper.

Mostofizadeh and Kulick (1998) subsequently constructed and tested a 100kW pilot SSHT using the $LiBr - H_2O$ working fluid in Germany. A simple economic calculation example for a SSHT is presented in this paper which may be of qualitative interest due to the experiential knowledge of the research group obtained throughout the lifetime of their own unit. The cost of the 20kW unit (with a COP of 0.48 and a GTL of 55 °C) was estimated at ∼1.7million Deutschmark (€0.87million), giving a predicted simple payback period of 2.4 years.

Scott et al. (1999a) conducted a study upon the various different methods of incorporating a SSHT into a Swedish sugar mill. The AHT is powered using the waste heat from the plant's crystallisation unit, and is used to provide some of the heat to a multi-effect evaporator. The unit was designed to have both a multi-compartment generator, in order to accept a number of different heat source temperatures, and a multi-compartment absorber which is capable of supplying heating demands at various different temperatures along the multistage evaporation cycle. It was demonstrated that the amount of live steam required by the plant would be reduced by 11.8-16.4% using this heat transformer.

Ma et al. (2003) presented the results of having installed a SSHT in a Chinese synthetic rubber plant. The AHT is used to heat water from 95 °C to 100 °C using vapours at 98 °C as the heat source. The cycle operates with a COP of 0.47

and an ECOP of 0.8, and due to the reduction in steam requirements from 2.53 tonnes of steam per tonne of rubber produced to 1.04 tonnes of steam per tonne of rubber produced, gross savings of 3.458 million Yuan per year are achieved giving a payback period of 2 years.

Cortés and Rivera (2010) analysed the feasibility of incorporating a heat transformer into a pulp and paper mill. An exergetic and exergoeconomic study was conducted on the plant and a pinch analysis showed that the inclusion of a heat transformer to preheat water prior to it entering a boiler could potentially reduce the plant's steam consumption by up to 25%.

Zhang et al. (2014a) examined the potential inclusion of a $LiBr - H_2O$ SSHT and a flash evaporator (FE) into a CO_2 capture process which captures 3000 tonnes of CO_2 per day from a 660MW coal fired plant. The AHT-FE system could reduce heat requirements for the CO_2 capture by 2.62%. This energy saving corresponds to a saving of 2.94million RMB Yuan per year and a payback period of 2.4 years.

Huicochea et al. (2013b) examined the simultaneous combination of a fuel cell and a water desalination system with an absorption heat transformer. This combination was shown to improve the efficiency of the fuel cell by 12.4%, enabling a cogeneration efficiency of 57.1% for the combined SSHT-fuel cell pair.

1.5.2 Advanced Heat Transformer Case Studies

Abrahamsson et al. (1997) demonstrated in a case study that due to the achievable COP of 0.3, a two stage heat transformer was not considered economically feasible compared to other heat pumps for the purposes of heating water to 80 °C using hot air at 58 °C in a Swedish paper mill.

Rivera et al. (2003) present the benefits of adding either a SSHT or a DAHT to a distillation column so that the condenser energy at 85 °C may be used to provide some of the required heat to the reboiler at 155 °C. The study shows that installing a SSHT can reduce the boiler requirements by between 26-43% at specific operating conditions, but that the DAHT can reduce the boiler requirements by 28-33% over a wide range of conditions.

Costa et al. (2009) analysed the economic feasibility of incorporating a DAHT into a Canadian paper and pulp mill. The DAHT is used to produce large quantities of low pressure steam at 144 °C using condensate energy at 96 °C. Their system achieved this GTL of 48 °C with a COP of 0.35, and thus was shown to be a

very feasible option with a payback period of 1.6 years. This paper showed the first incorporation of a heat transformer into an energy system as a whole, as the energy leaving the DAHT's condenser was maintained at 60 °C and thus not discharged to atmosphere, but used to preheat fresh water entering the plant.

Ishida and Ji (2000) proposed the inclusion of a DSHT into a humid air turbine (HAT) system. The DSHT used both mulit-compartment absorbers and generators to minimise exergy losses. Using the DSHT to recover the waste heat from the HAT cycle exhaust gases improved the overall efficiency of the HAT cycle by 2% and increased its specific work output by 7.3%.

1.6 Research Motivation and Thesis objective

Throughout this chapter it has been demonstrated that much research has been conducted to date on absorption heat transformers. This work has been primarily focussed upon the thermodynamic optimisation of single stage and double stage units. Such systems are very useful in situations were only relatively small temperature augmentations are required, however in reality, the inability of these systems to achieve temperature increases of more than 50-80 °C limits the application of heat transformers to specific functions. From a thermodynamic perspective, absorption heat transformers have extremely positive attributes, and yet they appear to be a very under-utilised technology. Section 1.5 illustrated that only very few of such units have been built in industry. This is a somewhat unexpected finding, considering that heat transformers have the ability to recycle between 20% and 50% of a plant's waste heat energy with almost no electrical requirements and low maintenance costs (Ishida and Ji, 1999).

A unit such as an absorption heat transformer represents a substantial investment to a company and thus general applicability would be an attractive asset. For example, if a company has waste steam at 100 °C available and wishes to recycle this energy, an attractive proposition may be to convert this energy into a hot oil loop or steam supply at a high temperature such as 220 °C. This would mean that the recycled heat energy is converted into a general high temperature heat energy source which may distributed and used as required throughout the plant. Thus the heat transformer is not coupled directly to any one process, but is a general utility which may be used to recycle heat energy within the plant and reduce fuel requirements. This generality decreases the investment risk associated with a heat transformer, as the increased number of potential uses for the upgraded

heat energy increases confidence that the unit shall be used at (or adequately close to) its maximum capacity throughout its lifetime, ensuring sufficient energy savings. To attain such freedom of operation, a relatively large gross temperature lift is desirable to ensure that the recycled energy may be used in as many different processes as possible throughout the plant. These types of gross temperature lifts are not possible with either single or double stage heat transformers, but may be easily attained with triple stage systems.

Only very limited research has been conducted thus far on triple stage systems as demonstrated in section 1.3.3. No comprehensive analyses have been conducted examining the operation of such units or their design. Without such basic knowledge, it not possible to speculate upon whether or not they are suitable for installation within a plant from either an engineering or an economic perspective. Therefore the state of the art relating to triple absorption heat transformers (TAHTs) should be advanced to overcome such a lack of knowledge. This is the aim of this thesis. A detailed statistical analysis is conducted upon the potential operation of a TAHT, enabling the identification of points of operating optimum. The design of the cycle is also examined in order to develop optimum configurations of the unit, prior to conducting an industrial case study to determine whether a triple absorption heat transformer is an attractive proposition in an industrial setting and what the main factors affecting its economic performance are. A detailed analysis of the system's key unit operation, the absorber is also conducted, in order to ascertain whether current conventional configurations may be improved by utilising alternate designs.

1.7 Thesis Structure

The subsequent structure of this thesis is divided into three separate sections, namely the macroscopic analysis of a triple absorption heat transformer (TAHT) (Part I, Chapters 2 to 5), the detailed analysis of its most important unit operation, the absorber (Part II, Chapters 6 to 8), and the final discussions and concluding remarks (Part III, Chapter 9).

Part I - Whole System Analysis

- Chapter 2 outlines the basic modelling procedures utilised throughout the macroscopic analysis of the TAHT.

- Chapter 3 conducts a statistical analysis upon the TAHT examining all of its operating degrees of freedom and identifying general optimum settings which may be utilised for any TAHT. This section also identifies the largest sources of irreversibility within the cycle.
- Chapter 4 dissects the physical design of the TAHT and reassembles it using heat exchange network modelling techniques in order to determine whether internal heat recovery within the cycle may allow for a reduction in exergy losses.
- Chapter 5 conducts an industrial case study in which the thermodynamically optimised TAHT is applied to the Phillips 66 Whitegate oil refining plant in southern Ireland. A full economic analysis is conducted in order to gauge the attractiveness of such a system in this plant.

Part II - Bubble Absorption Analysis

- Chapter 6 describes the development of an experimental bubble column, enabling analysis of the absorption of steam bubbles in a hotter $LiBr - H_2O$ solution.
- Chapter 7 outlines the experimental findings from the bubble column developed in Chapter 6, and also describes the development of a heat and mass transfer model which may be used to predict the rate of collapse of single steam bubbles in a $LiBr - H_2O$ solution.
- Chapter 8 describes the development of a stochastic model which is used to examine the random behaviour associated with the vertical displacement of the collapsing experimental steam bubbles.

Part III - Discussion and Conclusions

- Chapter 9 reflects upon the findings from this thesis and summarises the conclusions from each chapter.

Part I

Whole System Analysis

Chapter 2

Thermodynamic and Heat Transfer Modelling

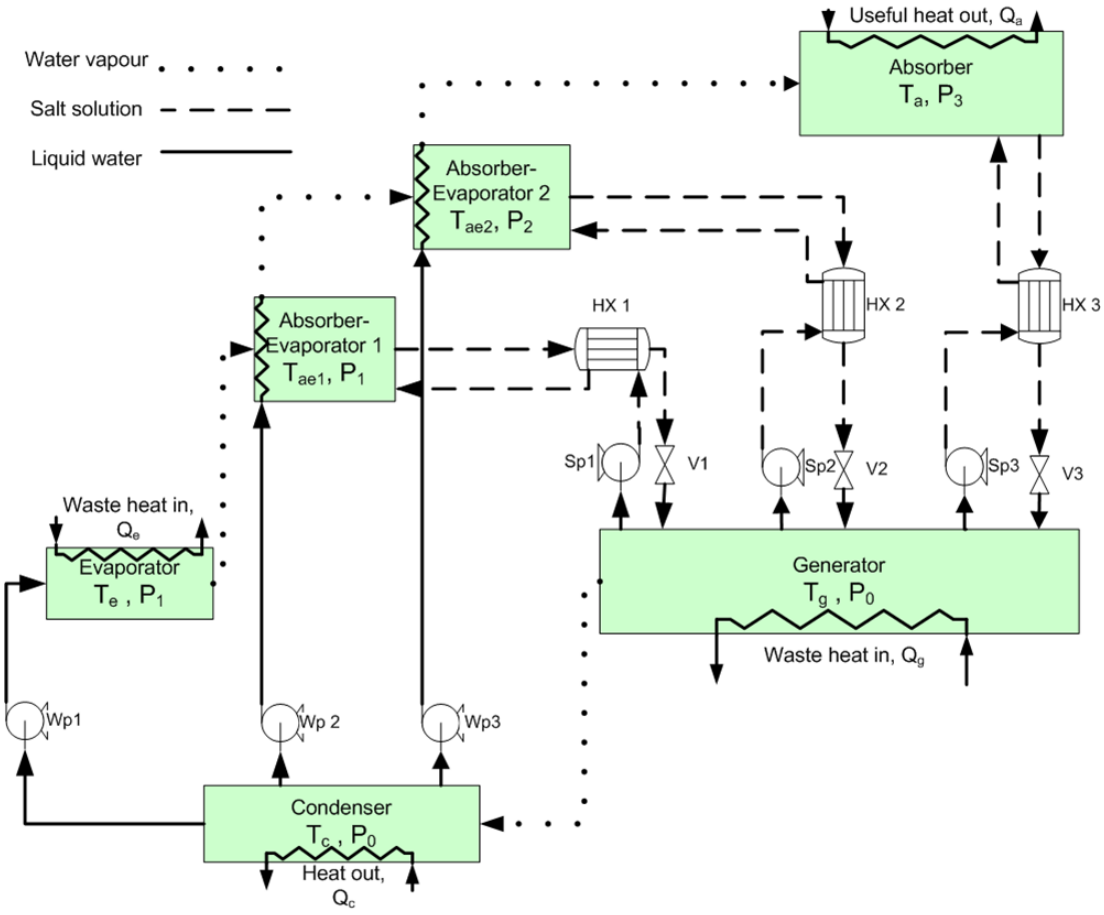


Figure 2.1: Schematic of the triple absorption heat transformer (TAHT) being simulated

2.1 Introduction

As outlined in Chapter 1, the triple absorption heat transformer (TAHT) is the focus of this thesis. The system is illustrated in Figure 2.1, and described in detail in section 1.3.3. In order to begin simulations and testing, a model of such a cycle was generated by the author in Matlab 2010b (Mathworks Inc., Massachusetts, USA). A brief overview of this simulation process is provided in this chapter. It was attempted to generate a generic model capable of predicting the thermodynamic performance of the unit, as well as providing details relating to the individual units within the system (such as equipment surface area). The heat transformer is being modelled assuming the lithium bromide and water working fluid combination ($LiBr - H_2O$).

Nomenclature

A	Surface Area (m^2)
COP	Coefficient of performance of the system
c_p	Specific heat capacity ($W/(m^2K)$)
dT_{Hx}	Minimum pinch temperature (heat transfer gradient) utilised in all system heat transfer operations (K)
D_c	Diameter of the finned tube collar (m)
D_i	Inside diameter of a tube (m)
D_o	Outside diameter of a tubbe (m)
D_s	Diameter of the shell in a shell and tube heat exchanger (m)
D_{tb}	Diameter of the tube bundle (m)
e	Specific exergy (J/kg)
ECOP	Exergetic coefficient of performance of the system
E_D	Total rate of exergy destruction in the heat transformer (W)
E_{dest}	Rate of exergy destruction in a unit operation (W)
F_p	Fin pitch (m)
FR	Flow Ratio in the heat transformer
g	Acceleration due to gravity (m/s^2)
gb	Specific Gibbs Energy (J/kg)
h	Specific enthalpy (J/kg)
h_{fg}	Specific latent heat of vaporisation (J/(kgK)
k	Thermal Conductivity (W/m.K)
L_t	Length of the tubes in a heat exchanger (m)
$\dot{m}$	Mass flowrate (kg/s)
N_r	Number of tube rows in an air-cooled heat exchanger
N_t	Number of tubes in a heat exchanger
N_{TR}	Number of tubes in a row in an air-cooled heat exchanger
m_{vel}	Mass velocity (the mass flowrate per unit area, $kg/(m^2s)$)
P	Pressure (N/m^2)
P_{fin}	Density of fins on a tube in an air-cooled heat exchanger ($\sim 127,000$fins/m)
P_t	Tube pitch (m)
P_l	Distance between tube rows in an air-cooled heat exchanger (m)
Q	Heat exchanger duty (W)
s	Specific entropy (J/kg.K)
S_{gen}	Rate of entropy generation in a unit operation (W)
t	thickness (m)
T	Temperature (K)
x	Salt mass fraction (kg/kg)
x_{eq}	Equilibrium LiBr mass percentage in absorber heat transfer correlation (%w/w)
x_{in}	Mass percentage entering the absorber (%w/w)

Nomenclature continued

x_{inlet}	Mass fraction of LiBr salt entering the generator (kg/kg)
x_{out}	Mass percentage leaving the absorber (%w/w)
x_{vap}	Vapour quality in two phase flow (kg/kg)
z	Distance from tube entrance (m)

Dimensionless Numbers

Gr	Grasshof Number $= (g\alpha_v (T_{Wall} - T_{BulkFluid}) D^3) / \nu^2$
Nu	Nusselt Number $= \alpha D/k$
Pr	Prandtl Number $= c_p \mu / k$
Re	Reynolds Number $= \rho v D / \mu$

Greek Symbols

α	Heat transfer coefficient (W/(m^{2}K))
α_v	Coefficient of thermal expansion (1/K)
ΔT	Difference in temperature between inside of tube and external fluid (K)
ΔT_{inlet}	Difference in temperature between hot an cold streams at the inlet of a heat exchanger (K)
ΔT_{outlet}	Difference in temperature between hot an cold streams at the outlet of a heat exchanger (K)
ρ	Density (kg/m^3)
δ	Film thickness (m)
μ	Dynamic Viscosity (kg/(m.s))
ν	Kinematic Viscosity (m^2/s)

Subscripts

a	Absorber
cb	Convective boiling
e	Evaporator
fin	Fin in an air-cooled heat exchanger
g	Generator
G	Vapour phase
L	Liquid phase
LO	Liquid only (assume that liquid occupies the entire tube)
nb	Nucleate boiling
o	Ambient conditions (T = 298K, P = 101325Pa)
strat	Stratified flow regime
lam	Laminar
trans	Transitional
turb	Turbulent

2.2 Physical Properties

The state functions of liquid water and the aqueous lithium bromide solution ($LiBr - H_2O$) are based upon the Gibbs free energy correlation published by Yuan and Herold (2005) (see the 'Mathematical Function Details' appendix). The individual properties are then determined by the following thermodynamic relations:

$$s = -\left(\frac{\partial gb}{\partial T}\right)_{P,x}, h = gb - T\left(\frac{\partial gb}{\partial T}\right)_{P,x}, v = -\left(\frac{\partial gb}{\partial P}\right)_{T,x} \tag{2.1}$$

The specific heat capacity and the volume correlations for water vapour are referenced from the DIPPR database (DIPPR, 2012). Its state functions are then calculated from the following relations:

$$h = \int_{T_o}^{T} c_p(T)\mathrm{d}T + \int_{P_o}^{P}\left[v - T\left(\frac{\partial v}{\partial T}\right)_P\right]\mathrm{d}P \tag{2.2}$$

$$s = \int_{T_o}^{T} \frac{c_p(T)}{T}\mathrm{d}T - \int_{P_o}^{P}\left(\frac{\partial v}{\partial T}\right)_P \mathrm{d}P \tag{2.3}$$

2.3 Thermodynamic modelling of the TAHT

In order to develop a macroscopic thermodynamic model of the triple absorption heat transformer and apply it for comparative purposes, a number of basic assumptions are made, namely:

1. The system is in thermodynamic equilibrium at all times, and is operating under steady state.
    - Heat transformers are expected to operate continuously as utilities in energy intensive plants. In such a scenario the transient start-up and shut-down periods are very short in comparison to the time spent by the system at steady state. As one of the primary objectives is to identify optimum operating conditions and configurations, it is not considered necessary to include the additional complexity of transient operation.

2. Heat losses from components are very small relative to heat fluxes, and are thus not included in the model.
    - Heat fluxes in the individual unit operations within a typical TAHT may be in the order of 1×10^7W.
    - Heat losses are intrinsically linked to the physical design of cycle itself and cannot therefore be examined in a general sense but should be quantified on a case by case basis.
3. Pressure drops across the system are very small relative to the system's pressure range, and are thus not included in the model.
    - Pressures within a TAHT may range from almost pure vacuum (∼-0.97barg) in the condenser and generator to almost 7 barg in the absorber.
4. The salt utilised in the absorbent solution (LiBr) is assumed to have negligible vapour pressure.
    - One of the advantages of using the lithium bromide salt is that it is non-volatile (Kurem and Horuz, 2001).
5. Ambient temperature is taken to be equal to 298.15 K (for exergy analysis).
6. Flows through valves are assumed isenthalpic.
    - It is anticipated that heat losses from the valves are negligible. This may also depend upon the ability to insulate the valve.
7. Pumps are assumed to have an isentropic efficiency of 80%.
    - The work required by pumps in a heat transformer is negligible, and generally ignored as it is extremely small (Siqueiros and Romero, 2007).
8. The refrigerant vapour is assumed to evaporate and condense completely in the two absorber-evaporators, the evaporator, and the condenser.
    - Once more this is completely dependent upon the physical design of individual systems.

2.3.1 Governing Equations

Each component (k) in the system is modelled by solving the mass and enthalpy balances given by equations 2.4 and 2.5 respectively.

$$0 = \left(\sum \dot{m}_{out} - \sum \dot{m}_{in}\right)_k \tag{2.4}$$

$$Q_k = \left(\sum \dot{m}_{out} h_{out} - \sum \dot{m}_{in} h_{in}\right)_k + W_k \tag{2.5}$$

As outlined in the objectives for this thesis, it is intended to determine the relative exergy destructions within each unit operation and to thus identify the greatest sources of irreversibility within the cycle. The specific exergy (J/kg) of any stream is defined as the specific work which it could generate using an ideal Carnot cycle, and is given by equation 2.6. In this equation, the subscript 'o' represents the reference ambient condition. Thus h_o represents the enthalpy which that stream would have if it were at ambient temperature and pressure.

$$e = [(h - h_o) - T_o (s - s_o)] \tag{2.6}$$

The total rate of exergy being destroyed in any one unit operation is defined as the exergy entering the unit, less the exergy leaving the unit as is given by equation 2.7.

$$(E_{dest})_k = \left(\sum \dot{m}_{in} e_{in} - \sum \dot{m}_{out} e_{out}\right)_k + Q_k \left(1 - \frac{T_o}{T_k}\right) - W_k \tag{2.7}$$

A simplified method of calculating the exergy destruction rate in any unit operation which eliminates the requirement for the definition of reference state enthalpies and entropies may be derived using the unit's entropy generation. The entropy generation (S_{gen}) across any steady state unit (k) is given by equation 2.8.

$$(S_{gen})_k = \left(\sum \dot{m}_{out} s_{out} - \sum \dot{m}_{in} s_{in}\right)_k - \left(\frac{Q_k}{T_k}\right) \tag{2.8}$$

Substituting equations 2.5, 2.6 and 2.8 into equation 2.7, leaves the simplified relationship between any unit's rate of exergy destruction and its entropy gener-

ation shown in equation 2.9.

$$(E_{dest})_k = T_o\,(S_{gen})_k \tag{2.9}$$

2.3.2 Dependent Factors

The dependent factors being analysed in this thesis can be broken up into first law and second law parameters. The first law parameters are the system's coefficient of performance (COP) and the flow ratio (FR), while the second law parameters are the exergetic coefficient of performance (ECOP) and the total rate of exergy destruction (E_D).

The system's COP is defined as the ratio of the useful heat product leaving the system with respect to the system's energy inputs. It can generally be regarded as the most important parameter that quantifies the operation of the system and the objective is to have it at the maximum possible value. Only the heat energy leaving the system from the absorber is considered useful, and therefore the COP is the ratio of the absorber's heat load to the quantities of waste heat entering the system and the work supplied to the pumps.

$$COP = \frac{|Q_a|}{|Q_e| + |Q_g| + \sum |W_{pumps}|} \tag{2.10}$$

The ECOP of the system represents the efficiency of the system with respect to retaining exergy. It is defined as the ratio of the maximum useful exergy available from the system to the total exergy entering the system, and it too should be maximised. Useful exergy is defined in this case as the maximum work which may be recovered from a reversible Carnot cycle using the absorber's heat energy. This maximum work is given by equation 2.11 (equation 2.11 is derived by conserving both enthalpy and entropy on a Carnot cycle).

$$W_{max} = |Q_a| \left(1 - \frac{T_o}{T_a}\right) \tag{2.11}$$

The maximum work available from the waste heat streams being supplied to the unit prior to the heat transformation process are calculated using equations analogous to equation 2.11. The ECOP is therefore simply the ratio of the maximum work achievable from absorber's heat load to the maximum work achievable from

the streams entering the system (equation 2.12).

$$ECOP = \frac{|Q_a|\left(1-\frac{T_o}{T_a}\right)}{|Q_e|\left(1-\frac{T_o}{T_e}\right)+|Q_g|\left(1-\frac{T_o}{T_g}\right)+\sum|W_{pumps}|} \tag{2.12}$$

The flow ratio is a measure of the approximate size of the unit based upon flow rates. It is defined as the ratio of the total mass flow rate of dilute solution entering the generator to the mass flowrate of refrigerant vapour leaving the generator. As the Flow Ratio gives an indication of the size of the heat transformer per unit heat output, the general aim is to minimize its value.

$$FR = \frac{\text{mass flow of salt solution entering the generator}}{\text{mass flow of vapour leaving the generator}} \tag{2.13}$$

The total rate of exergy destruction (E_D) is a quantitative measure of the lost work potential of the waste heat energy being fed to the system. It is the amount of this inputted energy which may no longer be used to produce mechanical work following the heat transformation process. It is generally utilised as a means of estimating the amount of irreversibility within the system (a reversible system, has no exergy destruction), and thus it should be minimised at all times. It is simply quantified by summing the exergy destruction for each component as outlined in equation 2.14.

$$E_D = \sum_{k=1}^{\text{number of unit operations}} (E_{dest})_k \tag{2.14}$$

It should be noted that while qualitatively they describe the same phenomenon (the quantity of irreversibility within the system), the ECOP and the E_D may show slightly different trends at times. This is due to the fact that while the ECOP considers merely the useful exergy leaving the system (i.e.: from the absorber), E_D accounts for the exergy destruction in every unit operation. For example if some change in operating variables were to cause the total exergy destruction in the unit to decrease (i.e.: E_D decreases), then the variable ECOP may either increase (if this change in variables causes an increase in the heat flow from the absorber) or decrease (if the change in variables instead causes an increase in the heat flow from the condenser which is not considered by the ECOP). Thus the ECOP and E_D trends should be considered separately, as they describe slightly different phenomena.

2.3.3 Heat of Absorption

The critical unit operation within a heat transformer is the absorber. It is this unit which enables the system to achieve an increase in the temperature of supplied waste heat energy. In the absorber, water vapour is absorbed into a concentrated salt solution. This absorption is highly exothermic and in many ways similar to pure condensation of the water vapour stream. The primary difference between such a single fluid condensation and this absorption is the dilution effect caused by the associated increase in the salt solution's water concentration (equation 2.15).

$$h_{abs} = h_{fg} + h_{dilution} \tag{2.15}$$

The most practical method of estimating this heat of absorption is to use the specific enthalpy of the $LiBr - H_2O$ solution as calculated in equation 2.1 to obtain the specific partial enthalpy of water in the $LiBr - H_2O$ solution (i.e.: the enthalpy of 1kg of water molecules in the $LiBr - H_2O$ solution at a particular concentration, temperature and pressure) as shown in equation 2.16.

$$h_{pw} = h_L - x\frac{\partial h_L}{\partial x} \tag{2.16}$$

This partial enthalpy of water can then be used to calculate the heat of absorption using a simple enthalpy balance (equation 2.17).

$$h_{abs} = h_G - h_{pw} \tag{2.17}$$

The relative magnitudes of the condensation and dilution terms in equation 2.15 may be visually compared in Figure 2.2 (where the pure fluid condensation is represented by the case where the salt mass fraction is equal to zero). It is clear that while a significant difference exists between the enthalpy of absorption and water's latent heat of vaporisation at high salt concentrations, the majority of the released energy is due to this condensation effect.

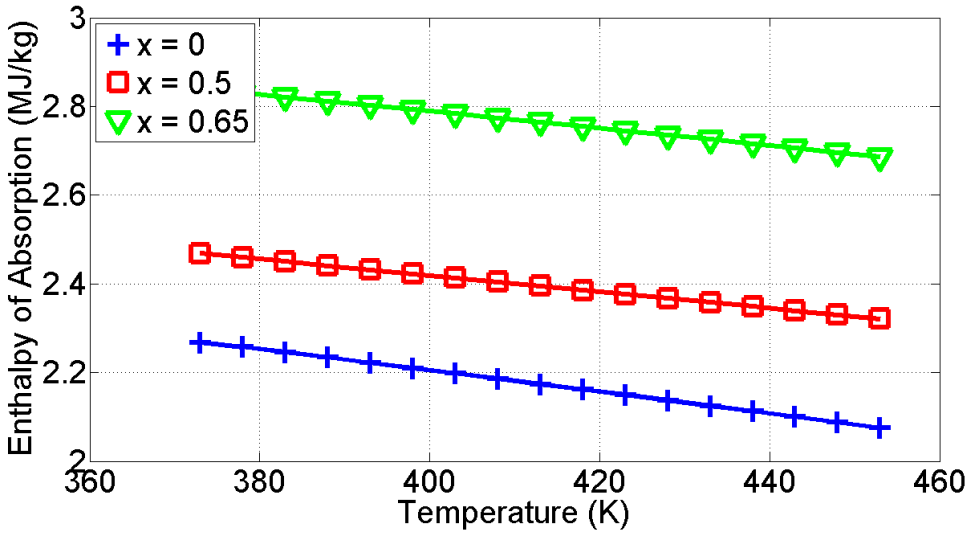


Figure 2.2: Comparison of the specific enthalpy of absorption of steam vapour in $LiBr - H_2O$ solution at different salt concentrations at atmospheric pressure (101325Pa)

2.4 Individual Unit design and modelling

Each individual unit operation is modelled separately using specific designs, in order to enable estimates of equipment sizes and related capital costs.

2.4.1 Solution Heat Exchangers

The solution heat exchangers in this cycle are designed as simple shell and tube units. Tube side flow is modelled using a correlation in which Nusselt numbers are calculated separately for the laminar, transition and turbulent regimes as demonstrated in equations 2.18 to 2.20 (Ghajar and Tam, 1994), where a, b and c are a set of constants which depend upon the flow conditions.

$$Nu_{lam} = 1.24\left[\left(\frac{RePrD_i}{z}\right) + 0.025\left(GrPr\right)^{0.75}\right]^{1/3}\left(\frac{\mu_{bulk}}{\mu_{wall}}\right)^{0.14} \tag{2.18}$$

$$Nu_{trans} = Nu_{lam} + \left(exp\left[\frac{(a - Re)}{b}\right] + Nu_{turb}^{c}\right)^{c} \tag{2.19}$$

$$Nu_{turb} = 0.023Re^{0.8}Pr^{0.385}\left(\frac{z}{D_i}\right)^{-0.0054}\left(\frac{\mu_{bulk}}{\mu_{wall}}\right)^{0.14} \tag{2.20}$$

Shell side heat transfer coefficients are estimated using the correlation presented by Taborek (1983) which calculates an ideal heat transfer coefficient in the shell side, and then applies correction factors to this figure to account for flows across baffle cuts (J_C), baffle leakage flows (J_L), unequal baffle spacings (J_R), flow over the tube bundle (J_B), laminar flow (J_S) and viscosity variations ($J\mu$) as shown in equations 2.21 and 2.22 (see the 'Mathematical Function Details' appendix).

$$\alpha_{ideal} = j_i(Re) m_{vel} cp Pr^{-2/3} \tag{2.21}$$

$$\alpha = J_C J_L J_B J_R J_S J_\mu \alpha_{ideal} \tag{2.22}$$

These heat transfer coefficients will be used (without being explicitly stated), in any shell or tube flows consisting of a single phase fluid.

2.4.2 Absorber

The absorber is modelled as a vertical falling film heat exchanger, as this is the most researched and documented type of $LiBr - H_2O$ absorber used in absorption heat transformers (Abrahamsson et al., 1995; Ma et al., 2003; Guo et al., 2012). A schematic of its operation is provided in Figure 2.3. Both the concentrated $LiBr - H_2O$ solution and water vapour enter the absorber from the top. They are then contacted on the outside of tubes, where the water vapour is absorbed exothermically into the $LiBr - H_2O$ solution. This heat of absorption is partially removed by a cooling stream (in this design Ethylene Glycol) which is flowing co-currently to the $LiBr - H_2O$ solution on the inside of the tube bank (this must be a co-current unit as the entering concentrated $LiBr - H_2O$ solution is initially at a lower temperature).

In order to model the absorber, correlations describing the heat and mass transfer in the unit are required. There are many models available in literature which analyse the absorber using detailed partial differential equation models, however as this is extremely computationally expensive, it was not considered feasible to include such analysis into this simulation. The experimental correlation proposed by Andberg and Vliet (1983) is selected instead which uses the inlet and outlet solution conditions to estimate the heat transfer coefficient using equations 2.23 and 2.24.

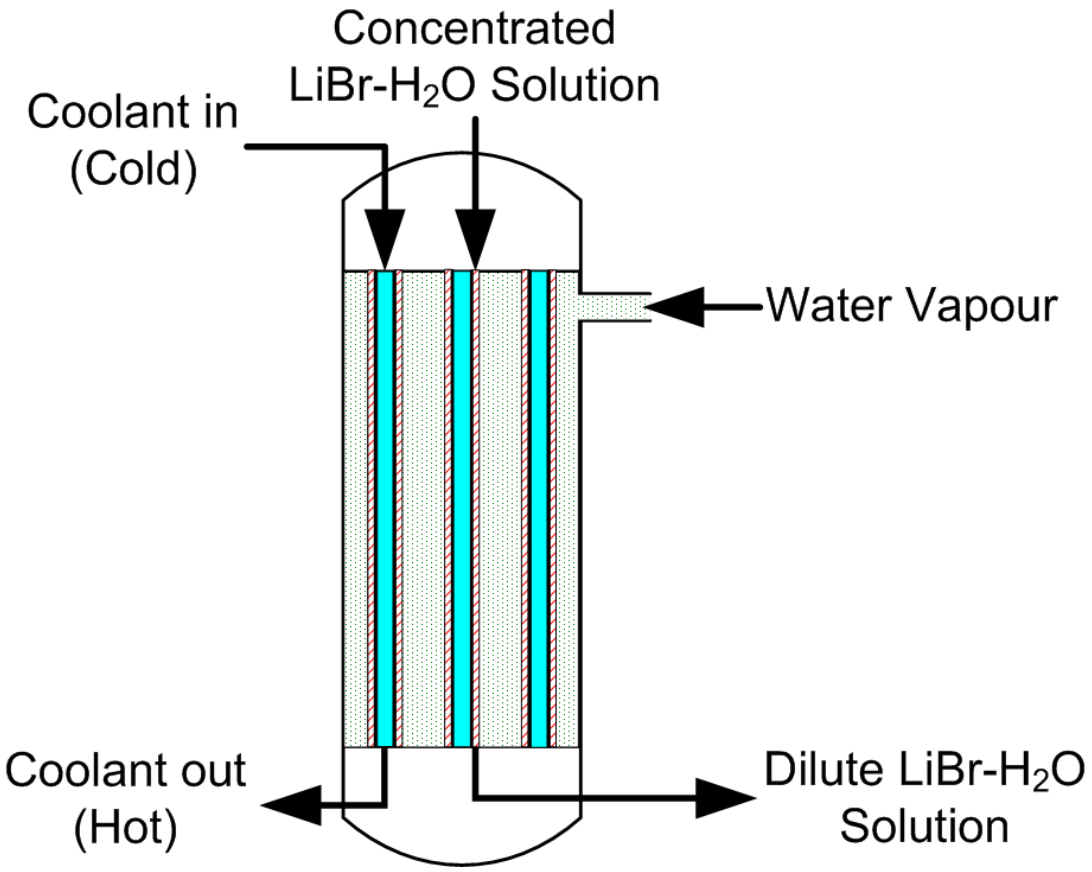


Figure 2.3: Schematic of the falling film absorber modelled in this heat transformer

$$\delta = \left(\frac{3\mu\Gamma}{\rho^2 g}\right)^{\left(\frac{1}{3}\right)}, \Gamma = fn(x_{in}, x_{out}, L_t, P) \tag{2.23}$$

$$\alpha = \frac{k}{\delta}\left(0.029 Re^{0.53} Pr^{0.344}\right) \tag{2.24}$$

The absorption is then assumed to be heat transfer rate limited, meaning that the rate of mass transfer may be deduced by comparing this heat transfer rate to the quantity of energy released during the absorption process.

2.4.3 Condenser

The condenser is a critical component of the cycle as it determines the cost of discharging the remaining waste heat energy to atmosphere. As cooling water supplies cannot be guaranteed in any plant, in order to ensure the generality of

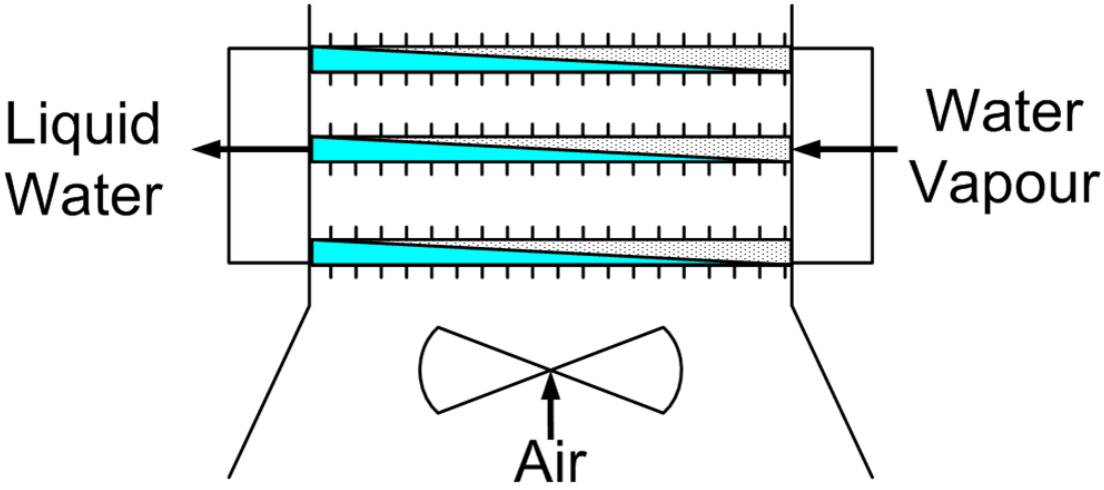


Figure 2.4: Schematic of an air-cooled condenser simulated in the heat transformer

this study's results, air-cooled heat exchangers are used to represent the condenser in this simulation (Figure 2.4). The correlation presented by Wang et al. (1996) is used to estimated the air side heat transfer coefficient in this study (equations 2.25 to 2.28). In this correlation, a Colburn factor (j) is calculated for each tube row (N) and then an average value (symbolised by $\langle\rangle$) is used to calculate the air-side heat transfer coefficient using equations 2.27 and 2.28, where all fluid properties are calculated using an average of the inlet and outlet air conditions.

$$j_4 = 0.14Re^{-0.328}\left(\frac{P_t}{P_l}\right)^{-0.502}\left(\frac{F_p}{D_i}\right)^{0.0312} \tag{2.25}$$

$$j_N = 0.991 j_4\left[2.24Re^{-0.092}\left(\frac{N}{4}\right)^{-0.031}\right]^{0.607(4-N)} \tag{2.26}$$

$$Nu = \langle j\rangle\, RePr^{1/3} \tag{2.27}$$

$$\alpha = \frac{(Nu)\,(k)}{D_c} \tag{2.28}$$

The tubeside condensation is modelled using the correlation proposed by Cavallini et al. (2006) shown in equations 2.29 to 2.34. This correlation compares the fluid's dimensionless mass velocity (J_G) to a limiting value (J_G^T) and thus determines whether the heat transfer coefficient is independent of the temperature gradient

between the external coolant and the condensing fluid (α_A, if $\mathrm{J_G} > \mathrm{J_G^T}$), or else dependent upon this temperature gradient (α_D).

$$J_G = \frac{x_{vap}\dot{m}}{\left(\frac{\pi D_i^2}{4}\right)\left[gD_i\rho_G\left(\rho_L - \rho_G\right)\right]^{0.5}} \tag{2.29}$$

$$X_{tt} = \left(\frac{\mu_L}{\mu_G}\right)^{0.1}\left(\frac{\rho_G}{\rho_L}\right)^{0.5}\left(\frac{1-x_{vap}}{x_{vap}}\right)^{0.9} \tag{2.30}$$

$$J_G^T = \left(\left[\frac{7.5}{(4.3X_{tt}^{1.111}+1)}\right]^{-3} + 2.6^{-3}\right)^{-\frac{1}{3}} \tag{2.31}$$

$$\alpha_{strat} = \frac{0.725\left(\frac{k_L^3\rho_L[g][\rho_L-\rho_G]h_{fg}}{\mu_L D_i(\Delta T)}\right)^{0.25}}{\left(1+0.741\left[\frac{(1-x_{vap})}{x_{vap}}\right]^{0.3321}\right)} + \left(1-x_{vap}^{0.087}\right)\alpha_{LO} \tag{2.32}$$

$$\alpha_A = \alpha_{LO}\left[1+1.128x_{vap}^{0.817}\left(\frac{\rho_L}{\rho_G}\right)^{0.3685}\left(\frac{\mu_L}{\mu_G}\right)^{0.2363}\left(1-\frac{\mu_G}{\mu_L}\right)^{2.144}Pr_L^{-0.1}\right] \tag{2.33}$$

$$\alpha_D = \left[\alpha_A\left(\frac{J_G^T}{J_G}\right)^{0.8} - \alpha_{strat}\right]\left(\frac{J_G}{J_G^T}\right) + \alpha_{strat} \tag{2.34}$$

2.4.4 Excess Energy Heat Exchangers

In many industrial scenarios, the waste heat energy may need to be cooled down to low temperatures such as 30-40 °C. In situations such as these, the heat transformer cannot accept all of this available energy as the temperatures of the evaporator and the generator are generally about 100 °C. Thus the evaporator and generator cool the waste heat energy to approximately ∼110 °C, before the remainder of the heat is discharged to atmosphere. Similarly to the condenser, an air-cooled heat exchanger is used for this purpose in this simulation. The waste heat energy flows on the inside of the tubes while air is passed over these using a fan.

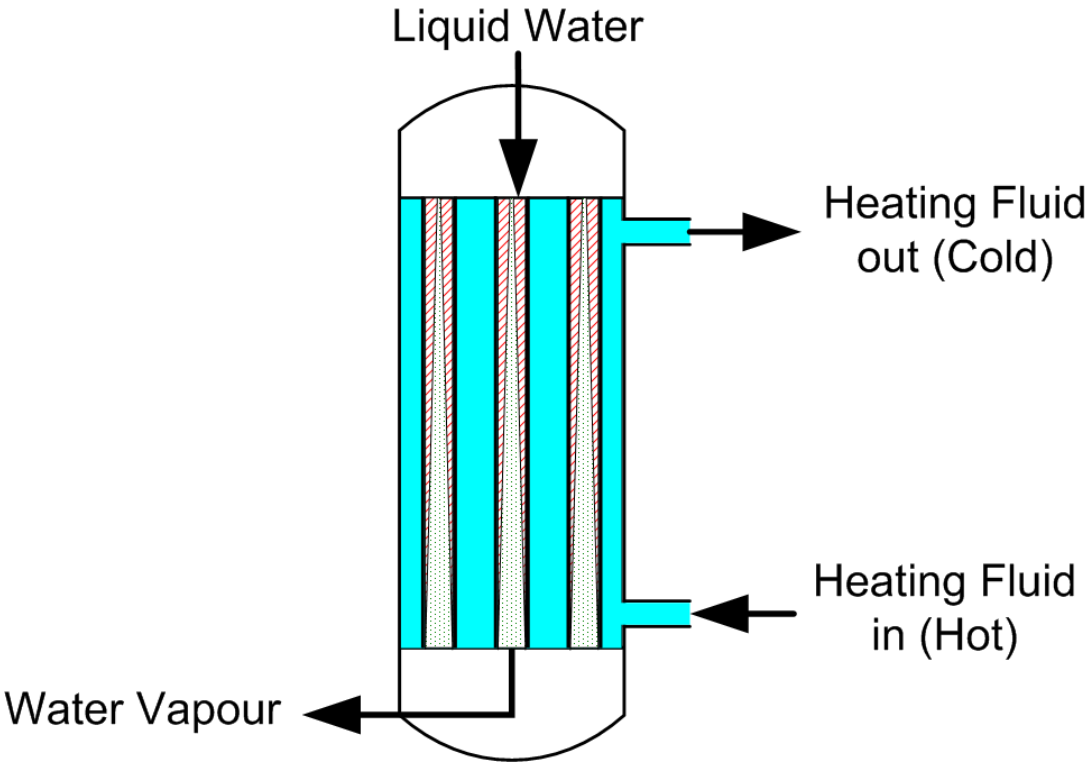


Figure 2.5: Schematic of the falling film evaporator modelled in this heat transformer

2.4.5 Evaporator

The evaporator is selected to be a vertical falling film unit. The evaporation is modelled to occur on the inside of the tubes, and thus a heat transfer coefficient for evaporating annular flow is used (Shah, 1982). This correlation calculates both convective (equation 2.37) and nucleate boiling coefficients (equation 2.38), and then selects the larger of the two as being the heat transfer coefficient (it should be noted that the nucleate boiling coefficient has different correlations under different conditions and thus equation 2.38 is presented here as an example).

$$N = \left(\frac{1 - x_{vap}}{x_{vap}}\right)^{0.8} \frac{\rho_G}{\rho_L}^{0.5} \tag{2.35}$$

$$Bo = \left(\frac{Q}{h_{fg}}\right)\left(\frac{D_i}{4N_t L_t \dot{m}}\right) \tag{2.36}$$

$$\alpha_{cb} = \frac{1.8\alpha_{LO}}{N}^{0.8} \tag{2.37}$$

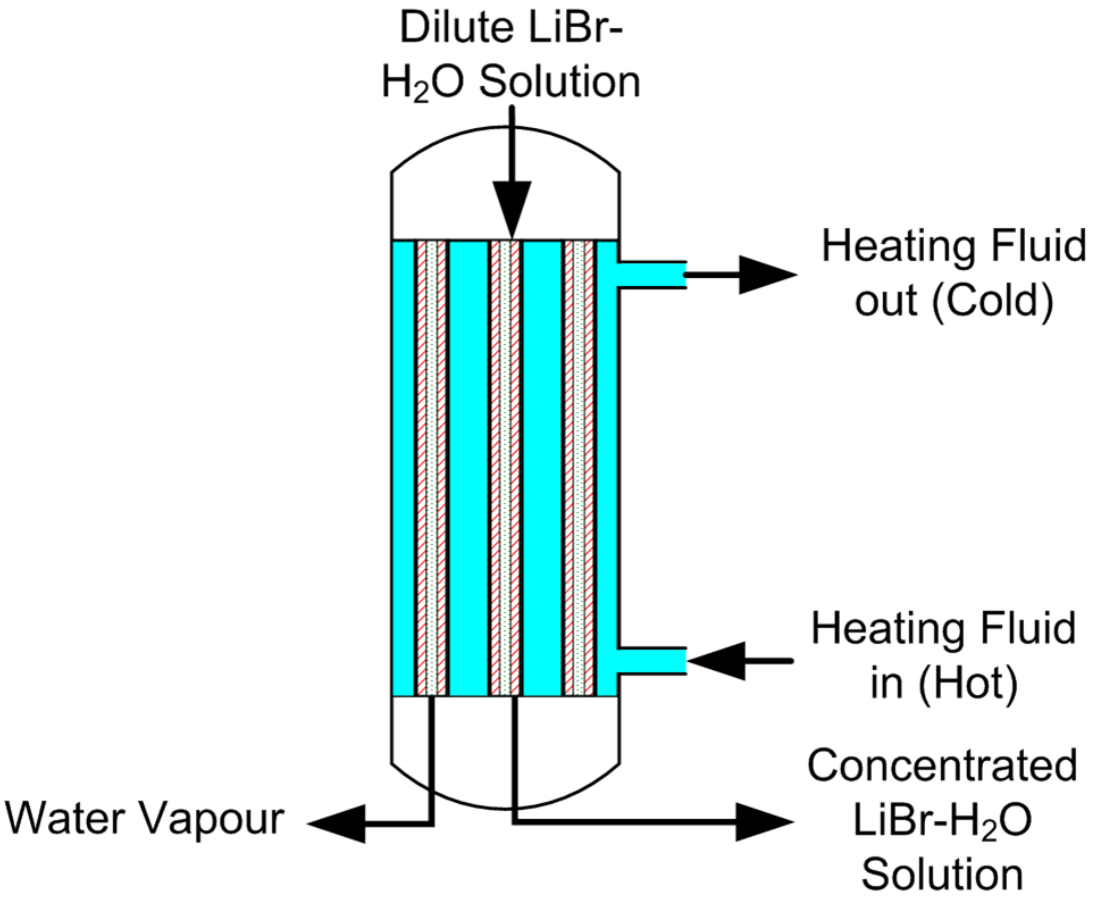


Figure 2.6: Schematic of the falling film generator modelled in this heat transformer

$$\alpha_{nb} = 14.7Bo^{0.5}exp(2.74N - 0.15) \tag{2.38}$$

2.4.6 Generator

Following similar reasoning as outlined in section 2.4.2, the equipment of choice for this unit operation is a falling film heat exchanger. Another motivation for this choice is the fact that overall heat transfer coefficients can be up to 4.37 times larger in vertical falling film units compared to similar pool boiling generators (Shi et al., 2010). The $LiBr - H_2O$ solution is spread along the inside surfaces of the tubes, and water is evaporated from its surface as it flows downwards. Similarly to the absorber, the mathematical modelling of this process is quite complex, and usually attempted using a rigorous partial differential equation approach. Once more a simple, yet validated correlation from literature (Shi et al., 2010) is used

	L_t/D_s	D_o (mm)	Tube Thickness (mm)
Absorber	5	38	2
Generator	3	38	2
Evaporator	3	38	2
Solution Heat Exchangers	5	38	2

Table 2.1: Basic design parameters selected for different shell and tube units in the TAHT

	N_r	N_{TR}	D_o (mm)	Tube Thickness (mm)
Condenser	8	104	25	1.2
Excess Energy HXs	8	50	25	1.2

Table 2.2: Basic design parameters selected for different air-cooled units in the TAHT

instead in this simulation. As demonstrated in equation 2.39, the correlation is derived based upon the inlet LiBr salt mass fraction (x_{inlet}), the heat flux at the wall and the Reynolds number. Similarly to the absorber, the process is then assumed to be heat transfer limited which allows the deduction of mass transfer rates from a combination of heat and mass balances upon the unit.

$$\alpha = 129.7712 \left(x_{inlet}^{-0.8058} \left(\frac{Q}{\pi D_i N_t L_t} \right)^{0.2422} Re^{-0.0856} \right) \tag{2.39}$$

2.5 Heat Exchanger Sizing

The main purpose of modelling each of the unit operations individually is to enable an estimation of the required heat transfer surface area in each piece of equipment. A brief summary of this calculation procedure is therefore provided in this section.

Tables 2.1 and 2.2 highlight the basic design parameters specified for each major piece of equipment. The algorithm for calculating the heat transfer surface area in each unit operation may be simplified as follows:

1. Conduct the mass and enthalpy balances outlined in section 2.3.1.
2. Calculate the duty of the heat exchanger (Q), using equation 2.5 on either the hot or cold stream.
3. Calculate the logarithmic temperature difference in the unit using equation 2.40.

$$\Delta T_{lm} = \frac{\Delta T_{inlet} - \Delta T_{outlet}}{ln\left(\frac{\Delta T_{inlet}}{\Delta T_{outlet}}\right)} \tag{2.40}$$

4. Find the length of the heat exchanger using an iterative approach:

   (a) If the heat exchanger is a shell and tube design (this includes falling film units):

      i. Guess a Length.

      ii. Calculate the diameter of the shell using the length to diameter ratio selected (see Table 2.1).

      iii. Calculate the number of tubes in the heat exchanger using this shell diameter and equations 2.41 and 2.42 (Sinnott, 2005). Note that this number of tubes is rounded to the nearest integer.

$$D_s \begin{cases} < 4mm & D_{tb} = D_s - 2mm \\ > 4mm & D_{tb} = D_s - (1.6mm + 4 \times 10^{-3} D_s) \end{cases} \tag{2.41}$$

$$N_t = 0.319 \left(\frac{D_{tb}}{D_o}\right)^{2.142} \tag{2.42}$$

      iv. Calculate the heat transfer surface area actually available in the heat exchanger using equation 2.43.

$$A_{available} = \pi D_o L_t N_t \tag{2.43}$$

   (b) If the heat exchanger is an air-cooler:

      i. Guess a Length.

      ii. Calculate the heat transfer surface area actually available in the heat exchanger using equations 2.44 to 2.47. Note that in these equations, fins are located at a density of $P_{fin} \simeq 127{,}000$ fins/m, and the thickness of a fin is 0.3mm.

$$D_{fin} = D_o + 30mm \tag{2.44}$$

$$A_{fin} = N_r N_{TR} P_{fin} L_t \left(2\pi \left[\left(\frac{D_{fin}}{2} \right)^2 - \left(\frac{D_o}{2} \right)^2 \right] + \pi D_{fin} t_{fin} \right) \tag{2.45}$$

$$A_{BareArea} = N_r N_{TR} \pi D_o L_t \tag{2.46}$$

$$A_{available} = A_{BareArea} + A_{fin} - [N_r N_{TR} P_{fin} L_t \pi D_o t_{fin}] \tag{2.47}$$

(c) Calculate the heat and mass transfer coefficients for all fluids using the equations outlined in section 2.4.

(d) Using the calculated heat and mass transfer coefficients, calculate the U-value in the unit using equation 2.48, where the fouling factors (F_i and F_o) are both taken as 9×10^{-5}m^{2}K/W (Florides et al., 2003).

$$U = \frac{1}{\left(\frac{D_O}{D_i}\right)\left(\frac{1}{\alpha_i}\right) + \left(\frac{D_O}{D_i}\right) F_i + \left(\frac{1}{2k}\right) ln\left(\frac{D_O}{D_i}\right) + F_o + \frac{1}{\alpha_o}} \tag{2.48}$$

(e) Calculate the heat transfer area required in the heat exchanger using equation 2.49. The correction factor F is equal to one in this simulation, as all heat exchangers are designed as single pass units.

$$A_{required} = \frac{\dot{Q}}{U F \Delta T_{lm}} \tag{2.49}$$

(f) Find the error between the heat transfer area required and the heat transfer area available (equation 2.50).

$$error = |A_{required} - A_{available}| \tag{2.50}$$

(g) Determine if this error is less than a specified tolerance. If it is, then exit the iteration, if it is not then continue iterating using the Newton-Rhapson method (continuously varying the length of the heat exchanger) until convergence has occurred.

5. Following convergence of the iteration loop, the heat transfer area of the heat exchanger is defined, and thus the calculation is completed for the heat exchanger.

Chapter 3

First and Second Law Multidimensional Analysis of a Triple Absorption Heat Transformer

Nomenclature

COP	Coefficient of performance of the system
dT_{Hx}	Minimum pinch temperature (heat transfer gradient) utilised in all system heat transfer operations (°C)
ECOP	Exergetic coefficient of performance of the system
E_D	Total rate of exergy destruction within the cycle (W)
FR	Flow ratio of the system

Statistical Terms

DOE	Design of experiment, in this case a full factorial model
OSSF	Pooled term containing all statistically significant factors/interactions whose absolute effect is less than that of the pooled insignificant factors.
PIF	Pooled term containing all factors/interactions deemed statistically insignificant.

3.1 Introduction

During the design and operation stages of any thermodynamic cycle, values must be assigned to all of its operating degrees of freedom. For example in a triple absorption heat transformer (TAHT), the temperatures of the different individual units must be specified every time the system is simulated/operated. It has been highlighted in Chapter 1 that many parametric studies have been conduced which attempt to determine such points of operating optima for single stage heat transformers (SSHTs). A smaller number of similar studies have also been conducted for double absorption heat transformers (DAHTs), generally attempting to identify the largest sources of irreversibility.

Heretofore only very basic studies have been published for triple absorption heat transformers however. Zhuo and Machielsen (1996) demonstrated that a TAHT can achieve GTL values of 145 °C while maintaining a COP of approximately 0.2, while Lee and Sherif (2000) conducted a basic study on the performance of a TAHT in which it is demonstrated that it achieves lower COPs and ECOPs but higher GTLs than both DAHTs and SSHTs. The TAHT's COP and ECOP were shown to increase with an increase in heat source temperature and decrease with an increase in the temperature of the condenser's coolant. No rigorous first or second law analyses upon the system and its variables have been presented however. This chapter therefore uniquely seeks to determine the first and second law behavioural characteristics of a TAHT, and to establish the most important

variables involved in the optimisation of such a system. An exergetic analysis of the individual components enables the identification of the greatest sources of non-idealities within the cycle, allowing improved system understanding and the potential for future optimisation of the most relevant units.

3.2 Mathematical Modelling

The mathematical model of a TAHT developed in Chapter 2 is used throughout this chapter. As the size and design of equipment has no impact the results of this analysis, for the sake of simplicity two further constraints are added to the basic model assumptions, namely:

1. The analysis is conducted with a refrigerant vapour flowrate of 1kg/s entering the absorber (this does not affect the performance variables being analysed in this study).
2. $LiBr - H_2O$ solutions leaving the two absorber-evaporators, the absorber and the generator are assumed to be saturated.

3.3 Multidimensional design of experiment

The analysis conducted in this chapter aims to determine the relative effect of each of the components and system settings upon the performance of the TAHT. Previously such studies have been conducted on single and double stage heat transformers in a linear fashion in which one variable is varied over a selected range while all others are maintained at a constant value. This type of analysis does however not allow interactive effects to be examined or for points of optimum performance to be applied in the general case. Thus in this chapter, a multivariate approach is applied, which attempts to analyse all variables and every possible interaction between them simultaneously. The dependent factors which are to be analysed are the four principal system outputs previously discussed in Chapter 2, namely COP, ECOP, FR and E_D. It is decided to use five levels for each manipulated factor listed in Table 3.1.

T_e	Temperature of the evaporator
T_c	Temperature of the condenser
dT_{Hx}	Minimum pinch temperature (heat transfer gradient) utilised in all system heat transfer operations.
GTL1	Difference between temperature of absorber-eaporator-1 and evaporator
GTL2	Difference between temperature of absorber-eaporator-2 and evaporator
GTL3	Difference between temperature of the absorber and the evaporator

Table 3.1: List of manipulated factors used in the multidimensional analysis

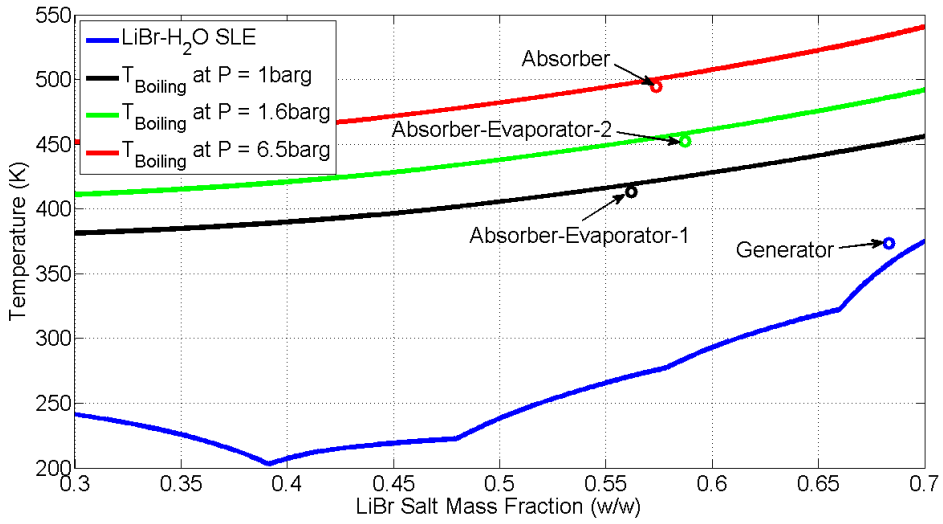


Figure 3.1: Schematic of the operational temperatures, pressures and concentrations within the main unit operations of a typical TAHT, illustrating the system's thermodynamic limitations

3.3.1 TAHT Thermodynamic Limitations

The maximum temperature lift achievable by the TAHT is dictated by the $LiBr - H_2O$ solid liquid equilibrium curve and the boiling temperature of the solution. Figure 3.1 shows the temperatures, pressures and concentrations of the $LiBr - H_2O$ salt solution in all absorber and generator units in a typical TAHT (achieving a GTL of 125 °C). The generator must operate above the solid-liquid equilibrium curve (to prevent crystallisation), while in turn the temperatures of all the absorbers must remain just below their respective boiling temperatures at the units' pressures and salt concentrations. As described in section 1.3.3.1, the concentrated salt solution leaving the generator is pumped to all three absorbers,

where it is diluted by absorbing water vapour. In order for the heat transformer to function, the concentrations of the salt solutions leaving the absorbers must always be less than the concentration of the solution leaving the generator. Visually this means that the markers representing the absorber units in Figure 3.1 must remain to the left of the marker representing the generator in the same plot. As the gross temperature lift (GTL) of the TAHT increases, the markers representing the absorbers in Figure 3.1 move further to the right (the solutions become more concentrated to enable higher temperatures to be reached without breaching the units' respective boiling temperatures). All of the absorbers are intrinsically linked (as the temperature of absorber-evaporator-1 increases, the pressure of absorber-evaporator-2 increases thus changing its boiling curve etc.), and therefore it is not practical to try and estimate the theoretical maximum GTL achievable from plots such as Figure 3.1. If all pressures were assumed to remain the same however, the absorber temperature could move along its boiling temperature curve until it reaches a temperature of approximately 525K, at which point its concentration is almost the same as that of the generator. Thus a maximum GTL of $\sim$150 °C would be predicted. In reality however the interactions between the units mean that such qualitative descriptions of the system are not very useful, and therefore it is easier to examine its performance numerically as is being conducted in this chapter. The benefit of Figure 3.1 is that it demonstrates a typical operational space between the $LiBr - H_2O$ solid-liquid equilibrium and boiling curves which the TAHT unit operations may occupy, giving a qualitative understanding of the limitations which must be considered in any TAHT model or design.

3.3.2 Level Selection

In practice, in any given scenario, a company implementing a TAHT will have a specific heat source which it wishes to utilise, and thus one must be able to specify the evaporation temperature. In addition, the company will have a purpose for this TAHT, and thus one must be able to specify the total gross temperature lift achieved by the system (GTL3). The dT_{Hx} used is generally a variable decided by economic analysis, and thus one should be able to specify this freely. In this type of system however, there are significant interactions between the manipulated variables, which lead to thermodynamic restrictions upon the values which they may take in any given scenario while allowing the cycle to achieve a specified output (due to issues such as crystallisation). Thus if T_e, GTL3 and dT_{Hx} may

be freely specified, the remaining factors will have defined ranges of operability. These variables may therefore take any values within these available ranges.

The only way to ensure that these full ranges are examined is to calculate the maximum value which the manipulated factor in question may take, the minimum value it may take and to then analyse this full range of values. As previously stated, these maximum and minimum values for any one factor may be highly dependent upon the values of the other factors. In order for these results to thus be meaningful, the values analysed in the experimental design shall not be the actual values taken by the variables (e.g.: a condensation temperature of 30 °C), but shall be level settings. These level settings shall represent the factor's selected position across its range of operability (i.e.: a level setting of 2 for the condensation temperature would indicate that the condensation temperature is two fifths of the way between the lowest temperature which it may possibly take in this scenario, and the highest value which it may possibly take in this scenario). For the three factors mentioned previously (T_e, GTL3 and dT_{Hx}) this range of operability is simply a defined experimental space, whereas for the others it represents the range of values thermodynamically available. The benefits of this method are demonstrated by the fact that in one simulation, the optimum condensation temperature may be 40 °C, while in the next experiment it could be shown to be 45 °C due to the varying of the remaining manipulated factors. In this case it would appear that the optimum condensation temperature has changed, however both of these values may simply represent the lowest condensation temperature available to the system. Thus in both cases, the optimum condensation level is 1 which allows for a grouping and simplification of the final results (vitally important as there are 6 factors and therefore a very large number of outputs). This feature also allows for generality to be achieved, for it allows simplified representations of findings such as 'the condensation temperature should always be kept to a minimum', instead of having to quote individual temperatures for specific scenarios. This means that the results from this chapter can be easily applied to any system operating within the defined experimental ranges.

Due to the large number of thermodynamic interactions between the factors within the system, a full factorial design is selected. As there are 6 factors, each with 5 levels, the total number of experimental simulations in this DOE is equal to $(5)^6 = 15{,}625$. The basic model algorithm operation is outlined below.

1. Define experimental temperature regions for T_e, GTL3 and dT_{Hx}.
    (a) Note: All subsequent steps are performed for each individual experi-

Variable	Lowest Value	Highest Value
T_e	85 °C	105 °C
GTL3	110 °C	150 °C
dT_{Hx}	2.5 °C	12.5 °C

Table 3.2: Definition of the experimental temperature regions for T_e, GTL3, dT_{Hx}.

mental simulation within the DOE based on the levels defined by that DOE simulation for T_e, GTL3 and dT_{Hx}.

2. Determine the maximum condensation temperature which may be selected in order to achieve GTL3.
3. Determine the minimum condensation temperature possible in order to avoid crystallisation in the generator.
   (a) Select the appropriate condensation temperature from this available range based upon the level specified by the DOE for this simulation.
4. Determine the maximum GTL1 which will ensure that the absorption in absorber-evaporator-1 remains at least adiabatic, based upon the selected T_e.
5. Determine the minimum GTL2 which will ensure that the absorption in the absorber remains at least adiabatic, based upon the selected GTL3.
6. Determine the minimum GTL1 which will ensure that the absorption in absorber-evaporator-2 remains at least adiabatic, based upon the minimum value which GTL2 may take.
   (a) Ensure that this minimum GTL1 is large enough so as to allow Hx_1 to function properly.
   (b) Select the appropriate GTL1 from its available range based upon the level specified by the DOE for this simulation.
7. Determine the maximum GTL2 which will ensure that the absorption in the absorber remains at least adiabatic, based upon the selected GTL1.
   (a) Ensure that this maximum GTL2 is less than the selected GTL3.
   (b) Ensure that the minimum GTL2 evaluated is greater than the selected GTL1.
   (c) Select the appropriate GTL2 from its available range based upon the

level specified by the DOE for this simulation.

The full factorial model developed by the author using Matlab R2010b (MathWorks Inc., Massachusetts USA) uses the experimental results from these DOE simulations to evaluate the first, second, third, fourth, fifth and sixth degree interactive effects of the factors using the sum squared residual (SSR) as the measure of absolute effect. To allow for easy interpretation of results and the selection of operating points of optimum, the optimum setting (i.e.: level) of each factor/interaction is evaluated by determining the setting with the largest/smallest average (i.e.: the average of the dependent variable outputs of all experimental simulations in which the factor/interaction is at the applicable setting).

3.3.3 Analysis of Results

In total there are 63 factors/interactions, and naturally some of these have a much greater influence than others. A test of statistical significance is used to initially determine which factors are appropriate to ignore (i.e.: are statistically insignificant). A 99% confidence level is used in this analysis, and due to the large number of experimental simulations, the Bonferroni correction is also utilised (Cabin and Mitchell, 2000). As all interactive effects are initially analysed, the experiment has an error of zero. Thus Lenth's method of estimating a pseudo standard error (PSE) is implemented (Dong, 1993). Using this PSE, all factors/interactions deemed insignificant are pooled (this pooled term is labelled PIF in the results shown in section 3.4) and used as the error term. Using these pooled effects, a conventional F-test is conducted using the student-t value as the critical F-value to determine whether any further factor/interactions should be pooled as insignificant effects.

In this chapter it is decided to analyse in detail only those factors/interactions whose absolute effect is greater than that of the pooled insignificant factors. All other statistically significant factors are pooled as a factor named 'other statistically significant factors (OSSF)' in the results discussed in section 3.4, and shall henceforth also be treated as statistically insignificant for simplicity purposes.

3.4 Results and Discussion

3.4.1 System Output Analysis

The breakdown of the most significant input variables (i.e. factors/interactions) for each dependent factor are discussed in this section, and also illustrated graphically in Figures 3.2, 3.3, 3.4 and 3.5. It should be noted that only the factors/interactions explicitely listed in these figures are being considered statistically significant in this study (as discussed in section 3.3.3).

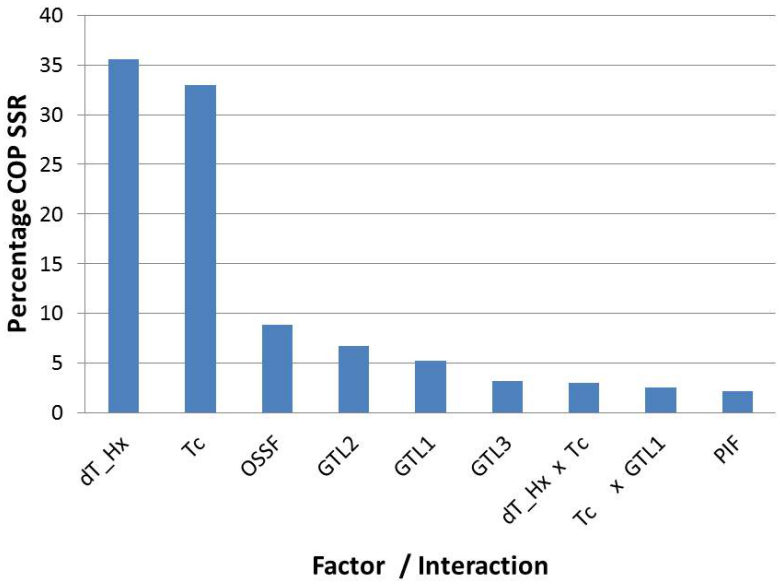


Figure 3.2: Relative influence of each factor/interaction upon the system's COP

The primary influences on the dependent variables (system outputs) of COP, ECOP and E_D are the pinch temperature and condensation level. In turn, the flow ratio is primarily affected by the condensation level and GTL1. These results give a very clear indication that the condensation level is the most important variable being selected, followed by dT_{Hx} and GTL1. However due to the high number of interactive effects between the manipulated variables (system inputs), it is not possible to state definitively the reason for this ranking, and therefore this should be a focus of any future work in this area. Figures 3.2, 3.3, 3.4 and 3.5 give an indication as to which are the most statistically important variables, while their corresponding optimum settings are discussed in the next section.

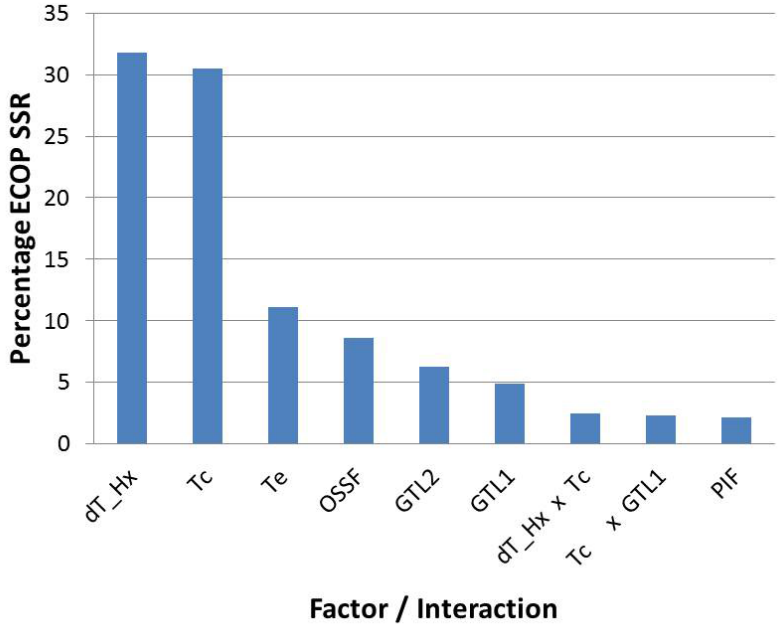


Figure 3.3: Relative influence of each factor/interaction upon the system's ECOP

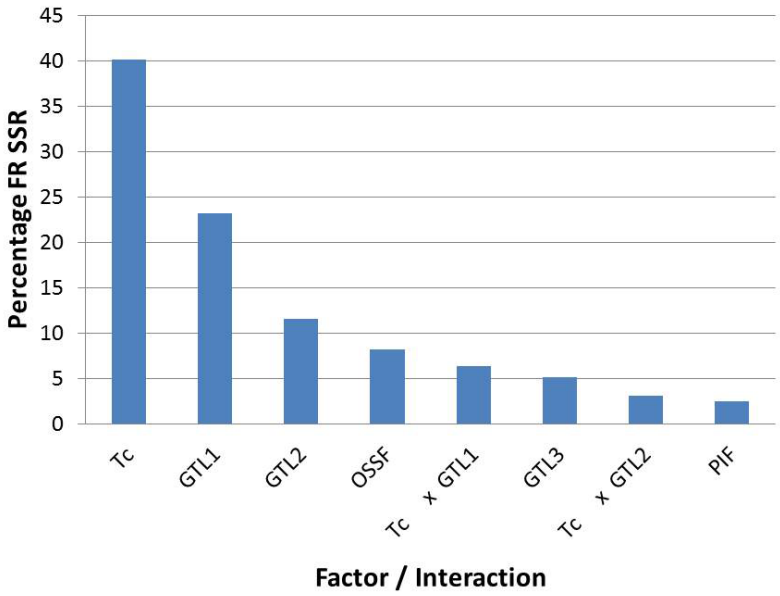


Figure 3.4: Relative influence of each factor/interaction upon the system's flow ratio (FR)

3.4.2 Manipulated Variable Analysis

The system under investigation is complicated with a large number of both manipulated and dependent variables (system inputs and outputs respectively). In section 3.4.1, the most influential manipulated variables and interactions have been identified for each dependent variable. In this section, the effects of the

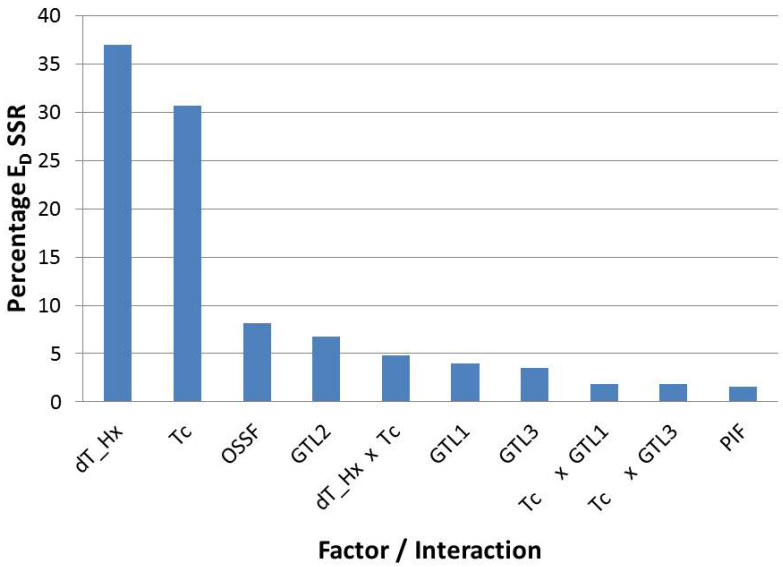


Figure 3.5: Relative influence of each factor/interaction upon the system's total rate of exergy destruction (E_D)

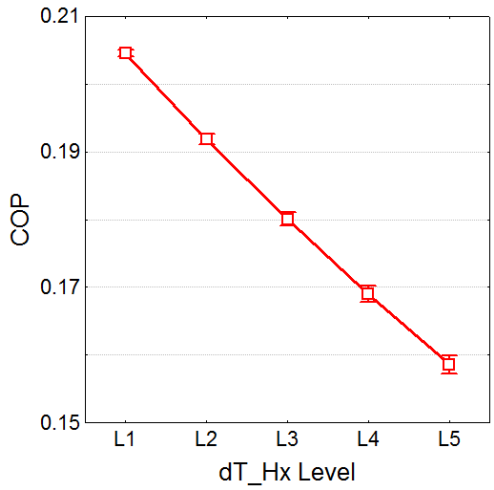
manipulated variables upon the various dependent variables are analysed and presented graphically, allowing the identification of possible points of operating optima. All illustrated error bars in this section represent 99% confidence intervals (2.576 standard deviations) as discussed in section 3.3.3.

3.4.2.1 Pinch heat transfer gradient (dT_{Hx})

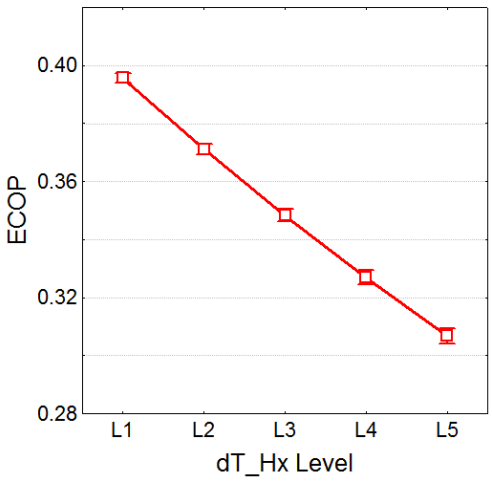
The pinch heat transfer gradient is the most influential factor for three of the four dependent variables (COP, ECOP and E_D). In all three of these cases the results show that this factor should be set to level one (see Figure 3.6). It also has a significant interactive effect with the temperature of the condenser for all three of these dependent factors. In all of these interactions, the influence of dT_{Hx} decreases with a lowering of T_c as shown in Figure 3.7. While the flow ratio increases slightly with a decrease in dT_{Hx} (Figure 3.6c), the effect is statistically insignificant (Figure 3.4) and may therefore be ignored. Thus it may be concluded that **dT_{Hx} should remain as small as economically possible**.

3.4.2.2 Total Gross temperature lift (GTL3)

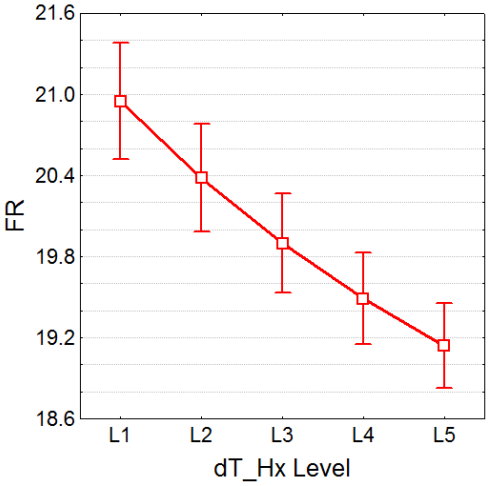
The total gross temperature lift appears as an important factor with respect to three of the dependent factors (COP, FR and E_D), and in all cases, its optimum setting is one (see Figure 3.8). It should however be noted that GTL3 is not as



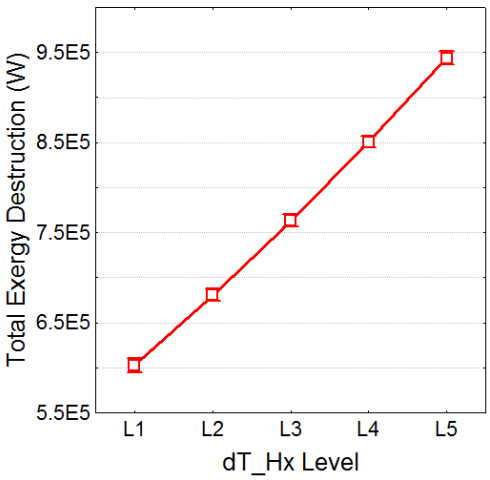
(a) Effect of dT_{Hx} upon the system's COP



(b) Effect of dT_{Hx} upon the system's ECOP



(c) Effect of dT_{Hx} upon the system's FR



(d) Effect of dT_{Hx} upon the system's E_D

Figure 3.6: Average (non-interacting) effect of dT_{Hx} upon the system's dependent variables showing a 99% confidence interval

important as one might have initially believed. It is only the 5th most influential effect for two dependent variables, 6th for another, and deemed insignificant with respect to the remaining system output. Most previous studies for single and double stage systems have focussed heavily upon this factor. An increase in GTL3 causes a slight increase in the system's ECOP, but as this is a statistically insignificant effect, **it is recommended that GTL3 take its minimum value in all situations**.

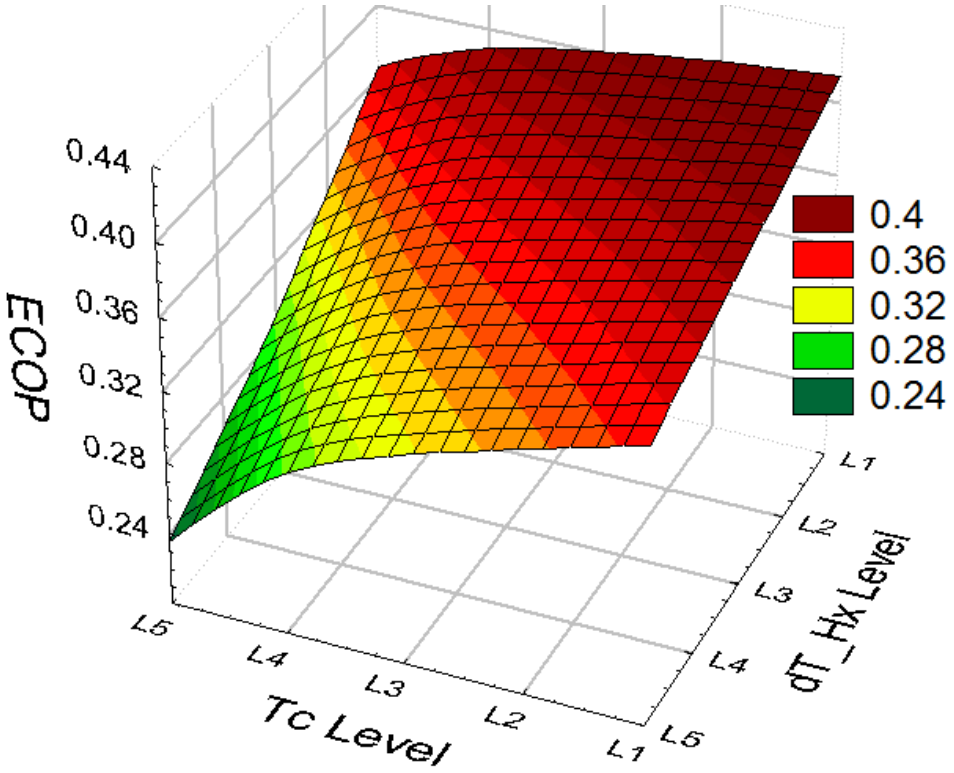


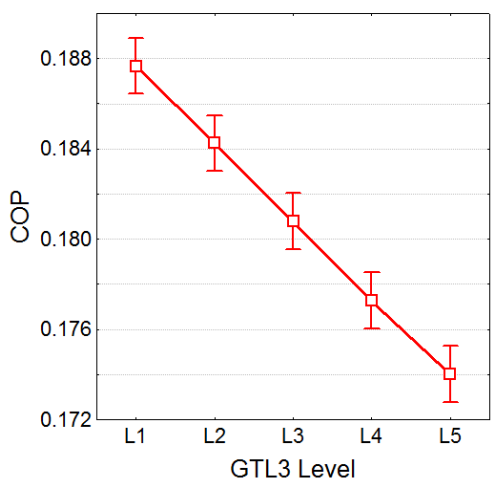
Figure 3.7: Interactive effect of T_c and dT_{Hx} on the system's ECOP

3.4.2.3 GTL1 and GTL2

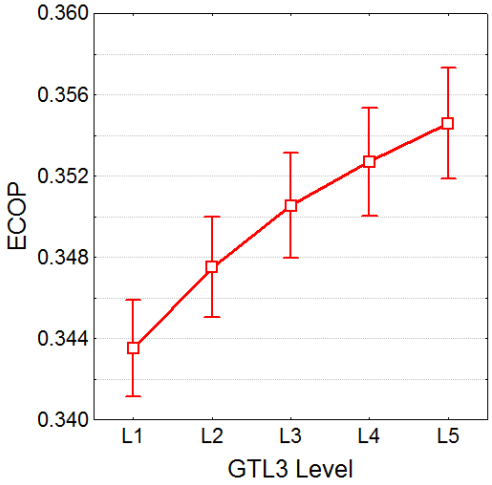
Both GTL1 and GTL2 have points of maxima with respect to all four dependent variables. In general, the optimum setting for both factors is in the region of the intermediate level setting of 3 (see Figures 3.9 and 3.10). The exact optimum point may be shifted slightly to either side by interactive effects with the condensation temperature in particular (see Figures 3.11 and 3.12), and thus must be found for any specific situation by partial differentiation. For any dependent variable, the exact optimum point occurs with the unique set of GTL1 and GTL2 values which allow its differential with respect to GTL1 and GTL2 to simultaneously equal zero (equation 3.1). In this study, the differentiation is carried out numerically using the central difference method, and the non-linear Newton method is then used to find the optimum GTL1 and GTL2 values.

$$0 = \frac{\partial(\text{ Dependent Variable})}{\partial GTL1} = \frac{\partial(\text{ Dependent Variable})}{\partial GTL2} \tag{3.1}$$

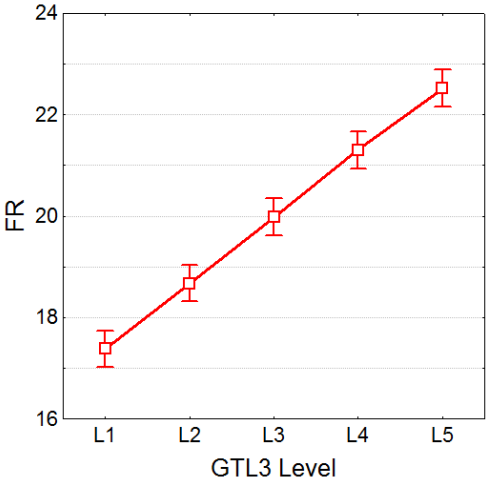
However, while equation 3.1 provides the exact optimum GTL values for any specific application, it may be computationally expensive. Figures 3.9 to 3.12 show



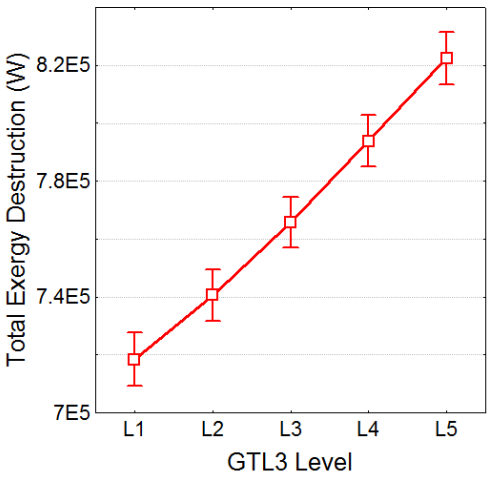
(a) Effect of GTL3 upon the system's COP



(b) Effect of GTL3 upon the system's ECOP



(c) Effect of GTL3 upon the system's FR



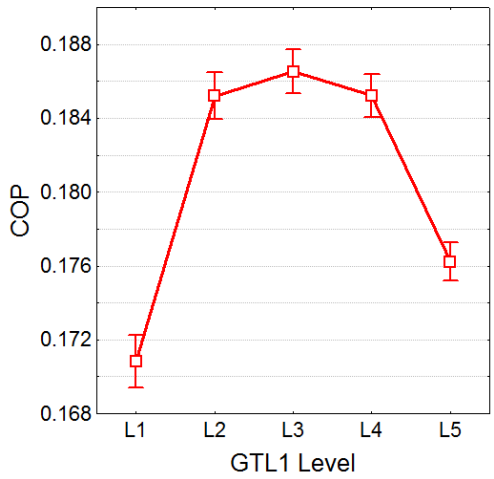
(d) Effect of GTL3 upon the system's E_D

Figure 3.8: Average (non-interacting) effect of GTL3 upon the system's dependent variables showing a 99% confidence interval

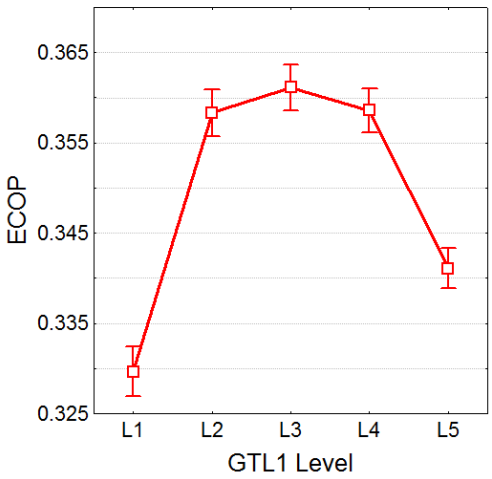
that in general the optimum point of operation for GTL1 and GTL2 is approximately located half way between their thermodynamic minimum and maximum values for all of the dependent variables. Only very slight benefits may be gained by using 3.1. Thus **it is recommended to use level three for both GTL1 and GTL2** unless a specific dependent variable requires particular optimisation (such as the flow ratio to minimise capital costs, etc.).

3.4.2.4 Condensation Temperature (T_c)

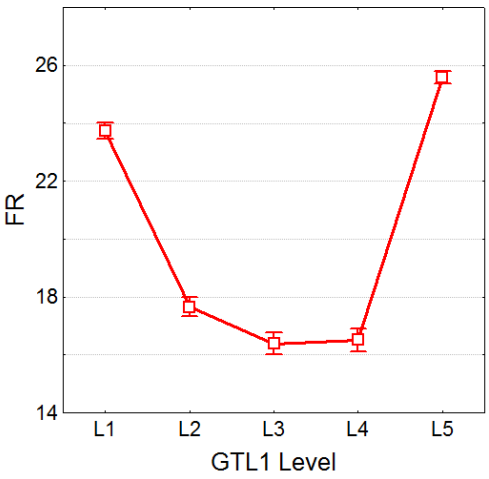
This is one of the top two most significant factors with respect to each dependent variable. Its optimum setting is setting one (lowest setting) in all cases except



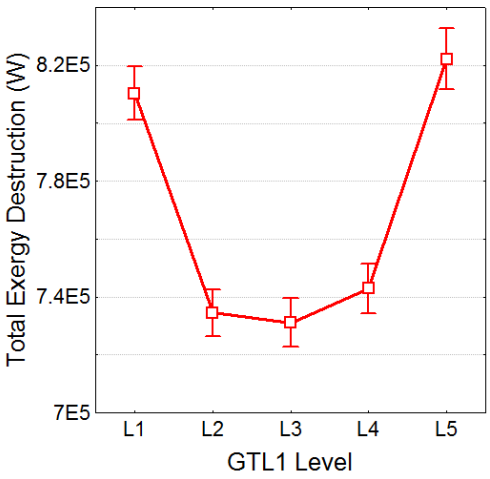
(a) Effect of GTL1 upon the system's COP



(b) Effect of GTL1 upon the system's ECOP



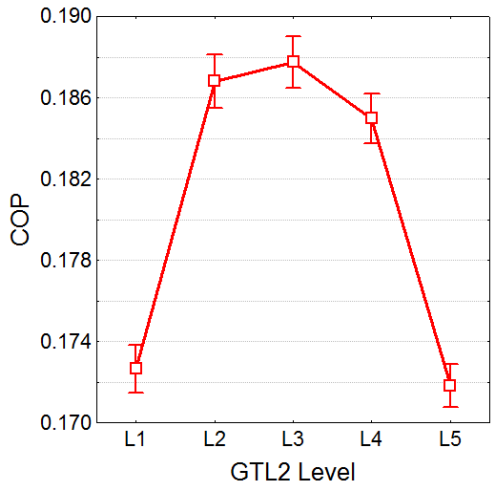
(c) Effect of GTL1 upon the system's FR



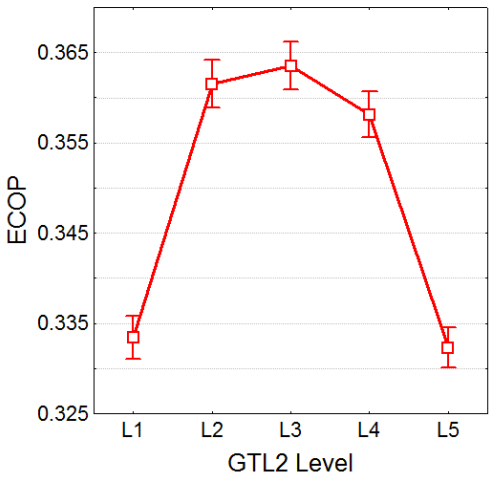
(d) Effect of GTL1 upon the system's E_D

Figure 3.9: Average (non-interacting) effect of GTL1 upon the system's dependent variables showing a 99% confidence interval

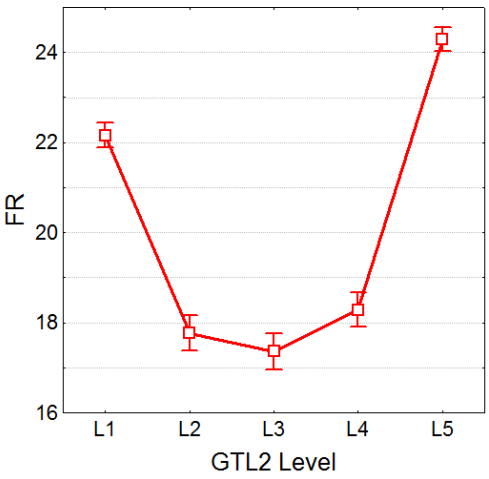
for the total rate of exergy destruction (E_D) which favours a higher condensation temperature as illustrated in Figure 3.13. This exception occurs as increasing the condensation temperature directly increases the quantity of exergy leaving the system from the condenser itself (see influence of temperature in exergy destruction definition in equations 2.8 and 2.9). This exergy is simply discharged to atmosphere as a waste however and it is therefore not of any tangible benefit. It also has a strong interactive effect upon other variables. It is involved in every single interaction whose effect is greater than that of the pooled insignificant factors as illustrated in Figures 3.2 to 3.5. Figures 3.7, 3.11, 3.12 and 3.14 illustrate that even with these interactive effects, the condensation temperature should always remain at its lowest setting (except for total rate of exergy destruc-



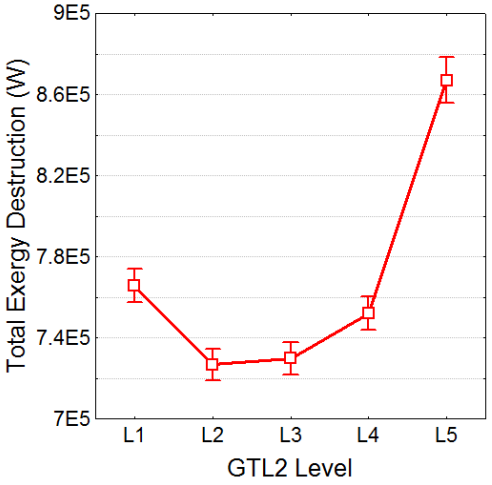
(a) Effect of GTL2 upon the system's COP



(b) Effect of GTL2 upon the system's ECOP



(c) Effect of GTL2 upon the system's FR



(d) Effect of GTL2 upon the system's E_D

Figure 3.10: Average (non-interacting) effect of GTL2 upon the system's dependent variables showing a 99% confidence interval

tion as discussed above), and that the level of the other manipulated variable in question should also be selected based upon its non-interactive optimisation discussion (i.e.: dT_{Hx} should be as low as possible etc.). The main effect of these interactions with the condensation temperature is to alter the importance of the level selection for the other manipulated variable in question (i.e.: Figure 3.11 shows that the selection of GTL1's level has a much greater influence upon the system's flow ratio at a low condensation temperature level than at a higher condensation level). Due to the above reasoning, **it is recommended to maintain the condensation temperature at as low a temperature as possible in the system**.

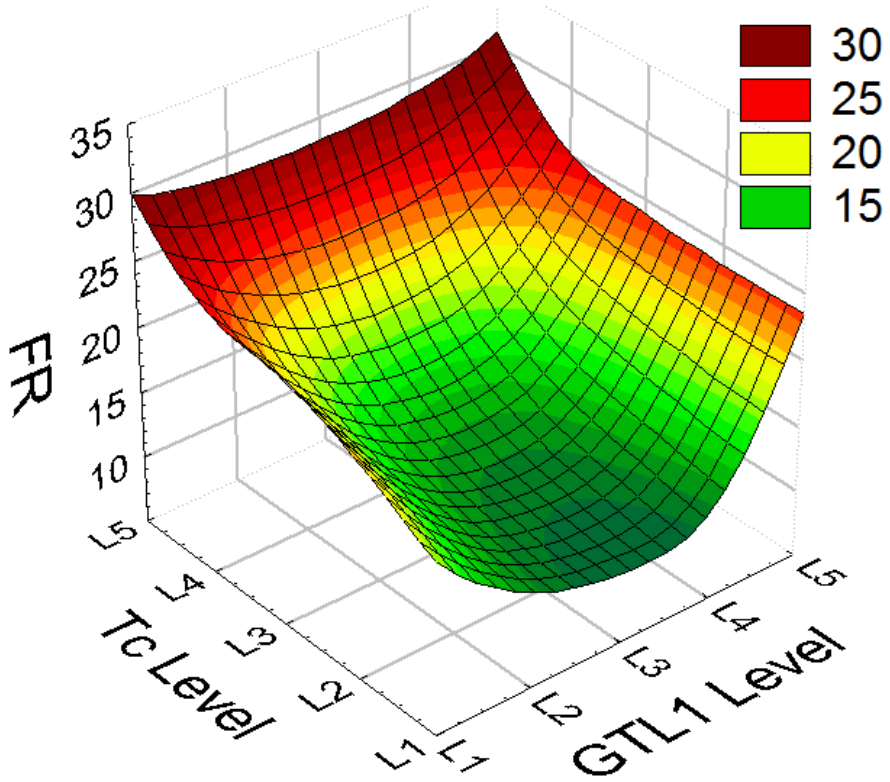


Figure 3.11: Interactive effect of T_c and GTL1 on the system's FR

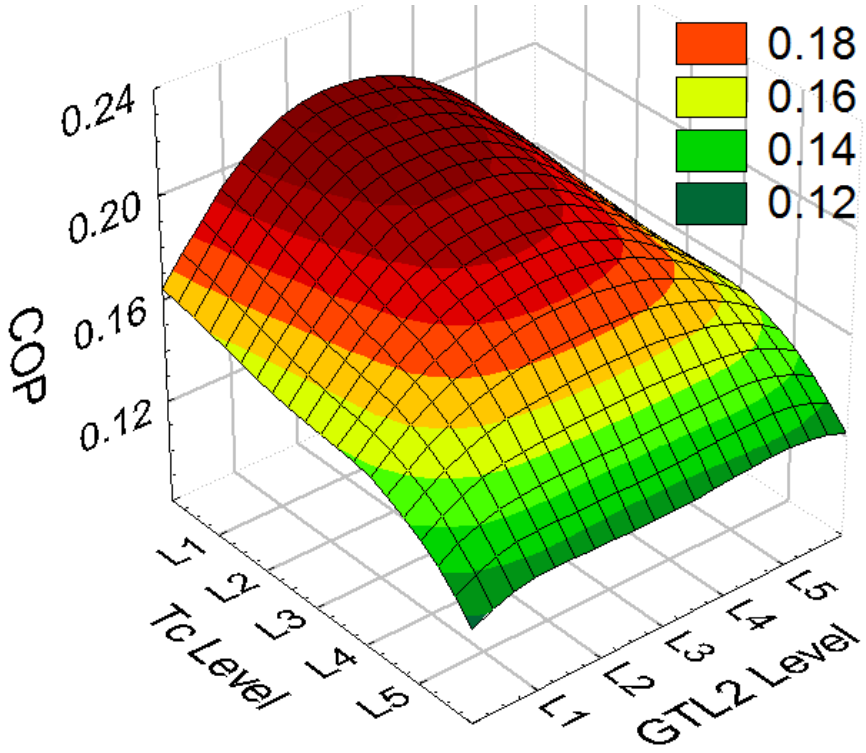
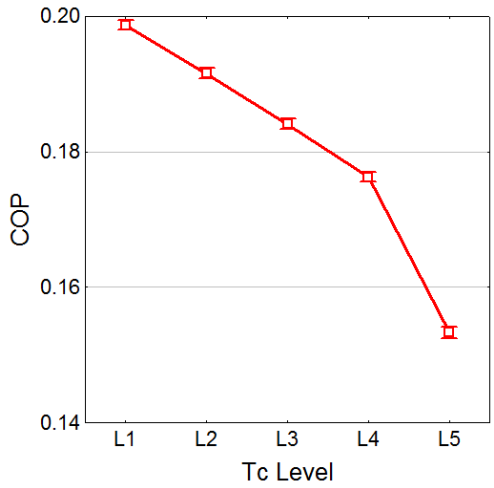
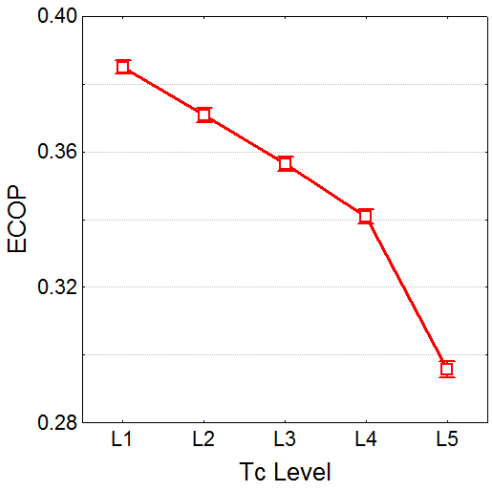


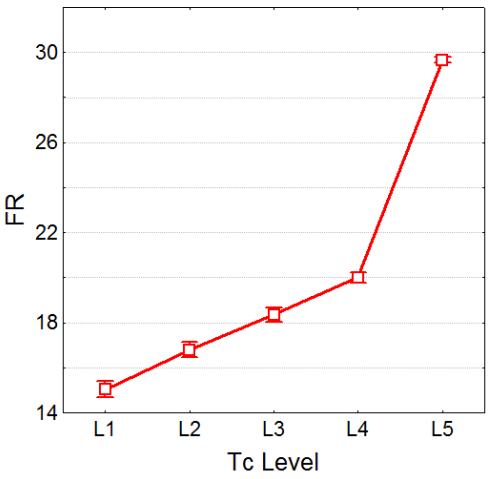
Figure 3.12: Interactive effect of T_c and GTL2 on the system's COP



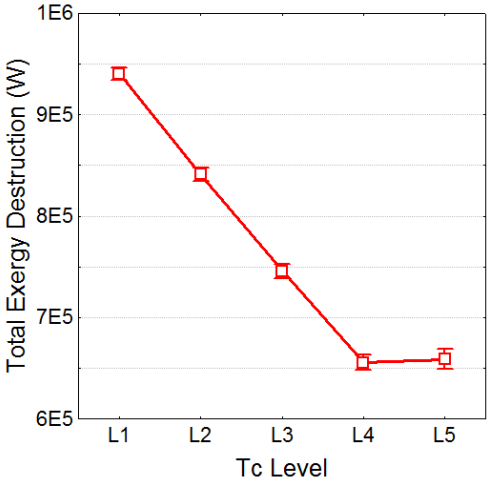
(a) Effect of T_c upon the system's COP



(b) Effect of T_c upon the system's ECOP



(c) Effect of T_c upon the system's FR



(d) Effect of T_c upon the system's E_D

Figure 3.13: Average (non-interacting) effect of T_c upon the system's dependent variables showing a 99% confidence interval

The reason that a lower condensation temperature leads to a better system performance is due to its influence upon the generator. The performance of the heat transformer is highly dependent upon the difference between the concentration of the solution leaving the generator and the concentrations of the solutions leaving the absorbers (as this dictates the quantity of heat being released in the absorbers). Larger concentration differences enable a better performance. The pressure in the generator must equal the vapour pressure of water at the condenser's temperature. A higher pressure in the generator (corresponding to a higher condensation temperature) means that the $LiBr - H_2O$ solution in the generator must have a lower concentration in order to keep it saturated (i.e.: at its boiling point). Thus the difference in concentration between the generator

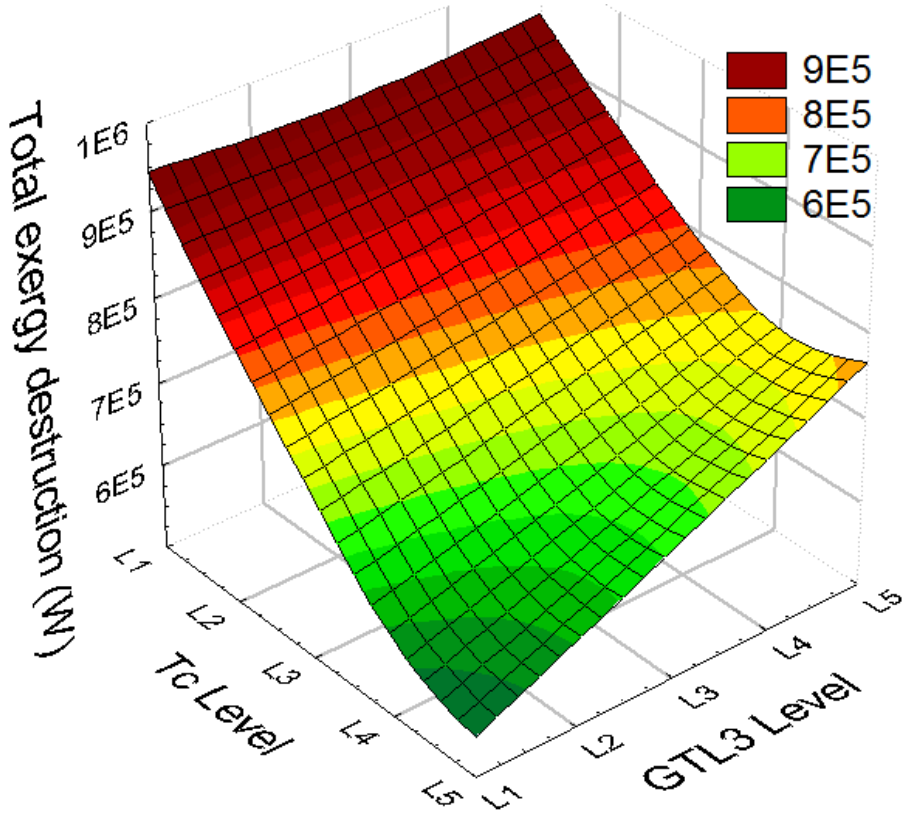
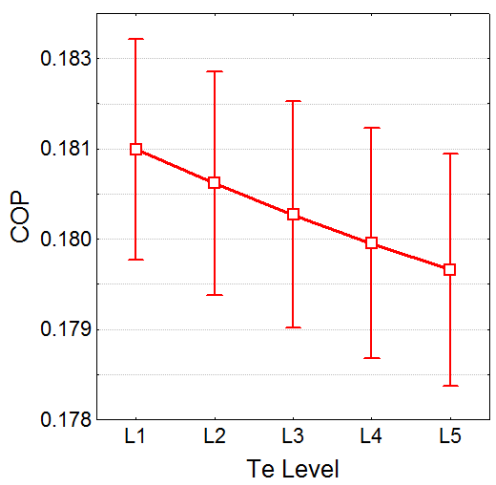


Figure 3.14: Interactive effect of T_c and GTL3 on the system's E_D

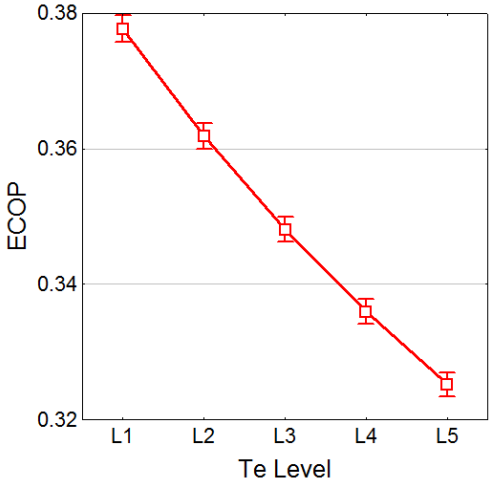
and the absorbers is reduced, decreasing the system performance. For this reason it is favourable to maintain as a low a condensation temperature as possible, in order to maximise the concentration gradients in the absorbers, and increase the system's performance.

3.4.2.5 Temperature of the evaporator (T_e)

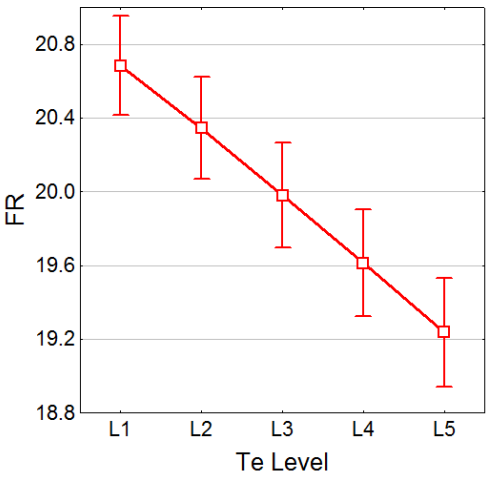
The evaporator temperature only appears as significant in the ECOP results. The ECOP is optimised by setting the evaporation temperature to level one (lowest setting, see Figure 3.15b) as the exergy input to a system such as this is reduced by reducing this temperature, but primarily as reducing the evaporation temperature reduces the temperature profile of the available condensation range (due to the fact that the temperature of the generator dictates the pressure of the condenser, a lower generator (and hence evaporator) temperature allows for a lower condensation temperature). It has already been shown that the condensation temperature is the most important variable in a TAHT, and thus this will positively affect the system's ECOP and COP. Therefore in order to opti-



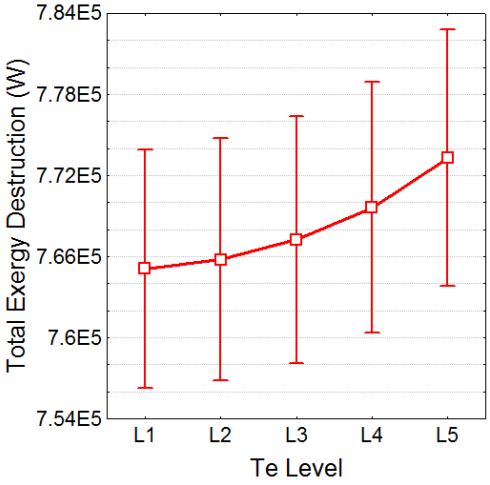
(a) Effect of T_e upon the system's COP



(b) Effect of T_e upon the system's ECOP



(c) Effect of T_e upon the system's FR



(d) Effect of T_e upon the system's E_D

Figure 3.15: Average (non-interacting) effect of T_e upon the system's dependent variables showing a 99% confidence interval

mise these two outputs, the evaporation temperature should be kept as low as possible, allowing the condensation temperature to decrease. If the condensation temperature is not able to decrease any further (due to constraints such as the atmospheric temperature etc.), then a decrease in the evaporation temperature will in fact begin to have the opposite effect, namely to decrease the ECOP. This is the result which was presented by Lee and Sherif (2000), who simulated a varying evaporation temperature while maintaining a fixed condenser temperature and demonstrated that in such a situation, the ECOP decreases with a decrease in the evaporation temperature. This influence of the condensation temperature is highlighted in Figure 3.16, where the condensation temperature is given a minimum value which it must exceed (in this case 40 °C) for a specific set of conditions.

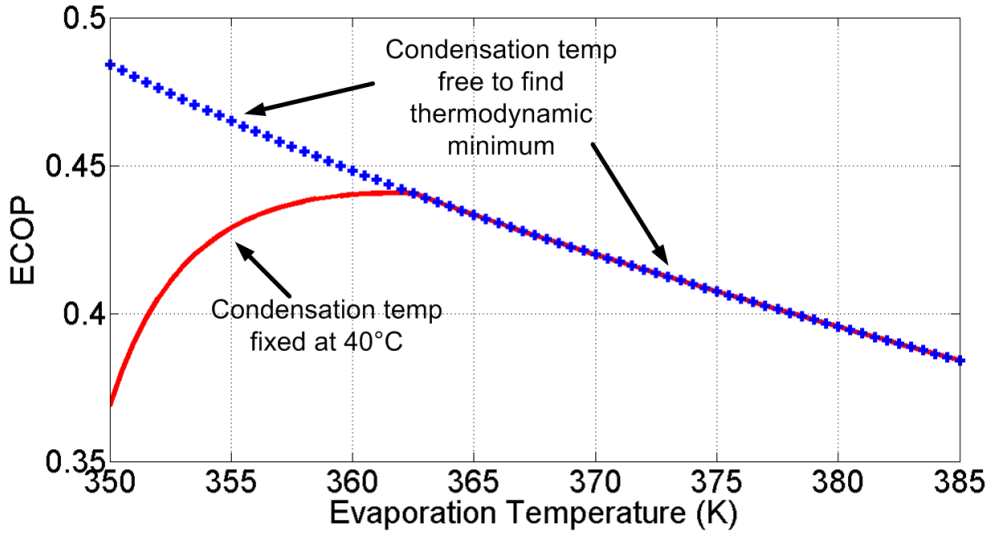


Figure 3.16: Varying effect of T_e upon the system's ECOP, highlighting the impact of letting the condensation temperature vary or keeping it fixed. This plot assumes the following levels: T_{cond} = 1, GTL1 = 3, GTL2 = 3 and the following settings: dT_{Hx} = 10K, GTL3 = 145 °C. The minimum allowable condensation temperature is set at 40 °C in this example.

The performance of this cycle is then compared to an identical cycle which has no such minimum condensation temperature. It is clear from this figure that when the condensation temperature is fixed (i.e.: at lower evaporation temperatures) the ECOP increases with an increase in the evaporation temperature as predicted by Lee and Sherif (2000). However once the condensation temperature is free to reach its thermodynamic minimum (set by the crystallisation limits in the generator) then the ECOP decreases sharply with any further increases in the evaporator's temperature.

In reality however, the temperature of the evaporator is intrinsically linked to the value of GTL3. If a plant requires heat energy at a particular temperature (for example 215 °C), then the lower the temperature of the evaporator, the larger GTL3 must be (as the absorber temperature is equal to the sum of the evaporator's temperature and GTL3). Thus when selecting the optimum value of the evaporation temperature, the behaviour of GTL3 must also be accounted for. While GTL3 only has a statistically significant effect upon COP, FR and E_D, T_e only has a significant effect upon ECOP. Therefore for the dependent variables which are only affected by GTL3 (COP, FR and E_D), the evaporation temperature should be selected so as to ensure that GTL3 is at its optimum value (instead of having the evaporation temperature at its optimum value). Thus by examining

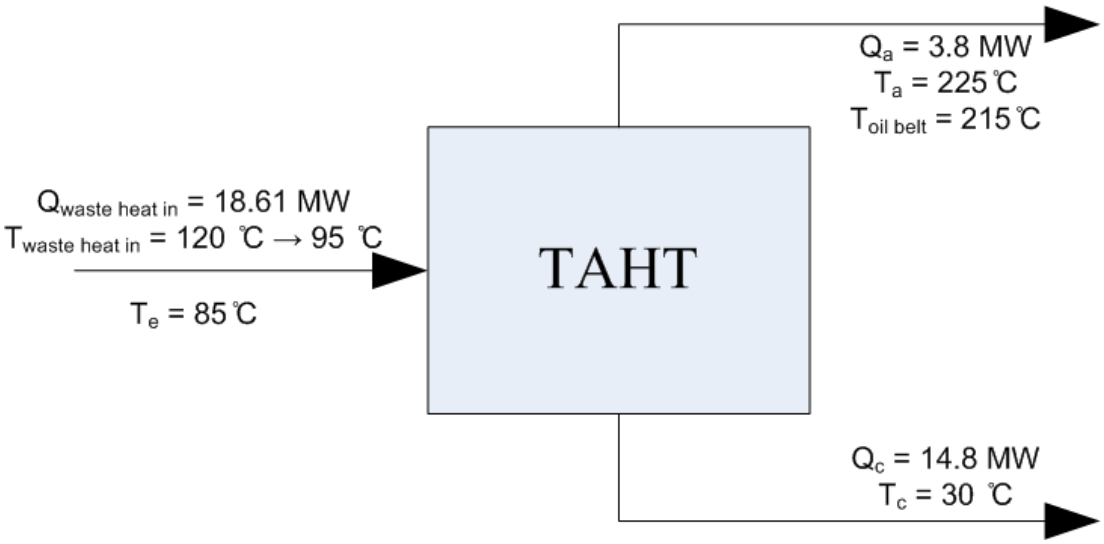


Figure 3.17: Schematic of the general temperature and energy adjustment achieved by the TAHT in the case study example discussed in section 3.4.3.

Figures 3.8 and 3.15, it may be seen that in order to optimise the system's COP, FR and E_D, T_e should be maximised (so as to minimise GTL3), while in order to maximise the ECOP T_e should be minimised as discussed previously.

Taking into consideration that in general the first law parameters of COP and FR have a greater impact in the both the engineering and economic performance of the TAHT, and also as it has been shown in Figure 3.16 that the ECOP only increases under the correct conditions with a decrease in evaporation temperature, **it is recommended that in general T_e be maximised in any triple absorption heat transformer**.

3.4.3 Example case study, showing potential optimised system operation

A demonstration is provided in this section, as to how the above results may be practically applied in an industrial setting. This example corresponds to a real case study in which an oil refinery has a crude oil distillation column from which the overhead vapours leave at 120 °C. Currently, these vapours are condensed and subsequently cooled to 40 °C in an air-cooled atmospheric heat exchanger. The total thermal power discharged by this heat exchange unit is approximately 22.7MW. The company wishes to create a hot oil circulation belt at 215 °C which may then be used as a heat source within the plant. It is company policy not to

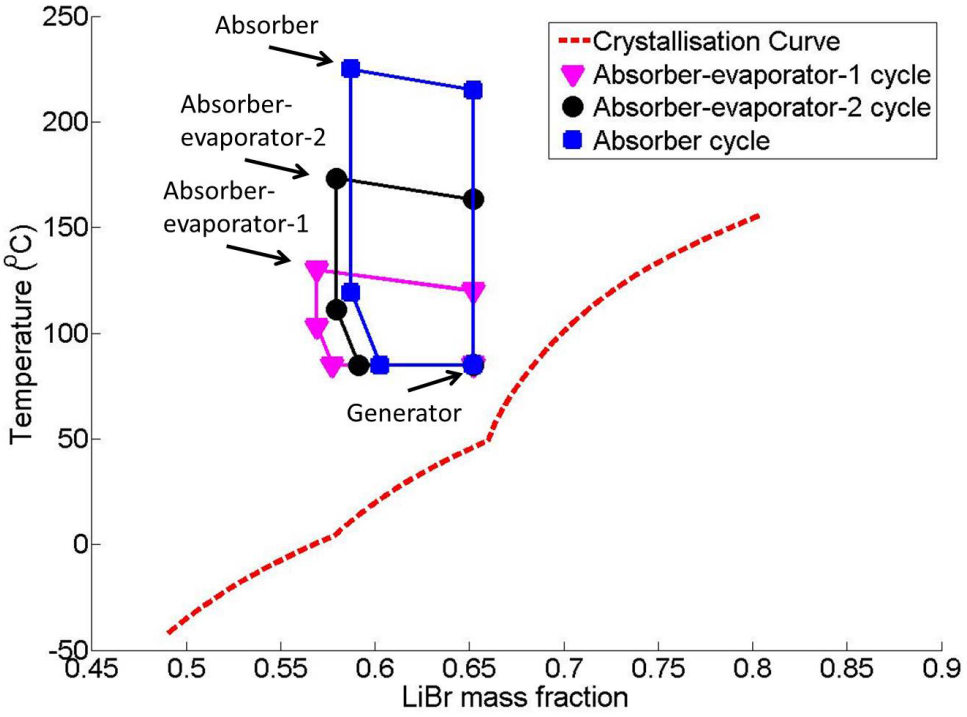


Figure 3.18: Salt concentrations within the cycle of the case study discussed in section 3.4.3 depicted against the LiBr − H_2O crystallisation curve referenced from Pátek and Klomfar (2006). The absorber-evaporator-1 cycle refers to the solution cycle circulating between the generator and Absorber-evaporator-1 in Figure 1.14, while the absorber-evaporator-2 and absorber cycles refer to the salt solutions circulating between these unit operations and the generator respectively.

use a pinch temperature gradient any smaller than 10 °C for economic and spatial reasons, and ambient temperatures are approximated at 20 °C.

A triple stage heat transformer (TAHT) utilising LiBr − H_2O as the working fluid pair (as depicted in Figure 1.14) could be used to allow a portion of this energy currently being discharged to atmosphere to heat the hot oil belt. The vapours would be condensed and cooled to 95 °C in the heat transformer, while the remaining energy is discharged as before to atmosphere. It should be noted at this point that although single and double stage systems show several very important advantages over the use of TAHTs in achieving temperature augmentations such as a lower capital cost, greater simplicity of design and higher thermodynamic performance (first and second law), these cycles cannot be used to achieve large temperature lifts such as that required by this case study. Herein lies the greatest advantage of the TAHT in that it can achieve temperature rises which are impossible with single or double stage systems due to limits imposed by crystallisation

in the generator (note that the relationship between the TAHT salt concentrations in this example and the $LiBr - H_2O$ crystallisation curve referenced from Pátek and Klomfar (2006) is illustrated in Figure 3.18). Thus triple stage cycles should be used only when the required GTL exceeds the temperature lift which single and double stage systems can achieve efficiently and are very suitable for application in scenarios where a high temperature product is required.

From the previous analysis in this chapter it has been demonstrated that the temperature of the condenser (T_c), the pinch heat transfer gradient (dT_{Hx}) and the total gross temperature lift (GTL3) should be selected so as to be as low as possible, while still allowing for the system to achieve its objectives. Thus $T_c = 30\,°C$, $dT_{Hx} = 10\,°C$ and GTL3 = 140 °C. The evaporation temperature (T_e) is maintained at its highest level, in order to maintain a low flow ratio at the cost of a slightly reduced ECOP, and thus $T_e = 85\,°C$. As previously discussed, points of optimum exist for both GTL1 and GTL2, which are generally defined as the temperatures half way between their maximum and minimum thermodynamically possible values. In section 3.4.2.3 it was also demonstrated that specific optimum values can be found using equation 3.1. This equation shall be used for the sake of example here to find GTL1 and GTL2, and in this case the COP is used as the dependent variable (as this is the most relevant industrial indicator of system thermodynamic performance). Therefore $(\partial COP/\partial GTL1) = (\partial COP/\partial GTL2) = 0$ is solved to give GTL1 = 47.67 °C (level 3.5) and GTL2 = 90.12 °C (level 2.8).

The resulting system outputs are: COP = 20.49%, ECOP = 44.07% and FR = 8.82 (E_D is not given here as it is not a dimensionless parameter like the other outputs, and thus in this case it would appear simply as an arbitrary figure). It is approximated that the TAHT would remove 82% of the energy from overhead stream due to condensation and cooling effects, and thus 3.814MW of thermal power could be recycled to the hot oil belt which is at 215 °C as illustrated in Figure 3.17.

The benefits of the results obtained in this chapter are clearly demonstrated in this example. Once the temperature of the heat stream is known and it has been decided what the required GTL should be, by using the simple results outlined in this chapter, without any further knowledge of the complicated interactions between factors and the non-linearity of their effects, the system can be very quickly and easily operated at its thermodynamic optimum without any use of limiting approximations.

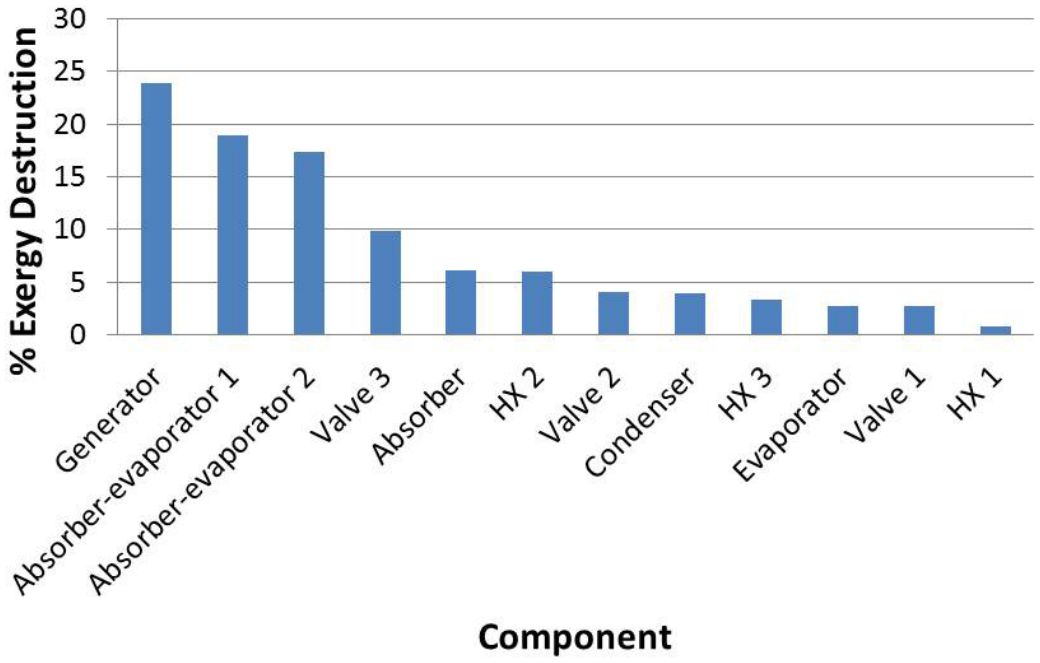


Figure 3.19: Percentage exergy destruction caused by each unit operation within the cycle

3.4.4 Unit Exergy Destruction

In the example discussed in section 3.4.3, the ECOP achieved is 41.1%. For a perfectly reversible system however, this would equal 100%, and thus no exergy would be destroyed. Such a reversible system is known as the Carnot cycle, and is a theoretical representation of a thermodynamic cycle with no entropy generation. Thus the COP of a reversible Carnot cycle (COP_{rev}) can be derived by simultaneously solving both enthalpy and entropy balances upon the system (as no entropy is being generated), and is shown in equation 3.2. Applying this equation to the TAHT in this example gives an achievable COP_{rev} of 42.9%. Thus the thermodynamic efficiency (η_{th}, equation 3.3) is ~0.5. This means that there are large irreversibilities within the cycle which must be identified to allow for future performance improvements. This section attempts to determine which of the system's unit operations cause the most irreversibility in this case study, by calculating the rate of exergy destruction within each unit using equation 2.7, and comparing their values.

$$COP_{rev} = \left(\frac{T_a}{T_e}\right)\left(\frac{T_e - T_c}{T_a - T_c}\right) \tag{3.2}$$

$$\eta_{th} = \frac{COP}{COP_{rev}} \tag{3.3}$$

From the data presented in Figure 3.19, it may be seen that together, the generator and the two absorber-evaporators account for just over 60% of the total non-ideality within the system. The generator is the largest source of exergy destruction, and therefore this represents an area for potential improvement within the cycle. This is an expected result due to the nature of exergy destruction. In order to minimise exergy destruction, one must eliminate concentration and heat transfer gradients. In the generator, four different concentrations of salt solution are being mixed and thus this leads to large exergy destruction, while in the absorbers, differing concentrations are being mixed at different temperatures. In single stage systems, the exergy destruction rate is greatest in the absorber (Rivera et al., 2010b), as the same mixing of concentrations takes place in this unit as in the generator except at a higher temperature. In a DAHT however, the majority of this irreversibility is shifted to the generator (Fartaj, 2004) due to the increase in the number of different streams entering it (coming from the absorber, as in the SSHT, but also from the absorber-evaporator). Thus it appears correct that this trend would also continue in the TAHT due to the presence of a further absorber-evaporator.

3.5 Conclusions

The influence of all manipulated variables, and all possible interactive effects between these, upon the TAHT's four main thermodynamic performance parameters (COP, ECOP, FR and E_D) have been determined in this chapter. The temperature of the condenser and the pinch temperature gradient used for heat transfer are demonstrated to generally have the greatest influences upon these dependent variables. In addition, the optimum levels for each of these variables have been quantified. Specifically:

- The system's condensation temperature, pinch temperature gradient used for heat transfer, and total gross temperature lift should always be kept to a minimum.
- The temperature of the evaporator should be maintained as high as possible.
- Temperatures for the two absorber-evaporators should be located around

the mid-point between the highest and lowest possible settings. For any given scenario, the exact points of optimum may be found for any of these dependent variables by partial differentiation.

The generator accounts for the largest single source of exergy destruction within the cycle, followed by the two absorber-evaporators. Together these three units generate over 60% of the cycle's irreversibility.

Chapter 4

Internal Energy and Exergy Recovery in High Temperature Application Absorption Heat Transformers

4.1 Introduction

In the previous chapter, it was demonstrated that a triple absorption heat transformer (TAHT) may be optimised by selecting the correct temperature levels for different unit operations within the system. In addition, the largest an most influential sources of exergy destruction, and hence irreversibility, were identified. If no exergy destruction occurred within the system, it would operate as an ideal cycle. Of course this is not feasible in practice however (it should be noted that the assumptions made in section 2.3 also represent sources of exergy destruction in reality). Chen (1995) demonstrated that reversible COPs can only be achieved in an absorption heat transformer if the absorber heat load (and hence quantity of recycled energy) is zero. This is due to the fact that temperature gradients within the cycle's unit operations and their associated heat sources/sinks would have to be infinitely small. As this is not possible in reality, many researchers have modelled heat transformers as what are termed 'endoreversible' cycles (Chen, 1995, 1997a,b; Qin et al., 2004b). An endoreversible cycle is a cycle which is internally reversible (i.e.: operates with Carnot efficiencies), but which takes into consideration irreversibilities which exist between the cycle and the surrounding environment (Figure 4.1). In all of these studies, the irreversibility between the cycle and the environment is quantified by a resistance to heat transfer and hence a temperature gradient between units and their respective heating or cooling fluids.

While better approximations may be generated using the endoreversible cycle approach than when assuming the system to be completely reversible, it will never in fact represent a working heat transformer. A heat transformer's operation is based upon phase changes, temperature gradients and concentration gradients, all of which are sources of entropy generation and hence exergy destruction. In order for a heat transformer to become endoreversible, all of these gradients and phase changes would have to become infinitely small. To visualise the infeasibility of such a scenario, an absorber is taken as an example (Figure 4.2). In the absorber, cold steam and cold concentrated $LiBr - H_2O$ solution are mixed in order to generate a hot dilute $LiBr - H_2O$ solution which leaves the unit. The rate of exergy of each stream is given by equation 4.1, leading to the definition of the total exergy destruction rate in the unit (equation 4.2).

$$E = \dot{m}\left[(h - h_o) - T_o\,(s - s_o)\right] \tag{4.1}$$

Nomenclature

COP	Coefficient of performance of the system
dT_{Hx}	Minimum pinch temperature (heat transfer gradient) utilised in all system heat transfer operations (°C)
e	Specific exergy (J/kg)
E	Rate of Exergy (W)
ECOP	Exergetic coefficient of performance of the system
E_D	Total rate of exergy destruction within the cycle (W)
E_{dest}	Rate of exergy destruction in a unit operation (W)
FR	Flow ratio of the system
GTL	Difference in temperature between the absorber and the generator (°C)
GTL1	Difference in temperature between absorber-evaporator-1 and the generator (°C)
GTL2	Difference in temperature between absorber-evaporator-2 and the generator (°C)
h	Specific enthalpy (J/kg)
$\dot{m}$	Mass flowrate (kg/s)
s	Specific entropy (J/kgK)

Temperatures (In ascending order)

T_o	Ambient temperature (298.15K)
T_c	Temperature of the condenser
T_e	Temperature of the evaporator
T_g	Temperature of the generator (equal to T_e in this study)
T_{ae1}	Temperature of the salt solution in absorber –evaporator-1
T_{ae2}	Temperature of the salt solution in absorber –evaporator-2
T_a	Temperature of the salt solution in the absorber

Pressures (In ascending order)

P_0	Pressure of the condenser and the generator. Equal to the vapour pressure of water at T_c.
P_1	Pressure of the evaporator and absorber-evaporator-1. Equal to the vapour pressure of water at T_e.
P_2	Pressure of absorber-evaporator-2. Equal to the vapour pressure of water at $T_{ae1} - dT_{Hx}$.
P_3	Pressure of the absorber. Equal to the vapour pressure of water at $T_{ae2} - dT_{Hx}$.

Subscripts

o	Ambient conditions (T = 298.15K, P = 101325Pa)

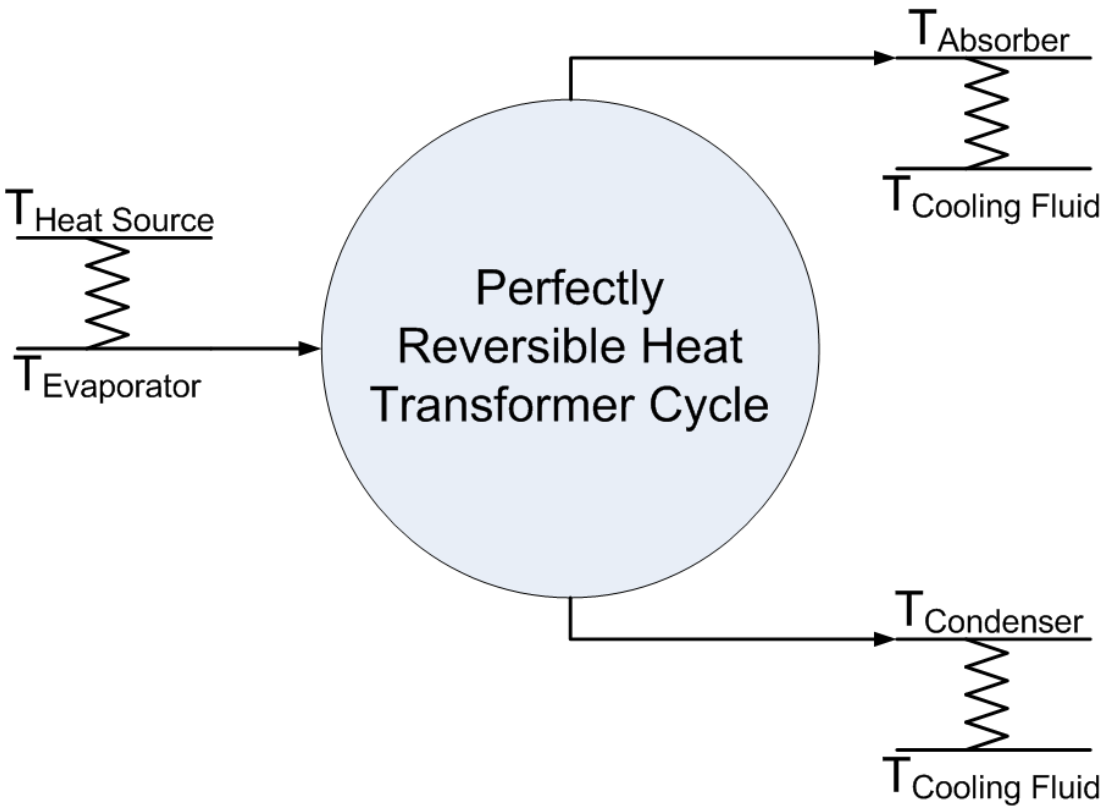


Figure 4.1: Schematic of an endoreversible heat transformer

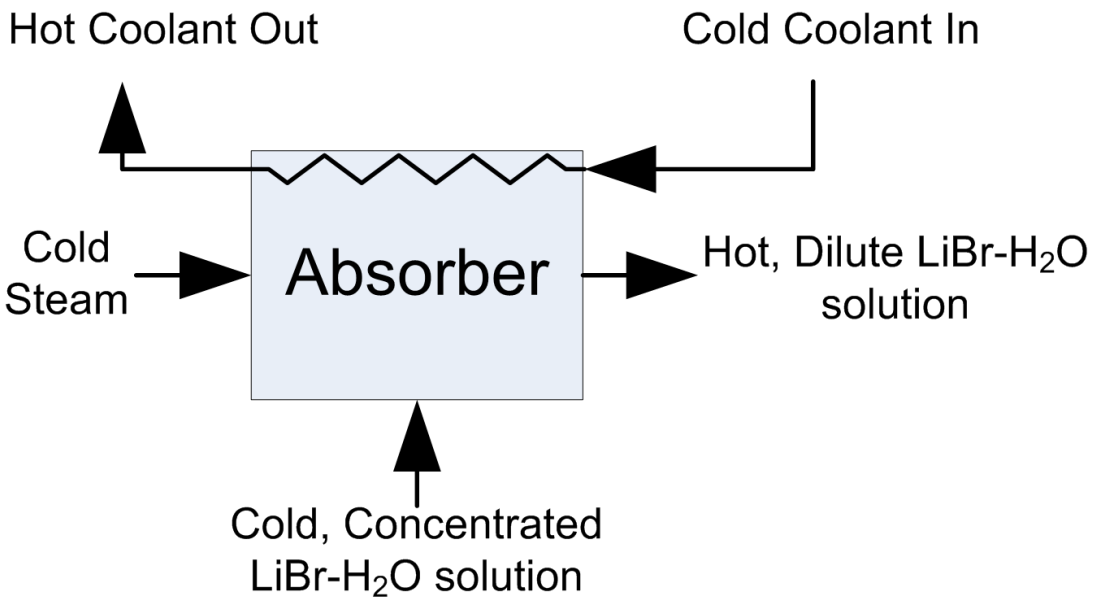


Figure 4.2: Schematic of an the flows entering and leaving an absorber in a heat transformer

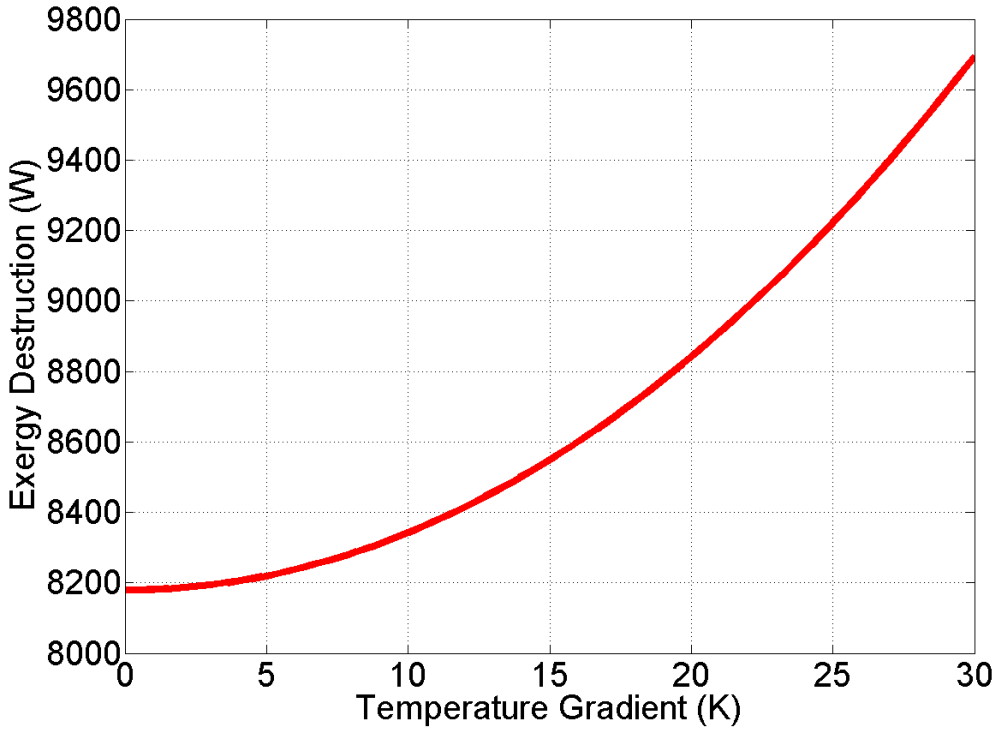


Figure 4.3: Variation in the absorber exergy destruction rate with an increase in the difference between the temperatures entering and leaving the absorber. This figure assumes the ratio of steam to solution entering the unit is 0.2, the inlet $LiBr - H_2O$ concentration is 0.65 (w/w) and the outlet temperature is 140 °C at atmospheric pressure.

$$(E_{dest})_k = \sum (E_{in} - E_{out})_k + Q_k \left(1 - \frac{T_o}{T_k}\right) - W_k \tag{4.2}$$

Natural gradients exist within this unit, the most obvious of which is the difference between the temperatures of the steams entering the absorber and the temperature of the dilute solution leaving it. If for the sake of an example, the temperatures of the entering streams (steam and the a concentrated $LiBr - H_2O$ solution) are taken to be equal, then by conducting an enthalpy balance upon the absorber and subsequently applying equations 4.1 and 4.2, the exergy destruction rate in the unit may be seen to increase exponentially with an increase in this temperature gradient (Figure 4.3). In turn, due to the phase change which is occurring in this unit, the only way of eliminating this exergy destruction rate is to reduce the entering steam mass flowrate to negligible quantities (Figure 4.4). However if the flowrate of steam is zero, then no exothermic reaction takes place in the absorber and the heat transformer cannot function. Hence it is clear that

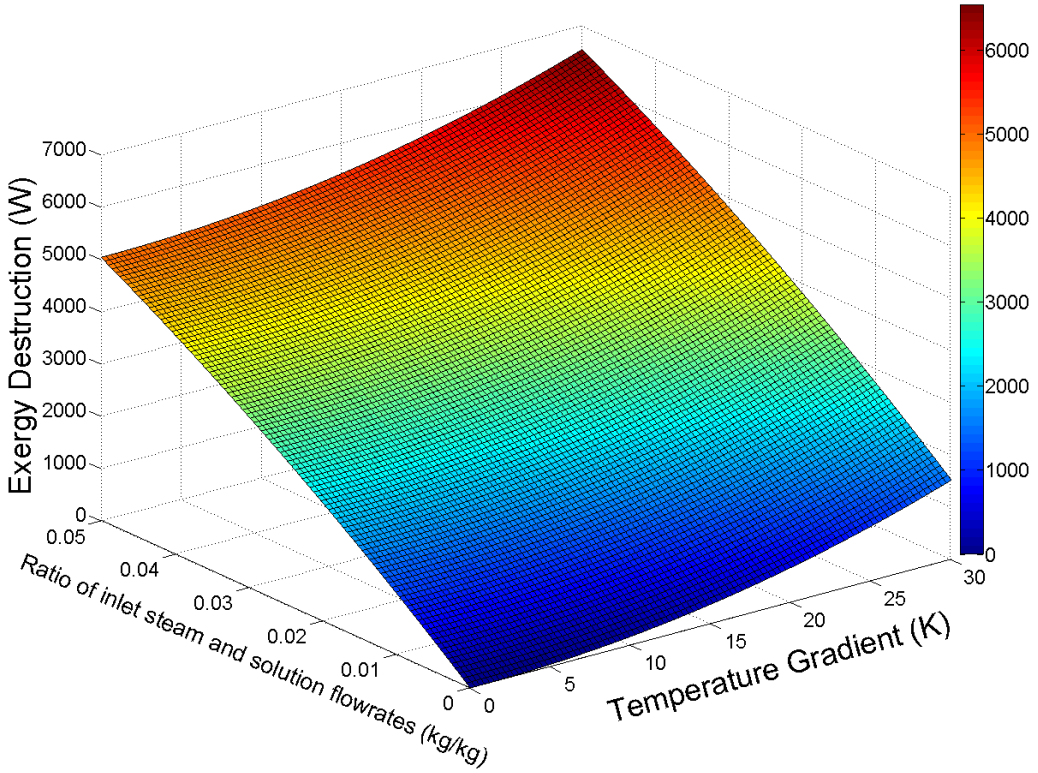


Figure 4.4: Absorber exergy destruction rate with a variation in the difference between the temperatures entering and leaving the absorber and a variation in the ratio of steam to solution entering the unit (mass flowrate of steam divided by mass flowrate of solution). This figure the inlet $LiBr - H_2O$ concentration is 0.65 (w/w) and the outlet temperature is 140 °C at atmospheric pressure.

irreversibilities must occur in the heat transformer in order for it to operate successfully and to recycle heat energy. The above scenario is merely a practical demonstration of the second law of thermodynamics.

The concentration gradient within the unit and the phase change which is occurring are fixed by the cycle's mass balance. The specific heating load (i.e.: the heat released from the unit with respect to the solution mass flowrate entering it) in an absorber increases with an increase in the difference between the salt mass fraction of the concentrated solution entering and the dilute solution leaving the unit (Barragán et al., 1996). Thus in general, it is not of practical interest to reduce the concentration gradient within an absorber, as such a reduction leads to a significant increase in the flow ratio of the system (i.e.: a greater solution flowrate is required to achieve the same heating load) (Barragán et al., 1997). Similarly, a reduction in phase change occurring within the unit also reduces its specific heat load. The optimised settings developed in the previous chapter in-

directly deal with these parameters and find their optimum values in order to minimise the flow ratio while maximising COP.

In contrast, the temperature gradient within a unit such as the absorber (and within any other unit in the system) may be reduced by increasing the heat recovery within the cycle. Figure 4.3 illustrates that such decreases in temperature gradients may lead to significant reductions in exergy destruction in each piece of equipment. Unlike reductions in concentrations gradients, improved heat recovery has no negative impacts upon the thermodynamics of the cycle, as it increases the specific heating loads of the absorbers (i.e.: less of the absorption's exotherm must be used to increase the temperature of the incoming streams and can therefore be removed as product). This chapter therefore aims to minimise exergy losses due to temperature gradients within the TAHT's units by examining in detail the cycle's internal heat recovery.

4.2 Internal Heat Recovery in Absorption Heat Transformers

In general, the design of multistage absorption heat transformers simply builds upon that of the single stage heat transformer (SSHT) by adding an absorber-evaporator and an extra heat exchanger to the cycle each time (Lee and Sherif, 2000). It has been shown however that the issue of internal heat recovery is critical to the performance of the heat transformer, and studies have demonstrated that an increase in the effectiveness of the internal heat exchangers within the system leads to a distinct increase in the overall thermodynamic output from the cycle (Martínez and Rivera, 2009). Thus especially as the systems' number of stages increase and gross temperature lifts become greater, these designs should be critically examined in order to determine whether they are in fact maximising this potential heat recovery. Certain aspects of internal heat transfer have been analysed to date, such as the replacing of conventional shell and tube heat exchangers in the generator, evaporator, condenser and internal solution heat exchanger with brazed plate units in order to increase the heat transfer coefficient and thus reduce capital cost (Genssle and Stephan, 2000). This adjustment does not influence the thermodynamic output of the cycle however. A second heat exchanger is included into a SSHT by a study which aims to analyse the effect of including an ejector into such a system (Sözen and Yücesu, 2007), while in

contrast it is demonstrated that due to the very low flow ratio employed in a SSHT being installed in a particular sugar mill, a very good performance may still be achieved even without any internal solution heat exchanger (Scott et al., 1999a). Many double absorption heat transformers have two internal solution heat exchangers (Fartaj, 2004), however other methods of achieving heat recovery in such cycles has been shown to be possible which require only one such heat transfer unit by allowing the hot dilute salt solution leaving the absorber to act as the concentrated salt solution entering the absorber-evaporator (Martínez and Rivera, 2009; Rivera et al., 2003). This method eliminates the need for a cold salt solution stream to enter the absorber-evaporator but will lead to increased flow ratios due to an undesirable reduction in the concentration gradient within the unit as discussed previously.

To the author's best knowledge, no complete dissection of the design of multi-stage absorption heat transformers has been conducted to date. This provides a motivation for this work. A full dissection of the design of a triple stage absorption heat transformer is conducted which aims to determine the optimum utilisation of internal heat transfer units within the cycle in order to maximise the system's thermodynamic output.

4.3 Mathematical Modelling

The mathematical model of a TAHT developed in Chapter 2 is used throughout this analysis, with the addition of the same two additional constraints as used in the previous chapter, namely:

1. The analysis is conducted with a refrigerant vapour flowrate of 1kg/s entering the absorber (this does not affect the performance variables being analysed in this study).
2. Dilute absorbent solutions leaving the two absorber-evaporators, the absorber and the generator are assumed to be saturated.

The TAHT model developed requires six thermodynamic inputs which are selected based upon the findings of the previous chapter:

1. The temperature of the condenser (T_c)
   (a) Throughout this chapter T_c is coded to always take its minimum available temperature (with respect to ambient temperature and crystalli-

sation in the generator).

2. The difference in temperature between absorber-evaporator-1 and the generator (GTL1)
   (a) Throughout this chapter GTL1 is coded to always take its intermediate temperature, halfway between its maximum and minimum thermodynamically allowable values.
3. The difference in temperature between absorber-evaporator-2 and the generator (GTL2)
   (a) Throughout this chapter GTL2 is coded to always take its intermediate temperature, halfway between its maximum and minimum thermodynamically allowable values.
4. Minimum pinch temperature (heat transfer gradient) utilised in all system heat transfer operations (dT_{Hx})
   (a) Throughout this chapter dT_{Hx} is given the value of 10 °C.
5. The temperature of the evaporator (T_e)
   (a) T_e's value is varied throughout the analysis and thus defined in the Results and Discussion section.
6. The difference in temperature between the absorber and the generator (GTL)
   (a) GTL's value is varied throughout the analysis and thus defined in the Results and Discussion section.

4.4 Heat exchange network modelling

The starting point for the modelling of this heat exchange network (HEN) is the basic triple absorption heat transformer (TAHT) excluding any internal heat recovery operations as illustrated in Figure 4.5. This system is entered into the HEN code developed by the author using the software Matlab R2010b (MathWorks Inc., Massachusetts USA). This code in turn breaks the system up into a collection of heat sinks (streams which need to be heated from a lower temperature to a higher one) and heat sources (streams which need to be cooled from a high temperature to a lower one). These heat sources and heat sinks are then

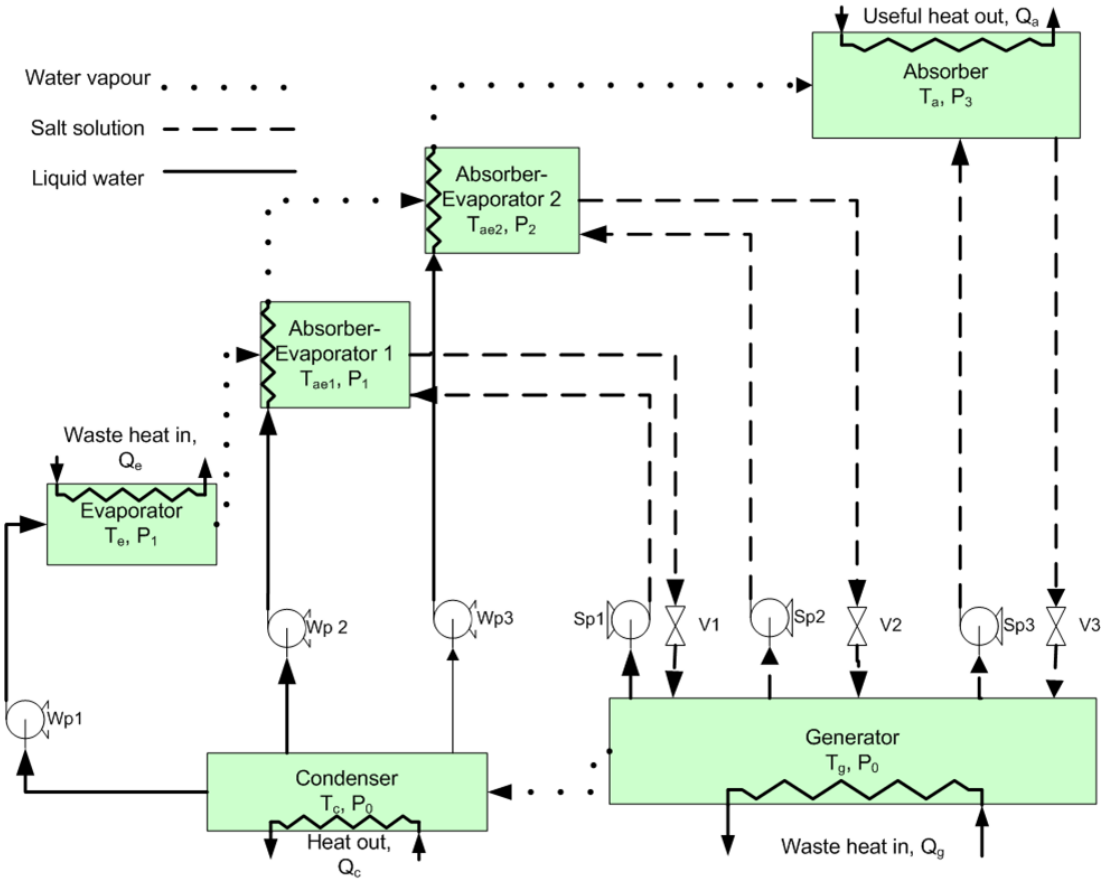


Figure 4.5: Schematic of the basic TAHT containing no heat exchangers

combined systematically in order to maximise the retention of exergy within the cycle. A basic breakdown of the steps within the code is presented below.

1. Identify all possible heat transfer combinations (i.e.: which heat source may be used to satisfy a heat sink).

   (a) The aim of steps 2 - 6 in this list is to find the hot and cold streams which are best suited to being combined together in a heat exchange operation (a heat exchanger). During this process, in order to retain exergy and emulate a reversible system as best possible, priority is given to high temperature combinations over lower temperature pairings. The method used throughout the code ensures that (if appropriate) higher temperature heat sinks are always dealt with before colder heat sinks.

2. Determine which of these combinations result in a complete elimination of the heat sink in question.

   (a) Elimination is henceforth referred to as a hot stream (heat source) completely satisfying the heating requirements of a cold stream (heat sink), thus effectively eliminating the heat sink from the list of streams available for the next combination.

3. If no eliminations are possible, identify whether any hot salt streams should be combined into a single heat source which may provide a better option for heat transfer.

   (a) If a combination does occur, repeat steps one and two.

4. If a number of complete eliminations have been identified, determine the most suitable combination based on stream properties such as temperatures and heat capacities of streams etc.

   (a) Determine whether any special combinations exist which should be dealt with before this elimination. If there are no such special cases, this combination is now the pairing of streams for the current heat exchanger.

5. If no complete eliminations are identified, determine whether any combinations allow for a partial elimination.

   (a) A partial elimination refers to the heating of a cold stream from its cold temperature to some temperature below its final hot temperature or the other way around (i.e.: if a cold stream must be heated from 100 °C to 150 °C. Partial elimination would refer to either heating the stream from 100 °C to e.g.: 140 °C or else from e.g.: 130 °C to 150 °C).

   (b) If partial eliminations do exist, determine the most suitable combination based on stream properties such as temperatures and heat capacities of streams etc., and this combination is now the pairing of streams for the current heat exchanger.

6. If no complete or partial eliminations are identified, fractional elimination must take place.

   (a) Fractional elimination refers to eliminating a fraction of the heat sink (i.e.: instead of sending the full cold stream to the heat exchanger, determine the fraction of the stream which can be successfully heated by the hot stream from its starting cold temperature to its final hot temperature, i.e.: eliminated).

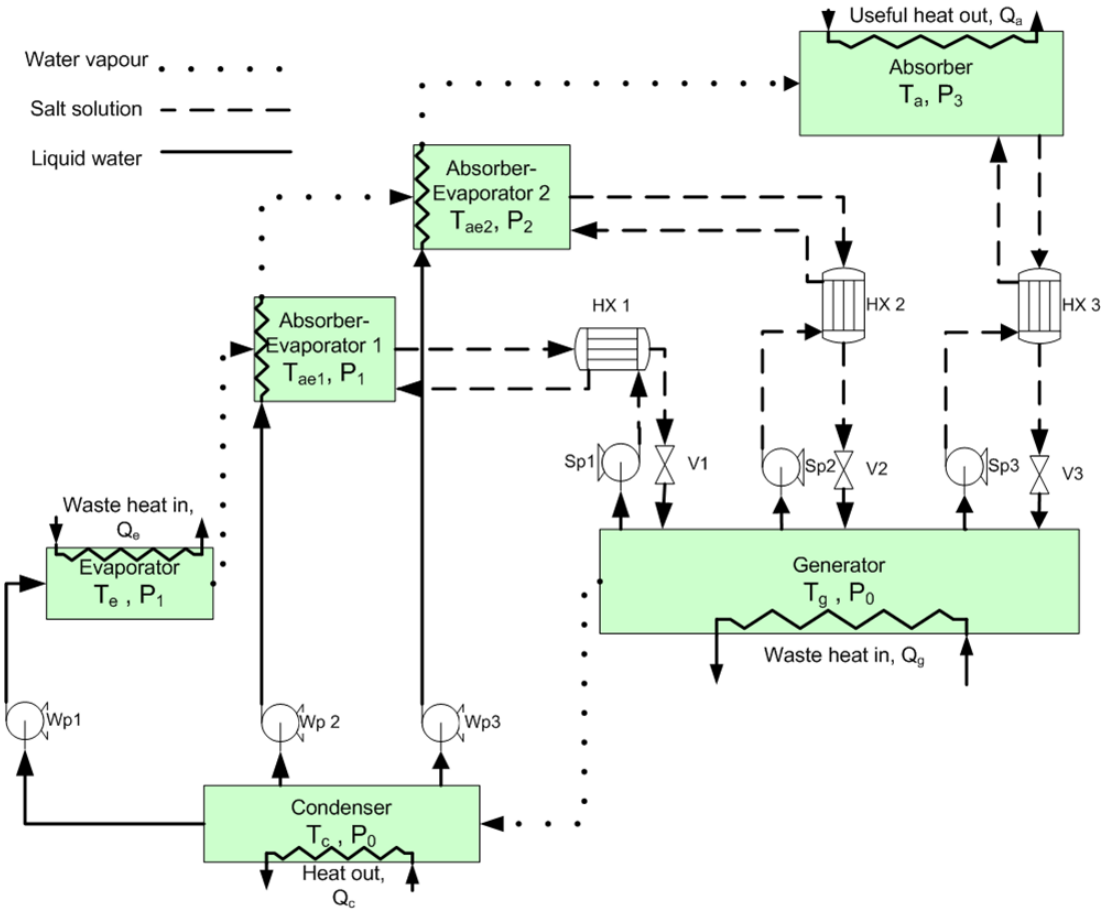


Figure 4.6: Schematic of the conventional triple absorption heat transformer (TAHT)

(b) Determine the most suitable combination based on stream properties such as temperatures and heat capacities of streams etc., and this combination is now the pairing of streams for the current heat exchanger

7. Using the stream combination selected in steps 2 - 6, model the thermodynamics of the heat exchanger being added to the cycle.

8. Repeat all of the above steps until no more heat exchanges are possible.

9. Add all of the heat exchangers to the original cycle and calculate the system's dependent variables (system outputs)

4.4.1 Selecting streams available for heat transfer and analysis

The analysis conducted in this chapter aims to determine the possible heat exchanges available within a TAHT and to identify which of these operations are most critical with respect to the overall system performance. In practice, the economic feasibility of a TAHT is dependent upon its thermodynamic performance and its capital cost. The optimum system would have a high COP and low flow ratio while requiring a minimum amount of internal heat exchangers. The conventional system shown in Figure 4.6 and described in detail in Chapter 1 has three heat exchangers (allowing for the preheating of each of the salt solutions flowing from the generator to the two absorber-evaporators and the absorber).

In this study, all possible internal heat energy recovery scenarios are to be analysed ranging from no heat exchangers within the cycle (the basic TAHT shown in Figure 4.5) to a full pinch analysis (Smith, 2005) which maximises all possible heat recovery options. In order to achieve this, it is to be assumed that all hot streams (heat sources) are at all times available for heat transfer, while heat sinks (cold streams) are made available systematically.

In order to select these heat sinks, a full factorial model is used in which the factors are all of the TAHT's cold streams. The levels for each factor in this analysis are simply logical operators which indicate whether that particular factor (cold stream) is available for heat transfer or not. Thus as there are 8 cold streams which are being considered in this HEN, and each of these streams has two levels (either it is available for heat transfer or not), there are $2^8 = 256$ possible designs in this study.

This method ensures that every heat exchanger is tested individually, which will quantitatively indicate its importance to the system, and that also the optimum combination of heat exchangers can be identified. It should be noted at this point that the true optimum combination would ideally be determined by economic analysis.

The list of available cold streams (heat sinks) being considered in this study are as follows:

1. Salt solution flowing from Sp_1 to absorber-evaporator-1.
2. Salt solution flowing from Sp_2 to absorber-evaporator-2.

3. Salt solution flowing from Sp_3 to the absorber.
4. Liquid water flowing from Wp_2 to be evaporated in absorber-evaporator-1.
5. Liquid water flowing from Wp_3 to be evaporated in absorber-evaporator-2.
6. Water vapour flowing from the evaporator to absorber-evaporator-1.
7. Water vapour flowing from the absorber-evaporator-1 to absorber-evaporator-2.
8. Water vapour flowing from the absorber-evaporator-2 to the absorber.

From this point on, these streams shall be referred to by the order in which they appear in this list, i.e.: heat sink 1 refers to the salt solution flowing from Sp_1, etc.

4.5 Results and Discussion

The results of this analysis show that in general the standard configuration as illustrated in Figure 4.6 does not in fact represent the optimum configuration of heat exchangers. Firstly the individual influences of the heat sinks are analysed to see which heat sinks when heated on their own have the greatest potential to influence the system's COP (section 4.5.1). Secondly, all possible combinations of heat exchangers are analysed to find the optimum combination which has the greatest positive influence upon the system's dependent variables while minimising the number of heat transfer units (section 4.5.2). For purposes of clarity and presentation of results, sections 4.5.1 and 4.5.2 are both based upon a single set of operating conditions thought to be relatively common for a TAHT application, which are $T_e = 100\,°C$ and $GTL = 140\,°C$. Section 4.5.3 then in turn analyses whether these results remain applicable once T_e and GTL are varied over defined temperature ranges.

4.5.1 Individual heat sink analysis

The results presented in Figure 4.7 show how much the COP of the basic TAHT is improved by the heating of each of the heat sinks respectively. The numbers show that the heating of the three vapour streams (heat sinks 6, 7 and 8) is quite unnecessary as this simply adds complexity and cost to the system without any notable improvement in the COP. Therefore these streams shall no longer

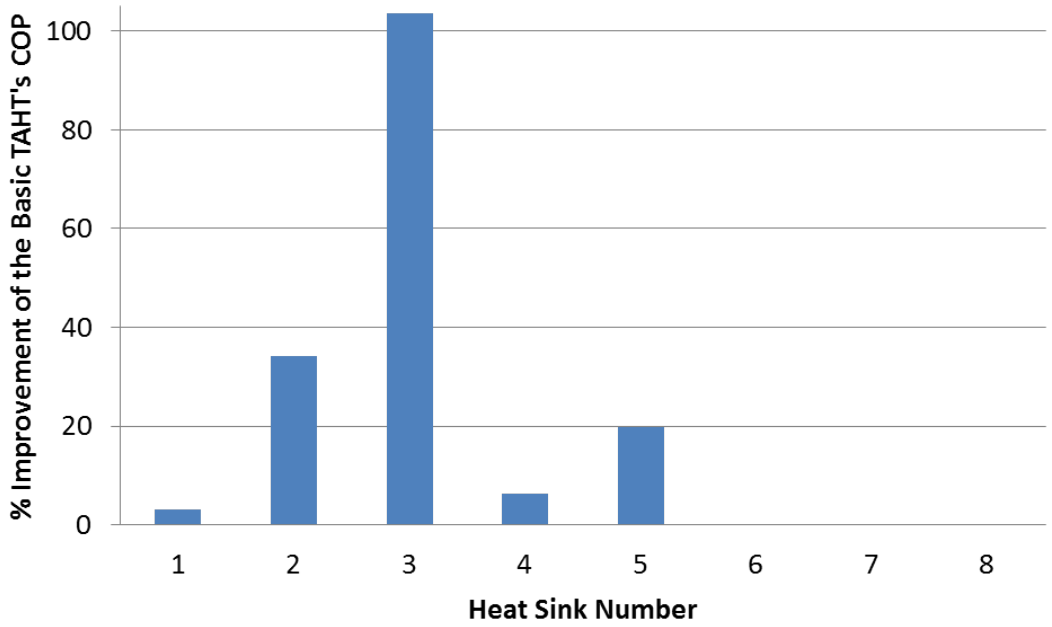


Figure 4.7: The percentage by which each of the individual heat sinks increase the basic TAHT's (Figure 4.5) COP

be considered in the analysis henceforth. Of the remaining 5 heat sinks, it is quite clear that the heating of the salt solution flowing from the generator to the absorber is by far the most important, as this stream has the largest temperature augmentation to overcome.

The second most important stream to heat is heat sink 2 which represents the salt solution flowing from the generator to absorber-evaporator-2. Again this makes intuitive sense, as this stream has the second highest flowrate of all the heat sinks, and also has one of the largest temperature augmentations.

Both heat sinks 2 and 3 are addressed in the conventional TAHT design. The value of such a configuration has been demonstrated above. However, the third heat sink which is heated in this conventional design, heat sink 1 which represents the salt solution flowing from the generator to absorber-evaporator-1, appears to make a minimal contribution, only improving the basic TAHT's COP by 3.14%. In contrast, heat sink 5 (water flowing from the condenser to be evaporated in absorber-evaporator-2) appears to have a much greater influence upon the cycle's performance. This can be attributed to the fact that heat sink 5 has a much greater temperature augmentation than heat sink 1, but also due to the fact that the specific heat capacity of a salt solution is significantly less than the specific heat capacity of pure water. Thus by the same arguments, heat sink 4 also has a

No. of Hx	COP	ECOP	FR	$E_D(\times 10^5$ W)
0	0.078	0.151	6.07	16.54
1	0.160	0.306	6.07	13.95
2	0.208	0.399	6.11	8.80
3 (Conventional)	0.213	0.410	6.15	8.40
3	0.238	0.457	6.13	6.64
4	0.248	0.477	6.20	6.04
5	0.253	0.486	6.24	5.75

Table 4.1: The best system performances (based upon the cycle's COP) for each number of heat exchangers included into the TAHT. The performance of the conventional TAHT design is also included as a reference.

greater influence than heat sink 1.

4.5.2 Heat exchanger combination analysis

The results of all the designs are analysed, and for each number of heat exchangers included in the cycle, the design is selected which gives the optimum system performance. It is found that variations in the COP are mirrored by the variations in the ECOP and the E_D, and thus COP is used as the output when determining the best performance. Interestingly, it is found that the flow ratio in fact increases with the number of heat exchangers added to the cycle, but that its value does not change greatly.

The results of these designs are summarised in Table 4.1, and show some very interesting trends. Firstly it should be noted that the performance of the system containing only two heat exchangers (see Figure 4.8) is very similar to that of the conventional TAHT design. The COP of this cycle is only 0.005 smaller, while its flow ratio is in fact decreased by 0.04. This contrast highlights very clearly the ineffectiveness of the third heat exchanger in the conventional TAHT which is being used to heat heat sink 1 prior to its entering absorber-evaporator-1. This extra heat exchanger would contribute significantly to the capital cost of the system, while having almost no influence upon its overall output.

It is also important to note that if three heat exchangers are to be utilised, the conventional TAHT configuration does not produce the best system outputs. In fact, there are two other designs which produce higher COPs and reduce

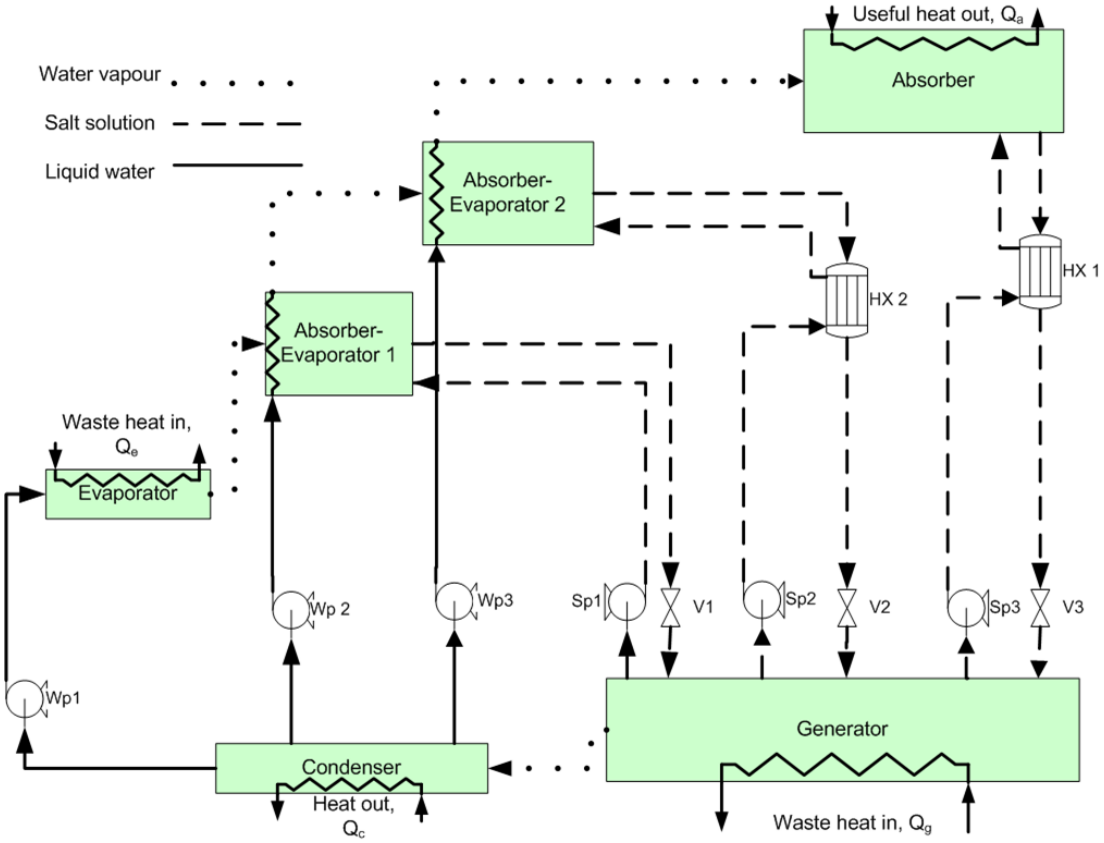


Figure 4.8: Schematic of the optimum design of the TAHT containing two heat exchangers

irreversibilities within the cycle using the same amount of heat exchangers. The best of these is illustrated in Figure 4.9, and shows that the improvement in performance is due to the heating of heat sink 5 instead of heat sink 1, which agrees with the conclusions drawn in section 4.5.1. This improved design also reduces the flow ratio of the cycle slightly.

At this point, the increases in the system's COP become smaller in magnitude for every heat exchanger which is added. The best design containing four heat exchangers also includes the heating of heat sink 4, the water flowing from the condenser to be evaporated in absorber-evaporator-1 (Figure 4.10). This inclusion causes the COP to rise to 0.248, while the flow ratio also increases slightly to 6.2.

Only once the fifth heat exchanger is added does the system address heat sink 1 (Figure 4.11). The addition of this extra unit causes only a small rise in the cycle's COP to 0.253 illustrating once more that this is the least important heat sink to be dealt with.

All of these results emulate the findings of section 4.5.1, and demonstrate that

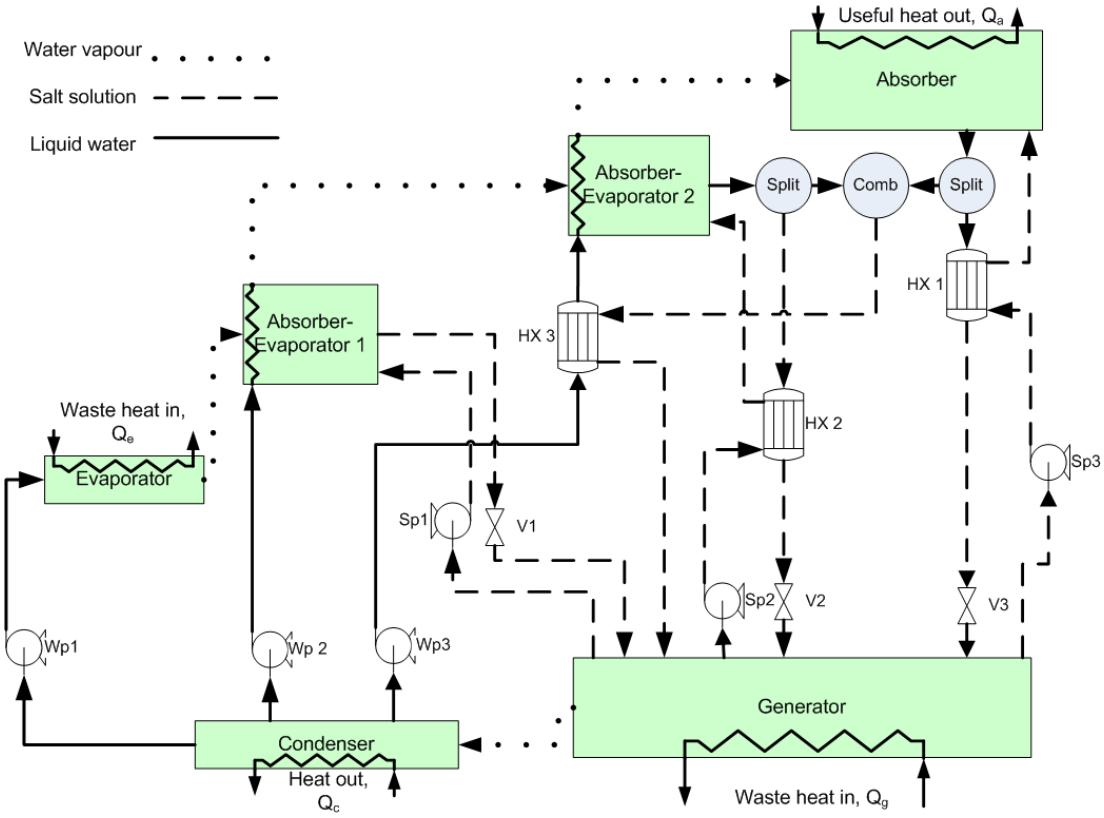


Figure 4.9: Schematic of the optimum design of the TAHT containing three heat exchangers

certain heat sinks should have a clear priority over others when designing internal heat recovery into the system. The system which represents the optimum design must be determined by means of economic analysis for the specific scenario in which the TAHT is being implemented. Depending upon the quantity of energy to be recycled, it may or may not be economically justifiable to include either the third, fourth or fifth heat exchanger into the system. At a very minimum however, it has been shown in this chapter that the cycle can operate with a high performance even with only two heat transfer units.

4.5.3 Temperature influence upon Optimum designs

As all of the results presented to this point refer to specific operating conditions, a study is now conducted to determine the effect which altering the evaporation temperature and the gross temperature lift has upon the selection of the optimum designs. The method which is used is to compare the COP of each of the designs to that of the conventional design ($\mathrm{COP_{HEN\ Design}} - \mathrm{COP_{Conventional}}$) to see how

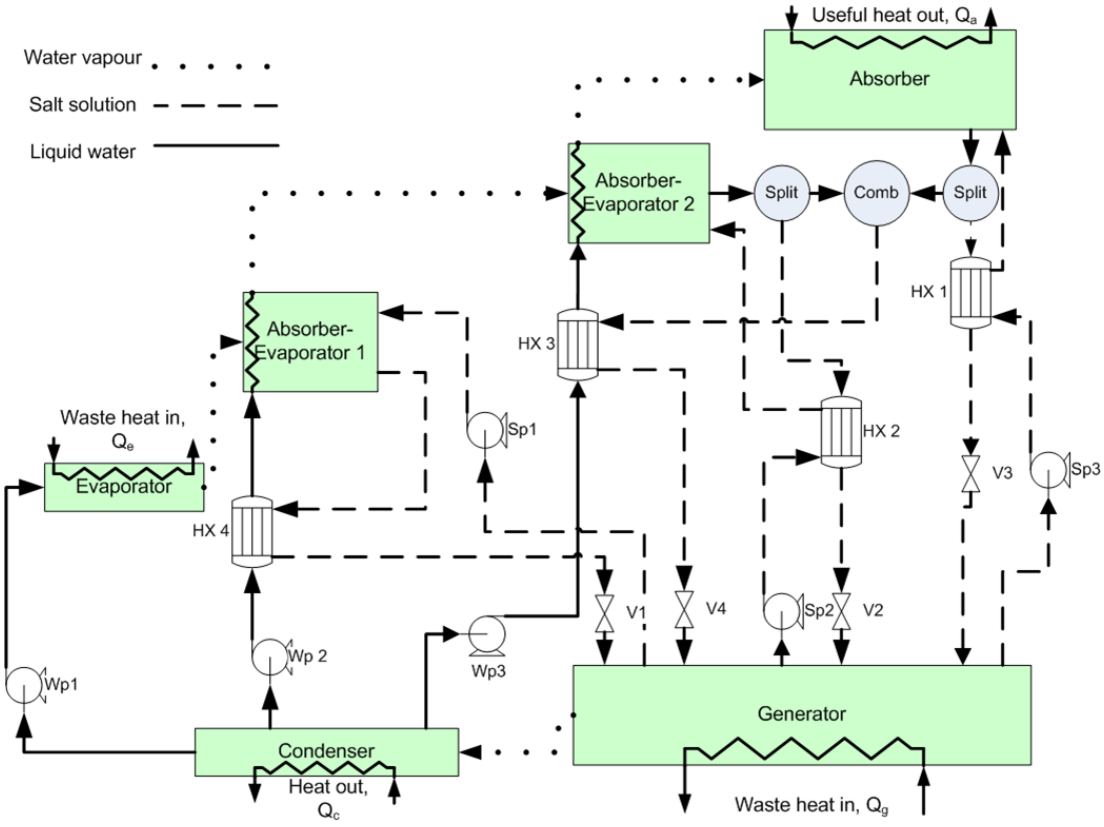


Figure 4.10: Schematic of the optimum design of the TAHT containing four heat exchangers

advantageous the suggested alterations are under different conditions. COP is used once more due to the reasons outlined in section 4.5.2. It is found that the HEN designs containing 2, 3, and 4 heat exchange units all behave similarly in this analysis. The pattern of results illustrated in Table 4.1 holds true for all system designs at high GTL and low evaporation temperature. The HEN designs containing 3 and 4 heat exchangers are always more advantageous if the GTL is maintained over roughly 115 °C. Similarly, the performance of the HEN design containing 2 heat exchangers remains very close to that of the conventional cycle, except for at high evaporation temperatures and GTLs below roughly 115 °C. The HEN design containing 5 heat exchange units, is also most advantageous at high GTLs and low evaporation temperatures, however its performance is always greater than that of the conventional cycle. The conclusion which may be drawn from this is that the heating of heat sink 1 is important at high evaporation temperatures and low gross temperature lifts, however once GTL values exceed 115 °C, its influence falls drastically, and thus may be ignored allowing for more efficient designs. Therefore the HEN designs presented in this chapter are ideally

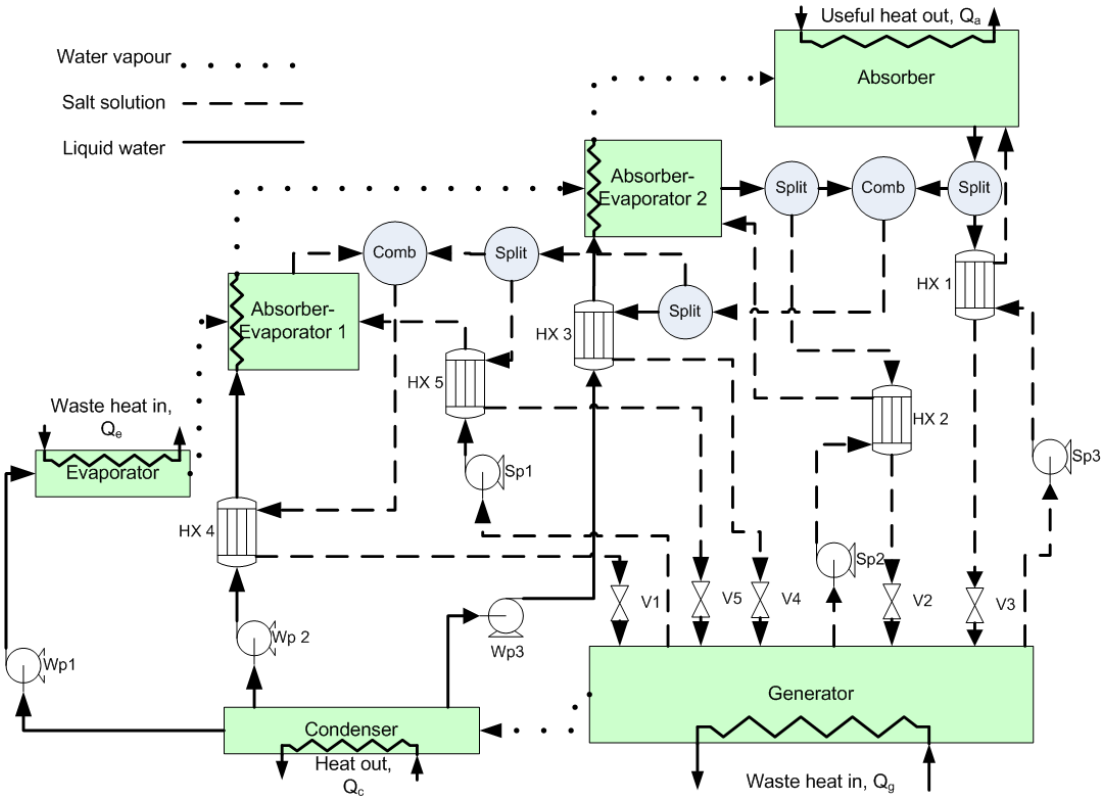


Figure 4.11: Schematic of the optimum design of the TAHT containing five heat exchangers

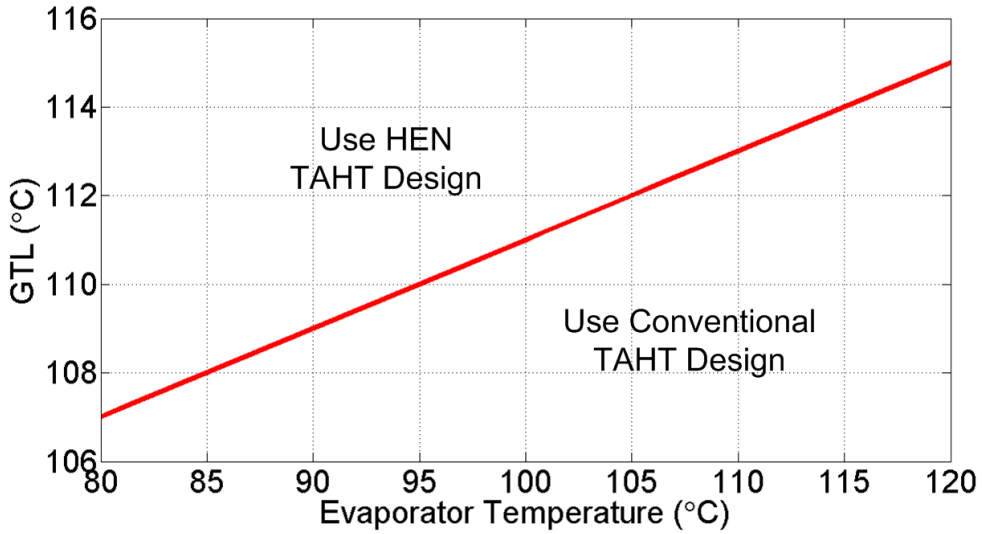


Figure 4.12: Limiting conditions of both evaporator temperature and system gross temperature lift (GTL) according to which either the conventional or HEN TAHT designs using three heat exchangers should be used.

suited to situations in which a high temperature product heat stream is required from the heat transformer.

As a quick reference guide to determine which of the designs containing three heat exchangers is more suitable (Figure 4.6 or Figure 4.9), the points where their two COP planes intersect may be approximated as a straight line, and in doing so the relationship between these two configurations outlined in equation 4.3 is developed (Note that this equation is based upon T_e having units of °C.). This limiting line is shown in Figure 4.12.

$$GTL - (T_e)\left(\frac{1}{5}\right) - 91 \begin{cases} > 0 & \text{Use HEN design} \\ < 0 & \text{Use conventional design} \end{cases} \tag{4.3}$$

4.6 Conclusions

Both the performance and capital cost of a triple absorption heat transformer are influenced greatly by the level of internal heat recovery within the system. In this chapter the cycle was dissected and reassembled using heat exchange network modelling. The most important heat exchangers to be included and their relative effects were determined. Results obtained show that the conventional design of the TAHT generally does not use its heat exchangers effectively, and that thus by rearranging these units the COP may be increased by 11.7% while the exergy destruction within the system (its irreversibility) is reduced by 21% at typical operating conditions. Strategically adding fourth and fifth heat exchangers increases the COP by 16.4% and 18.8% respectively while decreasing exergy destruction by 28% and 31.5% compared to the conventional TAHT design. These trends are in turn found to extend to all operating conditions tested at low evaporation temperatures or if the GTL is greater than 115 °C.

Chapter 5

Economic Evaluation of an Industrial High Temperature Lift Heat Transformer

5.1 Introduction

In the two preceding chapters, attempts have been made to optimise the operation and design of a triple absorption heat transformer (TAHT). Optimisations in terms of thermodynamic parameters such as the quantity of heat energy being recycled, the total irreversibility within the system or the flow ratio are vital engineering stages which must be conducted prior to evaluating the suitability of any new system or design. However unless there is an alternate motive such as health and safety requirements or the need to adhere to environmental regulations, the evaluation of a new system or design is generally conducted based upon economic analysis. Unless sufficient rates of return are achievable from the system, it is unlikely that any company will invest significant capital into the project.

The majority of previous heat transformer analyses conducted have focussed upon the engineering design of heat transformers and have neglected its economic aspect. Several studies have provided some data or results relating to the potential benefits of installing heat transformers in industrial settings such as Scott et al. (1999a) who conducted a study upon the various different methods of incorporating a single stage heat transformer (SSHT) into a sugar mill. The AHT which uses waste heat from the plant's crystallisation unit to provide some of the heat to a multi-effect evaporator is estimated to reduce the plant's live steam requirements by 11.8-16.4%. Similarly, Cortés and Rivera (2010) analysed the feasibility of incorporating a heat transformer into a pulp and paper mill. It is claimed that using a single stage heat transformer to preheat water prior to it entering a boiler could potentially reduce the plant's steam consumption by up to 25%.

Stating that a unit could save a certain quantity of steam each year is not adequate in terms of analysing the feasibility of its installation however. Depending on what that steam actually costs the plant and what the initial price of the heat transformer would be, this steam saving may in fact represent a long term loss to the company. Thus terms such as returns on investment and paypack periods should be used instead, as these attempt to take such issues into consideration. Some studies published to date do provide limited information relating to the economic performance of single stage heat transformers, such as Abrahamsson et al. (1995) who built a pilot self-circulating single stage heat transformer using the working fluid $NaOH - H_2O$, and incorporated it into an evaporation unit in a pulp and paper mill, achieving a predicted payback period of 4.4 years. Zhang et al. (2014a) examined the potential inclusion of a $LiBr - H_2O$ SSHT and a flash

Nomenclature

Economics Terms

CGP	Current Gas Price (€/kg)
DPBP	Discounted payback period of the TAHT design (years)
i	Discount rate applied over the project lifetime (13%)
N	Estimated TAHT lifetime (years)
NPV	Net present value of the TAHT design (€)
SPBP	Simple payback period of the TAHT design (years)

Greek Symbols

α	Heat transfer coefficient (W/(m^{2}K))
ρ	Density (kg/m^3)
μ	Dynamic Viscosity (kg/(m.s))

Dimensionless Numbers

Nu	Nusselt Number = $\alpha D/k$
Pr	Prandtl Number = $c_p\mu/k$
Re	Reynolds Number = $\rho v D/\mu$

AHT	Absorption heat transformer
COP	Coefficient of performance of the TAHT
c_p	Specific heat capacity (W/(m^{2}K))
COP_{total}	Total fraction of the waste heat stream energy content being recycled
D	Pipe Diameter (m)
k	Thermal Conductivity (W/(m.K))
LHV	Lower heating value of natural gas (J/kg)
Q	Thermal Power (W)
v	velocity (m/s)

Subscripts

a	Absorber
c	Condenser
e	Evaporator
g	Generator

evaporator (FE) into a CO_2 capture process, resulting in a potential payback period of 2.4 years, while Costa et al. (2009) analysed the economic feasibility of incorporating a DAHT into a paper and pulp mill and estimated a payback period of 1.6 years. To the author's best knowledge, the results of having installed a SSHT in a synthetic rubber plant presented by Ma et al. (2003) represent the only published industrial full scale application of an absorption heat transformer. The reduction in steam requirements achieved by the AHT from 2.53 tonnes of steam per tonne of rubber produced to 1.04 tonnes of steam per tonne of rubber produced ensured gross savings of 3.458 million Yuan per year were achieved, giving a reported payback period of 2 years.

Unfortunately, all of these before-mentioned studies simply present final estimated payback periods, and thus the reader has very little knowledge as to these figures' sensitivity to external socio-economic factors such as energy prices or simply the impact of a variation in the unit's capital costs. Such deeper analysis is vital however in order to determine why heat transformers are not currently being implemented by industry, as, according to the studies referenced in this section, they are capable of achieving large energy savings and potentially short payback periods.

All of the systems previously analysed using economic methods are either single or double stage systems which are being used to increase the temperature of some waste heat souce by 15-50 °C. For many energy intensive industrial scenarios however, this small temperature augmentation is not sufficient however, as temperatures of over 200 °C may be required for heating purposes. Thus the objective of this work is to conduct an industrial case study, analysing the economic feasibility of a triple absorption heat transformer in an Irish oil refinery. A comprehensive review of the factors influencing the system's economic indicators shall be conducted, and it is intended to determine under what conditions such a unit may be an attractive commodity to a company.

5.2 Case Study: An Oil Refinery

The oil refining industry is an extremely energy intensive sector and one which operates under tight profit margins, making it a primary candidate for energy recovery technology. This study has been conducted in conjunction with the Phillips 66 Whitegate oil refining plant in Ireland, aiming to determine whether the installation of an absorption heat transformer unit into their plant is a fea-

sible option. A number of waste heat streams which are of primary interest to the company have been identified and incorporated into this design. The temperature profile of the plant is such that only relatively high temperature thermal heat may be used within the existing heat exchange network (HEN), and thus a relatively large gross temperature lift will be required from the heat transformer. Following analysis of the waste streams available, it is determined that only a triple stage system can achieve these required lifts. Thus in this chapter, a triple stage absorption heat transformer (TAHT) system is designed for use in this oil refinery. Particular attention is paid to the economic performance of the unit as this has been highlighted by the company as the primary viability determining factor.

5.3 Mathematical Modelling

5.3.1 Thermodynamic

The triple absorption heat transformer model developed in Chapter 2 is being utilised in this study in conjunction with the optimised TAHT system design incorporating three heat exchanger discussed in the previous chapter and illustrated in Figure 4.9. The majority of the temperature settings in the system are obtained from the results outlined in Chapter 3, namely:

1. The temperature of the condenser (T_c) always takes its minimum available temperature (with respect to ambient temperature and crystallisation in the generator.
2. The difference in temperature between absorber-evaporator-1 and the generator (GTL1) always takes its intermediate temperature, halfway between its maximum and minimum thermodynamically allowable values.
3. The difference in temperature between absorber-evaporator-2 and the generator (GTL2) always takes its intermediate temperature, halfway between its maximum and minimum thermodynamically allowable values.
4. Minimum pinch temperature (heat transfer gradient) utilised in all system heat transfer operations (dT_{Hx}) is given the value of 15 °C in any air-cooled equipment and 10 °C in all other units.
5. The temperature of the evaporator (T_e) is selected so as to take its maxi-

mum value with respect to the waste heat energy's temperature.

6. The difference in temperature between the absorber and the generator (GTL) is adjusted based upon the temperature of the evaporator to ensure that the absorber retains a temperature of 230 °C.

7. A difference of 5 °C is maintained between the temperature of the dilute solution leaving any absorber and its boiling temperature.

As this is an industrial case study, the principle thermodynamic outputs from the system are its COP (equation 5.1) and the total coefficient of performance of the entire installed unit (COP_{total}). The system's COP is defined similarly as in previous chapters as the ratio of the useful heat product leaving the system with respect to the energy inputs into the TAHT.

$$COP = \frac{|Q_a|}{|Q_e| + |Q_g| + \sum |W_{pumps}|} \tag{5.1}$$

The total coefficient of performance of the installed unit (COP_{total}) is defined as the ratio of the useful heat leaving the system with respect to the total waste heat energy contained in the heat streams.

$$COP_{total} = \frac{|Q_a|}{|Q_{WasteHeat}|} \tag{5.2}$$

From the above two definitions, it is clear that the total COP of the system (COP_{total}) is a function of the COP (a measure of the TAHT's internal efficiency) and of how much of the total available heat contained in the waste heat streams is extracted into the evaporator and generators. Generally, the reason that some of the waste heat cannot be extracted is that these streams are being cooled to temperatures lower than those of the evaporators and generators. Thus this remaining energy must be discharged to atmosphere.

$$COP_{total} = COP \left[\frac{|Q_e| + |Q_g| + \sum |W_{pumps}|}{|Q_{WasteHeat}|} \right] \tag{5.3}$$

5.3.2 Costing

The costing of equipment is an imprecise task due to the large amount of indeterminacy which can affect the final figure. In an attempt to obtain estimates which

are as accurate as possible in this study through harnessing experiential knowledge, the costing of all equipment was conducted independently by the Capital Program Manager of the Oil Refinery. These costs are thus based upon data relating to previous purchases of similar equipment.

In order to quantify the savings achievable by the installation of the TAHT, the equivalent quantity (and hence price) of natural gas being saved due to the recycled heat is estimated. Based upon figures from the refinery, their furnaces have an efficiency of $\sim 80\%$, and thus savings are calculated using equation 5.4. The cost of burning natural gas for heating purposes is currently estimated by the refinery to be between \$600 and \$700 per tonne, and a figure of \$650 per tonne is thus selected as the current gas price in this case study. All costing in this study is conducted in Euro. Thus a conversion rate of 1.28(\$/€) recorded on July 10th 2013 is being used (as this represents the approximate average rate observed between July 2012 and July 2014), equating to a mid 2013 gas price (CGP) of €508 per tonne. The lower heating value of natural gas (LHV) is taken to be 47.14MJ/kg (Oak Ridge Laboratory, 2011).

$$Saving = GasPrice \left[\frac{EnergyRecycled}{0.8LHV} \right] \tag{5.4}$$

5.3.3 Economic Indicator

Three basic economic indicators are used in this study to determine the profitability of the TAHT installation, namely simple payback period (SPBP), discounted payback period (DPBP) and the net present value (NPV).

The SPBP gives a simple indication of how many years it will take to recoup the initial capital expenditure based upon the annual savings generated by the TAHT as shown in equation 5.5. It gives a very simple overview of the investment's feasibility, but doesn't however take into account the time value of money (due to inflation or interest etc.), and thus represents a crude economic reduction.

$$SPBP = \frac{AnnualSaving}{CapitalInvestment} \tag{5.5}$$

The DPBP is identical to the SPBP, except that it attempts to take into account the time value of money. Thus this parameter attempts to provide a more realistic indicator of the time period required to recoup an initial investment

(equation 5.6). While in some aspects the DPBP may be preferred to the SPBP by economists, it still suffers from the reality that the future time value of money can never be accurately predicted. Nevertheless it has been indicated by the refinery that a cost of capital of 13% is generally utilised during investment analyses in order to account for uncertainties, and thus a discount rate of 13% is applied to this investment (i = 0.13).

$$DPBP = \ln\left(\frac{1}{1 - \frac{(i)(CapitalInvestment)}{AnnualSaving}}\right) / log_e\,(1+i) \tag{5.6}$$

The NPV of an investment is an indicator of the total income which a company could generate from a capital investment over the defined lifespan of the project. It sums an assumed annual cash flow generated by the TAHT (taking into account some predicted time value of money) over a project's total projected lifetime (N, in this case taken as 20 years), and compares this figure to the total investment required. A positive value indicates a potentially viable investment, while a project with a negative NPV should in theory not be invested in.

$$NPV = \sum_{y=1}^{N} \frac{AnnualSaving}{(1+i)^y} - CapitalInvestment \tag{5.7}$$

5.4 Plant Conditions

Following consultation with the oil refinery, two streams of primary interest for waste heat recovery are identified, both of which are currently being cooled by means of air-cooled heat exchangers. The first stream consists of a residue oil line which is being cooled from 179 °C to 87 °C. This stream has a mass flowrate of approximately 46.8kg/s and is currently discharging 9.56MW to atmosphere. The second stream which is to be examined consists of Naphtha vapour coming off the top of a distillation column, and being condensed in an air-cooled heat exchanger. It enters at approximately 120 °C, is condensed and then subsequently cooled to 40 °C, discharging roughly 22.7MW of heat energy.

The company has stated that the most useful outcome would be to obtain a hot oil loop at 215 °C which can then be incorporated into their heat exchange network. This means that the heat transformer must be capable of increasing the waste heat streams' energy to approximately 225 °C, so that this heat energy may then be used to maintain the oil loop at 215 °C. Thus the waste streams

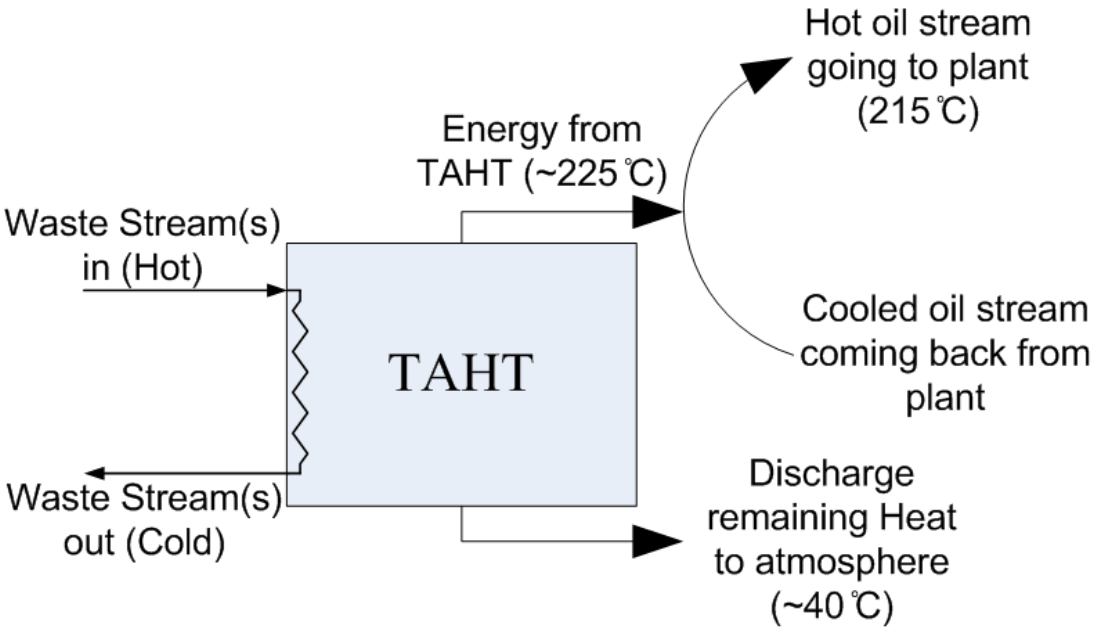


Figure 5.1: Schematic of the TAHT's operation in this case study

shall enter the TAHT and be cooled down to a temperature slightly greater than the temperature of the evaporator and generator (to allow heat transfer), while the hot oil circulation loop (Ethylene Glycol under slight pressure) will circulate between the TAHT and the plant's HEN as shown in Figure 5.1. The heat transformer will not be capable of carrying out all of the required cooling on the waste heat streams, due to their low final temperatures, and thus following the heat transformer, each stream shall pass through an air-cooler which will reduce its temperature to the desired level.

5.5 Results

5.5.1 Sizing

The specific heat transfer area requirements for each piece of equipment are given in Table 5.1. All falling film heat exchangers referenced in the below sections are vertical, and the areas quoted are the required heat transfer areas for the respective heat exchangers. The air-cooler is a finned unit, designed to match the equipment currently being used on site as closely as possible. Thus in the following sections, the area quoted for the air cooler is the bare area of the tubes. The total finned heat transfer area of the air cooler is approximately 18.5 times

Unit Name	Hx Type	Area(m^2)	Length(m)	Diameter(m)
Condenser	Air-Cooler	2574		
Evaporator-a	Falling Film	144	3.18	1.06
Evaporator-b	Falling Film	1815	7.06	2.35
Absorber-Evap-1	Falling Film	571	5.52	1.1
Absorber-Evap-2	Falling Film	574	5.52	1.1
Absorber	Falling Film	768	7.63	1.53
Generator-a	Falling Film	605	5	1.67
Generator-b1	Falling Film	3408	8.62	2.87
Generator-b2	Falling Film	3408	8.62	2.87
Hx-1	Shell & Tube	2528	11.11	2.22
Hx-2	Shell & Tube	4647	13.47	2.69
Hx-3	Shell & Tube	629	7.16	1.43
Excess Energy Hx-a	Air-Cooler	86		
Excess Energy Hx-b	Air-Cooler	431		

Table 5.1: Heat transfer surface area requirements of each piece of equipment in the TAHT, when it is being used to cool the Naphtha and Residue oil waste heat streams

greater than this bare area.

It should be noted that two evaporators and two generators are being used. This allows one evaporator and generator pair to cool the residue oil, and the other evaporator and generator pair to cool the naphtha. All other pieces of equipment remain as before.

The pieces of equipment which are satisfying the naphtha stream only are followed by '-a' (ie: Evaporator-a), while those in contact with the residue oil line are followed by '-b'. Note that due to the high viscosity of the residue oil coupled with its low density, all heat transfer areas which are in direct contact with the oil are larger than those in contact with the Naphtha stream. If a piece of equipment has been deemed to be too large, it is split into two identical pieces of equipment, as can be seen in Table 5.1 where a generator has been split into two smaller heat exchangers.

5.5.2 Costing

As outlined in section 5.3.2 the capital cost analysis in this study is based upon the estimates obtained from the oil refinery's costing division. The total purchase cost of equipment is predicted to be approximately €5.3million.

In reality however, the purchase cost of the equipment is not a sufficient estimate

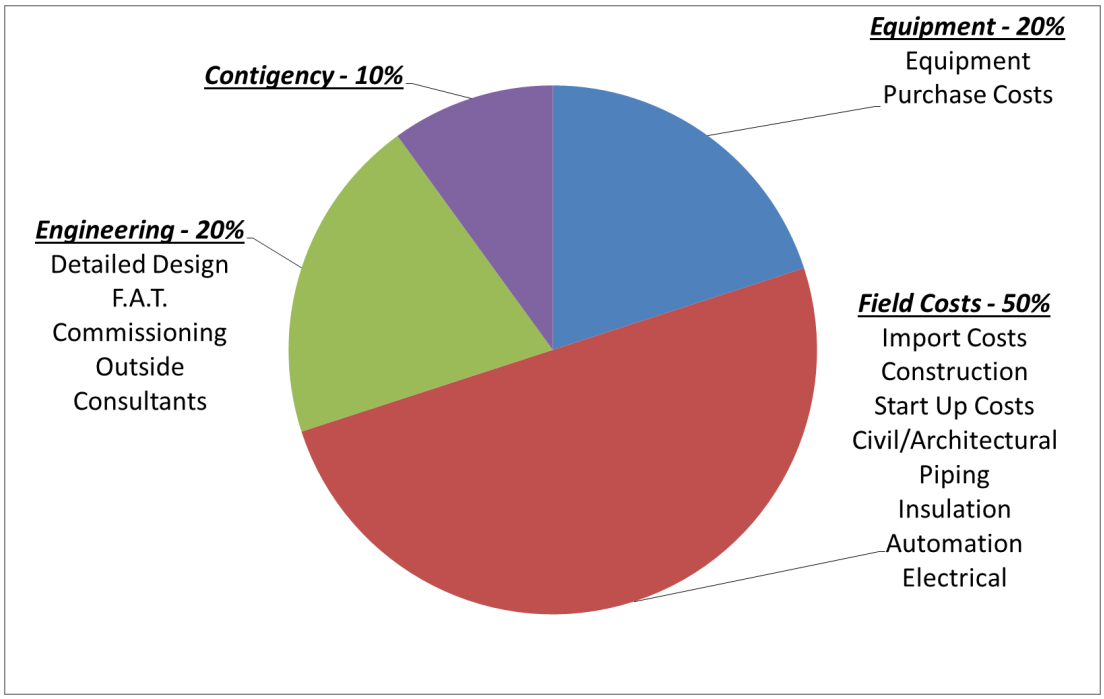


Figure 5.2: Breakdown of the general trend observed for project costs in the oil refinery

for the project budget as other ancillary factors must be taken into consideration. Based upon evidence of previous installed projects of a similar scale in the refinery, a cost breakdown similar to that outlined in Figure 5.2 has been recommended by the refinery costing division. This means that in general the project cost tends to be of the order five times greater than the bare equipment purchase cost. This factor is reduced to four in this case, as this unit would be installed in an existing plant, and thus would benefit from existing utilities and infrastructure. The revised total project cost is therefore approximately €21million. It should be noted that this factor (CapitalInvestment/EquipmentCosts $\simeq$ (4)) used to estimate the total project cost may vary between different operations. However as the refinery is being used as a working case study, the refinery figures are being referenced.

5.5.3 Thermodynamic Performance

For an industrial case study such as this, the thermodynamic performance of the system may be characterised by the COP of the TAHT, the overall COP of the waste heat recovery system (see section 5.3.1), and the total quantity of heat energy recycled (Q_a). A COP of 0.21 is achieved by the TAHT leading

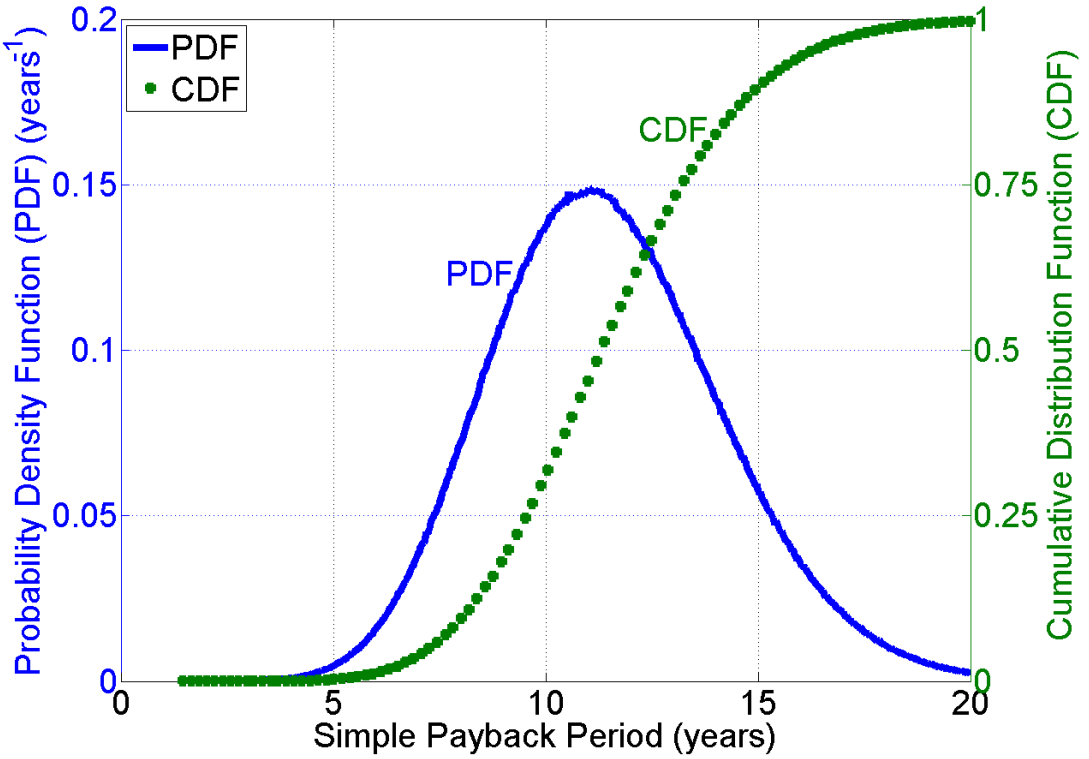


Figure 5.3: Probability and Cumulative distribution functions (PDF and CDF) of the simple payback period (SPBP) at the current gas price (CGP) as defined in section 5.3.2

to a COP_{total} of 0.14. Thus approximately 14% of all the waste heat streams' available energy is recycled, corresponding to approximately 4.5MW. This is due to the fact that the TAHT cannot accept waste heat at temperatures below its evaporator's temperature (in this case $\sim$ 100 °C), and thus any waste heat at lower temperatures must be discharged to atmosphere (in this example streams are being cooled to 40 °C and 87 °C respectively).

5.5.4 Economic Performance

The economic performance of this system is presented in terms of a simple payback period, a discounted payback period, and a net present value. Estimating future economic performance is by its very nature an imprecise and unpredictable activity. However, the potential viability of the TAHT in this study is considered by using a Monte Carlo simulation for capital costs and by means of scenarios in terms of energy prices. The primary sources of uncertainty in the model are the capital cost of equipment, the factorial method used to estimate the total project

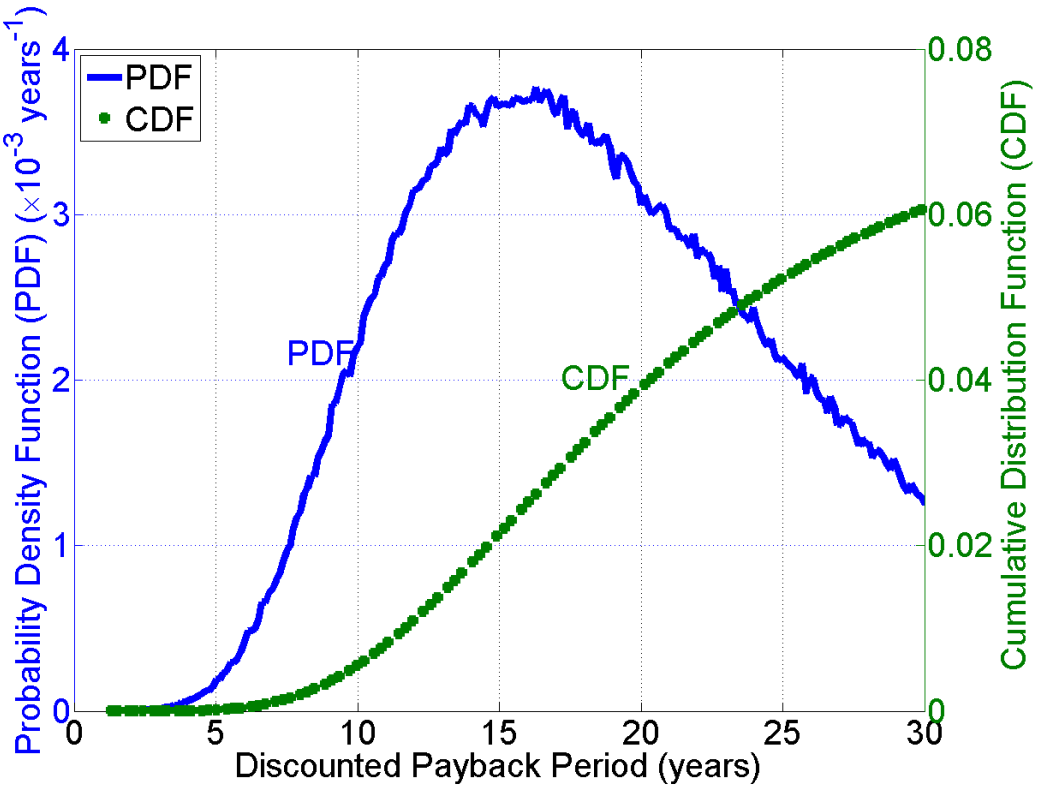


Figure 5.4: Probability and Cumulative distribution functions (PDF and CDF) of the discounted payback period (DPBP) at the current gas price (CGP) as defined in section 5.3.2

cost and the gas price. Based upon data gathered by the oil refinery, capital cost estimates at this stage of design may typically have errors of up to ±50%. In this study the equipment cost and the project cost factor are taken to be normally distributed with means represented by the values calculated/used in section 5.5.2. 99.7% of their variability is assumed to be contained within a domain of ±50% with respect to the mean to help account for capital cost uncertainty.

The results of these Monte Carlo Simulations are presented in terms of probability distribution functions (PDF) and cumulative distribution functions (CDF). The CDF illustrates the probability of any result up to the current result having occurred (thus for example a CDF of 0.7 for a SPBP of 5 years indicates that there is a 70% chance of the SPBP being 5 years or less).

The price of natural gas over the lifetime of a project is a hugely volatile and unpredictable function of the broad complex socio-economic, environmental and geopolitical system. It thus cannot be credibly predicted with any degree of certainty. Notwithstanding this reality, 'estimates' have still been proposed, such

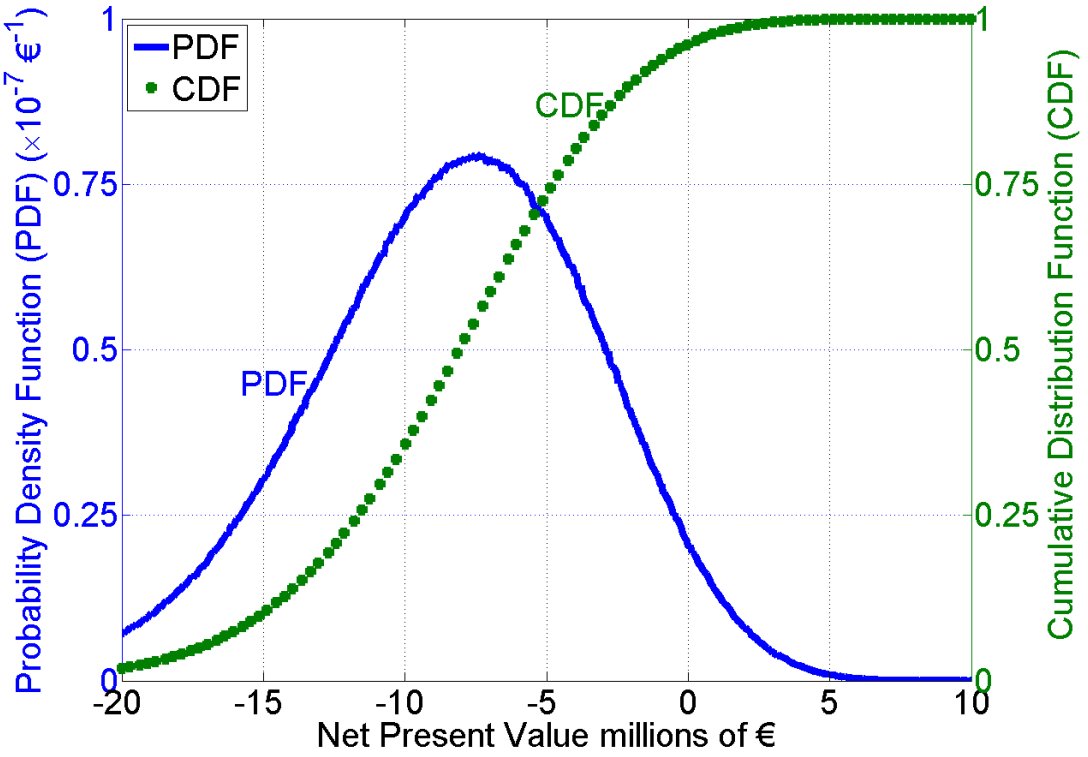


Figure 5.5: Probability and Cumulative distribution functions (PDF and CDF) of the net present value (NPV) at the current gas price (CGP) as defined in section 5.3.2

as the spot price projection which estimates that its commodity price will rise to a value of 5.23$/MMBTU by 2025 and 7.65$/MMBTU by 2040 (U.S. Energy Information Administration, 2014). Since 2008, the price of natural gas has varied by almost 300%, falling from a price of just under 12$/MMBTU in 2008 to a price of approximately 4$/MMBTU in 2013 (NASDAQ Stock Exchange, 2014). This price is vital to the economic success or failure of the TAHT, and thus making decisions based upon spot price predictions is dubious as it would generate meaningless results. Instead four different gas price scenarios are therefore tested in this chapter, all relative to the current gas price (CGP) as defined in section 5.3.2, namely 50%, 100%, 200% and 300% of the CGP.

Figures 5.3 to 5.8 show quite clearly the critical importance of the gas price. At the current price (CGP), the TAHT is not financially viable based upon industry norms. Using the simple payback period, there is only an approximate 27% chance that the project will pay for itself within the first 10 years of operation (Figure 5.3). In addition, the chance of any return being made upon the required investment over the system's entire lifespan of 20 years is approximately 4% based

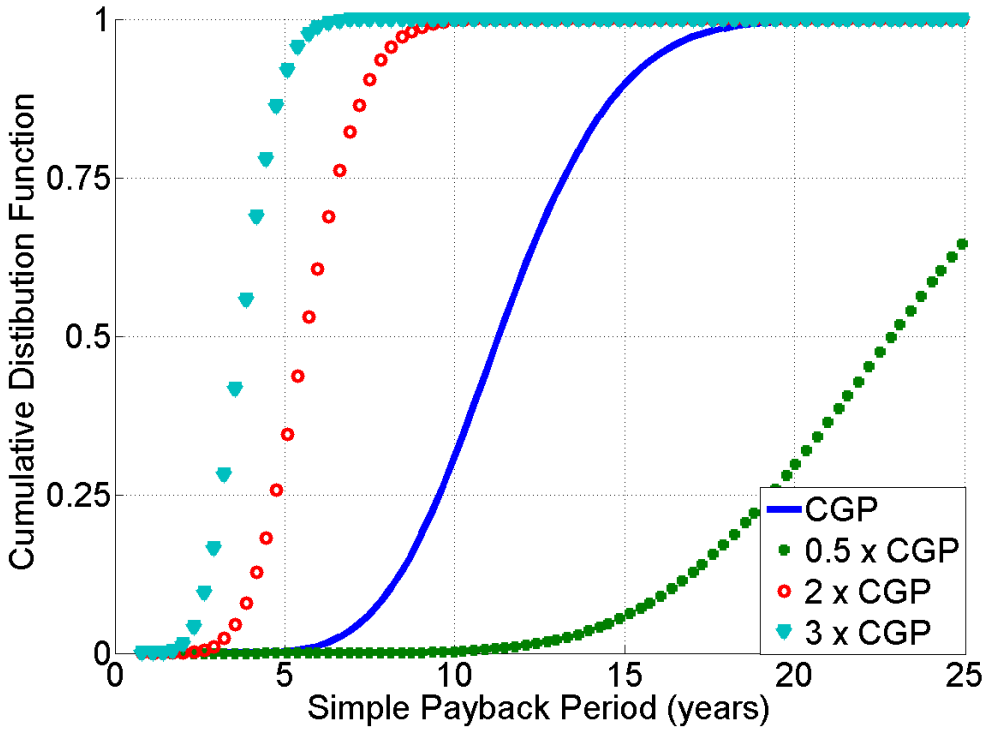


Figure 5.6: Cumulative distribution functions of the simple payback period (SPBP) at various potential gas prices based upon the current gas price (CGP) defined in section 5.3.2

upon the DPBP and the NPV indicators (Figures 5.4 and 5.5 respectively). In addition to the poor return on investment, the probability distributions exhibit a degree of unfavourable skewness. Figure 5.3 and in particular Figure 5.4 illustrate that the probability density functions are weighted to the right, and thus if a payback period were to be cited in terms of a plus or minus figure, the negative confidence interval (a favourable outcome) would have to be less than the positive confidence interval (an unfavourable outcome).

If the current gas price were to be halved for any reason, then investment in the TAHT would not appear to have any economic merit under any scenario considered in this study, with the probability of a negative net present value over the course of the project's lifetime effectively equal to 1 (Figure 5.8). A significant (though entirely credible) hike in the gas price, returning it only to prices experienced in late 2009 (approximately twice the current gas price) or in 2008 (approximately three times the current gas price) (NASDAQ Stock Exchange, 2014), tips the balance towards the economic attractiveness of the system. If the prices experienced in 2008 are taken, the model indicates that the TAHT has

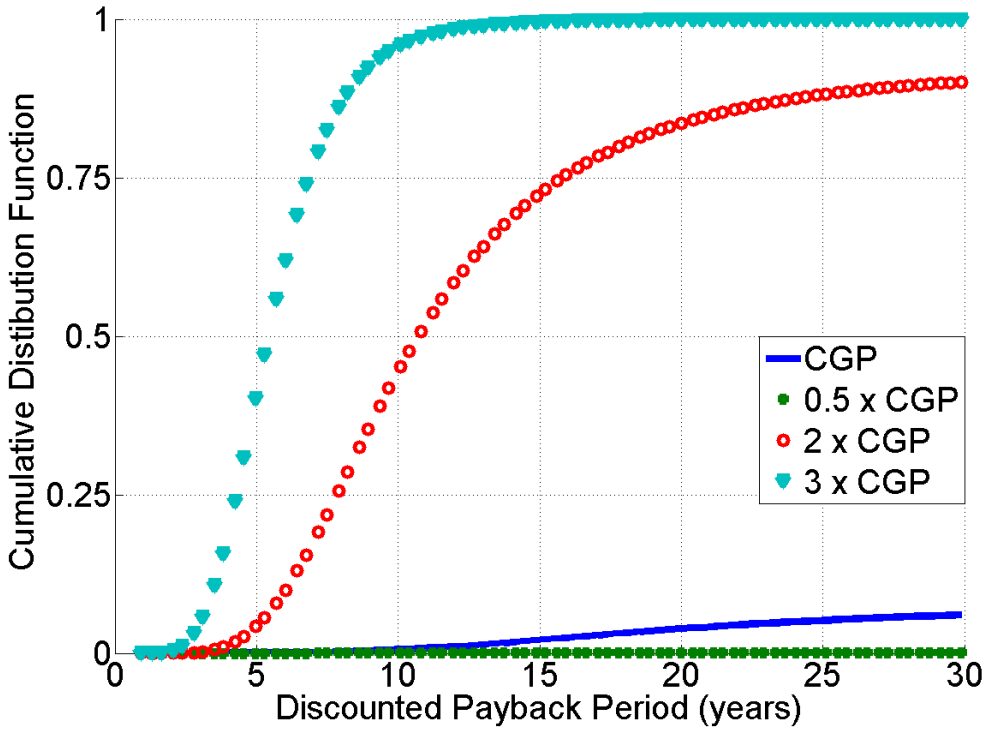


Figure 5.7: Cumulative distribution functions of the discounted payback period (DPBP) at various potential gas prices based upon the current gas price (CGP) defined in section 5.3.2

a 92% chance of a simple payback period of five years or less, compared to the 90% chance of a SPBP of 15 years or less at the current gas price (Figure 5.6). If the current gas price were to be doubled (i.e.: revert to 2009 prices), then it is highly likely under all scenarios considered in this chapter that the system would generate a positive net present value over the project lifetime of 20 years as illustrated in Figure 5.8. From Figures 5.6 to 5.8 it may also be seen that an increasing gas price leads to a highly favourable tightening of the probability distribution functions, and thus significantly lower variability in projected payback times (especially apparent in Figure 5.6).

5.6 Discussion

Several important issues affecting the economic performance of the TAHT are discussed and analysed in this section. For simplicity, all results quoted in this section assume the current gas price (CGP = €508/tonne). Observed trends would be equally applicable for any gas price however.

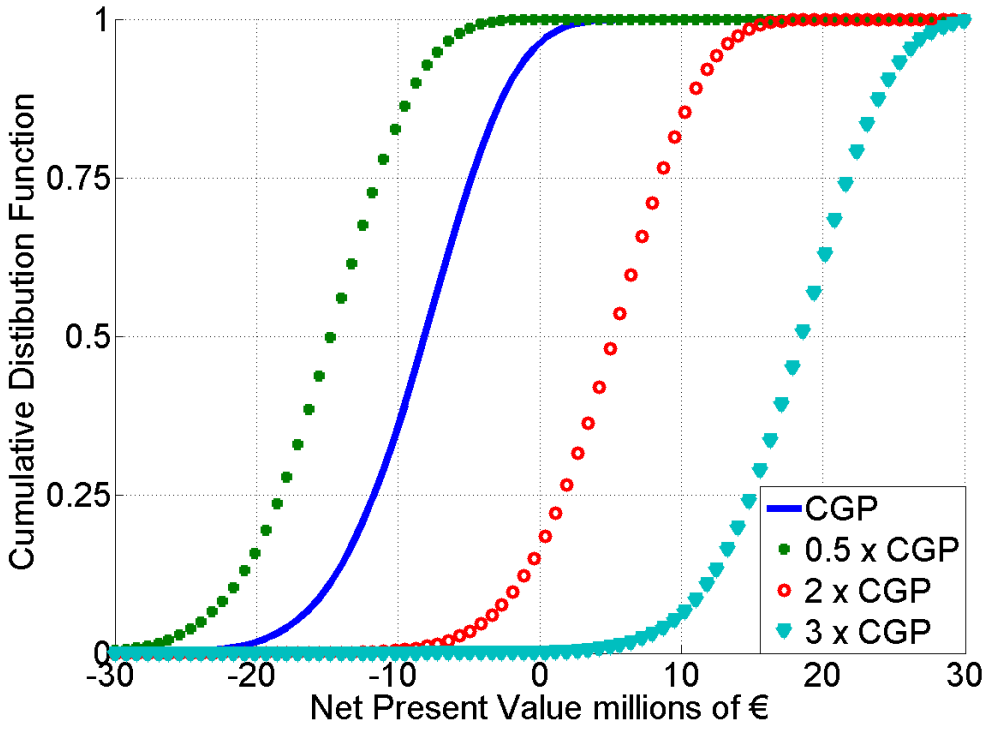


Figure 5.8: Cumulative distribution functions of the net present value (NPV) at various potential gas prices based upon the current gas price (CGP) defined in section 5.3.2

5.6.1 Waste Stream Physical Properties

The physical properties of the waste stream have a large influence on the economic success or failure of the heat transformer. This is identified to be mainly due to the direct influence which these waste streams have upon the size and hence costs of the evaporator and generators. To illustrate this, a simple example is used to determine the economic performance of the TAHT installed in this plant under three conditions.

1. The TAHT it is installed to just recycle the heat coming from the condensing Naphtha stream.
2. The TAHT it is installed to just recycle the heat coming from the residue oil stream undergoing a sensible heat change.
3. The TAHT it is installed to recycle the heat coming from a fictitious water stream which has the exact same mass flowrate and temperature change as in case 2 (where the residue oil line is the only waste stream).

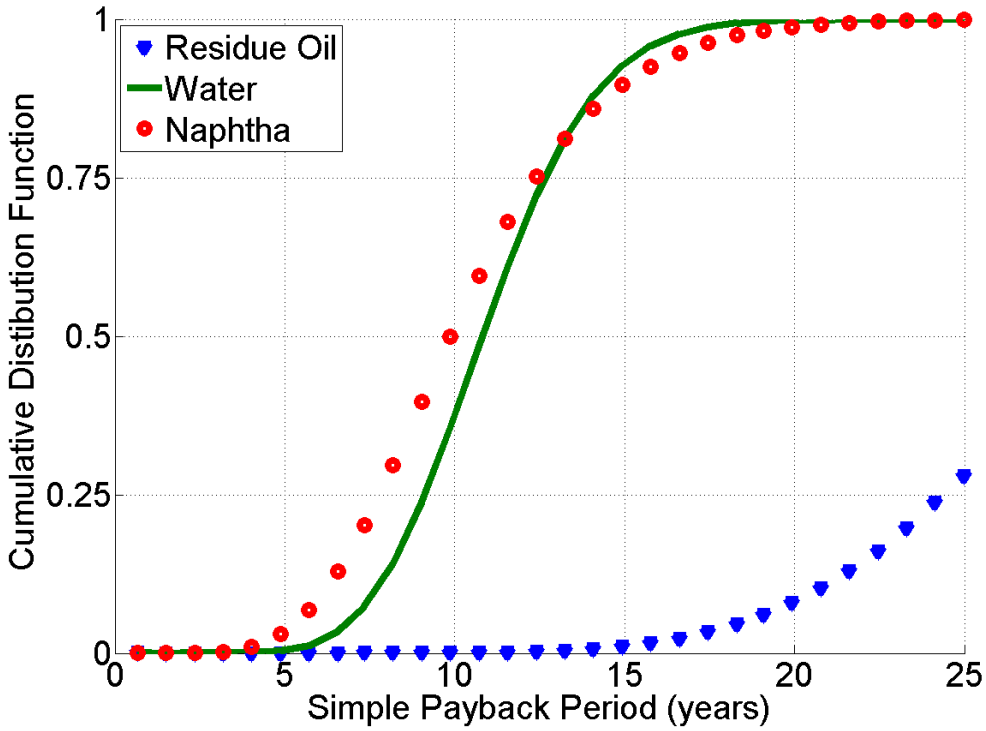


Figure 5.9: Cumulative distribution function of the TAHT's simple payback period (SPBP) highlighting the importance of the waste stream's physical properties

The results of these different test cases are shown in Figures 5.9 to 5.11. From these trends it may be seen that there is a big difference between the performance of the TAHT using the residue oil (case 2) and the other two test cases. Clearly the naphtha and water heat recovery cases are much more attractive than the residue oil case.

There are two reasons for this. The first of these is that condensing streams generally have much higher heat transfer coefficients compared to streams undergoing sensible heat changes. For example, the heat transfer coefficient of a condensing water vapour stream at 100 °C and atmospheric pressure in a vertical tube is approximately 18,000W/(m^{2}K) (assuming a vapour fraction of 0.5). In turn a liquid water stream at the same temperature and pressure (maintaining the same flowrates and tube conditions) has a heat transfer coefficient of ∼1,025W/(m^{2}K). In the heat transformer's evaporator, the waste heat stream is being cooled by the evaporation of pure water. The evaporation of water (using the same tube conditions once more) also has a very high heat transfer coefficient of approximately 20,000W/(m^{2}K). Due to this large evaporating heat transfer coefficient, the resistance to heat transfer is primarily due to the waste heat stream (assum-

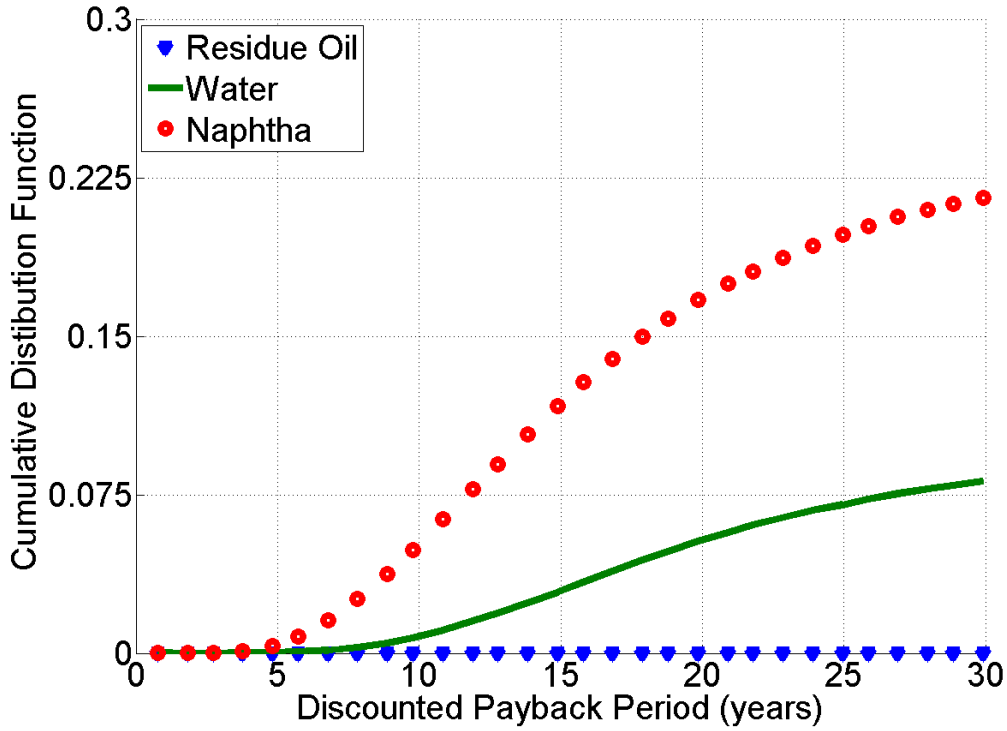


Figure 5.10: Cumulative distribution function of the TAHT's discounted payback period (DPBP) highlighting the importance of the waste stream's physical properties

ing the resistance of the metal wall is negligibly small). Thus if a condensing stream is used, then it is clear that a smaller heat transfer area will be required per unit of heat energy transferred.

The second reason is the difference in physical properties of the waste heat fluid. In general, Nusselt number correlations are functions of the flow's Reynolds and Prandtl numbers. The Dittus-Boelter equation for turbulent single phase pipe flow is shown as an example in equation 5.8. The same equation is then rewritten in terms of its basic components and the heat transfer coefficient in equation 5.9.

$$Nu = 0.023 Re^{4/5} Pr^{0.3} \tag{5.8}$$

$$\alpha = 0.023 \left[\frac{\rho^{0.8} c_p^{0.3} k^{0.7}}{\mu^{0.5}} \right] \left[\frac{v^{0.8}}{D^{0.2}} \right] \tag{5.9}$$

From equation 5.9 it can be seen that for efficient sensible heat exchanges with a waste stream, the stream should ideally have a high density, specific heat capacity

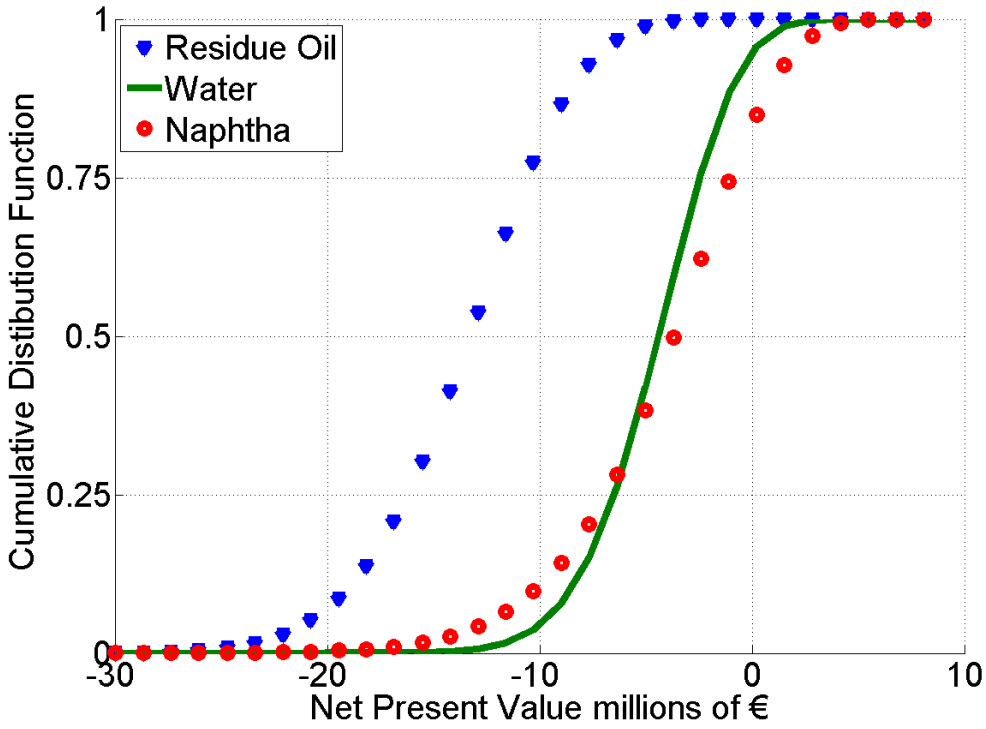


Figure 5.11: Cumulative distribution function of the TAHT's net present value (NPV) highlighting the importance of the waste stream's physical properties

and thermal conductivity while maintaining a low viscosity. As the condensing heat transfer coefficient correlation developed by Shah (1982) utilises equation 5.9 as a base (equation 5.9 is then modified by a function based upon the vapour fraction), this general principle may also (cautiously) be applied to condensing waste heat streams (the physical properties then refer the fluid's liquid phase).

The residue oil stream being utilised in this industrial case study satisfies none of the above physical property criteria. It is very viscous. For example, at 90 °C, its viscosity is more than 80 times that of water at the same temperature. In contrast however, its thermal conductivity is 7 times less than water's while its specific heat capacity and density are also lower. The result of this is that unacceptably low heat transfer rates are obtained in both the evaporator and generator serving it.

The Naphtha stream being condensed also has relatively poor physical properties compared to water (although not as bad as the residue oil). However it still has a slightly superior economic performance (Figures 5.9 to 5.11) which highlights the ability of a latent heat change to compensate for a stream's poor physical

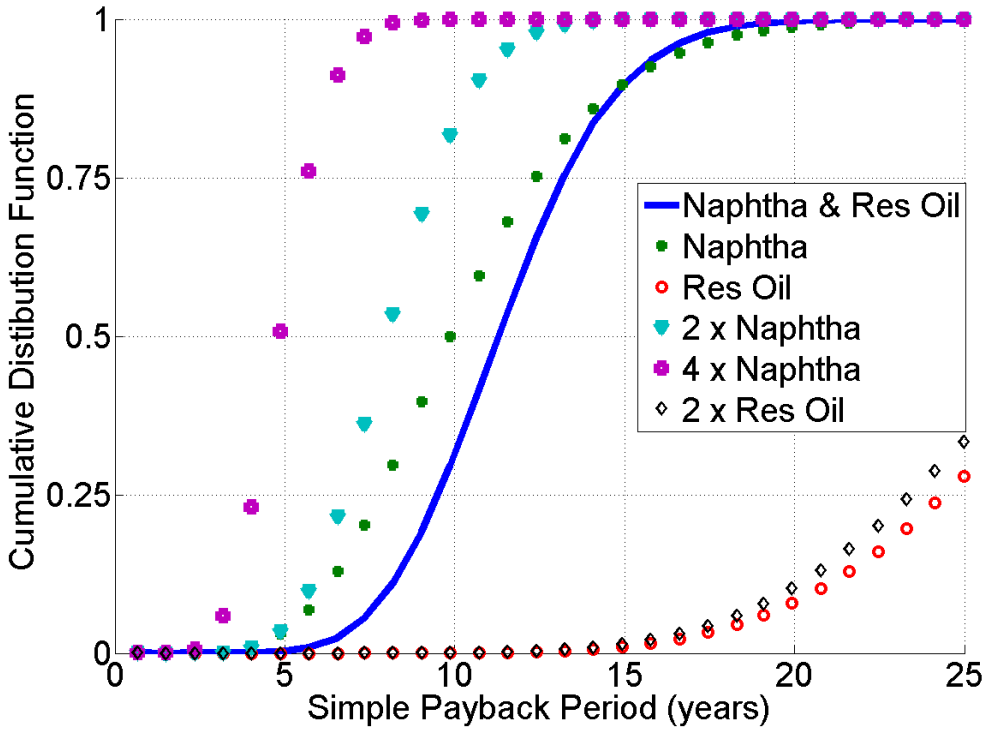


Figure 5.12: Cumulative distribution functions of the simple payback period (SPBP) utilising different quantities of waste heat streams in the TAHT

properties. An examination of the water and residue oil sensible heat change cases illustrates clearly however that physical properties are vital when comparing two similar heat sources (i.e.: two condensing streams or two streams undergoing sensible heat changes).

In the current design, the pieces of equipment associated with the Naphtha stream (labelled '-a' in the Table 5.1) are considerably smaller than those which are in contact with the residue oil line. Although the condensing stream contains approximately 2.4 times as much energy as the residue oil stream, the residue oil's evaporator requires approximately 12.6 times more heat exchange surface area. Thus it is clear that a judicious selection of waste heat streams plays a vital role in both the thermodynamic and economic success or failure of such a system.

5.6.2 Quantity of waste heat available

In section 5.6.1 the importance of correct stream selection was demonstrated. From Figures 5.9 to 5.11 it may be seen however that while utilising the condensing Naphtha stream in this case study allows the TAHT to achieve a better

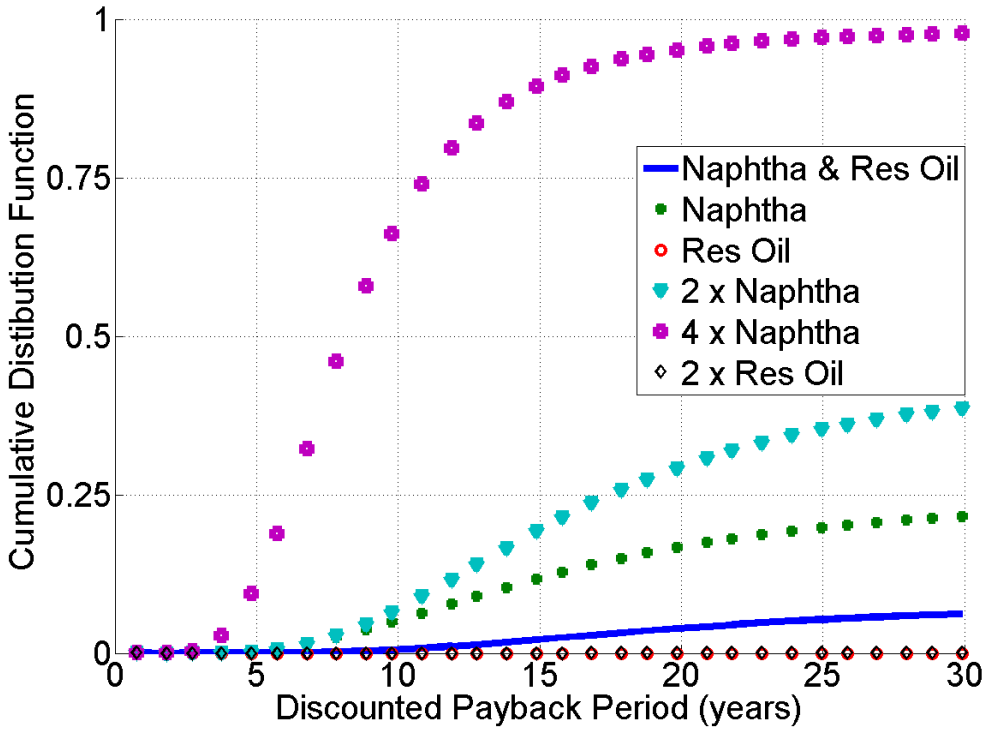


Figure 5.13: Cumulative distribution functions of the discounted payback period (DPBP) utilising different quantities of waste heat streams in the TAHT

performance than when using the viscous residue oil as a heat source, there still exists an approximate 50% chance that the unit will have a simple payback period of more than 10 years. Therefore this section aims to determine whether a larger supply of suitable energy would have any direct impact upon the economic performance of the heat transformer.

In Figures 5.12 to 5.14 the results of using different waste heat streams in the TAHT are presented. It can be seen that utilising the residue oil waste heat stream in the current case study decreases the economic performance of the heat transformer. It is very clear however that by utilising condensing streams with higher flowrates, or else by simply using more of such streams one can dramatically increase the attractiveness of the technology. If two condensing streams each having twice the flowrate of the Naphtha stream used in this example, were available, the probability of having a simple payback period of less than seven years increases from approximately 4% to almost 97%. Thus this is a strong indicator that triple stage heat transformers are highly influenced by scale, and that they are most suited to large energy intensive operations. The oil refinery currently being analysed is a small oil refinery, with a crude oil throughput of

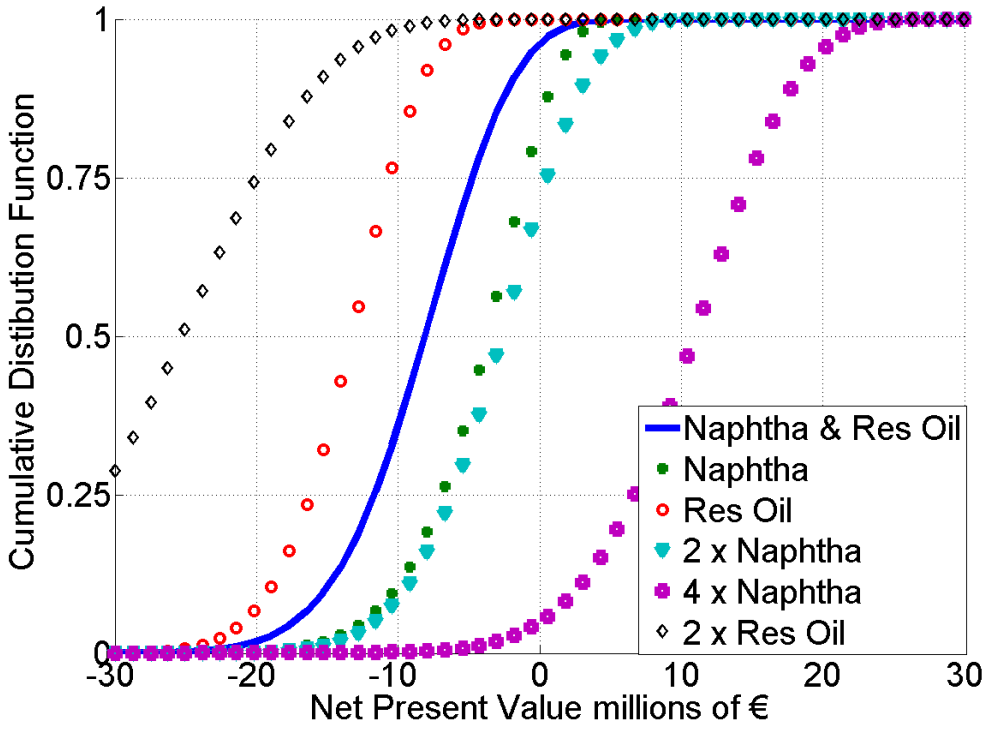


Figure 5.14: Cumulative distribution functions of the net present value (NPV) utilising different quantities of waste heat streams in the TAHT

approximately 70,000 barrels/day. In the worldwide oil refining industry, this represents a relatively small capacity, with some of the largest refining plants having a throughput of between 500,000-1,200,000 barrels/day. Therefore as this oil refinery is almost 100 times smaller than some other plants across the world which conduct approximately the same processes, it is very reasonable to assume that waste heat streams with at least twice the current flowrates would be available in such facilities. The economic viability of the TAHT increases rapidly with an increase in the waste heat energy available which means that such a system, while excessively expensive in this small refinery at current gas prices, would be well suited to larger plants.

5.6.3 System Design

The results in section 5.5.4 indicate the TAHT outlined in this study does not currently merit investment at the current gas price due to excessive payback times. Generally energy projects such as this would be required to demonstrate payback periods of less than three to five years to merit consideration in the examined

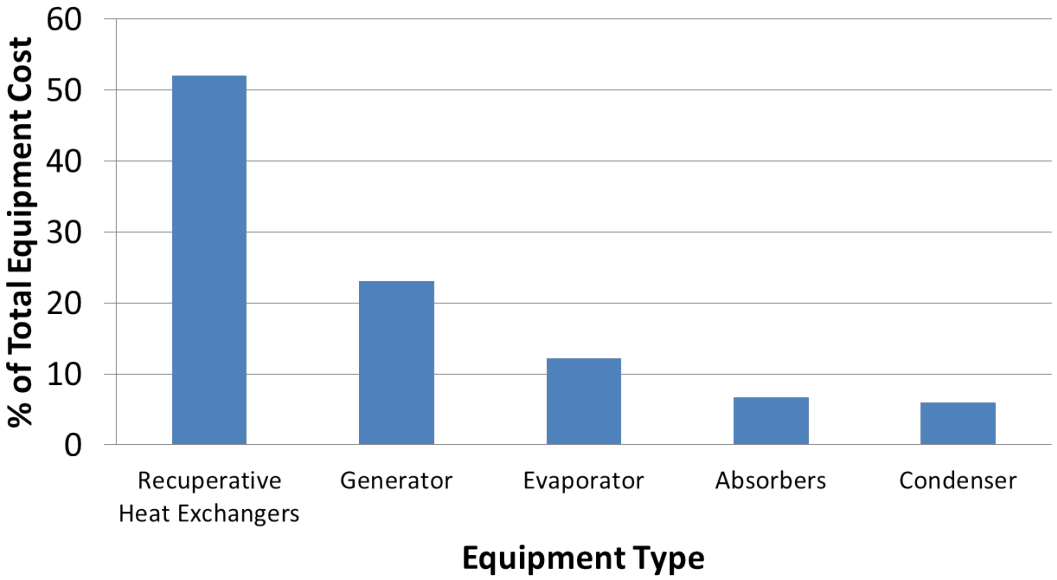


Figure 5.15: Percentage of the total TAHT cost allocated to each type of equipment

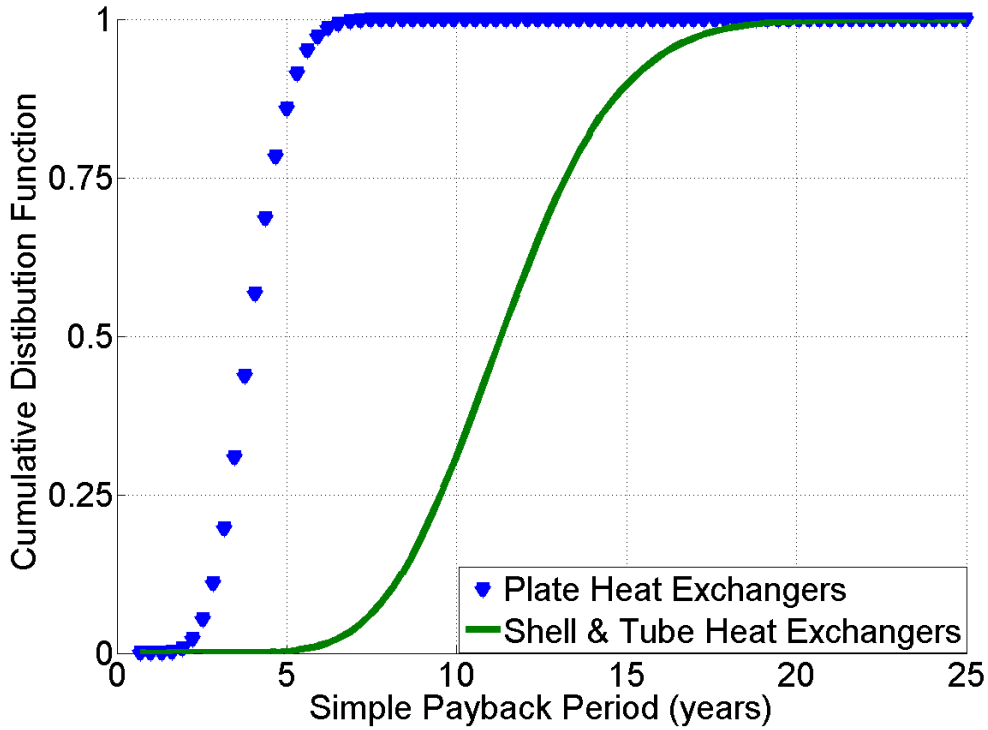


Figure 5.16: Cumulative distribution functions of the simple payback period (SPBP) assuming the benefits of plate heat exchanger usage (Genssle and Stephan, 2000)

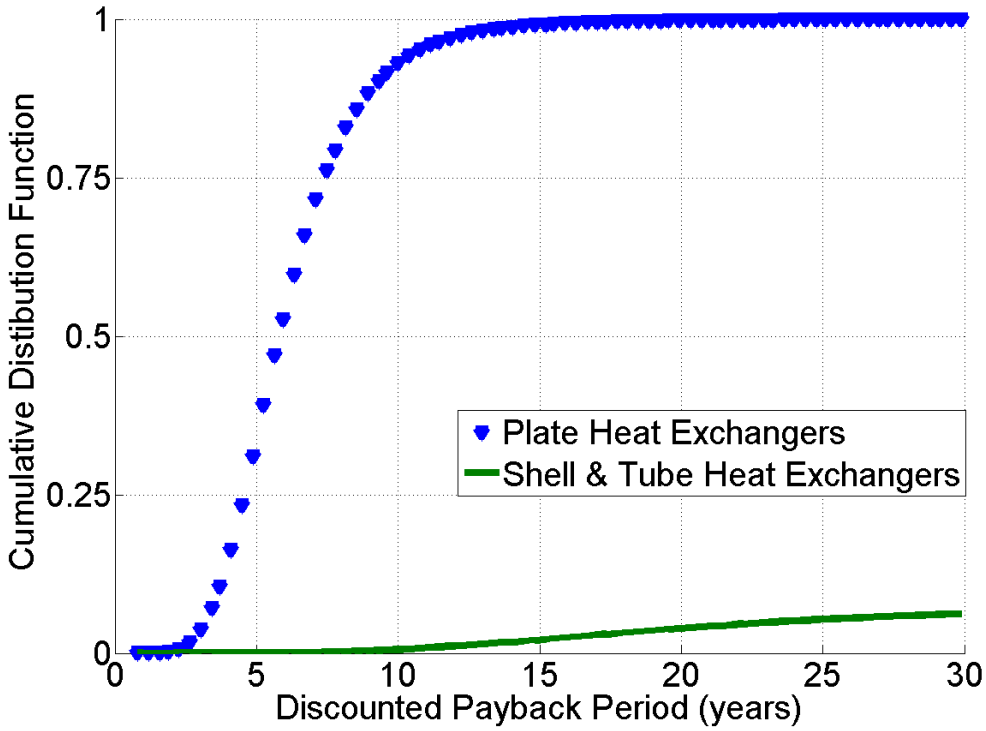


Figure 5.17: Cumulative distribution functions of the discounted payback period (DPBP) assuming the benefits of plate heat exchanger usage (Genssle and Stephan, 2000)

industry. The reason for this unfavourable economic performance is primarily the purchase cost of the equipment. In this case study, the equipment cost is estimated to be approximately €5.3 million, leading to a total project cost of ∼€21million. In order to reduce this figure, the mechanical design of the individual pieces of equipment could be examined to determine whether significant savings are possible. In Figure 5.15 the allocation of costs to each type of equipment (as obtained from the refinery's costing analysis) is presented. It is clear that the main problem can be associated with the recuperative heat exchangers Hx_1, Hx_2 and Hx_3. These units together account for approximately 52% of the total equipment cost. An experimental study conducted previously by Genssle and Stephan (2000) proposes the use of brazed plate heat exchangers within a heat transformer (instead of conventional shell and tube units), as this allows for a reduction in the required capital investment. The investigation shows that using plate heat exchangers in the generator and evaporator decreases the required heat exchanger area by 77% compared to shell and tube heat exchangers. The study goes further to state that this reduction in surface area would in turn

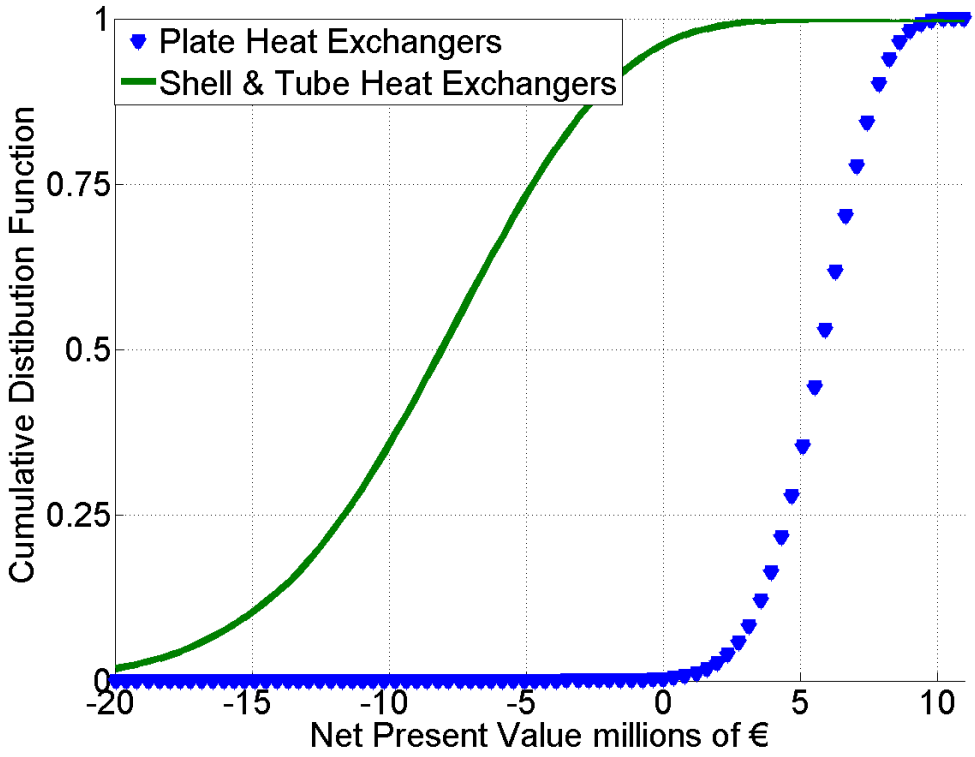


Figure 5.18: Cumulative distribution functions of the net present value (NPV) assuming the benefits of plate heat exchanger usage (Genssle and Stephan, 2000)

lead to a 70% reduction in the cost of these units based upon statements from manufacturers.

Genssle and Stephan (2000) indicate that dramatic decreases in the capital cost of a heat transformer are possible by using more efficient and cost-effective equipment. In order to demonstrate the effect that such a cost reduction would have on the economic viability of the TAHT in this study, an analysis is conducted which assumes that the generator, evaporator and solution heat exchangers are all replaced by plate units, and that the predicted 70% reduction in the capital cost is realised (Genssle and Stephan, 2000). The results of this simulation (outlined in Figures 5.16 to 5.18) illustrate that a reduction in capital cost such as this would make the TAHT economically considerable in almost all permutations with a ∼90% chance of simple payback period of five years or less, and a positive net present value in almost all considered scenarios. In addition it may be observed that the variability in projected payback time has decreased significantly, and that the cumulative distribution function now has a much sharper step change from almost 0 to approximately 1. This means that investments may be made

with a much higher assurance of achieving the desired outcome.

Shell and tube heat exchangers have become an industry standard which are well understood. Companies are comfortable using well established equipment such as these as many potential installation, maintenance and operating issues are familiar as are methods available for dealing with them. The oil refinery would prefer shell and tube heat exchangers as a preferred technology for the above reasons. Moreover, switching to plate heat exchangers (or something similar) in heat transformers is not as trivial a task as it may appear initially. The use of plate heat exchangers is generally more common in lower temperature scenarios, where rubber gaskets may be used to seal gaps between plates. The requirement for higher temperatures ($\sim 230\,^{\circ}\mathrm{C}$) and non atmospheric pressures (up to $\sim$ 6barg) mean that such gaskets may not be suitable, and thus more novel, less practised solutions would be required (such as welded plates for example). Nonetheless it has however been shown in this example that the potential benefits from such redesigning may be significant, and could make a big difference to the viability of heat transformer technology.

The figures from this hypothetical plate heat exchanger simulation are simply meant to act as an illustrative example to show that the main economic issue associated with the TAHT, namely it's capital cost, can be addressed by relatively simple changes and could potentially make such a system much more economically viable. Instead of plate heat exchangers one could use heat pipe technology (Jouhara et al., 2013) which has already shown significant benefits when used in heat recovery in air handling units (Jouhara and Ezzuddin, 2013). It should be noted that if the benefits of more efficient equipment demonstrated in section 5.6.3 could be combined with the benefits associated with the suitable selection of streams illustrated in section 5.6.2, then the TAHT would become an extremely economically attractive entity (at the current gas price), which could dramatically enhance the potential implementation of the technology. As illustrated in section 5.5.4 a returning of gas prices to levels observed in 2008 or 2009 would have a similar effect, and may represent a more likely driver in practice. Most research to date has focussed upon the thermodynamic performance of heat transformers, while little has been published which explains why their uptake has been so scarce. The discovery that capital costs may be excessive indicates that future research efforts might best be directed towards reducing the size and hence cost of its equipment, as it has been demonstrated in this study that this is a key determining factor in whether or not such units are suitable for industrial implementation.

5.7 Conclusions

A case study has been conducted which examines the economic rationale for installing a triple stage heat transformer in a small oil refinery ($\sim 70,000$ barrels/day). Monte Carlo Simulation methods are utilised to express capital cost approximations across a range of projected equipment and whole project costs. A number of different gas price scenarios are considered and the probability of a favourable financial return from an investment in this heat recovery technology is explored. The results indicate that at the current gas price, the capital cost of equipment is too high to make the investment financially attractive in this refinery as excessive payback periods are likely. It is demonstrated that a return to energy/natural gas prices observed in 2008 and 2009 would ensure that payback periods are reduced to acceptable levels, where attractive returns on investment are predicted over the lifetime of the system. The availability of suitable waste heat energy streams is also identified as a key limitation within this case study. It is demonstrated that a TAHT such as this would be well suited to a larger plant or a plant which has more waste energy available to it, as investor confidence can be greatly increased with the sufficient availability of condensing waste heat streams. The other potentially significant improvement which is identified is the application and development of more efficient and cost effective equipment. It is demonstrated that a unit's economic performance increases dramatically if previously reported benefits of utilising plate heat exchangers instead of conventional shell and tube bundles are realised.

Part II

Bubble Absorption Analysis

Chapter 6

Bubble Column Development

Nomenclature

A	Surface Area (m^2)
D	Bubble diameter (m)
F	Force (N)
g	Acceleration due to gravity (m/s^2)
m	Mass (kg)
$\dot{m}$	Rate of mass flow (kg/s)
P	Perimeter (m)
T	Temperature (K)
t	Time (s)
v_T	Terminal vertical bubble velocity (m/s)
V	Volume (m^3)
x	Lithium Bromide mass Fraction (kg/kg)

Greek Symbols

α_{therm}	Liquid thermal diffusivity = $k/(\rho c_p)$ (m^2/s)

Subscripts

B	Buoyancy
L	Bulk liquid

6.1 Experimental Objectives

Following the realisation in the previous chapter that the economic performance of a triple absorption heat transformer is intrinsically linked to the capital cost of the system, it was decided to examine in detail the cycle's most pivotal unit, the absorber, to determine whether potential improvements may be made to its design. The absorber is selected as it is the heat transformer's fundamental unit (it is the unit operation which enables the energy's temperature to be increased), and has also been demonstrated in Chapter 3 to cumulatively represent approximately 40% of the TAHT's exergy destruction rate (i.e.: total exergy destruction rate in the two absorber-evaporators and the absorber). Thus by improving its design, two potential problems may be addressed simultaneously, namely a reduction in the capital cost of the system and an increase in its thermodynamic performance. The absorber has been demonstrated to be the largest source of irreversibility for single stage systems (Rivera et al., 2010a,b; Gomri, 2009; Sözen and Yücesu, 2007), and may account for as much as 80% of the cycle's non-ideality (Sözen, 2004). Therefore a further advantage of examining this unit is that the results are not applicable only to triple stage units, but to any heat transformer or indeed

absorber heat pump.

The conventional method of vapour absorption is the falling film method where a lithium bromide solution ($LiBr - H_2O$) flows down either vertical or horizontal tubes as a thin film while absorbing water vapour from the surrounding environment (Guo et al., 2012). The heat of absorption is removed by a cooling fluid flowing on the inside of the tubes. Several studies have been conducted on such falling film absorbers. Nusselt and Sherwood numbers were correlated experimentally for a vertical falling film absorber by Miller and Keyhani (2001) (based upon inlet conditions to the absorber), who obtained heat and mass transfer coefficients of approximately 570W/(m^2K) and 3.15×10^{-5}m/s respectively. Alternative designs in which the solution flows on the inside of vertical tubes were subsequently shown to not achieve any appreciable improvement in performance (Medrano et al., 2002).

One possible method of increasing the performance of an absorber is to increase the vapour-liquid interfacial surface area. Spray absorbers aim to achieve this by atomizing the $LiBr - H_2O$ solution prior to contacting it with the water vapour. The liquid is sprayed into the top of the absorption vessel through a nozzle, while the water vapour enters from the bottom. An experimental spray absorber was built by Warnakulasuriya and Worek (2008) and was shown to increase the Sherwood number of horizontal tube absorbers by roughly fourfold while mass transfer coefficients of 6×10^{-5}m/s were reported. Different designs of gravity driven adiabatic absorbers have also been tested and compared (Arzoz et al., 2005). The film flow method (a film of $LiBr - H_2O$ solution falling freely through a vessel containing water vapour) tested achieved the best results in this study, with mass transfer coefficients of 1.5-2$\times10^{-4}$m/s reported. It has been demonstrated that this value may be improved by using a conically shaped falling sheet which can realise mass transfer coefficients of up to 7×10^{-4}m/s (Palacios et al., 2009). A possible disadvantage of such absorbers is however that they require a separate heat exchanger to cool the solution following absorption. This is in contrast to other absorber designs which achieve both cooling and absorption in one single step.

Bubble absorbers aim to achieve a high vapour-liquid interfacial area by means of bubbling the vapour stream into the continuous liquid phase. A detailed numerical analysis has been conducted upon the absorption and eventual collapse of a single ammonia bubble in a $NH_3 - H_2O$ solution (Merrill and Perez-Blanco, 1997). Very high mass transfer coefficients of 1.15×10^{-3}m/s are reported in that

study. The paper demonstrates how the bubble's diameter remains almost constant for the first approximately 0.06 seconds due to two way mass transfer, but then begins to decrease steadily until finally collapsing. A direct comparison between the performance of a vertical falling film absorber (with $NH_3 - H_2O$ solution and water vapour contacting on the inside of the tubes) and the performance of a bubble absorber using the same working fluids has been conducted (Castro et al., 2009). The results show that for the same solution mass flowrates, the bubble absorber always has a higher absorber load and is therefore more efficient. These higher mass transfer coefficients may be explained by the fact that in bubble columns, the dispersed vapour phase is physically translating through the continuous liquid phase, inducing mixing in the liquid region directly adjacent to the bubble. In comparison in falling film units, both the vapour and liquid may be termed continuous phases in their respective regions, which flow adjacent to each other without any mixing or (significant) disturbances. It has been demonstrated in a combined numerical and experimental analysis that in order to minimise its required height, the bubble absorber should be operated in counter-current mode while keeping solution temperature and concentration as well as the entering vapour mass flow rate to a minimum (Lee et al., 2003). A study which examined factors influencing bubble properties during the absorption of ammonia into a $NH_3 - H_2O$ solution found that the residence time of bubbles in the absorber increases with an increase in the initial bubble diameter and the liquid concentration (Kang et al., 2002).

From the above review, it may be seen that bubble absorbers appear to have significant advantages compared to conventional absorber designs such as falling film units. In addition, bubble absorbers may be used to reduce exergy losses within the system. Scott et al. (1999b) demonstrated that bubble column absorbers may be very easily adapted into multi-compartment units, which have been demonstrated to significantly reduce irreversibilities (Ji and Ishida, 1999). However, to the author's best knowledge, no bubble absorber studies have been conducted thus far using the working fluids $LiBr - H_2O$ even though this is the most commonly used solution in absorption heat transformers (Abrahamsson et al., 1997). Thus this chapter develops an experimental bubble column which may be used to analyse the absorption of steam bubbles in concentrated $LiBr - H_2O$ solution.

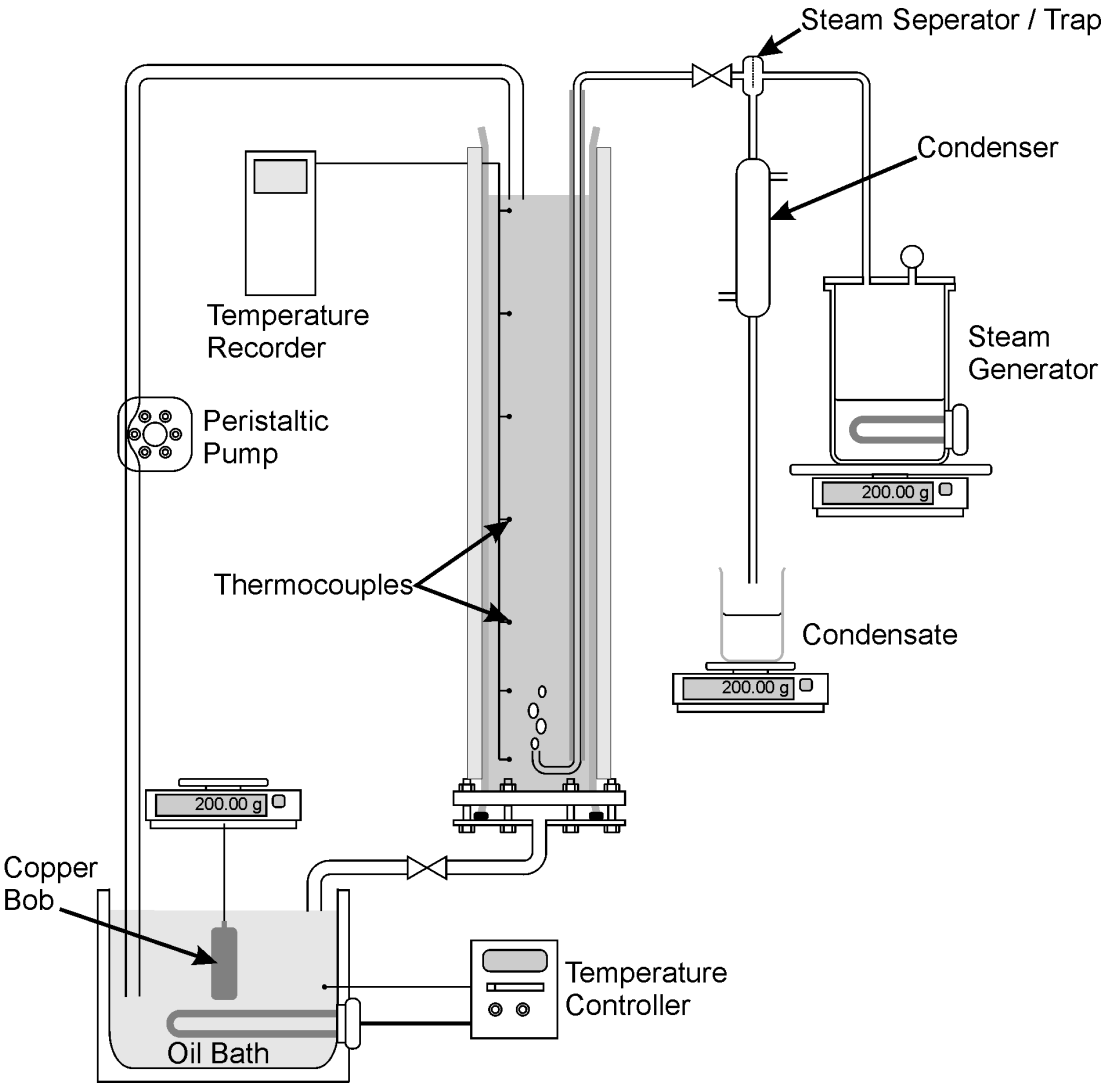


Figure 6.1: Schematic of the bubble absorber column developed for this study

6.2 Bubble Column Experimental Set Up

No existing experimental rig was available for use during these experiments, and thus the required apparatus needed to be constructed and fabricated in conjunction with the technical staff in the department. The final experiental set up, shown schematically in Figure 6.1 and photographically in Figure 6.2, is explained in detail throughout this chapter.

In order to visualise the collapsing bubbles, glass was selected as the material of choice for the column. Thus the experimental bubble column consists of a 1m high, 10cm wide glass cylinder, bolted on to a stainless steel base plate. The glass cylinder is insulated with 37mm thick fibreglass insulation covered with a

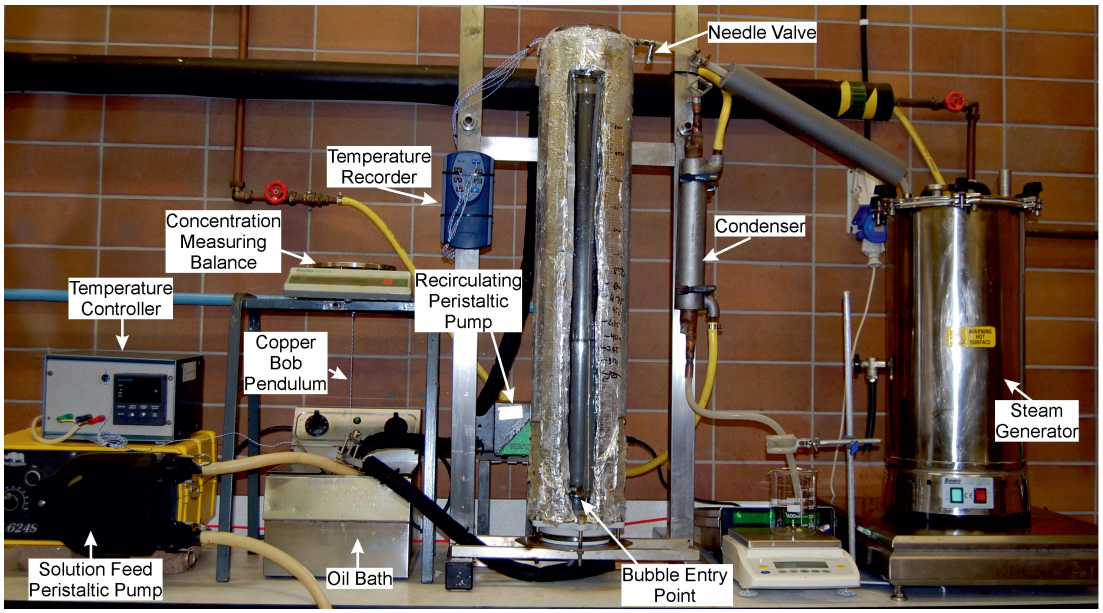


Figure 6.2: Photograph of the experimental set up

reflective foil to minimise heat losses (Figure 6.2). An aperture 7cm wide is cut from the front of the fibreglass to allow a clear view of the gas sparger and hence bubbles.

The cylinder is filled with approximately 32.5cm of aqueous lithium bromide (Figure 6.3), and the solution is maintained at a constant temperature by circulating it through a temperature controlled oil bath at a flowrate of 29ml/s. The solution flows by gravity (controlled by a valve) from the bottom of the cylinder by means of insulated flexible tubing (Saint-Gobain flexible silicone tubing) directly to the oil bath. The oil bath is operated in on-off mode, controlled by a Honeywell UDC 3000 PID controller, and the solution is pumped from the oil bath back into the cylinder by means of a Watson Marlow 505S peristaltic pump. At the top of the cylinder, it is connected to one of four stainless steel tubes through which it flows down to the liquid level within cylinder. The appropriate stainless steel tube is selected in order to ensure that the solution enters the cylinder just below its liquid level in an attempt to minimise any splashing, excess convection currents, or air entrainment within the solution.

Saturated steam for the experiment was produced in a 53x25cm stainless steel cylindrical steam generator (Figure 6.4). The steam generated travels by insulated flexible tubing to the top of the cylinder. Condensed steam is prevented from entering the bubble column by making all steam flow through a steam separator, and the flowrate of steam entering the cylinder is controlled by means

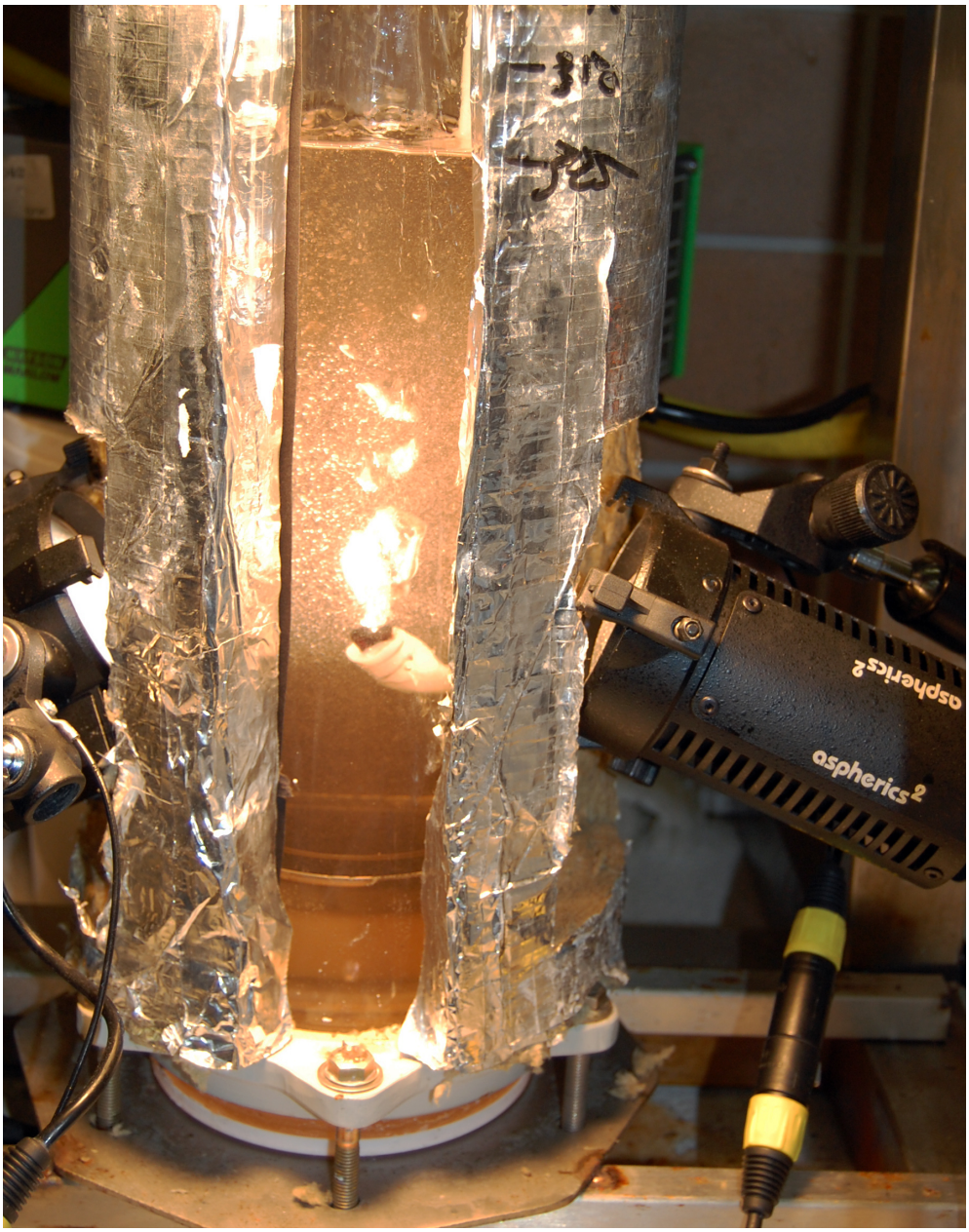


Figure 6.3: Photograph of bubbles forming in the $LiBr - H_2O$ solution in the bubble column

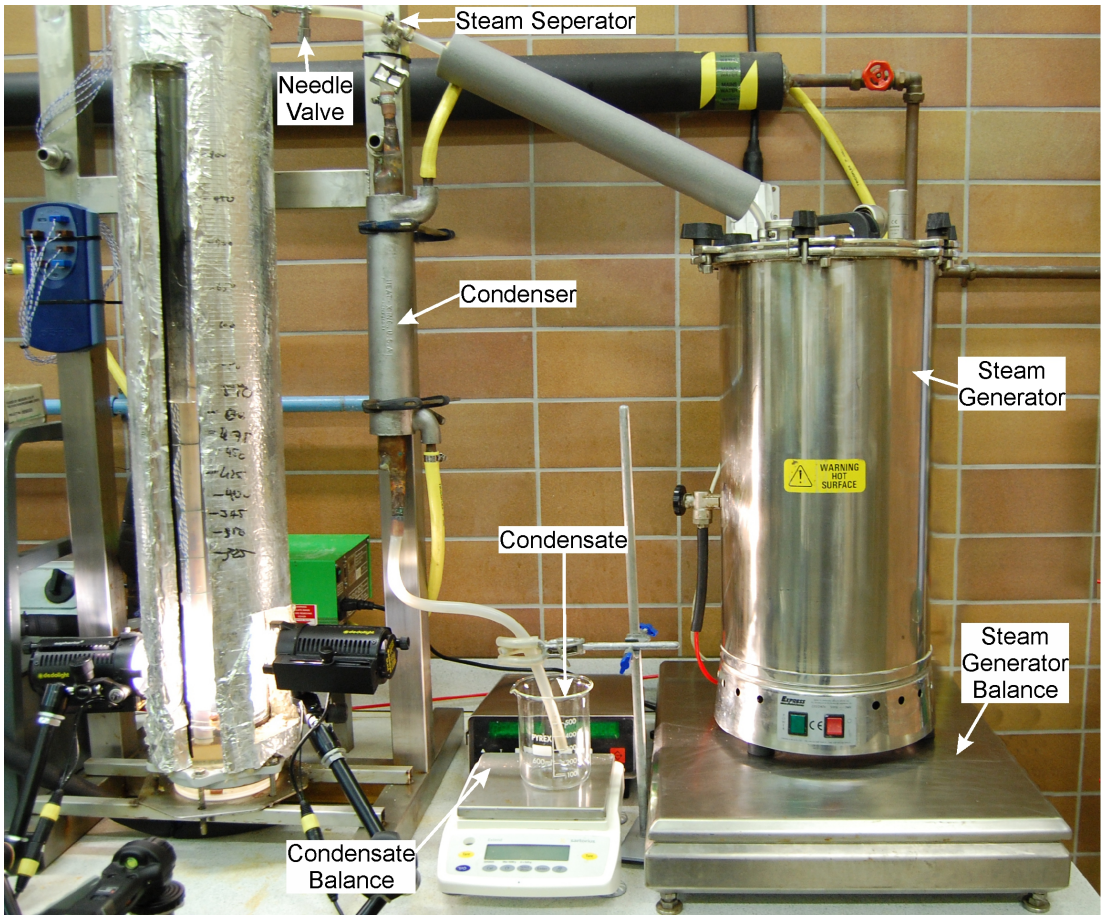


Figure 6.4: Photograph of the steam generation system

of a needle valve following this steam trap. All excess steam being produced is forced through the steam trap's condensate line. This vapour-liquid mixture is fully condensed in a condenser and flows into a containment vessel. Following the needle valve, the steam entering the bubble column is connected to a 2.15mm diameter stainless steel pipe (secured to the inside of the cylinder) through which it flows to the bottom of the cylinder. This pipe has a 180 degree bend at its submerged end, and thus acts as a sparger through which the steam bubbles are formed (Figure 6.5).

6.3 Properties Measurement

Measurement of some solution properties was made difficult due to the high temperature and concentration of the $LiBr - H_2O$ solution. The concentration of Lithium Bromide in solution is often measured using a refractometer (Huicochea



Figure 6.5: Photograph of a bubble in the $LiBr - H_2O$ solution

et al., 2013a), however no reference data relating the solution's refractive index to lithium bromide concentration at temperatures of interest in this research (∼140 °C) could be located. Thus the buoyancy force exerted by the solution on a copper bob of known mass and volume is measured by suspending the copper mass in the solution contained within the oil bath from a mass balance (Precisa 3610 CD-FR) (positioned directly above the oil bath, see Figures 6.1 and 6.2). Simultaneously the temperature of the oil bath was recorded by means of a thermocouple connected to the temperature recorder being used (Pico Log R5). By using equation 6.1 and the measured temperature, the mass fraction of lithium bromide salt in the solution may be found using the $LiBr - H_2O$ solution density correlation reported by Stankus et al. (2007).

$$\rho_L(T_L, x_L) = \frac{F_B}{gV_{CopperMass}} \tag{6.1}$$

The temperature profile within the bubble column is measured by means of 7 type T thermocouples located at regular intervals along its length. These thermocouples which have an accuracy of ±0.8 °C are then connected to the temperature recorder (Pico Log R5). Upon start-up, the temperature within the bubble column is lower than in the oil bath. Thus the solution is allowed to circulate until

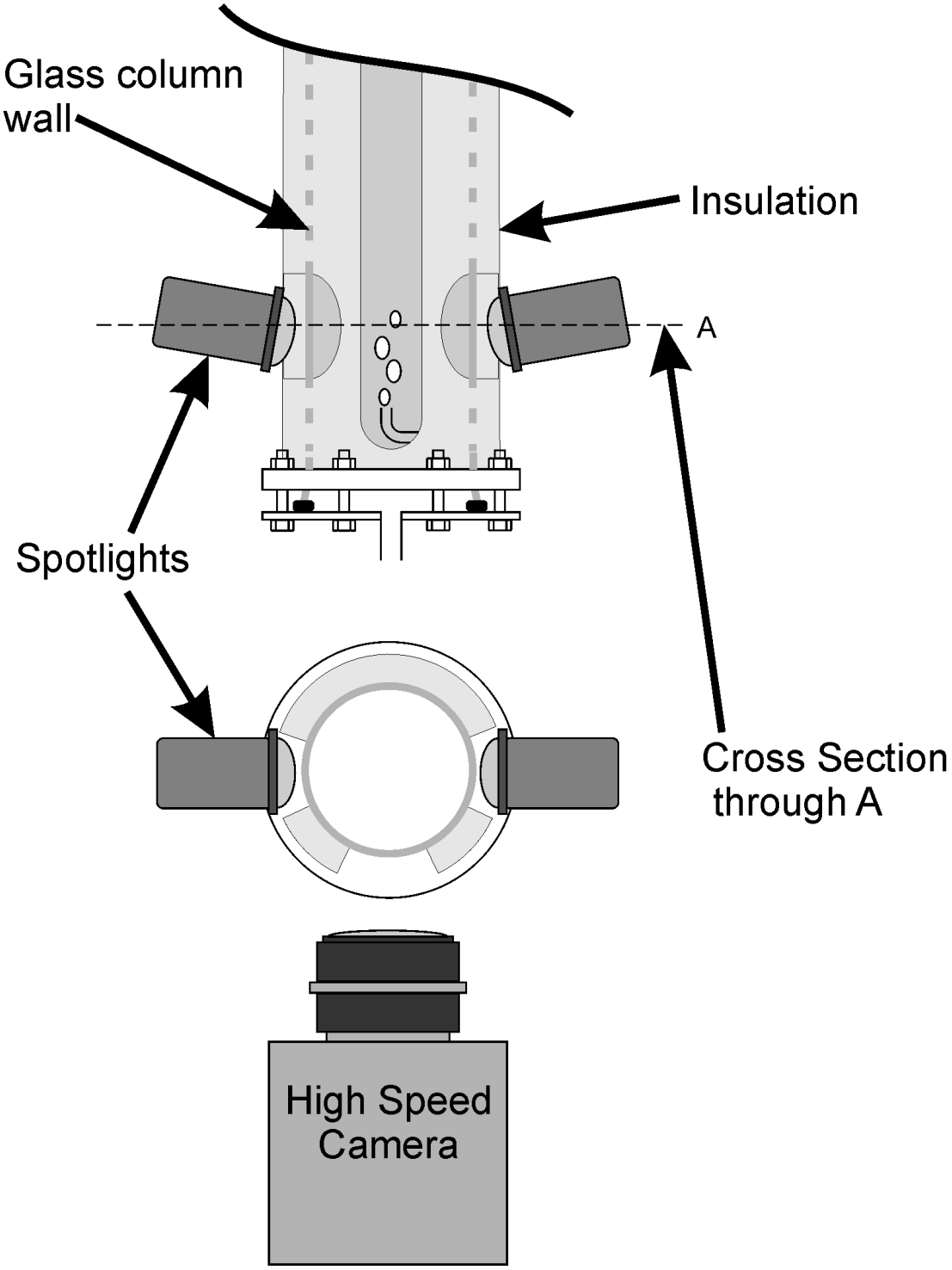


Figure 6.6: Schematic of the high speed camera set up during the experimental runs

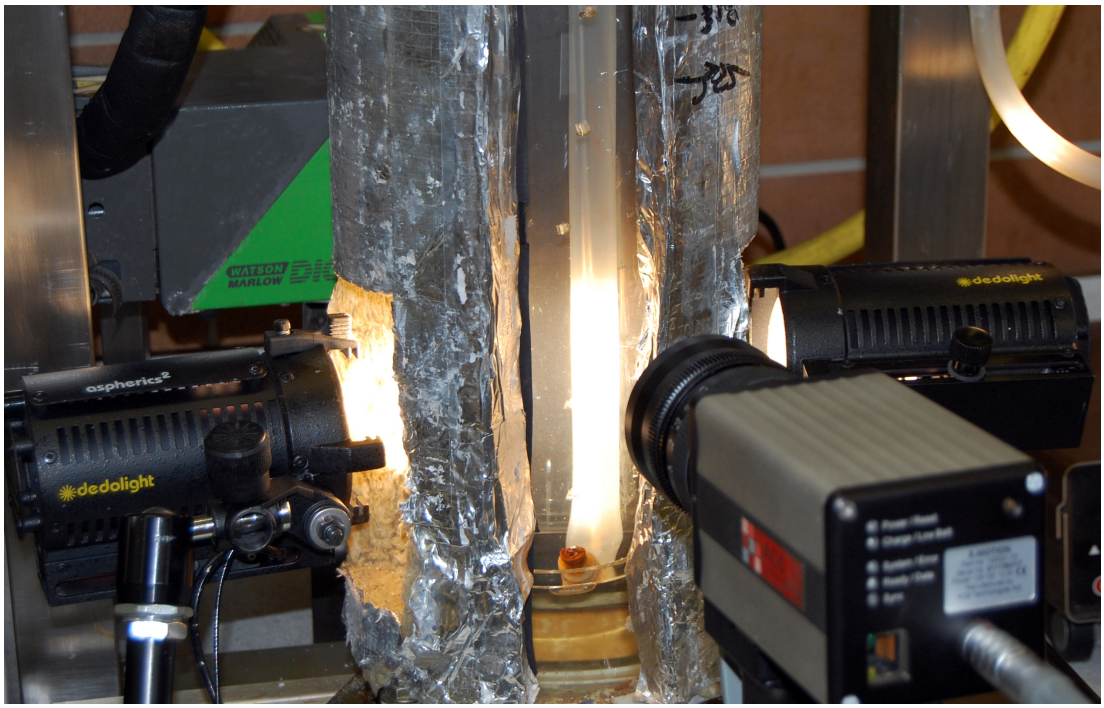


Figure 6.7: Photograph of the high speed camera used to track the bubble collapse

no further changes in temperature are measured by any of the thermocouples (to within experimental accuracy of the thermocouples). At this point the system is assumed to have reached steady state.

The mass fowrate of steam entering the bubble column cannot be easily measured by means of a simple flowmeter, due to the fact that it is saturated and would thus begin to condense giving false measurements. Therefore a simple method based upon mass balance is used instead (see Figure 6.4). The steam generator is placed upon a Berkel digital mass balance, accurate to within 10 grammes. All steam leaving the steam generator which does not enter the bubble column is passed through a condenser and is collected in a container. The mass of this container is recorded throughout the duration of any experimental run (using a Sartorius ED4202S scale balance), as is the total mass of the steam generator. Therefore using equation 6.2, the average mass flowrates of steam leaving the generator and the excess steam being condensed can be used to find the average mass flowrate of steam entering the bubble column.

$$\dot{m}_{steam} = \frac{d}{dt}\left(m_{GeneratedSteam}\right) - \frac{d}{dt}\left(m_{CondensedSteam}\right) \tag{6.2}$$

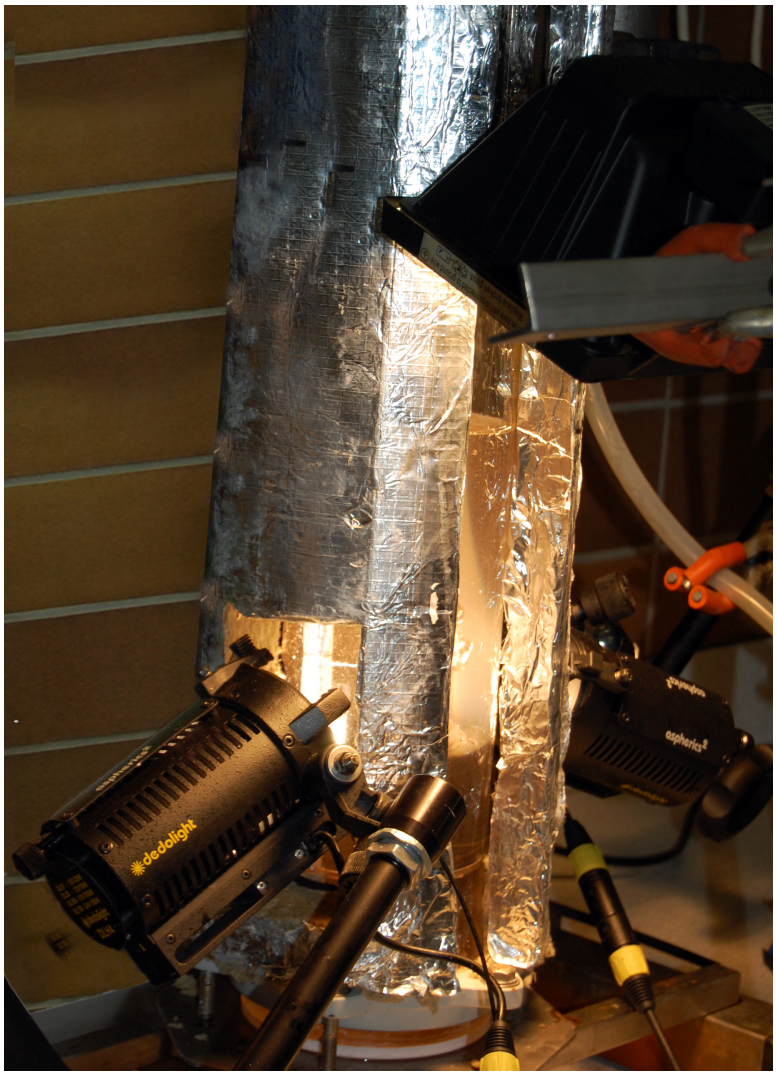


Figure 6.8: Photograph of the experimental lighting set up

6.4 Calibration

The method being implemented to measure the concentration of the $LiBr - H_2O$ solution relies upon the accurate knowledge of the mass and volume of the copper bob. In order to estimate the volume, calibration runs were conducted at the beginning of every experimental day. The copper bob was suspended from its Precisa 3610 CD-FR balance into a $LiBr - H_2O$ solution at a known temperature, and its weight reading recorded. The density of the solution was then measured using a 25ml density bottle. To minimise experimental error, three such density readings were taken and the average density found. This allowed the volume of the copper bob at this reference temperature to be calculated using equation 6.1. Using this volume at the reference temperature enabled the volume at other temperatures to be calculated using equation 6.3, where the volumetric

Concentration (%w/w)	Temperature (°C)		
46	111	119	122
51	121	126	132
56	131	136	141

Table 6.1: All of the concentrations and temperatures used in the experiment

thermal expansion coefficient was referenced from Hahn (1970). Prior to beginning experimental runs, the density being predicted by equation 6.1 using the copper volume given by equation 6.3 was compared with measured densities at two different temperatures. The mean deviation in the predicted densities over the course of all calibrations was 0.24%. The use of the thermal expansion coefficient in equation 6.3 was identified to be vital to the accuracy of these predictions however.

$$V = V_{Calibration} exp\left[\alpha_V \left(T - T_{Calibration}\right)\right] \tag{6.3}$$

6.5 Experimental Procedure

A full factorial analysis involving three concentrations and temperatures was conducted for this experiment. Three mass fractions (of lithium bromide salt) were selected based on what are believed to be typical of concentrations to be observed in a heat transformer absorber. At each concentration, three different temperatures were then analysed. As the pressure of the system remains atmospheric, the temperatures selected for each concentration are limited by the boiling temperature of the solution. Thus for each concentration, temperatures were selected so that one is $\sim 3.5\,^{\circ}$C, one is $\sim 10\,^{\circ}$C, and one is $\sim 15\,^{\circ}$C below the boiling temperature for the solution. The resultant temperatures and concentrations used in the experiment are outlined in Table 6.1. In order to reference the different parameter settings in a simple fashion, the concentrations and temperatures are named using levels which may be read from Table 6.1. Concentration levels run in ascending order from top to bottom and temperature levels in ascending order from left to right in Table 6.1. For example, 'Concentration 1-Temperature 2' means that this experimental run utilises a concentration of 46%(w/w) and a temperature of 119 °C.

Upon start-up, a certain mass of air was contained within the steam generator. Therefore initially the needle valve controlling vapour flow into the bubble column

was closed completely for approximately 30 minutes following the onset of boiling in the generator in order to ensure that as much air is removed from the system as feasible.

Once the steam had been sent to waste for 30 minutes and the circulating solution was deemed to have reached steady state at the desired temperature, the experimental runs could begin. The steam-feed's needle valve was opened slightly and adjusted until an appropriate flowrate was achieved which allows the formation of single bubbles (if the flowrate is too high then jets of steam are produced, and if the flowrate is too low then bursts of bubbles are produced at irregular intervals) as shown in Figure 6.5. Two experimental runs were conducted for each concentration and temperature setting at different flowrates, with each experimental run lasting ten minutes. The bubbles were recorded using an AOS X-Motion high speed camera operating with a shutter speed of 500 frames per second (Figures 6.6 and 6.7). In order to ensure high visibility of the bubbles for the recordings, the bubble point of entry is illuminated using two Dedolight 150W Tungsten Aspherics spotlights and a Luxform 500W Halogen spotlight (Figure 6.8). The reflection of light off the bubble caused by these three spotlights ensures that there is sufficient contrast between the bubble and its surrounding fluid. In addition, the inside of the fibreglass insulation surrounding the bubble column is lined with a matted black material in an attempt to minimise reflections. Three recordings are taken during each experimental run at evenly spaced intervals.

6.6 Data Analysis

Each recording was analysed using the ProAnalyst Contour Tracking software package (Xcitex Inc.). This software was used to determine both the perimeter and projected area of each analysed bubble (in pixels, Figure 6.9). From each recording, three bubbles were selected at random (one from the beginning, one from the middle and one from the end of the recording) for analysis in order to ensure that representative results were obtained.

All perimeter and projected area readings are recorded in pixels. The bubble is produced by the gas sparger, and thus these are (at least initially) located in the same plane relative to the camera. Therefore the width of the sparger is measured using a micrometer (Figure 6.10) and compared to its width in pixels as recorded by the high speed camera. This allows for a conversion between pixels and length to be established which takes into consideration all refractive

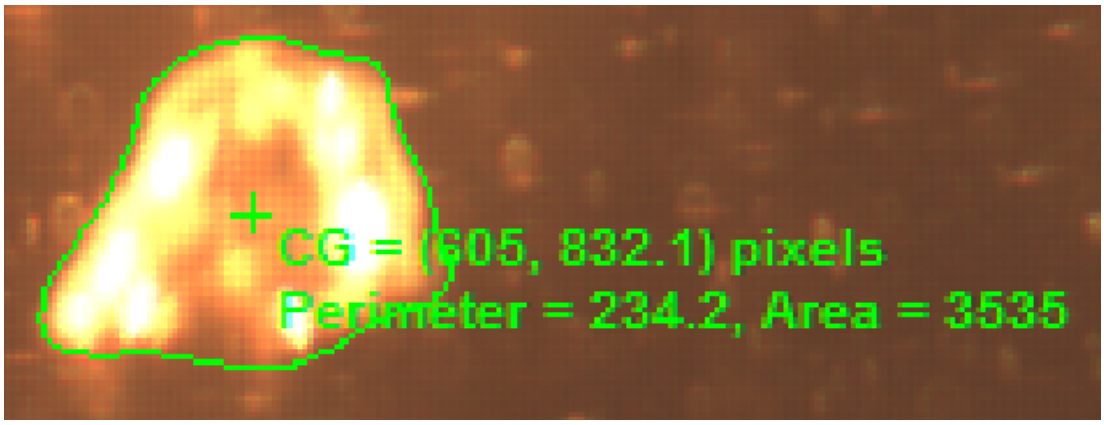


Figure 6.9: Example of a bubble being tracked using the Pro Analyst Software



Figure 6.10: Demonstration of measuring the sparger width using a micrometer

obstacles encountered by the light. This conversion ratio was measured for every single bubble analysed, as small movements of the camera or its refocusing may otherwise cause discrepancies. Errors of parallax are deemed negligible as the maximum vertical displacement measured for the bubbles was on average ∼1.6cm.

Chapter 7

Absorption of Steam Bubbles in Lithium Bromide Solution

Nomenclature

A	Surface Area (m^2)
$A_{projected}$	Projected area looking down at the top of the bubble (m^2)
C	Water concentration (mol/m^3)
C_D	Drag coefficient
c_p	Solution specific heat capacity at constant pressure (J/(kg.K))
D	Bubble diameter (m)
D_{ab}	Mass diffusivity of water in $LiBr - H_2O$ solution (m^2/s)
F	Force (N)
f	Frequency of bubble oscillation (Hz)
g	Acceleration due to gravity (m/s^2)
H	Enthalpy (J)
h	Specific enthalpy (J/kg)
h_{pw}	Partial specific enthalpy of water in $LiBr - H_2O$ solution (J/kg)
k	Thermal conductivity (W/(m.K))
m	Mass (kg)
n	Moles
$\dot{m}$	Rate of mass flow (kg/s)
P	Pressure (N/m^2)
P^*	Vapour Pressure (N/m^2)
P^v	Partial Pressure (N/m^2)
Q	Rate of enthalpy flow (W)
R	Radius (m)
T	Temperature (K)
T_{sat}	Boiling temperature of the solution (K)
t	Time (s)
u	Liquid velocity (m/s)
v	Bubble vertical velocity (m/s)
v_T	Terminal vertical bubble velocity (m/s)
V	Volume (m^3)
x	Lithium Bromide mass Fraction (kg/kg)
y	Volumetric Fraction in the vapour phase m^3/m^3

7.1 Introduction

In the previous Chapter, it was demonstrated that bubble absorbers have significant potential benefits compared to conventional absorber designs such as falling film units. Thus experiments were conducted in order to observe the collapse of steam bubbles in a hotter lithium bromide solution ($LiBr - H_2O$), the results of which are presented in this chapter.

Nomenclature continued

Dimensionless Numbers

Nu	Nusselt number = $\alpha D/k_L$
Pe	Peclet Number = $RePr$
Pe_m	Mass Transfer Peclet Number = $ReSc$
Pr	Prandtl Number = $c_{pL}\mu_L/k_L$
Re	Reynold Number = $\rho_L v_b D/\mu_L$
Sc	Schmidt Number = $\mu_L/\rho_L D_{ab}$
Sh	Sherwood number = $\beta D/D_{ab}$
We	Weber Number = = $\rho_L v_b^2 D/\sigma_L$

Greek Symbols

α	Liquid side heat transfer coefficient (W/m^2K))
α_{therm}	Liquid thermal diffusivity = $k/(\rho c_p)$ (m^2/s)
β	Liquid side mass transfer coefficient (m/s)
ϵ	Amplitude factor of the bubble oscillation
ρ	Density (kg/m^3)
μ	Viscosity (Ns/m^2)
σ	Surface Tension (N/m)

Subscripts

abs	absorption
B	Buoyancy
b	Bubble
D	Drag
expt	Experimental
H_20	Water
i	Bubble-Liquid interface
L	Bulk liquid
LiBr	Lithium Bromide
v	Vapour
vm	Virtual mass (or added mass)

A model is also developed which allows the behaviour of the bubble to be predicted throughout its collapse. Much work has been conducted on the modelling of mass transfer in bubble columns using CFD in recent years, such as the use of the discrete bubble model to simulate the absorption of CO_2 in NaOH solution (Darmana et al., 2005), or the mass transfer of dye from gas bubbles in both homogeneous or heterogeneous regimes (Krishna and van Baten, 2003). Different mass transfer coefficient theories were compared in a bubble column simulation using a CFD-PBM (population balance model) approach by Wang and Wang (2007), while the simultaneous heat and mass transfer process of superheated vapour bubbles rising in a direct contact evaporator has also been modelled using a finite volume approach (Campos and Lage, 2000b).

The development of detailed CFD models has many advantages, however in this chapter a simple model, capable of predicting the collapse of a steam vapour bubble in a $LiBr - H_2O$ solution, is developed which should be suitable for use in absorber design calculations and in parametric studies. Thus it is based upon ordinary differential equations and does not require the use of CFD methods to obtain a solution.

7.2 Mathematical Modelling

The model being developed in this chapter is intended to comprise a simple set of ordinary differential equations which may be easily solved and therefore used in design calculations. The primary focus of the model is to predict the rate of collapse of the bubble, and hence the rate of mass and heat transfer between the liquid and the bubble. The bubble is treated as a single bubble in an infinite body of quiescent fluid.

In the model, the bubble itself is defined as the control volume of interest. The temperature of the bulk liquid in the system varies slightly over the length of the cylinder, but is shown to change negligibly with respect to time over the course of any one experimental run. The spatial distribution of temperature occurs gradually over the entire liquid height, however the vapour bubbles are found to absorb within the first few millimetres of contact liquid. Thus the temperature of the liquid is assumed to remain constant with respect to time at the average temperature as reported by the two closest thermocouples (on average within $\sim 0.17\%$ of each other).

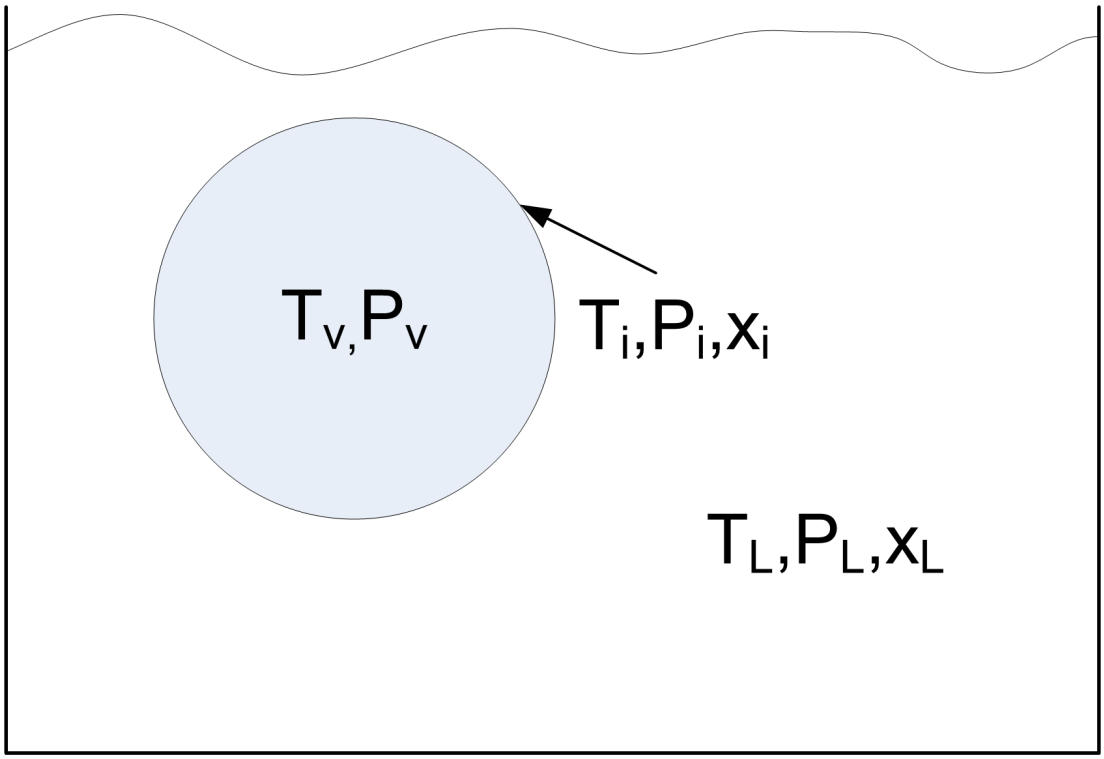


Figure 7.1: Schematic of the different temperatures and concentrations which exist around a collapsing bubble

In order to determine the bubble's volume from the experimentally obtained perimeter and projected area, sphericality of the bubble is assumed. Thus using equation 7.1 an equivalent hydraulic diameter can be calculated which leads to a definition for the equivalent volume of the bubble given by equation 7.2.

$$D_{experiment} := 4\left[\frac{Area}{Perimeter}\right] \tag{7.1}$$

$$V_{experiment} := \frac{32\pi}{3}\left[\frac{Area}{Perimeter}\right]^3 \tag{7.2}$$

7.2.1 Absorption Theory

The absorption of vapour bubbles into liquid solutions is a process which is encountered in many engineering applications. Absorption of a component from a vapour bubble to a liquid phase typically occurs when the bubble is translating through the liquid and some mass transfer inducing gradients exist. The most common example of such a mass transfer operation is the absorption of pure oxy-

gen bubbles into water in fermentation vessels. Mass transfer is induced in this scenario due to the differences which exist between the concentrations of oxygen and water in the vapour phase and in the bulk liquid. The mass transfer of these two components may be described by either diffusion or convection theories. Three primary concentrations develop in this type of a scenario, namely in the bubble, at the vapour-liquid interface and in the bulk liquid as shown in Figure 7.1 (assuming that the problem can be treated as being one dimensional). As the bubble consists initially of pure oxygen, a higher concentration of water will exist in the liquid phase than in the vapour phase and thus water will begin to transfer from the vapour liquid interface to the vapour phase. Simultaneously oxygen will flow in the opposite direction from the vapour phase to the vapour-liquid interface and then subsequently to the bulk liquid. Therefore two way mass transfer is occurring (oxygen flowing from the bubble to the liquid and water flowing from the liquid to the bubble). This will continue until such time that the partial pressures of oxygen and water in the bubble equal the vapour pressures of oxygen and water respectively at the vapour-liquid interface, and also the liquid concentrations of oxygen and water at the vapour-liquid interface equal to the bulk concentrations of oxygen and water in the liquid, i.e.: equilibrium has been achieved. This two way mass transfer process results in a residual vapour phase consisting of both water and oxygen which continuous to translate through the liquid phase.

This experimental investigation is examining the collapse of steam bubbles in a concentrated $LiBr - H_2O$ solution. This process is identical to that of the oxygen bubbles flowing through water as described previously, except that only one-way mass transfer takes place. The lithium bromide salt in the $LiBr - H_2O$ solution has negligible vapour pressure and therefore does not evaporate into the bubble. When an oxygen bubble travels through the water solution, the concentration of oxygen in the bubble decreases as the concentration of water in the bubble increases. This means that a certain point will be reached at which the concentration of oxygen is low enough to prevent any further mass transfer. In comparison, in the $LiBr - H_2O$ system, water vapour leaves the bubble, but no other component replaces it in the vapour phase. This means that the concentration of water in the bubble does not decrease with time and thus a driving force will always exist causing mass transfer until such time that the liquid phase becomes saturates with water. If the absorber is operated continuously (by continuously supplying it with concentrated $LiBr - H_2O$ solution while continuously removing the diluted $LiBr - H_2O$ solution), then the solution can be prevented from ever becoming saturated with water, meaning that steam bubbles can collapse

completely.

7.2.2 Absorption Rate

Heat energy transfer in the liquid phase is assumed to occur by convection, and thus the overall energy balance at the site of absorption may be represented by equation 7.3.

$$Q_{abs} = k_v A_b \left.\frac{\partial T_v}{\partial r}\right|_{interface} + \alpha_L A_b \left(T_i - T_L\right) \tag{7.3}$$

Upon examination of the experimental data, it is observed that significant shape deformation and oscillatory motion is occurring in the bubbles which will result in a high degree of turbulence within the vapour phase and hence mixing (Clift et al., 1978). Due to this mixing and also the small diameter of the bubbles ($\leq\sim 7mm$), it is decided to simplify equation 7.3 further by assuming a uniform temperature within the bubble. Thus it is postulated that the interface temperature is very rapidly advected throughout the bubble, and therefore ($\mathrm{T_i} \simeq \mathrm{T_b}$). Hence equation 7.3 may be reduced to equation 7.4.

$$Q_{abs} = \frac{\partial H_b}{\partial t} + \alpha_L A_b \left(T_b - T_L\right) \tag{7.4}$$

The heat of absorption is defined using a method similar to Islam et al. (2004), utilising the partial specific enthalpy of water in the $\mathrm{LiBr} - \mathrm{H_2O}$ solution (equation 7.5).

$$Q_{abs} = \frac{\partial m_v}{\partial t}\left[h_v\left(T_b, P_b\right) - h_{pw}\left(T_b, P_L, x_i\right)\right] \tag{7.5}$$

Thus the enthalpy balance across the vapour bubble is given by equation 7.6.

$$\frac{\partial H_b}{\partial t} = \frac{\partial m_v}{\partial t}\left[h_v\left(T_b, P_b\right) - h_{pw}\left(T_b, P_L, x_i\right)\right] - \alpha_L A_b \left(T_b - T_L\right) \tag{7.6}$$

Analogously to the heat transfer scenario, mass transfer across the bubble interface may be represented by equation 7.7. This equation describes the molar flow of water (not lithium bromide), and thus C corresponds to the concentration of water. However, as this study measures the mass fraction of lithium bromide

experimentally (instead of water concentration), equation 7.7 has been converted to mass units incorporating salt mass fraction terms (equation 7.8).

$$\frac{\partial n_v}{\partial t} = -\beta_L A_b \left(C_i - C_L\right) \tag{7.7}$$

$$\frac{\partial m_v}{\partial t} = -\beta_L A_b \left(\left(1 - x_i\right)\rho_i - \left(1 - x_L\right)\rho_L\right) \tag{7.8}$$

The effect of water inertia upon the collapse of the steam bubble is defined by the Rayleigh-Plesset equation shown in equation 7.9.

$$\frac{P_B(t) - P_L(t)}{\rho_L} = R_b \frac{d^2 R_b}{dt^2} + \frac{3}{2}\left(\frac{dR_b}{dt}\right)^2 + \frac{4\nu_L}{R_b}\frac{dR_b}{dt} + \frac{2\sigma}{\rho_L R_b} \tag{7.9}$$

Although this equation is derived based upon the assumption of no translational velocity between the vapour and liquid phases, it is being used in this study as it represents the limiting rate of bubble collapse (if heat and mass transfer were believed to occur extremely rapidly) and also approximates the relationship between the internal pressure of the vapour and the rate of change of its diameter.

Currently, 3 independent equations (equations 7.6, 7.8 and 7.9) have been derived, however four unknowns exist (T_b, x_i, P_b and R_b). Thus one further equation is required to provide closure. This is achieved by assuming saturation at the absorption interface (i.e.: the water vapour in the bubble is at equilibrium with the solution at the interface). As negligible pressure drop along the bubble radial direction is also being assumed, the vapour pressure at the bubble interface equals the pressure of the bubble (P_b). A slight residue of air exists in the bubble, therefore this must be accounted for in the vapour pressure model. Using the saturation condition within the bubble, the partial pressure of water within the vapour can be estimated (equation 7.10). The water-air mixture is treated as an ideal mixture and thus Dalton's Law is utilised to find the total pressure from the vapour volumetric fraction of water (equation 7.11).

$$P^v_{H_2O} = P^*_{LiBr}\left(T_b, x_i\right) \tag{7.10}$$

$$P_b = \left(\frac{1}{y_{H_20}}\right) P^*_{LiBr}\left(T_b, x_i\right) = \left(\frac{1}{y_{H_20}}\right) P^v_{H_2O} \tag{7.11}$$

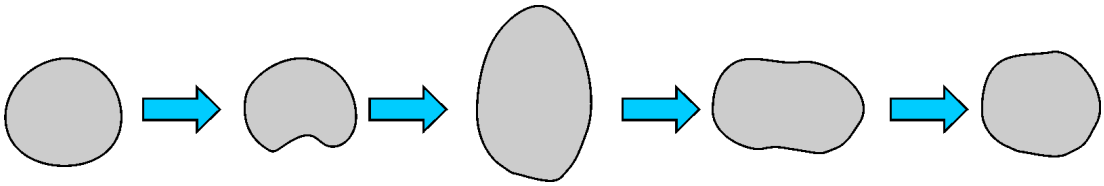


Figure 7.2: Typical shape deformation observed in the bubble. The bubble morphology alternates with time between spherical, oblate-spheroid and prolate-spheroid morphologies. In this figure the oscillation may be simplified as being approximately: spherical → oblate-spheroid → prolate-spheroid → oblate-spheroid → spherical

Equations 7.6, 7.8 and 7.9 and 7.11 represent a set of interdependent, non-linear differential equations which characterise the absorption of a steam bubble in a $LiBr - H_2O$ solution. These differential equations contain both liquid side heat and mass transfer coefficients (α and β respectively). These coefficients are calculated from the bubbles' Nusselt and Sherwood numbers using equations 7.12 and 7.13.

$$Nu = \frac{\alpha D}{k} \tag{7.12}$$

$$Sh = \frac{\beta D}{D_{ab}} \tag{7.13}$$

The bubbles in this experiment are not observed to be perfectly spherical throughout their collapse, but instead oscillate with time between different morphologies as illustrated in Figure 7.2. The general shape change may be qualitatively simplified to be an alteration between spherical, oblate-spheroid and prolate-spheroid morphologies (rotationally symmetric ellipsoids whose major axes are in the horizontal and vertical dimensions respectively). This type of flow is termed 'oscillating' by Clift et al. (1978), and is generally predicted for bubbles once the Reynolds number exceeds 200-1000 (the exact figure depends on the level of surfactants within the system). The Reynolds numbers of the bubbles in this study exceed these values in almost all instances (see section 7.3.2), and thus the fresh surface model for oscillating bubbles is used (equation 7.14) (Clift et al., 1978). Implementing the heat and mass transfer analogy, on the basis of analogous behaviour between heat and mass transfer, an equivalent Nusselt number correlation may be defined (equation 7.15).

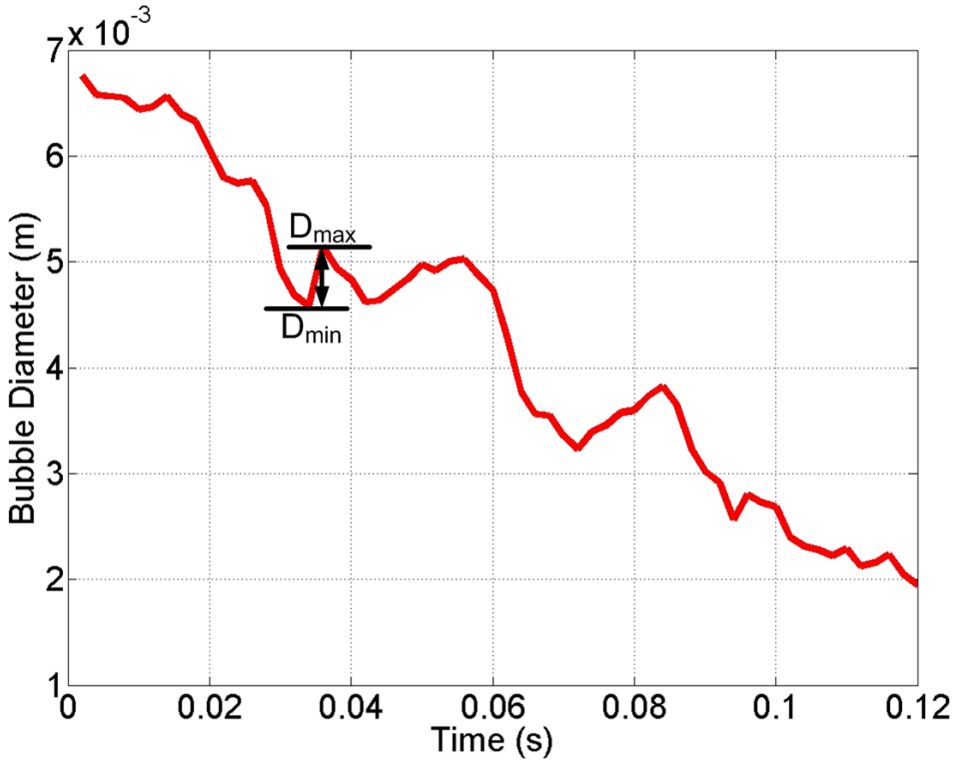


Figure 7.3: Experimental diameter versus time for a typical oscillating bubble showing the difference between maximum and minimum diameter at a particular time due to oscillation

$$Sh = \frac{2}{\sqrt{\pi}}\sqrt{\frac{D^2 f}{D_{ab}}}\sqrt{1+0.687\epsilon} \tag{7.14}$$

$$Nu = \frac{2}{\sqrt{\pi}}\sqrt{\frac{D^2 f}{\alpha_{therm}}}\sqrt{1+0.687\epsilon} \tag{7.15}$$

In equations 7.14 and 7.15, there are two terms which must be defined, namely the amplitude factor (ϵ) and the frequency of oscillation (f). The amplitude factor (ϵ) is simply an indication of the difference between the maximum and minimum surface areas observed during the oscillation (e.g.: if the bubble is oscillating between spheroid and oblate-spheroid morphologies then it will have a minimum surface area when it is a spheroid and a maximum surface area when it is an oblate-spheroid) as defined by equation 7.16. Converting from surface area to diameter values (equation 7.17) enables an estimation of this value. Applying equation 7.17 to all successive bubble diameter readings (an example is shown in Figure 7.3), the maximum calculated epsilon value for any bubble in the system is 0.398, and the minimum is 0.072. Clift et al. (1978) state that generally $\epsilon \simeq 0.3$

for bubbles, and thus this value is used in this study.

$$\epsilon = \frac{A_{max} - A_{min}}{A_{min}} \tag{7.16}$$

$$\epsilon = \frac{D_{max}^2 - D_{min}^2}{D_{min}^2} \tag{7.17}$$

By its very nature, the frequency of the bubble oscillation is difficult to predict, however Clift et al. (1978) state that it is in general less than or equal to the natural frequency of the bubble given by equation 7.18. Based upon the initial diameters measured in this analysis and using equation 7.18, typical values of f_N range from ∼500Hz to ∼700Hz. Thus as equation 7.18 represents the maximum value of f (the value of f_N will increase as the bubble collapses), the frequency is estimated at 500Hz in this model.

$$f_N = \sqrt{\frac{48\sigma}{\pi^2 D^3 \rho_L \left(2 + 3\frac{\rho_b}{\rho_L}\right)}} \tag{7.18}$$

Using this frequency, it is possible to check whether the bubble oscillation approximation is appropriate by using equation 7.19. According to Clift et al. (1978), if equation 7.19 is true then the effect of bubble oscillation is significant. Using the average bubble diameter observed (3.2mm), the average experimental velocity (0.23m/s) and a natural frequency (f_N) value of 500Hz, the left hand side of equation 7.19 equals 6.96, justifying the use of the oscillation assumption in equations 7.14 and 7.15.

$$\frac{f_N D}{v_T} > 0.15 \tag{7.19}$$

7.2.3 Statistical Analysis

In this analysis, experimental values of bubble diameter are being recorded. Each recorded bubble diameter will have a corresponding predicted diameter emanating from the model developed in section 7.2.2. In order to determine the effectiveness of the model, the agreement between the experimentally observed diameters and the predicted diameters is quantified using the coefficient of determination (R^2). The coefficient of determination quantifies the fraction of the experimen-

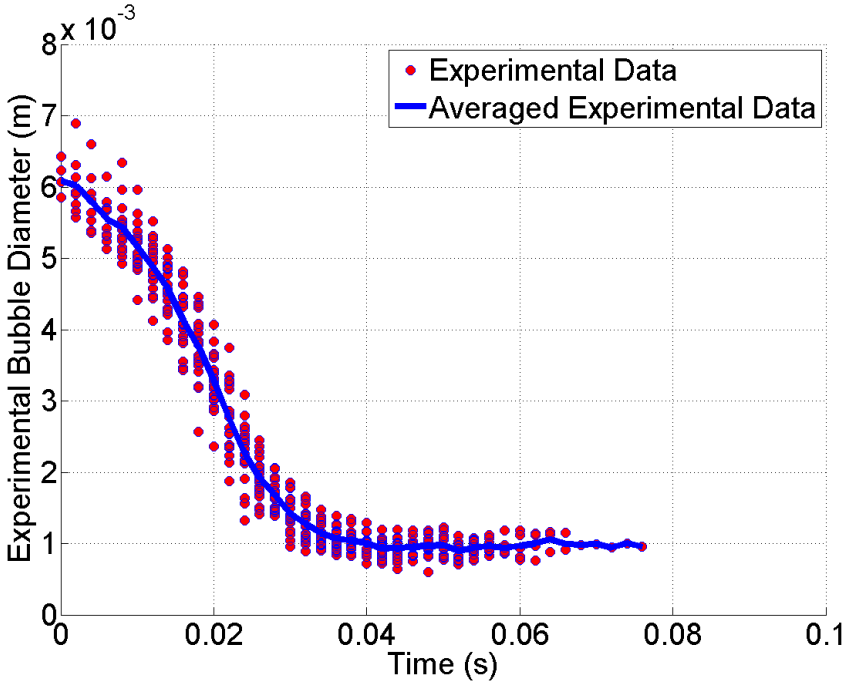


Figure 7.4: Experimental diameter versus time at concentration level 1 and temperature level 1

tal variance which is described by the model predictions, and is calculated using equation 7.20 (where $\langle\rangle$ indicates the mean value). A perfect model has an R^2 value equal to one.

$$R^2 = 1 - \frac{\sum \left(D_{predicted} - D_{expt}\right)^2}{\sum \left(D_{expt} - \langle D_{expt} \rangle\right)^2} \tag{7.20}$$

7.3 Results and Discussion

7.3.1 Experimental Results

The experimental results obtained highlight the speed at which the absorption of bubbles takes place. In contrast to the simulation results reported by Merrill and Perez-Blanco (1997), the bubble diameter is not found to remain almost constant during the first 0.06 seconds of the absorption process. This is due to the fact that unlike in the $NH_3 - H_2O$ system, only one way mass transfer takes place when using a $LiBr - H_2O$ solution (i.e.: mass transfer of water from the steam bubble into the solution). Indeed it can be seen that in general the majority of the absorption has been completed after 0.06 seconds (Figures 7.4 to 7.10).

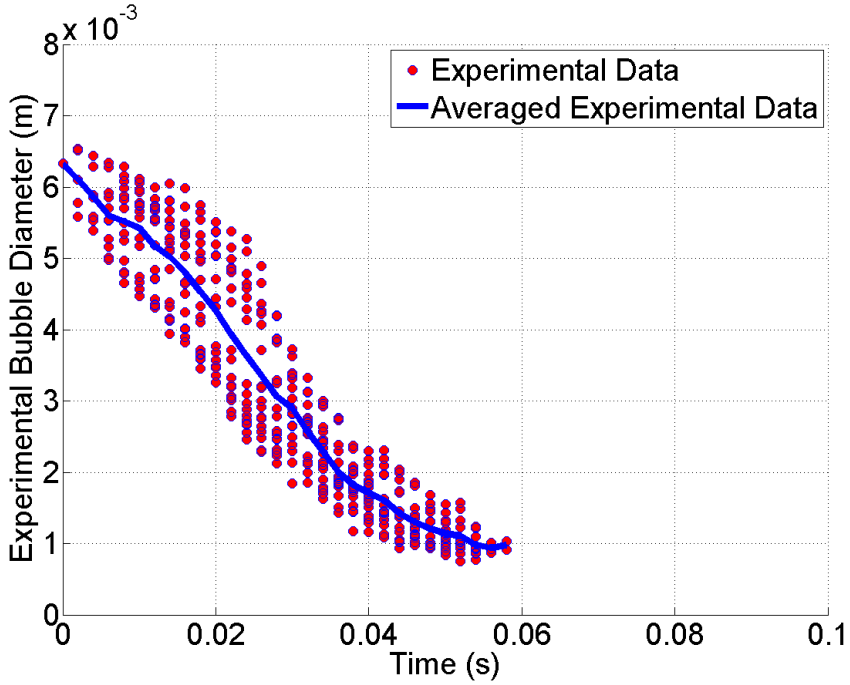


Figure 7.5: Experimental diameter versus time at concentration level 1 and temperature level 2

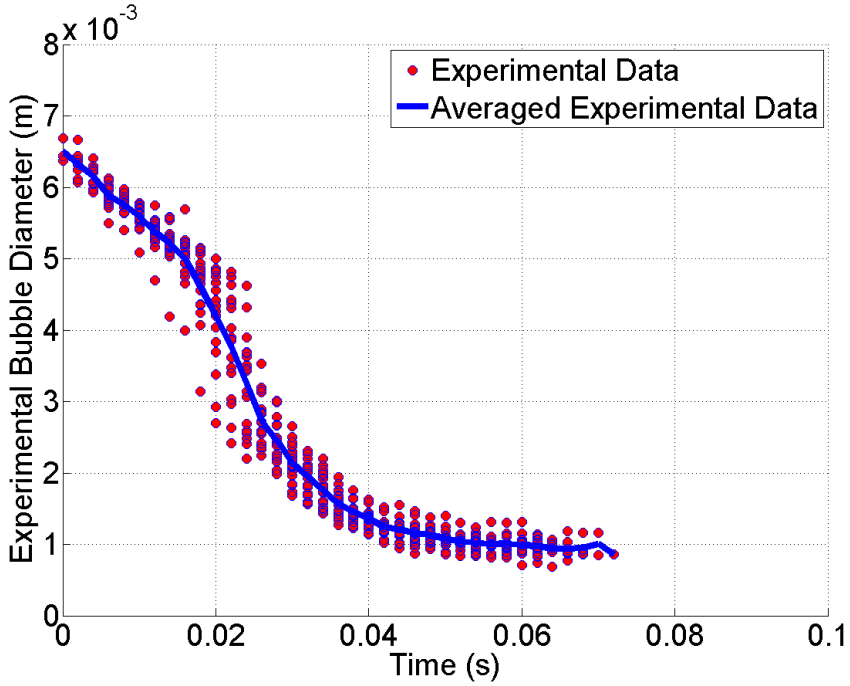


Figure 7.6: Experimental diameter versus time at concentration level 2 and temperature level 1

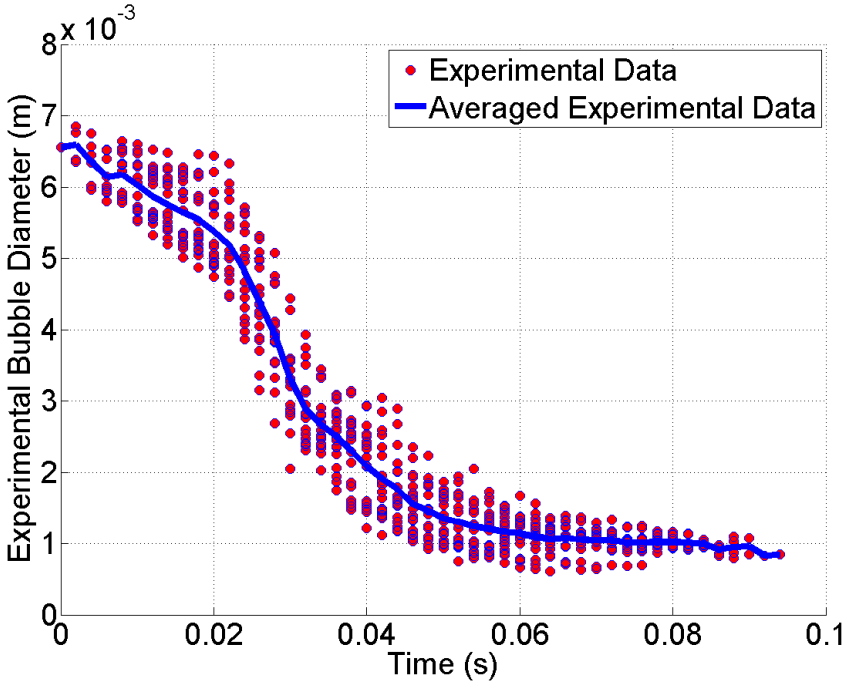


Figure 7.7: Experimental diameter versus time at concentration level 2 and temperature level 2

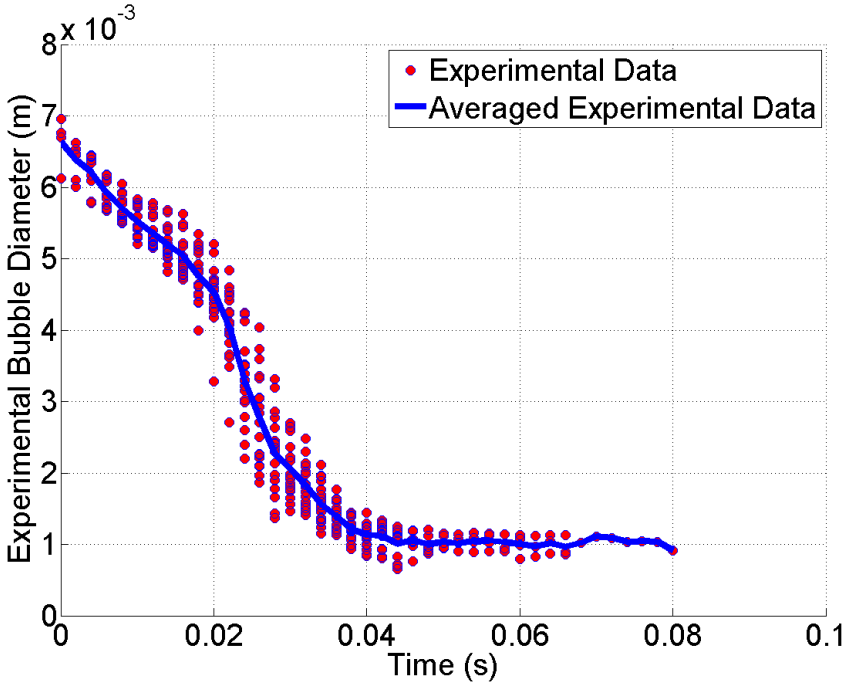


Figure 7.8: Experimental diameter versus time at concentration level 3 and temperature level 1

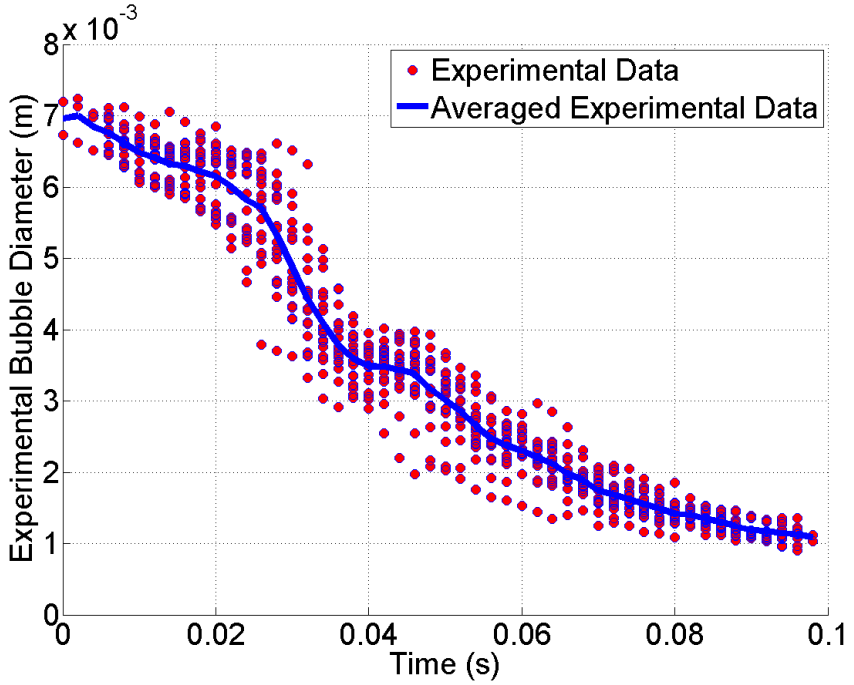


Figure 7.9: Experimental diameter versus time at concentration level 3 and temperature level 2

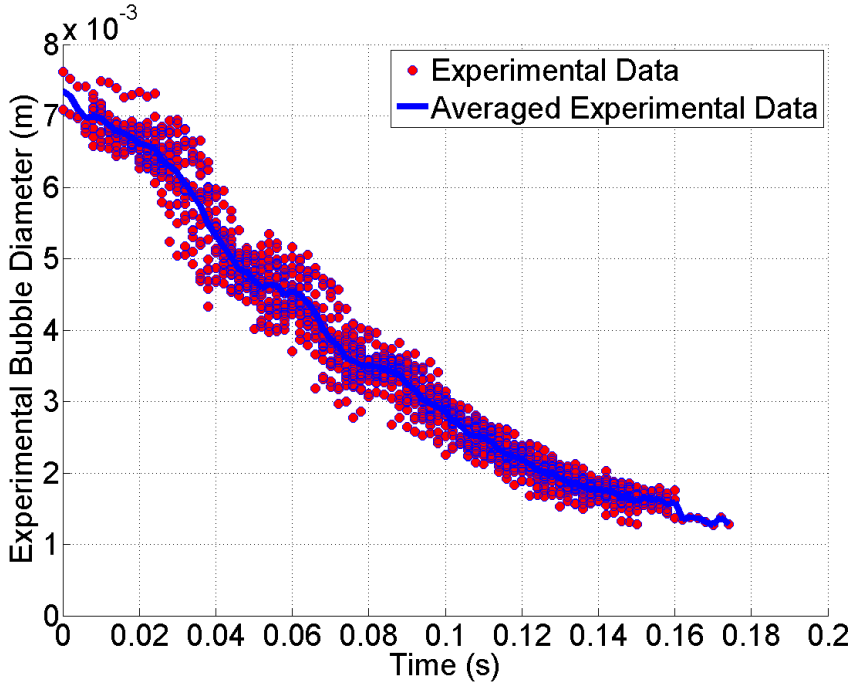


Figure 7.10: Experimental diameter versus time at concentration level 3 and temperature level 3

These figures show the observed diameters from all of the experimental runs (at the particular temperature and concentration) plotted against time. The average experimental bubble diameter profile for each setting is generated by combining the individual diameter (versus time) profiles for each bubble, using a method which minimises the residual between different profiles, and then finding the average diameter at any time step. These average bubble diameter profiles are also included in Figures 7.4 to 7.10. Absorption is found to be especially rapid at temperature level 1, while even at level 3 ($\sim$3.5 °C below the boiling temperature of the fluid) absorption occurs much more rapidly than has been previously achieved in any of the absorber studies cited in Chapter 6. The rapid absorptions depicted in Figures 7.4 to 7.10 represent an average mass transfer coefficient of $\sim$0.0012m/s. It should be noted however that this mass transfer coefficient corresponds to a single bubble in an infinite body of liquid. In reality, the bubble would form part of a bubble column, where convective currents and interactions between bubbles must be taken into account. Thus it is not expected that this exact mass transfer coefficient would be realised in a working absorber. However this value does give an indication of the order of magnitude which is possible for this coefficient in bubble columns.

The data in Figures 7.4 to 7.10 shows a degree of scatter. This is due to the fact that these plots represent the amalgamation of all of the experimentally observed data points for any one temperature and concentration. Due to the inherent variability of bubble shape and the reduction induced by two dimensional imaging analysis of three dimensional bubbles, this scatter is expected. Clear trends may be observed however by comparing the rates of bubble collapse obtained at different settings. The difference between the solution's temperature and its boiling temperature (i.e.: the temperature setting) appears to have the largest impact, with the collapse rate becoming significantly slower and more linear as this gradient decreases.

In Figures 7.4, 7.6 and 7.8 in particular it can be seen that the bubble diameter versus time profile has a sigmoidal shape. The rate of bubble absorption is initially relatively slow before speeding up and then beginning to plateau. It is hypothesised that this variation in absorption rate may be due to the oscillating nature of the bubble. Qualitative visual examination of the high speed video data appears to suggest that the bubble remains relatively spherical during its initial residence time, corresponding to the slower rate of absorption. Thereafter bubble oscillations become more apparent, and coincide with the period of rapid absorption. Oscillating bubble heat and mass transfer coefficients are greater

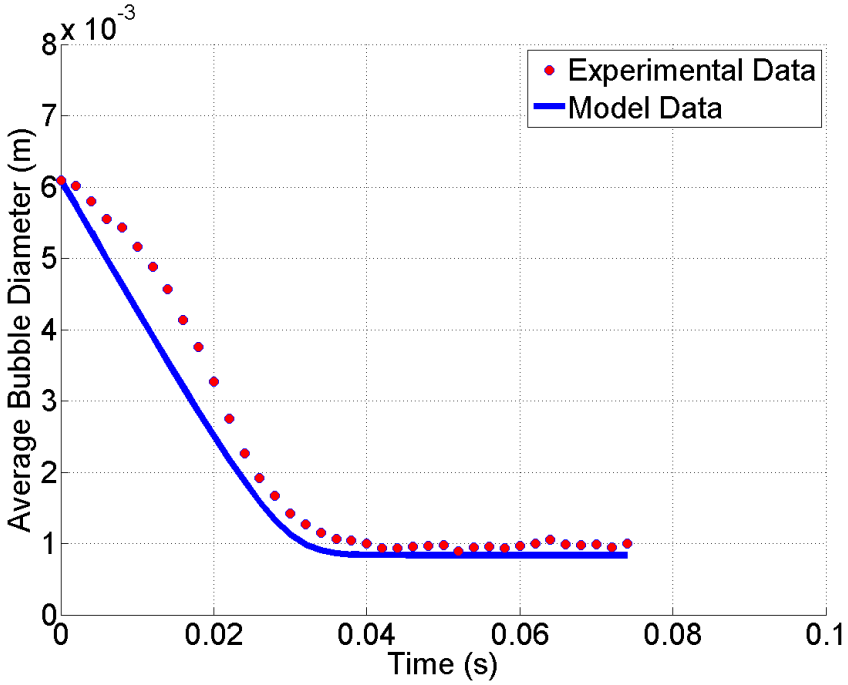


Figure 7.11: Averaged experimental bubble diameter compared to the diameter profile predicted by the model at concentration level 1 and temperature level 1

than those of spherical bubbles, and therefore an increase in the absorption rate is expected.

It is clear from Figures 7.4 to 7.10 and from the collected high speed videos that all of the vapour is not absorbed. This results in a vapour residue travelling vertically upwards at an almost constant volume. This is due to the slight mass of air contained within the bubbles. The initial volume fraction of air in any bubble is estimated by finding the initial volume fraction which allows the predicted modelled plateau to match the experimentally observed plateau for the setting concentration-3, temperature-1. This setting is selected, as it has the most definitive plateau over the largest number of data points (Figure 7.8). This air volumetric fraction is then assumed for all experimental runs. Although this estimated initial volume fraction is very small ($\sim 0.001 \mathrm{m}^3/\mathrm{m}^3$) it has a large effect upon the mass transfer capabilities of the bubbles. The effect of this air-presence is further discussed in section 7.3.4.

7.3.2 Modelling Results

The diameter values of the bubbles predicted by the model developed in section 7.2 are compared in this section to the diameters experimentally observed in

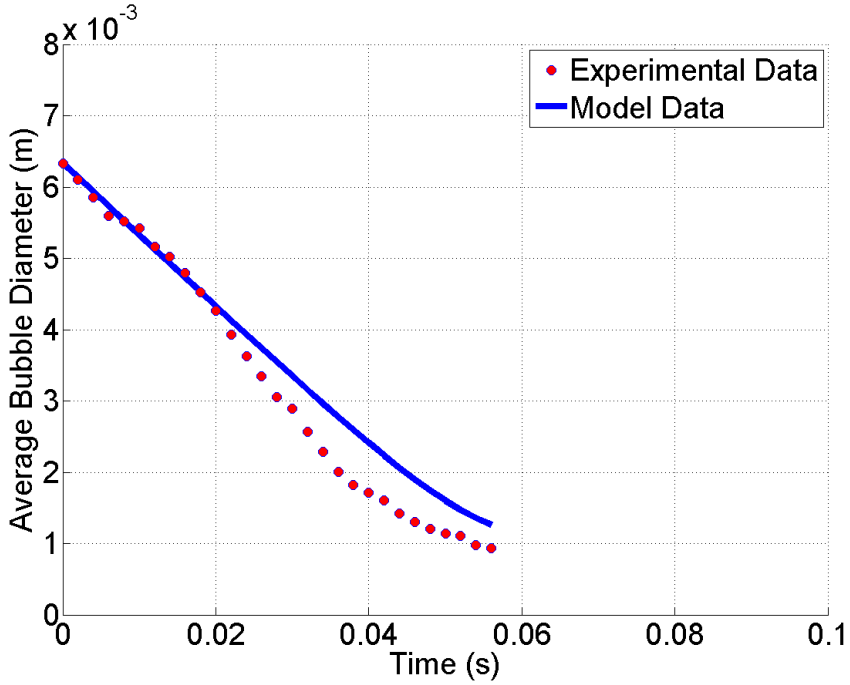


Figure 7.12: Averaged experimental bubble diameter compared to the diameter profile predicted by the model at concentration level 1 and temperature level 2

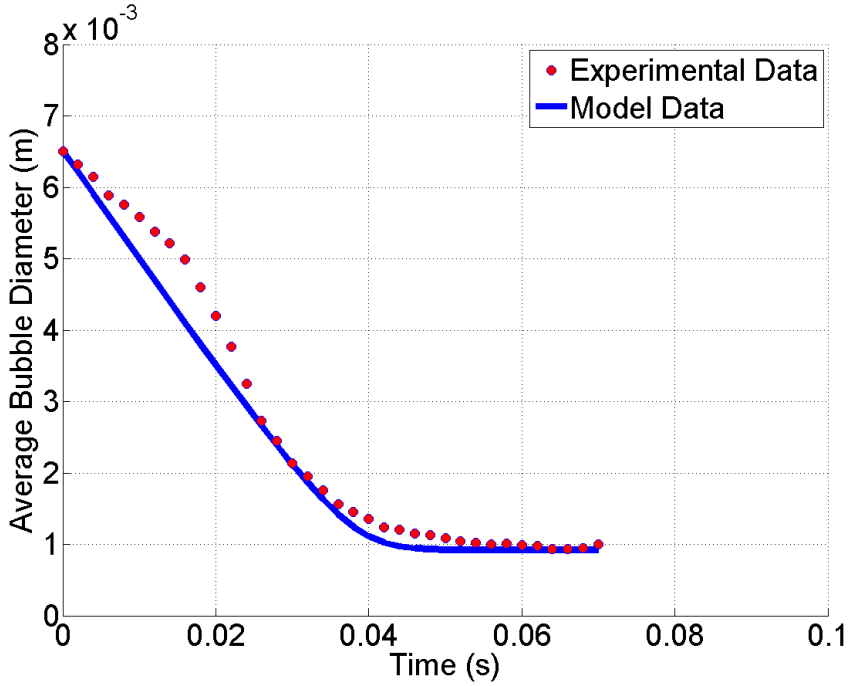


Figure 7.13: Averaged experimental bubble diameter compared to the diameter profile predicted by the model at concentration level 2 and temperature level 1

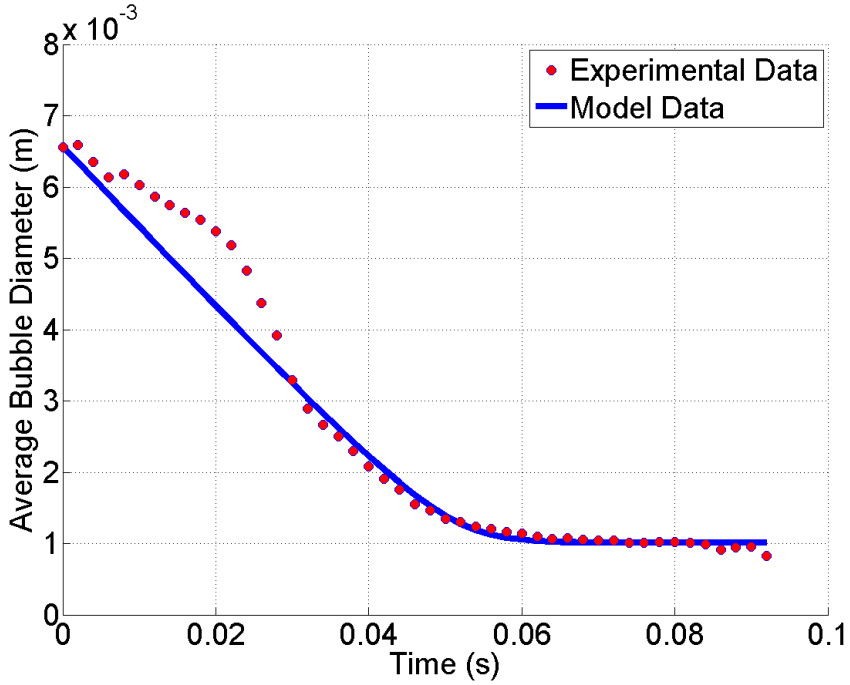


Figure 7.14: Averaged experimental bubble diameter compared to the diameter profile predicted by the model at concentration level 2 and temperature level 2

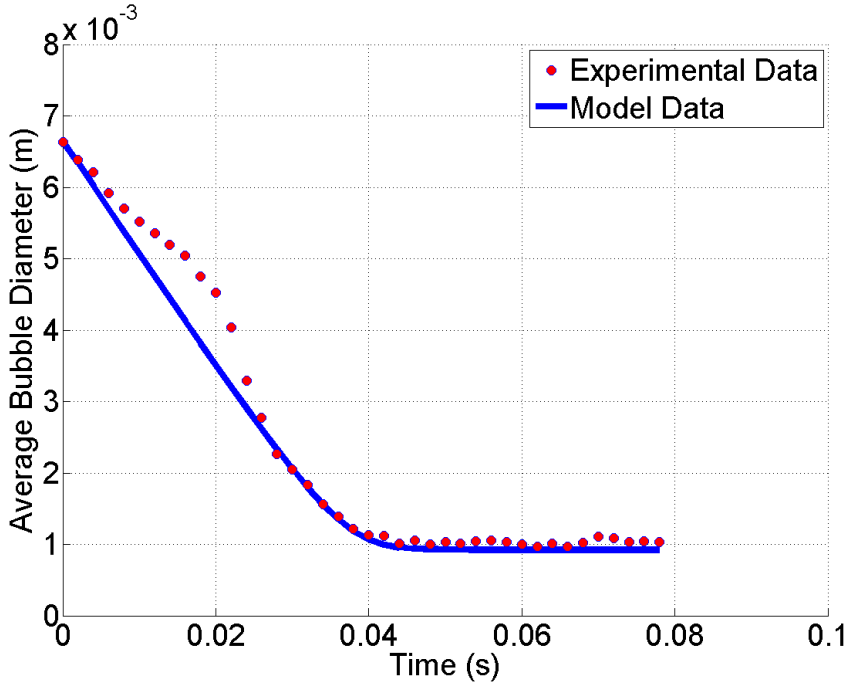


Figure 7.15: Averaged experimental bubble diameter compared to the diameter profile predicted by the model at concentration level 3 and temperature level 1

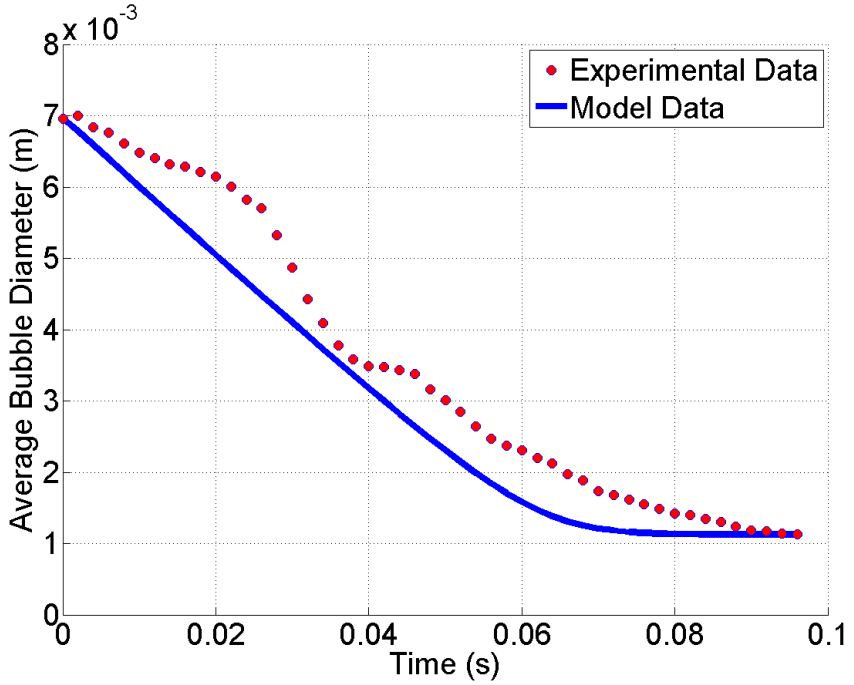


Figure 7.16: Averaged experimental bubble diameter compared to the diameter profile predicted by the model at concentration level 3 and temperature level 2

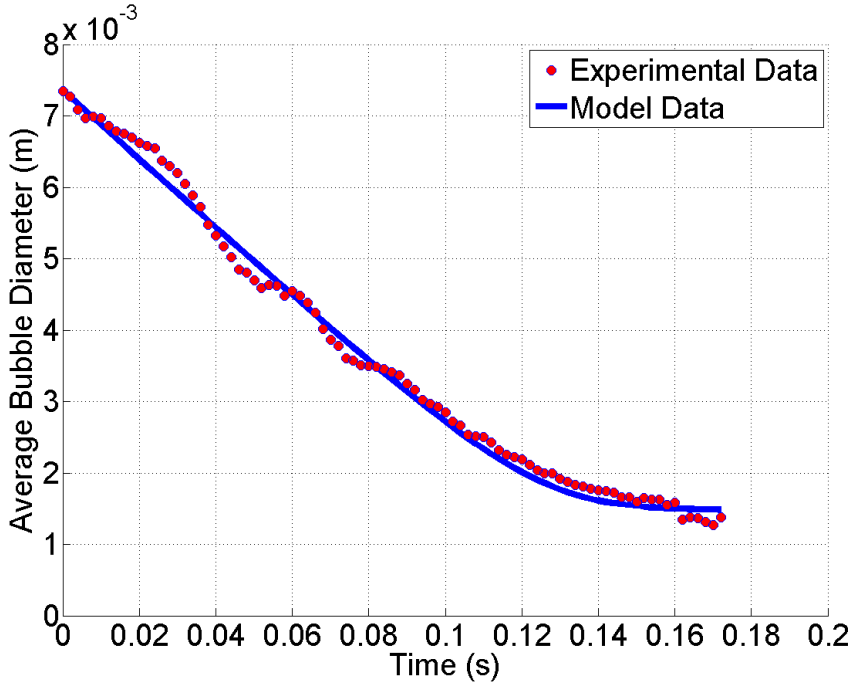


Figure 7.17: Averaged experimental bubble diameter compared to the diameter profile predicted by the model at concentration level 3 and temperature level 3

	Units	C1-T1	C1-T2	C2-T1	C2-T2	C3-T1	C3-T2	C3-T3
μ_L	$Ns/m^2 \times 10^{-4}$	8.11	7.77	9.68	9.54	11.74	11.10	10.79
ρ_L	kg/m^3	1414	1413	1489	1493	1567	1560	1560
ρ_v	kg/m^3	0.64	0.57	0.62	0.59	0.58	0.57	0.55
σ_L	N/m	0.073	0.072	0.073	0.072	0.073	0.072	0.071
D_{ab}	$m^2/s \times 10^{-9}$	1.64	1.64	1.66	1.66	1.69	1.69	1.69
k_L	$W/m.K$	0.53	0.53	0.51	0.51	0.49	0.49	0.49
c_p	$K/kg.K$	2371	2368	2225	2216	2092	2099	2096

Table 7.1: Average solution properties at each experimental setting, where C1-T1 represents the setting Concentration 1-Temperature 1 etc.

	We_L	Re_L	Nu_L	α (W/m^2K)	Sh_L	β (m/s)
Minimum	0.14	112.7	46.35	38,338	454	0.0012
Maximum	24.5	3890.5	601.3	40,549	5636.4	0.0013
Mean	6.5	1462.7	249.3	39,043	2368.1	0.0012

Table 7.2: Ranges of bubble absorption parameters estimated by the model

section 7.3.1. This model, describing the time dependent collapse of the steam bubble, is dependent upon the inclusion of heat and mass transfer coefficients (α and β respectively). It is found that the correct selection of these parameters is of pivotal importance to the accuracy of predictions. As described in section 7.2.2, the bubbles are not perfectly spherical but appear to have an oscillating morphology as illustrated in Figure 7.2. The average values of solution properties utilised in the model are listed in Table 7.1, and the resultant heat and mass transfer coefficient ranges predicted are shown in Table 7.2. It may be observed in Table 7.2 that both the Reynolds and Weber Numbers are relatively high, once more indicating that bubble oscillations and shape deformations would generally be expected. Due to the linear dependence of both the Nusselt and Sherwood Number correlations upon the bubble diameter (equations 7.14 and 7.15), the values of the heat and mass transfer coefficients are insensitive to the changing bubble diameter (i.e.: the diameter term cancels once equations 7.14 and 7.15 are substituted into equations 7.12 and 7.13). This results in relatively narrow ranges of values for these two parameters.

The predictions of the model developed in this chapter are compared to the average experimental diameters (see section 7.3.1) for each concentration and

temperature setting in Figures 7.11 to 7.17. A consistent over-prediction of the collapse rate is evident during the first ∼0.02 seconds. A possible explanation for this trend may be that the bubble oscillation does not begin until this time, as discussed in section 7.3.1. It is extremely difficult to accurately quantify the exact point at which oscillation begins (Clift et al., 1978), and therefore no attempt has been made to do so in this chapter. The approximation that the bubble oscillates throughout its entire residence time leads to a satisfactory agreement between experimental and predicted data in Figures 7.11, 7.13, 7.14, 7.15 and 7.17. In Figure 7.12 the model slightly under-predicts the rate of collapse, especially at the latter stages, while in 7.16 the model over predicts the speed of bubble absorption. In general however, the model is capable of predicting the general trends observed in this bubble collapse to within acceptable error margins.

The model's goodness of fit is demonstrated in Figure 7.18. In this figure, each experimentally recorded diameter is plotted with respect to its corresponding diameter predicted by the model. If the predicted diameter were exactly equal to the experimental diameter, then the plotted point would lie on a line whose intercept is (0,0) with a slope of 1. Thus in Figure 7.18 all predicted values are plotted with respect to their experimental diameters. The figure shows a degree of scatter due to the variability of the bubble morphology discussed in section 7.2.2. The slight over-prediction of initial bubble absorption rate which is visible in Figures 7.11 to 7.17 is also apparent in Figure 7.18 (i.e.: the under-prediction of bubble diameter at large diameters). However except for this slight over prediction of the initial absorption rate, the scatter in Figure 7.18 appears to be evenly distributed above and below the line and does not imply any bias. The developed model achieves a coefficient of determination (R^2) of 0.96, which implies that it is capable of describing 96% of the observed experimental variance.

7.3.3 Effect of Temperature and Concentration

In section 7.3.2 the model developed has been validated using the experimental results outlined in section 7.3.1. In the next three sections, this model shall be used to conduct some sensitivity studies upon the bubble collapse in order to identify whether any parameters have a significant effect upon the rate of absorption.

In the experimental analysis, a number of different temperature and concentration settings have been tested. It is evident from Figures 7.11 to 7.17 that a

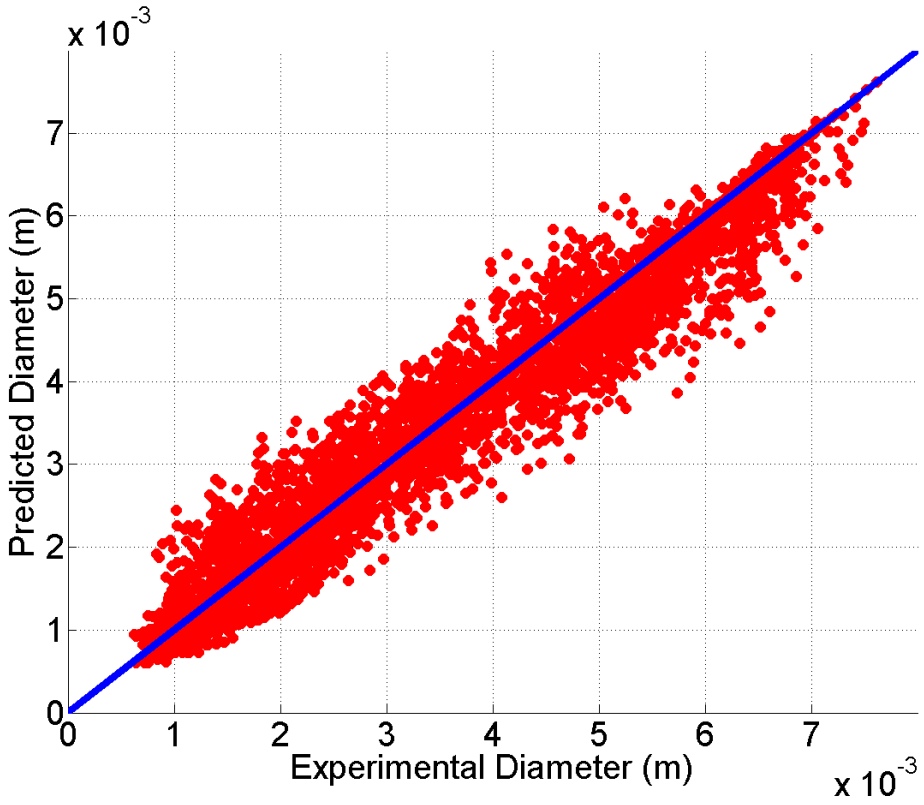


Figure 7.18: Illustration of the goodness of fit between the model and the experimental data

marked difference in bubble absorption rates exist at different settings. In order to quantify the effect of each parameter, this section examines the time required for the volume of a 4mm initial diameter bubble to reduce by 95%.

Figure 7.19 highlights the importance of the temperature gradient in this absorption. The time required for absorption rises exponentially as the temperature gradient decreases while in contrast the effect of concentration is minimal. At lower temperature gradients, a very slight decrease in absorption time is predicted at lower concentrations, however this decrease is negligible. Due to the intrinsic link which exists between the solution concentration and the temperature of the absorber, this result may be extended to say that the rate of absorption of steam bubbles in $LiBr - H_2O$ solution is almost temperature invariant across the ranges analysed, but depends solely upon the difference between this temperature and the boiling temperature of the solution. Thus during the design of a $LiBr - H_2O$ bubble absorption column, the bulk temperature of the solution should at all times be maintained at least $\sim 8\,^{\circ}C$ below the boiling temperature of the solution at the specified pressure and concentration. While it is possible to achieve

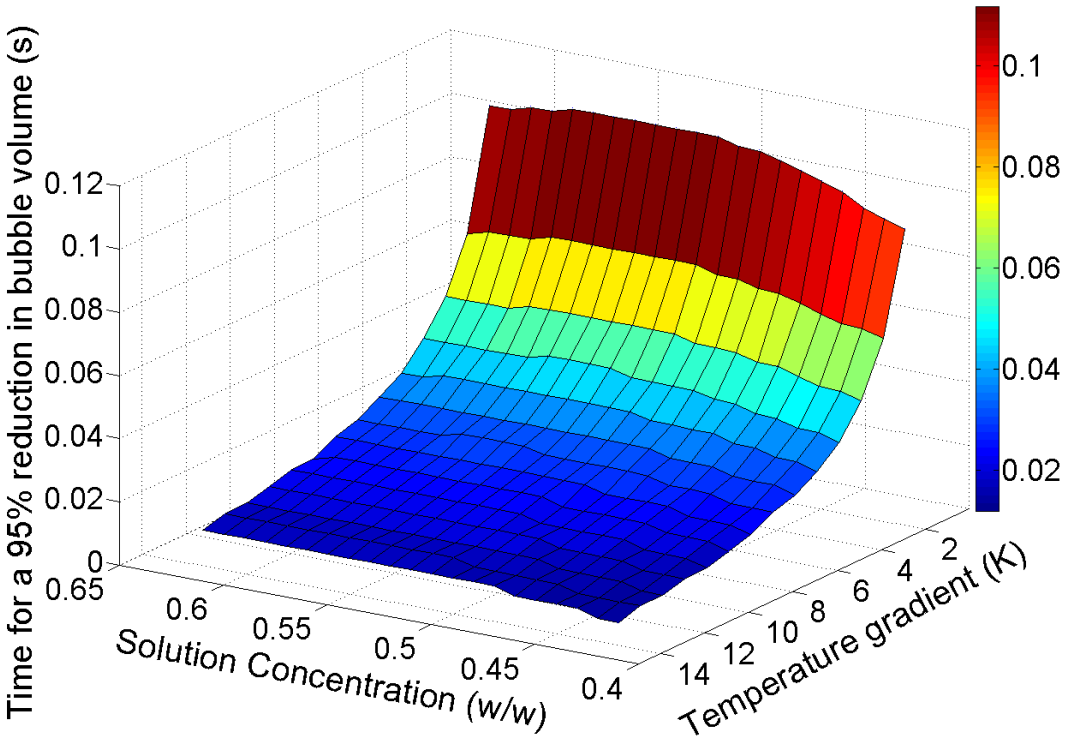


Figure 7.19: Comparison of the time required for a 95% reduction in bubble volume at different concentrations and temperature gradients (i.e.: the difference between the boiling temperature of the solution and the temperature of the solution) for a 4mm initial diameter bubble

absorption at lesser temperature gradients, the bubble residence time, and hence the cost of the absorber, begins to grow exponentially as this gradient reduces. No significant benefits are derived from maintaining a larger gradient.

It should be noted that these results highlight a subtle difference to previously reported findings by Castro et al. (2009) and Kang et al. (2002) discussed in Chapter 6. These two papers state that the collapse of an ammonia bubble in a $NH_3 - H_2O$ solution is dependent upon the temperature and concentration of the solution. In this study we have demonstrated that it appears that it is in fact not the concentration nor the temperature which is important, but the difference in temperature between that of the solution and its boiling point. This result may be explained by examining equation 7.8. The rate of mass transfer is dependent upon the difference between the solution's bulk salt concentration and the corresponding concentration at the vapour-liquid interface. The interface concentration is calculated by assuming it to be saturated with liquid water (equation 7.11) at the interface's temperature (i.e.: the bubble temperature). The further

the temperature of the solution is from its boiling temperature (i.e.: the lower its temperature), the higher the water concentration at the interface can be (hence the lower the salt concentration), thus increasing mass transfer of water away from the bubble into the bulk solution.

By selecting bulk solution temperatures with respect to the solution's boiling temperature in this manner, a change in bulk solution concentration is always accompanied by a change in the temperature of the bulk solution which effectively negates the influence of the concentration change. An example of this would be if the salt concentration of the bulk solution were increased, the boiling temperature of the solution would increase, which in turn would increases the salt concentration at the vapour liquid interface. Therefore as both the salt concentration at the interface and in the bulk solution have increased, it may be seen from equation 7.8 that the influence upon the mass transfer rate of this concentration change is reduced. In contrast if the concentration were to be maintained constant but the temperature of the solution were to be decreased, then the salt concentration at the interface would decrease which increases the difference between the bulk and interface salt concentrations leading to greater mass transfer.

7.3.4 Effect of Air Presence

In section 7.3.1 it is demonstrated that a very small residue of air exists in the bubbles (initially ~ 0.001 m^3/m^3). From Figures 7.11, 7.13 and 7.15 it may be seen however that even such a small air presence prevents the bubble absorption from nearing completion and results in a significant residue of vapour at the end of the absorption process. In Figure 7.20 it is demonstrated that depending upon the difference between the solution's temperature and its boiling temperature, bubble collapse may begin to almost cease at water volume fractions as high as $\sim$ 0.63-0.88. Heat transformers using $LiBr - H_2O$ as the working fluid generally have to operate with sections of the cycle at sub-atmospheric pressures (Zhuo and Machielsen, 1996), and therefore a certain leakage of air into the system may be unavoidable. Thus this section examines the effect which such small quantities of air may have upon the overall absorption rate of the steam bubbles.

A comparison is conducted which examines the rate of collapse of a 4mm initial diameter bubble in a 50% $LiBr - H_2O$ solution, maintaining a 10 °C temperature difference between the solution's temperature and its boiling temperature (Fig-

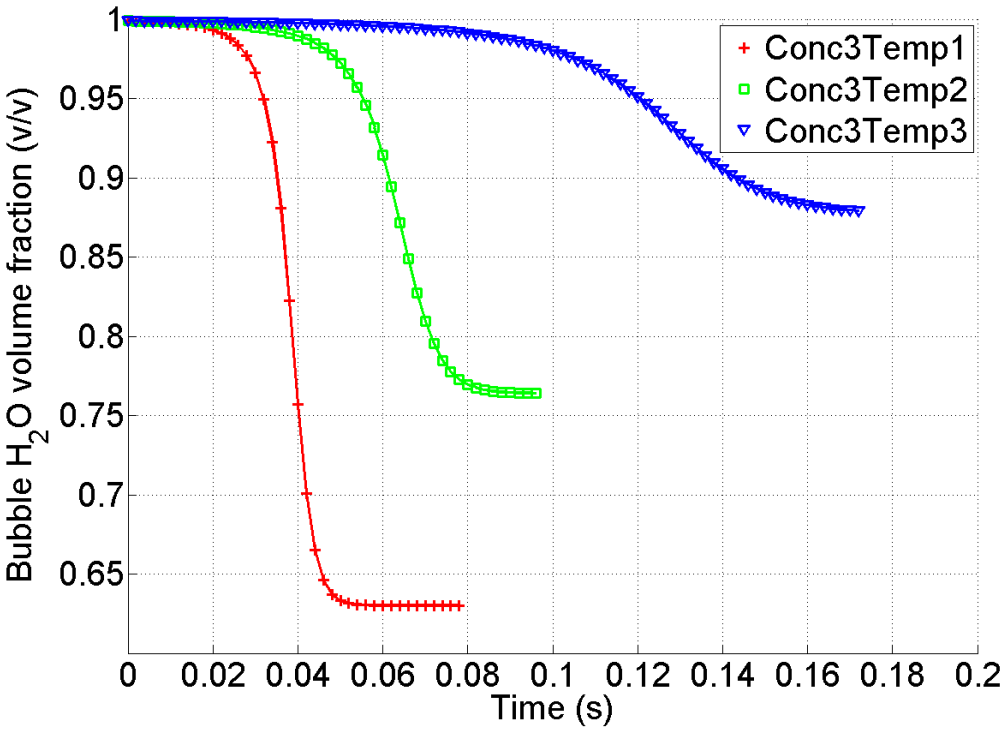


Figure 7.20: Variation of water volume fraction within the bubble throughout its collapse at different temperature settings for concentration level 3

ures 7.21 to 7.22) at different initial water volumetric fractions in the bubble. As expected, the bubble consisting of pure water vapour continues to collapse until it effectively disappears. However even an extremely small fraction of air representing 0.001 of the initial volume causes the bubble collapse to plateau once it reaches ∼0.6mm (Figure 7.21). The rate of collapse up to this point is only negligibly affected. A similar, yet more pronounced trend is observed as this initial volume fraction of air is increased. If an initial air volumetric fraction of 0.03 is present, then the bubble merely collapses to approximately half of its initial diameter prior to the absorption ceasing.

Figure 7.22 shows that a common volumetric fraction exists at which plateauing occurs for a temperature-concentration setting, and appears in this case to be ~ 0.725 $(m^3/m^3, H_2O))$. This common fraction could be used as a stop criteria in design calculations for systems in which it cannot be guaranteed that non-condensables will not be present (i.e.: assume that once this fraction has been reached, no more absorption takes place).

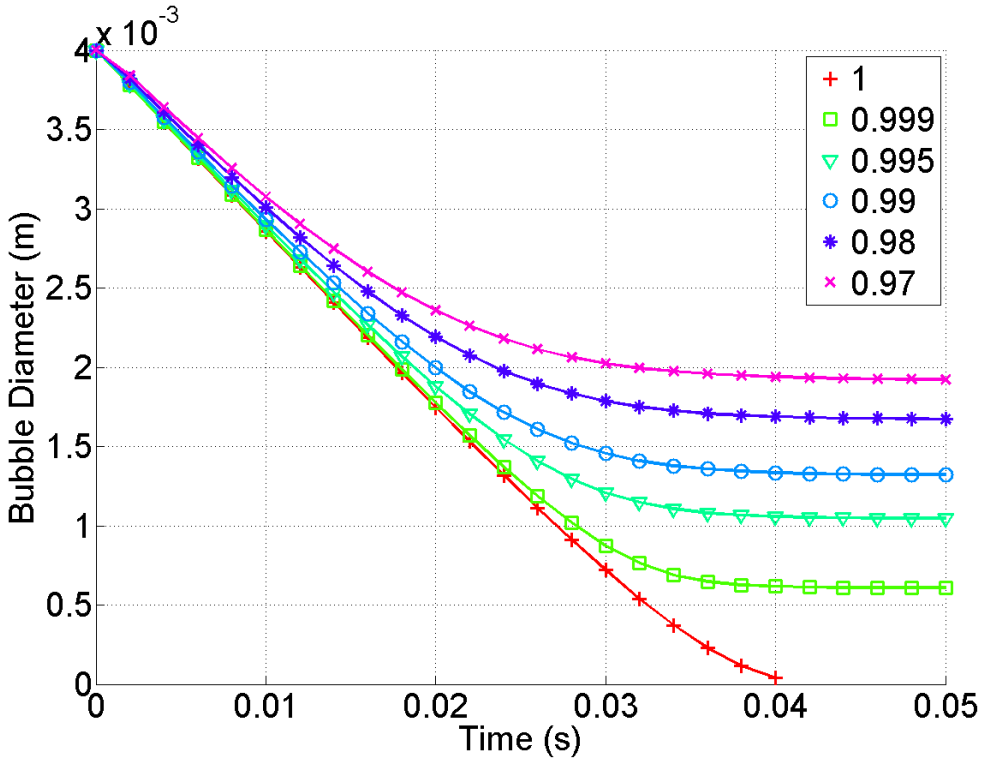


Figure 7.21: Simulation of the diameter versus time profile for a bubble collapsing with different initial volumetric fractions of water present in the vapour phase. A 4mm initial bubble is modelled in a 50% (w/w) solution with a temperature difference of 10 °C between the solution's temperature and it boiling temperature.

7.3.5 Effect of Initial Bubble Diameter

In a bubble column, the initial diameter of bubbles may be estimated based upon theoretical approximations (Azbel and Kemp-Pritchard, 1981). However such predictions are invariably associated with a degree of error, and thus it is important to know what effect the initial diameter has upon the rate of bubble absorption. A number of different bubbles with varying initial diameters are therefore simulated in a 50% $LiBr - H_2O$ solution maintaining a 10 °C difference between the solution's temperature and its boiling temperature. From Figure 7.23 it is evident that the absorption time increases linearly with an increase in bubble diameter (the slope of the line in this figure is marginally greater than one). However, as the volume of a bubble increases with respect to D^3, this implies that the total time required per unit volume of vapour present in fact decreases with an increase in bubble diameter (Figure 7.24). This implies that individual collapsing bubbles such as this achieve higher mass transfer rates at larger initial diameters, primarily due to increases in the bubble surface area and mass transfer coefficient.

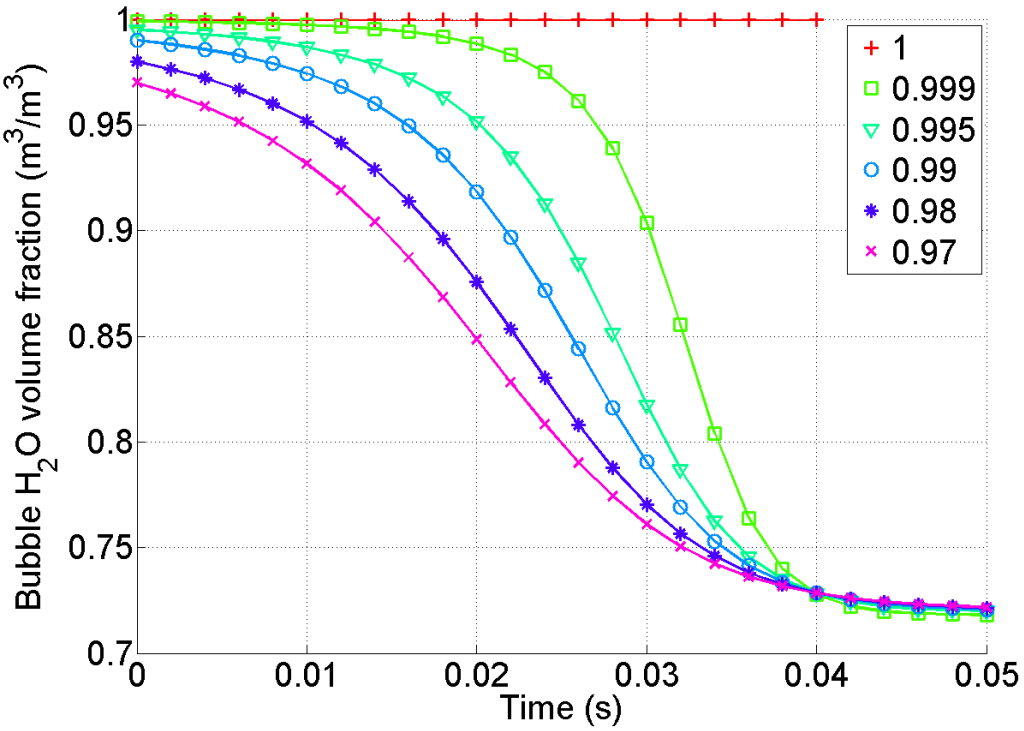


Figure 7.22: Simulation of the bubble H_2O volumetric fraction versus time profile for a bubble collapsing with different initial volumetric fractions of water present in the vapour phase. A 4mm initial bubble is modelled in a 50% (w/w) solution with a temperature difference of 10 °C between the solution's temperature and its boiling temperature.

However once the bubble diameter exceeds a certain size it is more efficient to split a larger bubble into two smaller bubbles as this increases the surface area per unit volume of the vapour (while still maintaining sufficient mass transfer coefficients). Other effects must also be considered in a commercial bubble column, such as the transition point between homogeneous and heterogeneous regimes (Krishna and van Baten, 2003), and thus it is appropriate that optimum values of initial bubble diameter should be found during absorber design.

7.4 Conclusions

An experimental analysis has been conducted which examines the absorption of single steam bubbles in an aqueous lithium bromide solution. The bubbles are tracked using a high speed camera, and the rate of absorption of the bubbles is modelled using a simple ordinary differential equation model. Accurate model

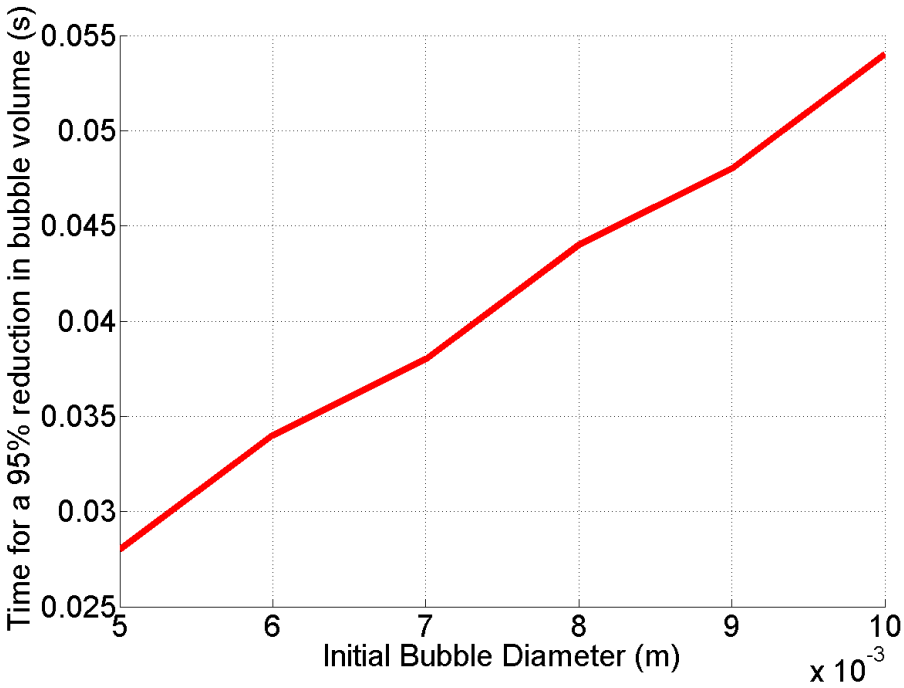


Figure 7.23: Variation of the bubble absorption time (for a 95% reduction in bubble volume) with respect to initial bubble diameter. The bubble is simulated in a 50% LiBr – H_2O solution, whose temperature is 10 °C below its boiling temperature.

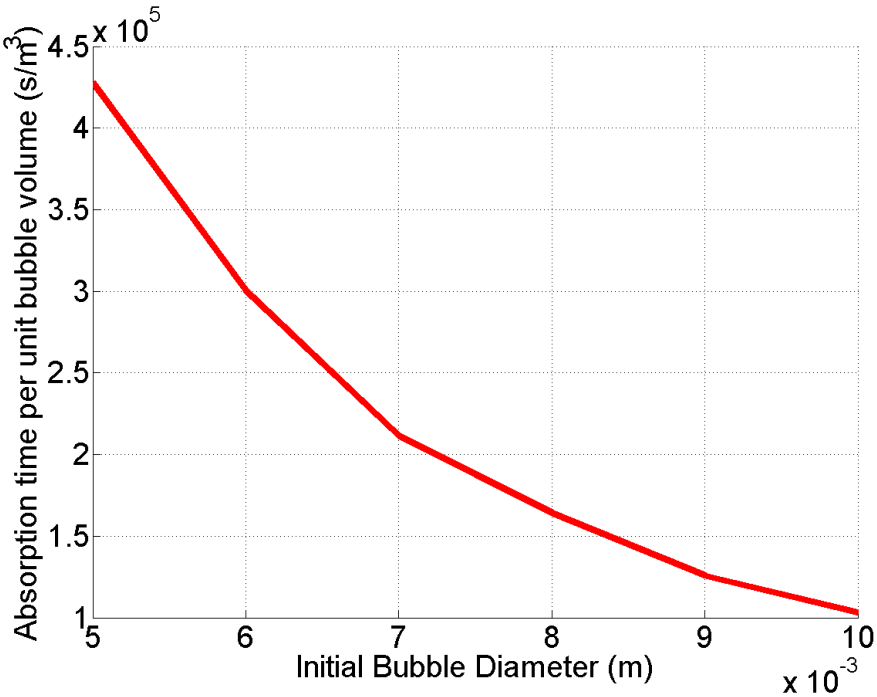


Figure 7.24: Variation of the bubble absorption time (for a 95% reduction in bubble volume) per unit bubble volume with respect to initial bubble diameter. The bubble is simulated in a 50% LiBr – H_2O solution, whose temperature is 10 °C below its boiling temperature.

predictions are obtained when oscillating bubble Nusselt and Sherwood number correlations from literature are utilised. The generated model is capable of describing over 96% of the experimental observed variability. Very large mass transfer coefficients of approximately 0.0012m/s are observed, which is significantly higher than any previously reported values obtained in $LiBr - H_2O$ heat transformer absorber designs. It is demonstrated that the difference between the temperature of the solution and its boiling temperature is of pivotal importance to the absorption rate (a temperate of difference of $\sim 8\,^{\circ}C$ is recommended), while the temperature/concentration of the solution has a negligible effect. If non-condensables exist in the vapour phase, then a temperature-concentration specific minimum volumetric fraction of water in the bubble can be predicted below which effectively no more absorption takes place. The overall rate of absorption is shown to increase with an increase in the bubble's initial diameter for individual small bubbles, however effects such as reduction of the vapour's overall surface area per unit volume ratio and regime change should be taken into consideration in commercial absorbers if trying to make use of this property.

Chapter 8

Analysis of Collapsing Bubble Motion with Random Process Theory

Nomenclature

a	Bubble semi-major axis (m)
a_o	Initial bubble semi-major axis (m)
a_∞	Semi major axis at which the experiment is considered to be finished for any bubble (m)
b	Bubble semi-minor axis (m)
A_p	Vertically projected bubble surface Area (m^2)
C_D	Drag force coefficient
C_H	History force coefficient
C_{vm}	Virtual mass force coefficient
F	Force (N)
g	Acceleration due to gravity (m/s^2)
m	Mass (kg)
N	Number of probability distribution samples in a random realisation
p	probability density function
R	Radius (m)
R_ζ	Bubble aspect ratio random component correlation function
R_η	Bubble semi-major axis random component correlation function
S	Random component spectral density
t	Time (s)
u	Bubble vertical velocity (m/s)
u_L	Liquid velocity (m/s)
$u_{a,\rho}^{terminal}$	Terminal velocity of a bubble at constant semi-major axis and aspect ratio (m/s)
V	Bubble Volume (m^3)

8.1 Introduction

The two phase translational flow of vapour bubbles through a liquid is a complex phenomenon that is encountered in many different areas of chemical engineering such as in biological reactors or in absorption columns. Often other phenomena may be connected to the bubble rise, such as a simultaneous chemical reaction or heat and mass transfer. Two alternative approaches to examining bubble motion are theoretical analysis and numerical CFD techniques. Developing analytical solutions of such flow scenarios is extremely difficult however and generally relies upon assumptions such as negligible liquid viscosity or creeping flow conditions (Re$\rightarrow$0) (Clift et al., 1978). While detailed analytical formulae developed under such assumptions are extremely useful from the perspective of gaining a better understanding of underlying principles, they do not generally apply to real world

Nomenclature continued

Dimensionless Numbers

Re	Reynold Number $= \rho_L v_b D/\mu_L$
We	Weber Number $= \rho_L v_b^2 D/\sigma_L$

Greek Symbols

β_a	Semi-major axis linear collapse rate (m/s)
β_ρ	Aspect ratio linear collapse rate (1/s)
μ	Viscosity (Ns/m^2)
ζ	Bubble aspect ratio zero-mean component
η	Bubble semi-major axis zero-mean component (m)
ρ	Bubble aspect ratio
ρ_o	Initial bubble Aspect Ratio
ρ_L	Solution density (kg/m^3)
ρ_v	Bubble density (kg/m^3)
σ	Standard Deviation
σ_L	Solution surface tension (N/m)
τ_C	Random component characteristic time (s)
ϕ	Bubble sphericity
$\phi_\parallel$	Bubble lengthwise sphericity
$\phi_\perp$	Bubble crosswise sphericity
ω_U	Auto-correlation parameter

Subscripts

am	Added Mass
B	Buoyancy
D	Drag
H	History
L	Bulk liquid
LiBr	Lithium Bromide
term	Terminal
v	Vapour
vm	Virtual mass (or added mass)
w	weight
ζ	Bubble aspect ratio zero-mean component
η	Bubble semi-major axis zero-mean component

situations in which liquid viscosities or Reynolds numbers may be significant. More recently much work has been conducted examining such situations using detailed CFD simulation techniques (Krishna and van Baten, 2003; Campos and Lage, 2000b,a). CFD enables parameters such as the mass transfer rate, bubble size, velocity fields and gas hold-up to be investigated in addition to pure flow phenomena (Darmana et al., 2005; Wang and Wang, 2007; Lau et al., 2012). CFD also has the advantage of permitting detailed analysis of the influence of turbulence on bubble motion (Ekambara and Dhotre, 2010; Silva et al., 2012). Such detailed CFD approaches are extremely beneficial as they allow an insight into the complex processes which are taking place at the vapour-liquid interface and in the bubble wake.

In Chapter 7, the experimental heat and mass transfer rates of steam bubbles being absorbed in a $LiBr - H_2O$ solution were examined. A model was developed describing the heat and mass transfer process, and it was demonstrated that these bubbles are prone to shape oscillations and deformations, leading to significant amounts of random behaviour. This unpredictability implies that significant variability exists within the system. In a design scenario, it is very important to be able to quantify this unpredictability, especially the variability associated with the vertical displacement of the bubbles as it impacts directly upon the required height of the bubble column.

The objective of this chapter is to develop a model of the motion (velocity and displacement) of condensing steam bubbles in an aqueous $LiBr - H_2O$ solution. The primary focus is on the randomness associated with this motion so that the mean and variance in displacement versus time can be predicted. As the system is very complex, a standard deterministic model of bubble motion is selected by making simplifying assumptions which allow basic but adequate descriptions of the process. Correct identification and quantification of the forces acting on a bubble is a prerequisite. Drag (Roghair et al., 2011) and lift (Dijkhuizen et al., 2010) force equations have previously been examined using DNS (Direct Numerical Simulation) techniques, while the importance of including the added mass, wake and history forces was demonstrated by Zhang and Fan (2003). To the author's best knowledge no previous studies exist however which examine the random behaviour of collapsing bubbles, and therefore this chapter investigates the unpredictability associated with the vertical displacement of steam bubbles being absorbed into a concentrated $LiBr - H_2O$ solution. The model developed in this chapter utilises probabilistic methods to predict the vertical displacement of the bubble as it collapses under the action of heat and mass transfer. It should

be noted that the experimental data discussed in the previous chapter shall be used in this analysis once more, and that each setting will be analysed by averaging all of the data at that setting using a method identical to that outlined in Chapter 7.

8.2 Mathematical Modelling

8.2.1 Bubble Shape Model

Solution of the differential equation of motion for the bubbles requires prior knowledge of their size and shape and their dynamic evolution with time. The real bubbles have a very complex morphology that does not conform to any standard geometry and moreover changes very significantly with time. They emanate from a sparger pipe, at the base of the column of liquid, with an approximately spherical shape before becoming pronouncedly non-spherical. One approach to model the dynamic change in size and shape is to treat the bubble as being an oblate spheroid (Clift et al., 1978) (Figure 8.1) which is an ellipsoid where two of the axes are the same length (the semi-major axis, a), while the third is shorter than the other two (the semi-minor axis, b). For a bubble, the shortened axis is parallel to the motion direction. This approach permits shape variation to be explored without an excessive number of unknown degrees of freedom.

As discussed in Chapter 7, a small residual of air is contained in these bubbles which causes the collapse rate to decrease towards the end of the bubble's lifetime. Once the bubble's volume reduces to a certain level, the volumetric fraction of air in the bubble begins to increase rapidly, decreasing the water concentration at the vapour-liquid interface and essentially causing mass transfer from the bubble to cease. This means that the bubble continues to travel at (almost) constant volume without any further absorption. As this study is examining the vertical displacement of a collapsing bubble, experimental data is used only up the point at which this air fraction becomes dominant (a_∞). In this context, a_∞ is the semi-major axis which remains constant with respect to time once the bubble collapse has effectively ceased.

The aspect ratio, ρ, volume and vertically projected cross sectional area of the ellipsoid are defined in equations 8.1 to 8.3.

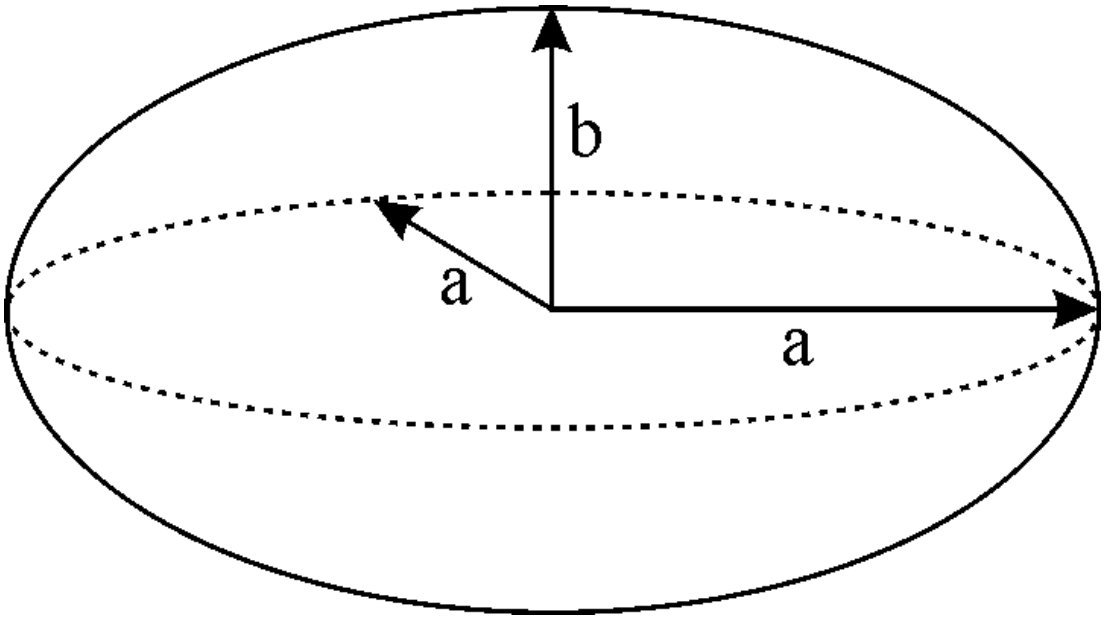


Figure 8.1: Oblate Spheroid bubble shape approximation

$$\rho = \frac{b}{a} \tag{8.1}$$

$$V = \frac{4\pi a^2 b}{3} \tag{8.2}$$

$$A_p = \pi a^2 \tag{8.3}$$

Figure 8.2 shows a representative experimental bubble semi-major axis versus time curve that was found for the system (up to a_∞). The steam bubbles are being absorbed into the lithium bromide solution as they flow vertically upwards, and therefore the magnitude of the bubble's semi-major axis is dependent upon the rate of heat and mass transfer from the bubble. Initially the bubbles have a characteristic dimension of between 4 and 5 mm and this falls down to ∼1mm within approximately 0.1 s. For the purpose of this analysis it is assumed that the average rate of bubble collapse with time is approximately linear and therefore, a regression line can be drawn reasonably well through the data with slope, β_a (Figure 8.2). The residual can be treated as a zero-mean random signal versus time, $\eta(t)$ and is discussed in the next section.

$$a(t) = a_o + \beta_a t \quad for \quad a_\infty < a < a_o \tag{8.4}$$

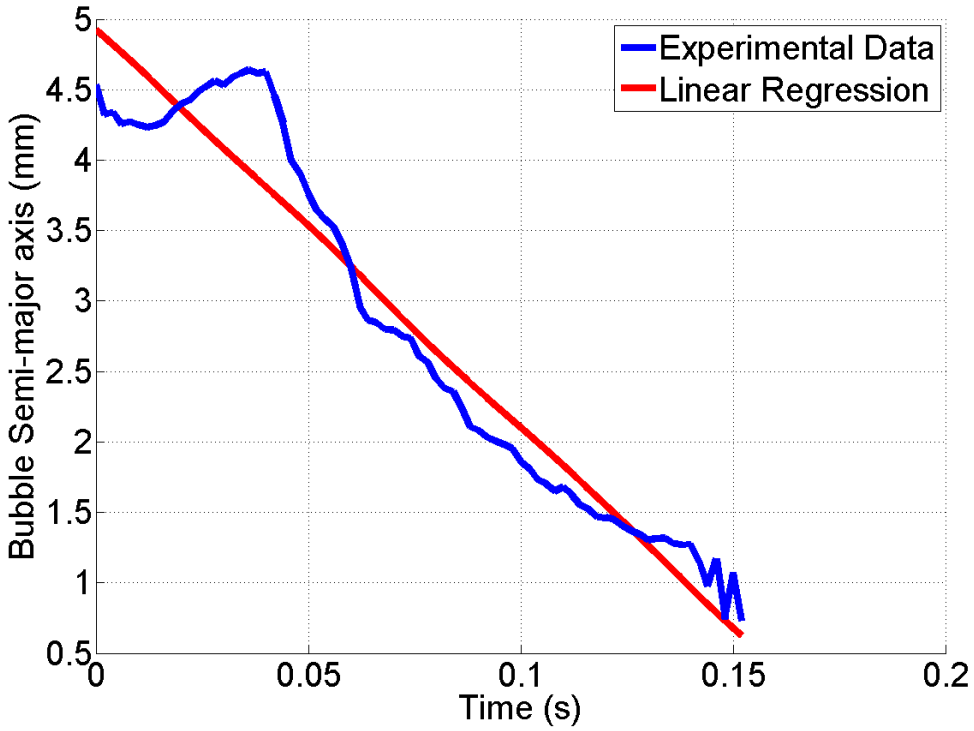


Figure 8.2: Regressed bubble semi major axis for Concentration 3 - Temperature 3 highlighting the random behaviour of this variable

A typical graph of bubble aspect ratio versus time is shown in Figure 8.3. Initially the bubbles tend to have a high aspect ratio close to 1 reflecting their approximate sphericity, but on average this aspect ratio decreases with time. Once more the actual experimental profile is decomposed into a deterministic linear component quantified by a linear regression line with a slope β_ρ and a zero-mean random residual component, $\zeta(t)$.

$$\rho(t) = \rho_o + \beta_\rho t \tag{8.5}$$

8.2.2 Deterministic Bubble Kinematic Model

In order to predict its displacement, the forces acting on the bubble must be quantified. The bubble is being treated as a single bubble in an infinite body of quiescent liquid and thus the lift force is excluded. The weight, buoyancy and drag forces are defined in equations 8.6 to 8.8.

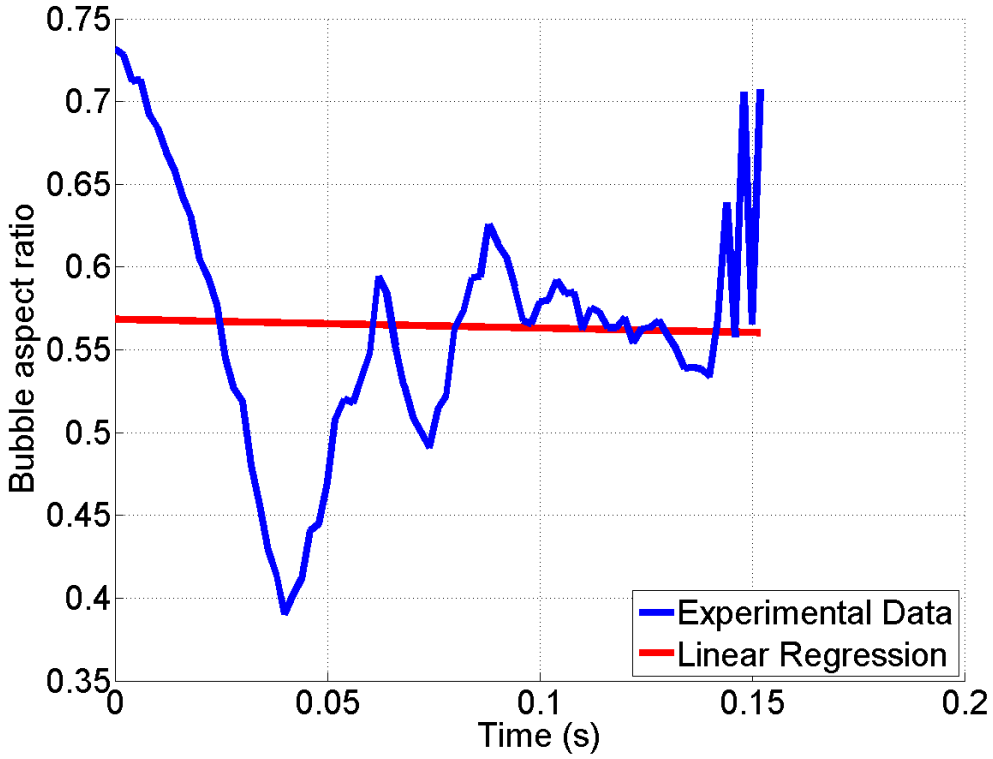


Figure 8.3: Regressed bubble Aspect Ratio for Concentration 3 - Temperature 3 highlighting the random behaviour of this variable

$$F_w = -\rho_v V g \tag{8.6}$$

$$F_B = \rho_L V g \tag{8.7}$$

$$F_D = -\frac{1}{2}\rho_L u^2 C_D A_p \tag{8.8}$$

The virtual mass force acting upon a bubble is due to the small volume of liquid which moves with the bubble as it rises through the liquid. This liquid adheres to the vapour phase due to frictional effects primarily at the top of the bubble and effectively acts as a thin layer sitting upon the vapour. It is a force which is usually neglected when examining solids moving through vapour or other media as the mass of the solid is significantly greater than that of the small fluid layer, however this is not possible for vapours moving through liquids. The volume of the liquid layer is small in comparison to that of the bubble, but its influence

may be significant due to the much higher density of the liquid phase compared to that of the vapour.

As the surrounding fluid is assumed to be in a steady, isotropic state, the term $D(u_L)/Dt = 0$, and thus the virtual mass force expression used in this model may be simplified to equation 8.9.

$$F_{vm} = -\frac{\partial}{\partial t}\left(C_{vm} V \rho_L u\right) = -\rho_L C_{vm}\left[V\frac{\partial u}{\partial t} + u\frac{\partial V}{\partial t}\right] \tag{8.9}$$

The Basset history force is a force which accounts for the vorticity diffusion in the surrounding liquid and disturbances caused by acceleration or deceleration of the particle (Rostami et al., 2006). This force is defined for spherical particles at finite Reynolds numbers by equations 8.10 and 8.11, where R is the radius of the particle (Odar and Hamilton, 1964).

$$F_H = -6R\pi\mu_L C_H \int_{-\infty}^{t} \sqrt{\frac{\rho_L R^2}{\pi\mu_L\left[t-\tau\right]}}\left(\frac{\partial u}{\partial \tau}\right) d\tau \tag{8.10}$$

$$C_H = 0.48 - \frac{0.32}{\left(\frac{2u^2}{R\left|\partial u/\partial t\right|} + 1\right)^3} \tag{8.11}$$

The overall hydrodynamic model is given in equation 8.12 by applying Newton's Law of motion to the bubble.

$$m_v \frac{du}{dt} = F_D + F_w + F_B + F_{vm} + F_H \tag{8.12}$$

This formulation assumes the liquid is stationary and portions of it are gradually accelerated (decelerated) with the bubble. It ignores the small steady flow that exists in the experimental $LiBr - H_2O$ solution. It also ignores the slight disturbances which may be present in the liquid due to the motion of previous bubbles. Inserting equations 8.6 to 8.11 into equation 8.12 and noting that the mass of the bubble is given by $m_v = \rho_v V$, produces the equation of motion presented in equation 8.13.

$$\rho_v V\left[\frac{du}{dt}\right] = \rho_L V g - \frac{1}{2}C_D\rho_L A_p u^2 - \rho_L C_{vm}\left[V\frac{du}{dt} + u\frac{dV}{dt}\right] - 6C_H R\sqrt{\pi\rho_L\mu_L}\int_{-\infty}^{t}\sqrt{\frac{R^2}{t-\tau}}\frac{du}{d\tau}d\tau \tag{8.13}$$

As vapour density is negligible compared to liquid density, this equation may be reduced further (equation 8.14).

$$2C_{vm}\left[\frac{du}{dt}\right] = 2g - C_D\left[\frac{A_p}{V}\right]u^2 - 2C_{vm}\frac{1}{V}\frac{dV}{dt}u - \frac{12C_H R\sqrt{\pi\mu_L}}{V\sqrt{\rho_L}}\int_{-\infty}^{t}\sqrt{\frac{R^2}{t-\tau}}\frac{du}{d\tau}d\tau \tag{8.14}$$

The equation of motion can be seen to be a non-linear, first-order integro-differential equation with non-constant coefficients. These coefficients primarily depend on geometrical information of the bubble, principally its volume and its area cross sectional to the flow direction and how these parameters change dynamically with time. The situation is made more complex because as the bubble moves upwards through the solution, its volume and cross sectional area vary in both an erratic and systematic fashion with time. The problem is compounded by the limited information that is available concerning the dynamic change in bubble shape and size due to the two dimensional nature of the recorded data. Treating the bubble as an oblate spheroid, the differential equation becomes:

$$2C_{vm}(t)\left[\frac{du}{dt}\right] = 2g - C_D(t)\left[\frac{0.75}{a(t)\rho(t)}\right]u^2 - 2C_{vm}(t)\left[\frac{3}{a(t)}\frac{da}{dt} + \frac{1}{\rho(t)}\frac{d\rho}{dt}\right]u - \frac{9C_H(t)\sqrt{\mu_L}}{a(t)^2\rho(t)\sqrt{\pi\rho_L}}\int_{-\infty}^{t}\sqrt{\frac{a(\tau)^2}{t-\tau}}\frac{du}{d\tau}d\tau \tag{8.15}$$

Due to the changing bubble size and velocity, the drag, virtual mass and history force coefficients will also vary with respect to time. The drag force acting upon a bubble is highly dependent upon the choice of drag coefficient (C_D). Vapour bubbles in a pure liquid which does not contain any trace of surfactants experience a drag force which is much less than that acting upon an equivalent liquid drop or solid particle (Clift et al., 1978). However in the presence of contamination, surfactants accumulate at the vapour-liquid interface reducing internal circulation

within the bubble and causing it to experience a drag force similar to that of a solid particle (Moore, 1965). As no special emphasis has been placed upon ensuring that there are no surfactants present, the drag coefficient correlation for solid non-spherical particles presented by Hölzer and Sommerfeld (2008) is utilised in this study (equation 8.16), which is primarily a function of the bubble's sphericity (ϕ).

$$C_D = \frac{8}{Re}\frac{1}{\sqrt{\phi_\parallel}} + \frac{16}{Re}\frac{1}{\sqrt{\phi}} + \frac{3}{\sqrt{Re}}\frac{1}{\phi^{3/4}} + 0.42 \times 10^{0.4[-log(\phi)]^{0.2}}\frac{1}{\phi_\perp} \tag{8.16}$$

The virtual mass coefficient (C_{vm}) is a function of the aspect ratio of the bubble. For an oblate spheroid in unbounded fluid, this coefficient is given by equation 8.17 (Clift et al., 1978).

$$C_{vm} = \frac{(\rho)\, cos^{-1}(\rho) - \sqrt{1-\rho^2}}{\rho^2\sqrt{1-\rho^2} - (\rho)\, cos^{-1}(\rho)} \tag{8.17}$$

As no expression for the history force of an oblate spheroid at finite Reynolds numbers could be obtained by the author, the expression for a spherical particle shall be used (equations 8.10 and 8.11), using the bubble semi-major axis in place of the radius. While this is a slight oversimplification of this force, it has previously been demonstrated that it only has a very small effect upon a particle translating through a quiescent liquid at high Reynolds numbers (Rostami et al., 2006).

8.2.3 Probabilistic Modelling

As stated in section 8.2.1, bubble size (represented by the semi-major axis) and bubble shape (represented by aspect ratio) can be characterised as having both deterministic and random components. The 'deterministic' component reflects the fact that bubble volume reduces fairly consistently with time due to absorption. The 'random' component exists as this size reduction may be erratic and also due to unpredictability in how the shape changes with time. Hence semi-major axis and aspect ratio are more fully described using equations 8.18 and 8.19, where $\eta(t)$ and $\zeta(t)$ are zero-mean random processes.

$$a(t) = a_o + \beta_a t + \eta(t) \tag{8.18}$$

$$\rho(t) = \rho_o + \beta_\rho + \zeta(t) \tag{8.19}$$

Examination of the experimental data gave no indication of any cross correlation between the random processes and thus they are assumed to be independent.

Any random process is defined by its auto-correlation function and probability density function. Regarding the former for $\eta(t)$ and $\zeta(t)$, the key task is to identify the nature of the correlation function for each and to obtain the magnitudes of the parameters that will define them. Correlation function identification must primarily come from analysis of the temporal structure of the measured data informed by physical reasoning. The measured correlation coefficient falls monotonically from unity and crosses the lag time axis to give negative values at long lag times. The fact that no periodicity is present in the data and that statistically significant negative values are found for both signals indicate that the correlation function corresponding to band-limited white noise may be appropriate for $\eta(t)$ and $\zeta(t)$ (equations 8.20 and 8.21), where τ is the lag time and $\omega_{U\eta}$ and $\omega_{U\zeta}$ are the auto-correlation parameters for each signal.

$$R_\eta(\tau) = \frac{\sigma_\eta^2}{\omega_U} \frac{sin\,(\omega_{U\eta}\tau)}{\tau} \tag{8.20}$$

$$R_\zeta(\tau) = \frac{\sigma_\zeta^2}{\omega_U} \frac{sin\,(\omega_{U\zeta}\tau)}{\tau} \tag{8.21}$$

To provide an indicative measure of de-correlation, a de-correlation time scale, can be defined as the time of the first crossing of the lag time axis by the auto-correlation function, τ_C. Also at this point, where the correlation coefficient equals zero, the function given by equation 8.22 must be satisfied, and hence the magnitudes of the parameters ω_U can be found.

$$\omega_U = \frac{\pi}{\tau_C} \tag{8.22}$$

The statistical structure of the random component of the semi-major axis and aspect ratio can also be quantified in the frequency domain using the relationship that mean square spectral density of $\eta(t)$ and $\zeta(t)$ will be given by the Fourier transform of the associated auto-correlation function. As equations 8.20 and 8.21 are even real functions, the normalised (continuous) spectral densities are given

by equations 8.23 and 8.24.

$$S_\eta(\omega) = \frac{1}{\pi}\int_0^\infty \frac{\sigma_\eta^2}{\omega_{U\eta}}\frac{sin\left(\omega_{U\eta}\tau\right)d\tau}{\tau}cos\left(\omega\tau\right)d\tau = \frac{\sigma_\eta^2}{2\omega_{U\eta}} \tag{8.23}$$

$$S_\zeta(\omega) = \frac{1}{\pi}\int_0^\infty \frac{\sigma_\zeta^2}{\omega_{U\zeta}}\frac{sin\left(\omega_{U\zeta}\tau\right)d\tau}{\tau}cos\left(\omega\tau\right)d\tau = \frac{\sigma_\zeta^2}{2\omega_{U\zeta}} \tag{8.24}$$

Equations 8.23 and 8.24 can be interpreted as giving the contribution to the total variance in the random component of each signal attributable at each frequency level. Given $S(\omega)$ is constant at a value up to ω_U and then is zero at frequencies beyond that, it implies that only frequencies below ω_U contribute to the variance in the signal.

In addition to a description of the correlation structure of the random processes in time, information is also needed on the amplitudes of both signals. Analyses of the distribution in the magnitudes of both signals indicated that they follow the Gaussian probability density function, and are defined by equations 8.25 and 8.26.

$$p(\eta) = \frac{1}{\sqrt{2\pi\sigma_\eta^2}}e^{-\left[\frac{\eta^2}{2\sigma_\eta^2}\right]} \tag{8.25}$$

$$p(\zeta) = \frac{1}{\sqrt{2\pi\sigma_\zeta^2}}e^{-\left[\frac{\zeta^2}{2\sigma_\zeta^2}\right]} \tag{8.26}$$

8.2.4 Numerical Simulation

For the deterministic model of motion, the governing differential equation for bubble velocity was solved in MATLAB using the Euler method and a time step of 0.02ms (the experimental time step is 2ms). The Euler method is selected instead of higher order methods such as the Runge-Kutta method as care is being taken not to cause any smoothing or averaging of the randomly fluctuating data. High order algorithms such as Runge-Kutta evaluate the function at a number of different increments and then average these values. By using the Euler method this averaging is avoided. The trapezoidal rule numerical integration scheme was used to obtain displacement. For the probabilistic approach, equation 8.27 is

employed to generate realisations of the random component of semi-major axis (an identical scheme is used for aspect ratio).

$$\eta(t) = \frac{\sigma_\eta}{\sqrt{N}} \sum_{j=1}^{N} p_j cos\left(\omega_j t\right) + q_j sin\left(\omega_j t\right) \tag{8.27}$$

For each value of j, the magnitudes of the coefficients p and q are drawn from the unit Gaussian distribution.

$$p \leftarrow N\left[0,1\right], \qquad q \leftarrow N\left[0,1\right] \tag{8.28}$$

Similarly for each value of j, the magnitudes of ω are drawn or randomly sampled from the distribution whose probability density function is defined as the mean square spectral density of $\eta(t)$ (which is the continuous uniform distribution as given by equation 8.23).

$$\omega \leftarrow U\left[0,\omega_U\right] \tag{8.29}$$

The Central Limit Theorem will ensure that the summation of equation 8.27 (for sufficiently large values of N) will give a Gaussian distribution for $\eta(t)$ with zero mean and unit variance. Scaling the returned values by σ_η means the particular Gaussian distribution for the magnitude of random deviation bubble semi-major axis is obtained. The sampling routine employed for p and q ensures that the realisations of $\eta(t)$ have the correct distribution in magnitude while the routine used to sample ω, ensures $\eta(t)$ realisations have the correct frequency components. The Monte Carlo method was employed to generate the random process according to the procedure outlined in this section. For equation 8.27, N was set at 50. The solution procedure employed was:

1. Generate a realization of $\eta(t)$ and $\zeta(t)$ using a time-step of 0.02ms
2. Numerically evaluate the derivatives of these random processes from the realizations above.
3. At each time step, input the values of both random processes and their derivatives into equation 8.15 and evaluate velocity at that point in time.
4. Hence evaluate bubble velocity and displacement over the lifespan of the bubble.

	Units		C1-T1	C1-T2	C2-T1	C2-T2	C3-T1	C3-T2	C3-T3
μ_L	Ns/m^2	$\times 10^{-4}$	8.11	7.77	9.68	9.54	11.74	11.10	10.79
ρ_L	kg/m^3		1414	1413	1489	1493	1567	1560	1560
ρ_v	kg/m^3		0.64	0.57	0.62	0.59	0.58	0.57	0.55
σ_L	N/m		0.073	0.072	0.073	0.072	0.073	0.072	0.071

Table 8.1: Solution properties at each experimental setting, where C1-T1 represents the setting Concentration 1-Temperature 1 etc.

5. Repeat 2,000 times and calculate variance in displacement versus time and compare to experimental value.

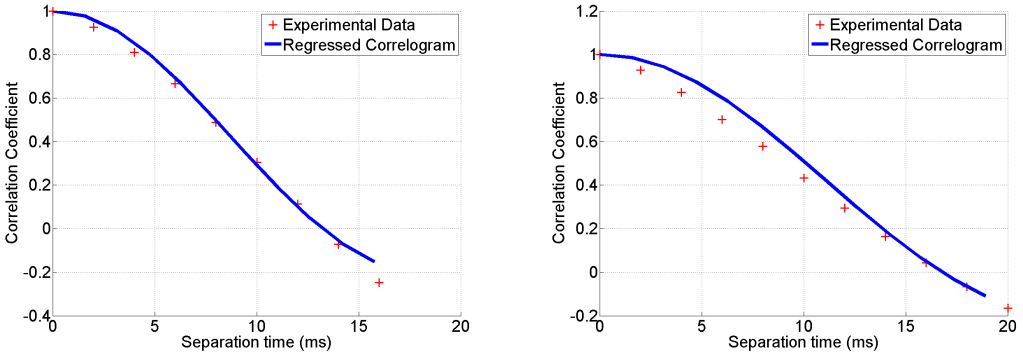
8.2.5 Model Empirical Parameter Selection

The added mass force given by equation 8.9 quantifies the force acting on the bubble due to acceleration or deceleration of the liquid directly surrounding the vapour phase. The second term in this expression accounts for the fact that the bubble volume does not remain constant with time, but is constantly changing. In this experimental study however, it is found that the bubble collapse occurs so rapidly that this term causes an over-prediction of the bubble velocity. Examining the collected high speed camera data, it may be seen that the rate of collapse of the semi-major axis has the same order of magnitude as the average vertical velocity of the bubble over its lifetime. As these two velocities are acting in opposite directions at the top of the bubble, the acceleration/deceleration of the liquid at this point will be reduced significantly. Thus it was found that it was necessary to add an additional coefficient, C^*_{vm}, to this equation to account for this phenomenon (equation 8.30). A sensitivity study demonstrated that on average a C^*_{vm} value equal to $\sim$0.2 gives the best results.

$$F_{vm} = -\rho_L C_{vm} \left[V \frac{\partial u}{\partial t} + C^*_{vm} u \frac{\partial V}{\partial t} \right] \tag{8.30}$$

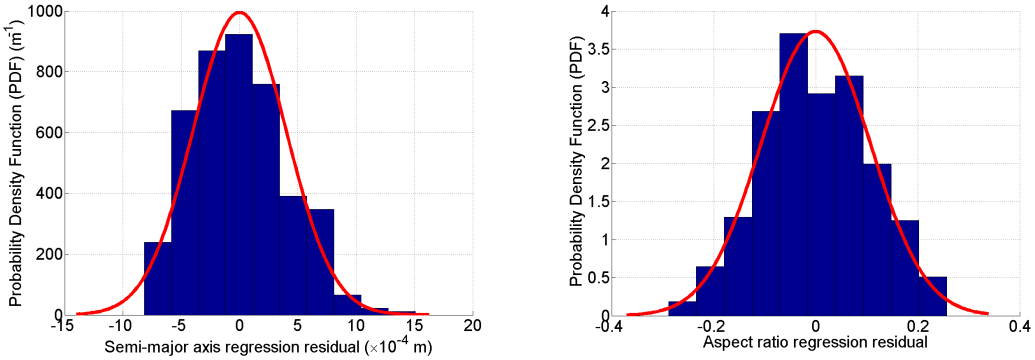
	C1-T1	C1-T2	C2-T1	C2-T2	C3-T1	C3-T2	C3-T3
Re_L	694	2143	873	1042	776	1126	1785
We_L	1.75	7.32	2.93	3.72	3.25	5.10	9.18

Table 8.2: Average solution dimensionless numbers at each experimental setting, where C1-T1 represents the setting Concentration 1-Temperature 1 etc.



(a) Bubble semi-major axis (b) Bubble aspect ratio

Figure 8.4: Experimental and regressed correlograms at Concentration 1-Temperature 2



(a) Bubble semi-major axis (b) Bubble aspect ratio

Figure 8.5: Probability Density Functions of the residual resulting from the linear regressions at Concentration 1-Temperature 2

Setting	a_o (mm)	β_a (mm/s)	ρ_o	β_ρ
Conc1Temp1	4.4	-91.3	0.65	-8.77
Conc1Temp2	4.9	-77.1	0.53	-0.95
Conc2Temp1	4.7	-72.1	0.63	-7.59
Conc2Temp2	4.8	-71.9	0.64	-4.48
Conc3Temp1	4.7	-84.5	0.65	-5.54
Conc3Temp2	4.8	-48.8	0.55	0.86
Conc3Temp3	4.9	-28.1	0.57	-0.05

Table 8.3: Regression data for all concentration and temperature settings

8.3 Results and Discussion

8.3.1 Evolution of Bubble Shape with Time

As previously discussed, the bubbles in this study are generally not spherical, but are found to vary erratically with time as they collapse. This deformation is primarily due to pressure variations over the surfaces of the bubbles which cause them to adapt a morphology closer to that of an oblate spheroid (Magnaudet and Eames, 2000). While to the author's best knowledge, no critical Weber number has been published which defines the transition point between spherical and deformed bubbles, large Reynolds and Weber numbers generally result in secondary motion and shape oscillations (Clift et al., 1978). Theoretical equations correlating the Weber number of the surrounding liquid to the aspect ratio of the bubble are available under creeping flow conditions (Re$\rightarrow$0) (Moore, 1965), however no such theoretical solutions appear to be available at the high Reynolds numbers experienced in this study ($690 < \mathrm{Re} < 2200$, see Table 8.2). Therefore the bubble aspect ratio and semi-major axes are being regressed from experimental data as discussed in section 8.2.1. The parameters for this regression are presented in Table 8.3. It is clear that, in accordance with the results previously presented in Chapter 7, lower temperature levels lead to more rapid rates of collapse while the solution's concentration does not appear to have as strong an impact. The aspect ratio appears to consistently reduce with respect to time (i.e.: negative values for β_ρ), however there does not appear to be a clear correlation between this rate of change and the concentration and temperature settings. The highest rates of aspect ratio reduction are recorded at temperature level one, indicating that an increased rate of collapse of the bubbles leads to a greater level of shape deformation.

Setting	σ_η (mm)	ω_η	$\tau_{c\eta}$ (ms)	σ_ζ ($\times 10^{-2}$)	ω_ζ	$\tau_{c\zeta}$ (ms)
Conc1Temp1	0.52	473.6	6.6	10.9	636.7	4.9
Conc1Temp2	0.40	395.7	7.9	9.2	610.4	5.1
Conc2Temp1	0.71	422.7	7.4	12.2	542.9	5.8
Conc2Temp2	0.55	278.7	11.3	10.4	298.4	10.5
Conc3Temp1	0.59	348.8	9.0	11.2	456.8	6.9
Conc3Temp2	0.43	236.1	13.3	9.4	188.3	16.7
Conc3Temp3	0.41	170.5	18.4	8.8	153.0	20.5

Table 8.4: Regression data for all concentration and temperature settings

Table 8.4 summarises the output of the probabilistic analysis of bubble motion giving the magnitudes of the standard deviation, the de-correlation times and the corresponding cut-off frequency levels for semi-major axis and aspect ratio. From the data presented in this table for both the bubble semi-major axis and its aspect ratio, it may be seen that, similarly to the bubble semi-major axis collapse rate discussed previously, the standard deviation of the random signals as well as their cut off of frequency levels (ω_U) increase with a decreasing temperature level but show no obvious correlation with the solution's concentration. The characteristic times (i.e.: the time at which the correlation coefficient becomes negative) of all setting averaged bubbles are also listed in Table 8.4. The collected experimental data consists of images taken every two milliseconds. It is essential that the bubbles' characteristic times (τ_C) are greater than this experimental time in order to use this data for model verification purposes. From the results presented in Table 8.4 it is clear that this criterion is satisfied for all settings.

Figure 8.4 compares the experimentally observed correlograms to the regressed correlogram functions using equations 8.20 and 8.21 for concentration 3 - temperature 2, demonstrating the appropriateness of the selected auto-correlation function.

Figure 8.5 illustrates the experimentally measured distribution in the random components of semi-major axis and aspect ratio in frequency histogram form. The Gaussian distribution is superimposed for each and while the experimental data has a slight positive skewness, it can be seen that the fit is good.

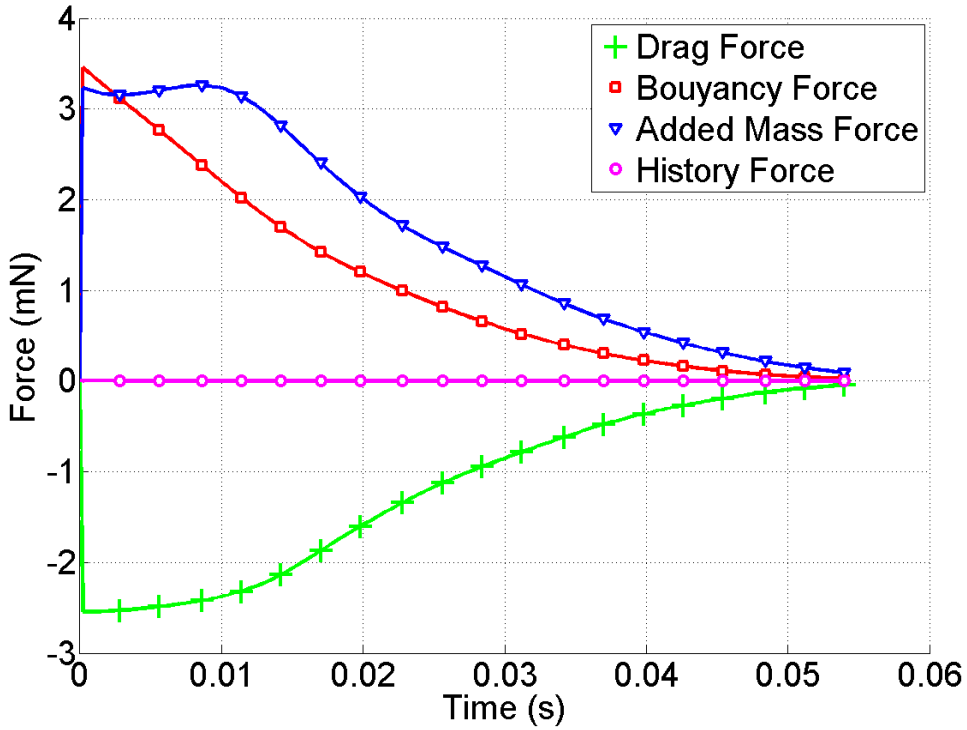
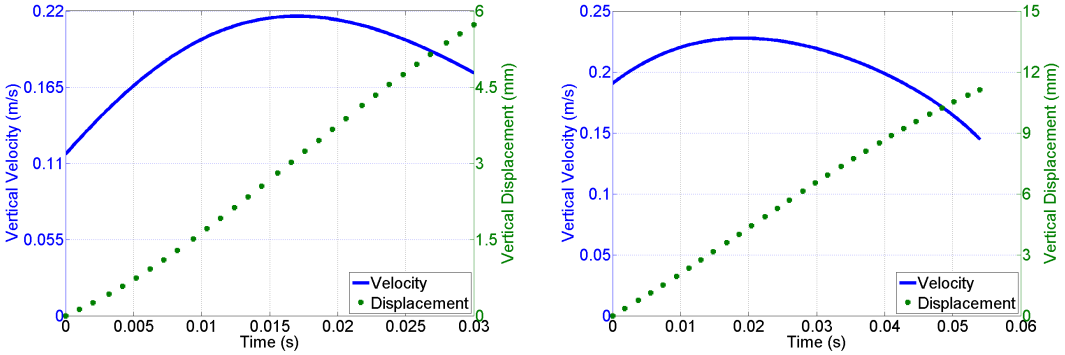
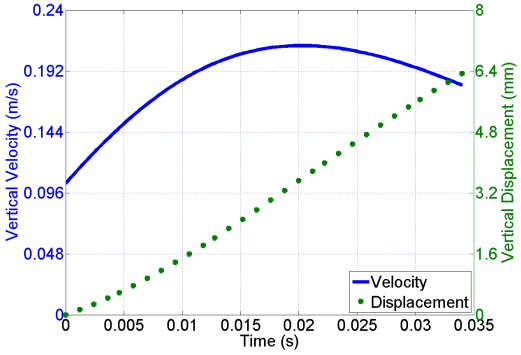


Figure 8.6: Comparison of mean forces acting upon the collapsing bubble at Concentration 2 - Temperature 2

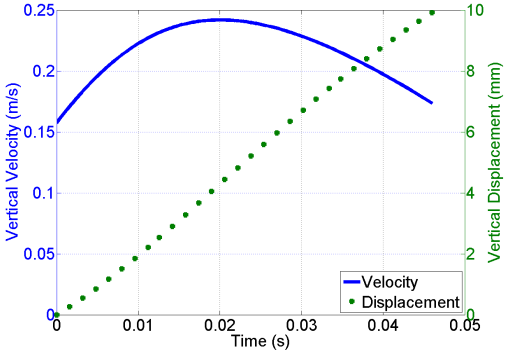


(a) Concentration 1-Temperature 1 (b) Concentration 1-Temperature 2

Figure 8.7: Deterministic model velocity and displacement versus time at concentration 1

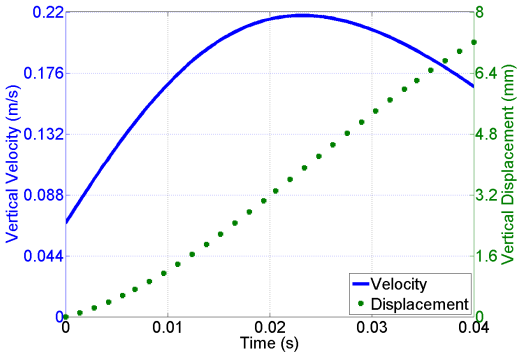


(a) Concentration 2-Temperature 1

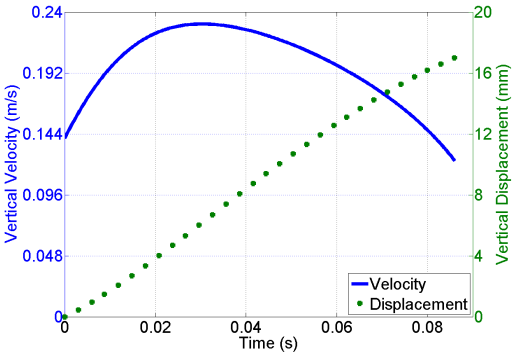


(b) Concentration 2-Temperature 2

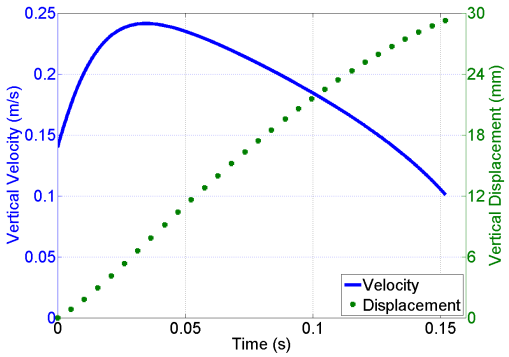
Figure 8.8: Deterministic model velocity and displacement versus time at concentration 2



(a) Concentration 3-Temperature 1



(b) Concentration 3-Temperature 2



(c) Concentration 3-Temperature 3

Figure 8.9: Deterministic model velocity and displacement versus time at concentration 3

8.3.2 Deterministic Analysis of Bubble Motion

The primary forces acting upon the bubble are the drag, virtual mass, history and buoyancy forces. As the bubble weight force has been termed negligible in section 8.2.2, equation 8.13 may be rewritten as follows:

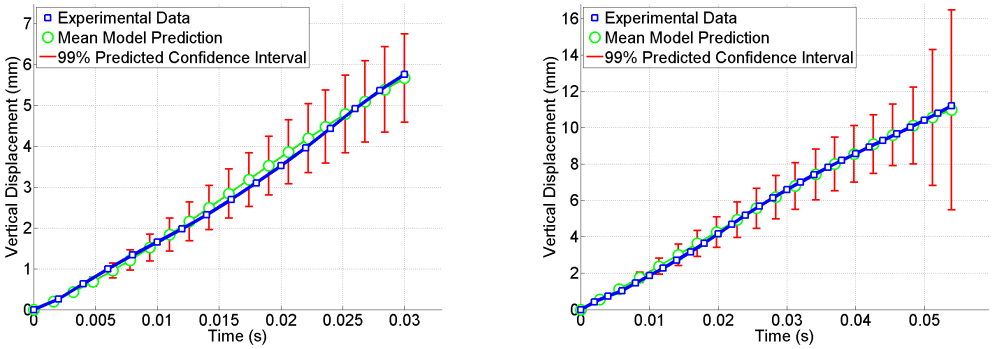
$$\rho_v C_{vm} V \left[\frac{du}{dt}\right] = \rho_L V g - \frac{1}{2} C_D \rho_L A_p u^2 - \rho_L C^*_{vm} C_{vm} \frac{dV}{dt} u - 6 C_H a \sqrt{\pi \rho_L \mu_L} \int_{-\infty}^{t} \sqrt{\frac{a^2}{t-\tau}} \frac{du}{d\tau} d\tau \tag{8.31}$$

In this new arrangement, the term $\rho_L C_{vm} V$ may be interpreted as the effective mass of the bubble. Therefore, while the buoyancy, drag and history forces remain unchanged, in this section the term 'added mass force' shall be used to describe the portion of the virtual mass expression (equation 8.30) which results from the changing bubble morphology as defined in equation 8.32.

$$F_{am} := -\rho_L C^*_{vm} C_{vm} \frac{\partial V}{\partial t} u \tag{8.32}$$

Figure 8.6 shows a comparison between the different forces acting upon the bubble at the setting Concentration 1 – Temperature 2. It is evident that the added mass force (as defined in equation 8.32) has a significant effect upon the motion of the bubble. This force acts vertically upwards due to the shedding of entrained liquid from the bubble's surface as its size decreases. While the buoyancy force initiates the motion, this added mass force rapidly exceeds it in magnitude and becomes the dominant force causing vertical translation. In direct contrast, the history force is demonstrated to have negligible effect upon the displacement of the bubble. As expected, the magnitudes of the buoyancy, drag and added mass forces decay with time as bubble volume decreases.

Figures 8.7 to 8.9 display the deterministic velocity and displacement model predictions for all three concentration settings (i.e.: equation 8.15 is solved using only the deterministic components of the bubble semi-major axis and aspect ratio). Tracking of the experimental bubbles using the high speed camera begins once the bubbles have fully detached from the sparger pipe. Thus, these bubbles have a finite initial velocity. The average initial velocities of all of the bubbles at any setting are used as the initial conditions when solving equation 8.15. In Figures 8.7 to 8.9 it may be observed that the bubble's velocity initially increases



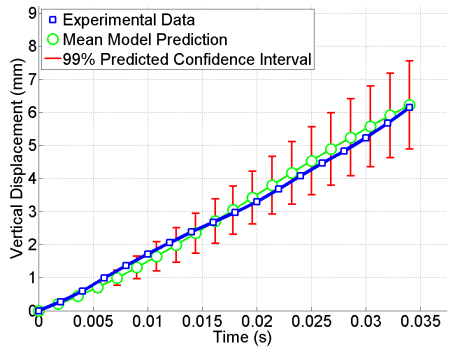
(a) Concentration 1-Temperature 1 (b) Concentration 1-Temperature 2

Figure 8.10: Experimental and Modelled Displacement versus time at concentration 1

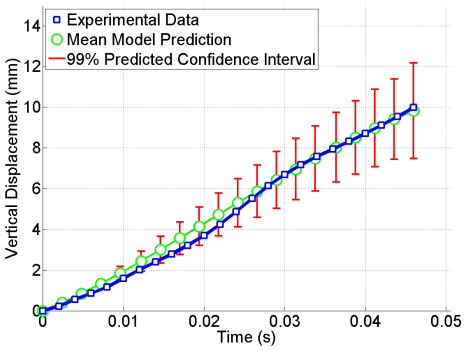
under the action of the buoyancy and added mass forces in an attempt to reach its terminal velocity. The terminal velocity of a bubble at a constant volume at any moment in time is given by equation 8.33 (the history force has been neglected here as it has been demonstrated have a negligible contribution).

$$u_{a,\rho}^{terminal} = \sqrt{\frac{8a\rho g}{3C_D}} \tag{8.33}$$

As discussed in section 8.3.1, both the bubble's semi-major axis and its aspect ratio decrease with time. Thus while the bubble is constantly trying to reach its terminal velocity, this terminal velocity is itself decreasing with time. This results in the steadily decreasing bubble velocities illustrated in Figures 8.7 to 8.9. In general a maximum velocity of between 0.21m/s and 0.24m/s is achieved by the bubbles prior to entering this deceleration phase. The nature of this constantly changing velocity does not impact significantly upon the displacement pattern, which remains almost perfectly linear. As expected, bubbles with slower collapse rates (i.e.: at higher temperature levels) have longer residence times, and hence also significantly larger vertical displacements. In Figure 8.9 it is evident that the difference between selecting a temperature level of one (Figure 8.9a) and a temperature level of three (Figure 8.9c) can result in a fourfold difference in final vertical displacement and hence a fourfold difference in the required absorber height.

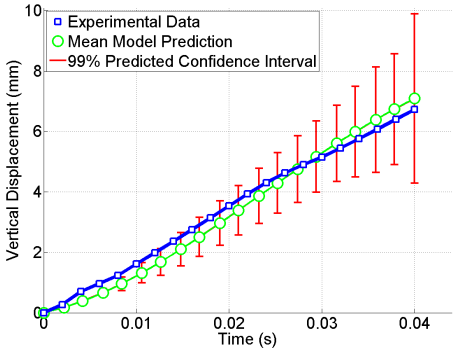


(a) Concentration 2-Temperature 1

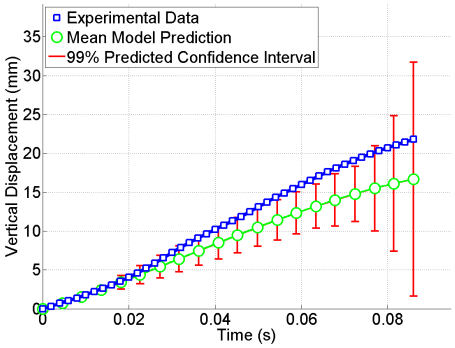


(b) Concentration 2-Temperature 2

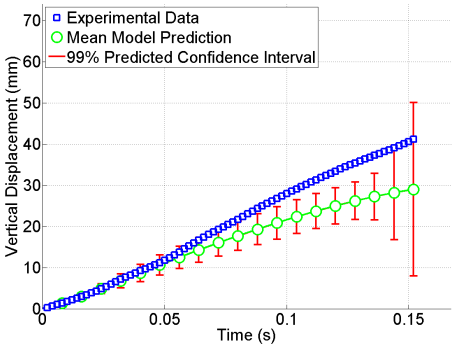
Figure 8.11: Experimental and Modelled Displacement versus time at concentration 2



(a) Concentration 3-Temperature 1



(b) Concentration 3-Temperature 2



(c) Concentration 3-Temperature 3

Figure 8.12: Experimental and Modelled Displacement versus time at concentration 3

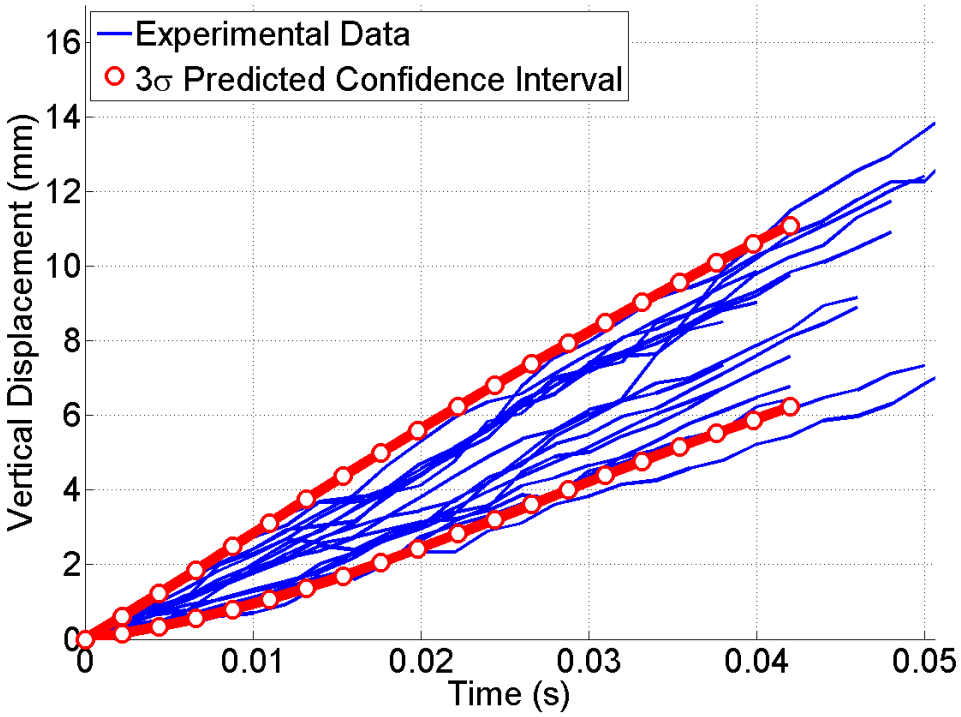
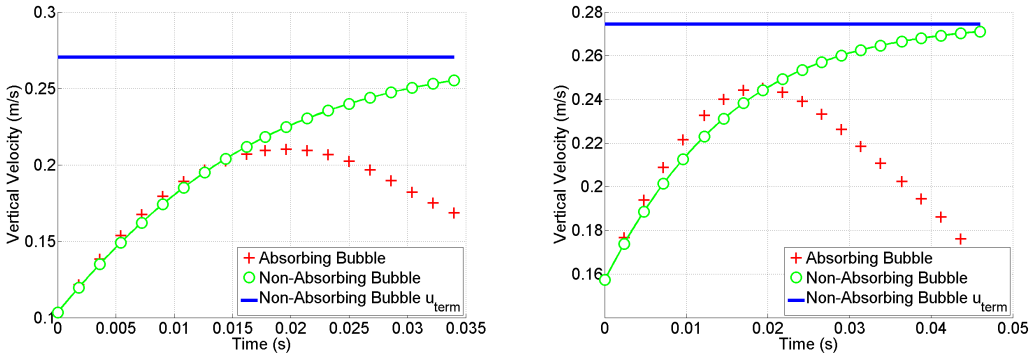


Figure 8.13: Experimentally observed vertical displacements versus confidence intervals predicted by the model at Concentration 1- Temperature 2

8.3.3 Probabilistic Analysis of Bubble Motion

The Monte Carlo model is used to generate random realizations of the evolution of bubble shape and size with time and these are then used in the bubble motion model (equation 8.15). The model is firstly used to predict the mean displacement observed in the experimental data for each concentration and temperature setting and then dispersion in displacement is examined. The results emanating from the probabilistic displacement model are plotted in Figures 8.10 to 8.12. These graphs have been generated by combining the results of the 2000 random simulations described in section 8.2.4. It is evident that the agreement between the modelled and experimental data is quite good. The mean displacements predicted in Figures 8.10, 8.11 and 8.12a almost perfectly match the averaged experimental data for those respective settings. The model slightly under-predicts the vertical displacement in Figures 8.12b and 8.12c. This under-prediction is attributed to the empirical factor C^*_{vm}, which was introduced in order to counteract the effect of the extremely rapid bubble collapse. The collapse rates at these two settings are significantly lower however (Table 8.3), and therefore this factor becomes less applicable.



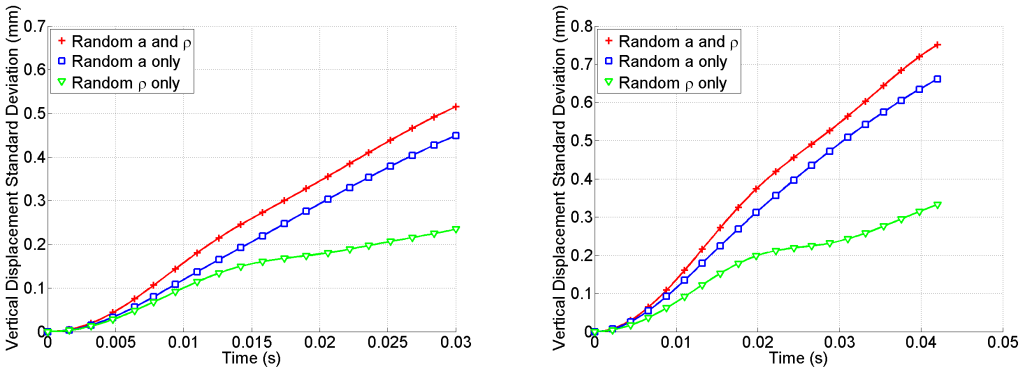
(a) Concentration 2-Temperature 1 (b) Concentration 2-Temperature 2

Figure 8.14: Comparison between absorbing and non-absorbing bubble vertical velocities at Concentration 2

Experimentally it is noted that there is a large degree of variability in the motion of the bubbles as they move up the column. Figure 8.13 demonstrates the use of the probabilistic model to predict potential dispersion in vertical displacement. This figure shows the data from individually tracked bubbles at concentration 1-temperature 2, as well as the confidence interval predicted by the stochastic model corresponding to three standard deviations. From these results it is clear that the model does in general predict an appropriate degree of uncertainty. Dispersion in the final experimental vertical displacement of up to 100% may be seen in Figure 8.13 (∼7mm - ∼14mm) highlighting the inherent uncertainty associated with this variable.

8.3.4 Comparison with Non-Condensing Bubbles

In section 8.3.2 the influence of the bubble collapse upon the vertical velocity of the bubble was briefly discussed. It was demonstrated that this velocity tends to a maximum of approximately 0.21m/s to 0.25m/s before the bubble begins to decelerate. In this section, the behaviour of these steam bubbles shall be compared with the behaviour of identical bubbles which retain both their initial aspect ratios and semi-major axes throughout their life-span (i.e.: they do not collapse). In Figure 8.14 it may be seen that the vertical velocity of the absorbing bubble is essentially the same as that of the non-absorbing bubble up to this point of maxima. After this the velocity of the constant-volume bubble continues to increase asymptotically to its terminal velocity while the velocity of the absorbing bubble decreases rapidly.



(a) Concentration 2-Temperature 1 (b) Concentration 2-Temperature 2

Figure 8.15: Comparison between the vertical displacement standard deviations under different conditions of either probabilistic or deterministic semi-major axes and aspect ratios at Concentration 2

8.3.5 Parameter impact upon Variability

It has been demonstrated in section 8.3.3 that much variability is associated with the vertical displacement of the steam bubbles. Both the bubble semi-major axis and its aspect ratio are being treated as variables which have a random component associated with them. The aim of this section is to determine whether unpredictability in the bubble size or its shape has a greater impact upon the random behaviour of the vertical displacement. This is achieved by examining the unpredictability of the vertical displacement when only the semi-major axis has an associated random component, and then subsequently conducting the same analysis using only a random aspect ratio.

Figure 8.15 shows clearly that the variability associated with the bubble semi-major axis is significantly more influential than that of the aspect ratio. The vertical displacement standard deviation predicted at the end of the bubble's collapse when the semi-major axis has a random component is almost twice as large as that predicted when the aspect ratio is considered random. Another important finding from this sensitivity study is that the standard deviations associated with the random behaviour of the semi-major axis and the aspect ratio are not additive. In Figure 8.15 the vertical displacement standard deviation associated with semi-major axis fluctuations is only marginally smaller than the total standard deviation predicted when both the semi-major axis and the aspect ratio have random components. This leads to the conclusion that controlling the bubble size is more important than morphology in order to minimise dispersion.

8.4 Conclusions

The results presented in this chapter indicate the ability of a standard ordinary differential equation model to predict the vertical displacement of a bubble which is collapsing under the action of both heat and mass transfer. The added mass force acting upon the bubble has been demonstrated to be of pivotal importance in such a model, as it is the dominant force causing vertical translation. The extremely rapid collapse rate encountered in this study meant that an empirical factor needed to be introduced in order to dampen the effect of this added mass force. Selecting the correct solution temperature level has been demonstrated to have the potential to cause up to fourfold reductions in the final mean bubble vertical displacement (and hence absorber height), hence reiterating the importance of this variable as identified in the previous chapter. The vertical displacement dispersion observed in the experimental data, and predicted by the model, indicates that the accurate prediction of bubble residence time is extremely difficult however. Variability of up to 100% has been highlighted at a particular experimental setting, which would have a significant impact upon the design and operation of such a unit. The majority of this dispersion is due to uncertainty in the bubble size, while only marginally amplified by fluctuations in the bubble morphology. It should also be noted that this unpredictable behaviour has been demonstrated in this chapter using single steam bubbles collapsing in a concentrated $LiBr - H_2O$ solution. In reality however, this collapse would generally occur in a fully functioning bubble column in which interactive effects may begin to dominate, further amplifying this uncertainty.

Part III

Discussion and Conclusions

Chapter 9

General Conclusions

Heat transformers are a potentially attractive technology to upgrade intermediate waste heat to more useful high temperature energy. Triple absorption heat transformers (TAHT) are capable of increasing the temperature of approximately 20-25% of supplied waste heat energy by up to ∼145 °C. Heretofore no comprehensive studies have been conducted on these systems however, and thus this was a motivation for the present work which has attempted to further the state of the art of this technology.

In Chapter 3, the relative influence of all the different TAHT system inputs (manipulated variables) and their interactive effects were quantified for each of the main system outputs (dependent variables) using a full factorial analysis, in order to identify general operating points of optima. It was demonstrated that the primary influences on the COP, ECOP and E_D (exergy destruction rate within the cycle) are the pinch heat transfer temperature gradient maintained in heat transfer unit operations and the temperature of the condenser. In turn, the flow ratio (FR) is primarily affected by the condenser's temperature and the temperature of absorber-evaporator-1. These results give a very clear indication that the condenser's temperature is the most important variable during the design phase from a thermodynamic perspective, followed by the pinch heat transfer temperature gradient and the temperature of absorber-evaporator-1. It was demonstrated that the pinch heat transfer gradient should be maintained as small as possible in all heat exchanger equipment, as should the temperature of the absorber. The temperature of the absorber is however not as influential as initially expected, as it is only the 5th most influential effect for two dependent variables, 6th for another, and deemed insignificant with respect to the remaining system output, although most previous studies for single and double stage systems have focussed heavily upon this factor. Due to the inevitable connection between the temperature of the evaporator and the total gross temperature lift which must be achieved by the system, the evaporator temperature should be maximised in any TAHT. In contrast, the temperature of the condenser should be maintained at as low a temperature as thermodynamically possible, and it is demonstrated to be involved in every interactive effect between manipulated variables deemed statistically significant. The temperatures of both the absorber-evaporators have distinct points of optima which are always located approximately half way between the highest and the lowest temperatures which these units may take in the system.

Together, the generator and the two absorber-evaporators account for over 60% of the total exergy destruction in a TAHT, while the generator represents the largest single source of irreversibility at approximately 23%. In order to reduce exergy

losses due to temperature gradients, heat exchange network modelling techniques are used in Chapter 4 to examine various heat recovery options within the cycle, and to present configurations which minimise the temperature differences between streams entering and leaving each unit operation. It is demonstrated that it is most important to preheat the concentrated solution entering the absorber, while the concentrated salt solution entering absorber-evaporator-2 has the second largest influence. A full factorial analysis was conducted which analysed the different possible combinations of internal heat exchangers in order to identify the best internal heat recovery cycle configurations. It was demonstrated that reducing the number of internal solution heat exchangers to two would only decrease the COP of the system by 2.3% and increase the exergy destruction (its irreversibility) by 4.8% compared to the standard TAHT design (as outlined in Chapter 1) at typical operating conditions. In contrast, using one of the heat exchangers to preheat the water stream being evaporated in absorber-evaporator-2 (instead of the salt solution entering absorber-evaporator-1) allowed the COP to be increased by 11.7% while the exergy destruction within the system was reduced by 21%. Strategically adding fourth and fifth heat exchangers increased the COP by 16.4% and 18.8% while decreasing exergy destruction by 28% and 31.5% respectively compared to the conventional TAHT design. The effects of varying the evaporator and generator or else the absorber temperatures upon these results were analysed, and it was demonstrated that these results hold in all cases at low evaporation temperatures or GTL values greater than $\sim$115 °C. This allows for the development of a simple algebraic expression which may be used as a guide indicating under what conditions the advantages of using the alternate configurations presented may be realised.

All of the thermodynamic optimisations outlined in Chapters 3 and 4 are attempts to increase the quantity of heat energy being recycled so that the triple stage absorption heat transformer (TAHT) may represent an attractive investment opportunity in industry. Thus following these optimisations, a case study is conducted in Chapter 5 which examines the installation of a potential heat transformer in the Phillips 66 Whitegate oil refining plant in Ireland. It is demonstrated that while the designed unit is capable of recycling 14% of all the waste heat energy currently being discharged to atmosphere from the two waste streams selected for this study, the economic performance of the system is not predicted to be sufficiently attractive to merit investment under current conditions, particularly with respect to international energy prices. It is identified that the physical properties of the waste heat streams have a significant impact upon the success or

failure of the TAHT, due to the heat transfer coefficients which may be obtained by these waste heat streams in both the evaporator and generator. It is shown that ideally, the waste heat source should be undergoing a latent heat change (condensation) and have a high density, specific heat capacity and thermal conductivity while maintaining a low viscosity. Using the two streams selected in this study, a simple payback period of approximately elven years is predicted at the current gas price, while the chances of a positive net present value at the end of the TAHT's useful lifetime is very low. However it is shown that if the mass flowrate of streams with favourable physical properties (such as condensing streams) available to the system were increased, that the economic performance of the TAHT also increases rapidly. Thus this is a strong indicator that triple stage heat transformers are highly influenced by scale, and that they are most suited to large energy intensive operations.

A rise in the price of energy is demonstrated to have a significant impact upon the system's economic performance. A reduction in gas prices from the current rates would mean that the TAHT would not be suitable for investment under any tested scenario. If the higher gas prices experienced in 2008 were realised once more however ($\sim$3 times the current gas price), then the model indicates that the TAHT has a 92% chance of a simple payback period (SPBP) of five years or less, compared to the 90% chance of a SPBP of 15 years or less at the current gas price. The reason that unattractive economic returns are predicted for the TAHT is the high capital cost of its equipment. The heat transformer in this case study consists primarily of shell and tube heat exchangers as this is the preferred equipment type in the oil refining industry. It is demonstrated however that if the previously reported benefits of utilising plate heat exchangers instead of such shell and tube units (Genssle and Stephan, 2000) were realised, then this would make the installation of a triple absorption heat transformer a viable option even at the current gas price, with a $\sim$90% chance of a simple payback period of five years or less predicted.

Using bubble column absorbers may be an efficient method of partially reducing this capital cost of equipment and also increasing the thermodynamic efficiency of the system. A bubble column was constructed and tested in order to examine the absorption of steam bubbles in a hotter $LiBr - H_2O$ solution, using a high speed camera to track the bubble collapse (Chapters 6 and 7). A simple ordinary differential model was generated, capable of predicting over 96% of the observed experimental variance. Large oscillations in bubble morphology were observed in the collected video data, leading to very high heat and mass transfer

coefficients of approximately 40,500W/(m^{2}K) and 0.0012m/s respectively. These figures are significantly higher than values previously reported in the literature. Conventional vertical falling film absorbers using LiBr − H_2O have achieved heat and mass transfer coefficients of 570W/(m^{2}K) and 3.15×10^{-5}m/s respectively (Medrano et al., 2002), while adiabatic absorbers have been shown to achieve mass transfer coefficients of $\sim7\times10^{-4}$m/s (Palacios et al., 2009).

Parametric studies were conducted using the developed model, examining several factors which potentially influence the rate of absorption. The concentration of the LiBr − H_2O solution is found to have a negligible effect upon the absorption time of a bubble, and thus it may be concluded that the results achieved in this study are almost equally applicable for all three absorbers in a TAHT, or in the absorber of any heat transformer or heat pump. The difference between the solution's temperature and its boiling temperature is identified as a pivotal factor in determining the absorption rate however. It is demonstrated that the absorption time increases exponentially with a decrease in this gradient. Therefore it is recommended that a difference of $\sim8\,^{\circ}$C is maintained between these two temperatures. The small presence of air in the experimental bubbles (~0.001m^3/m^3) had a significant effect upon the heat and mass transfer capabilities of the bubble during the absorption. Results showed that for a particular concentration and temperature, there exists a unique water volumetric fraction in the bubble, which is independent of the initial air content and may be as high as 0.88m^3/m^3, at which absorption effectively ceases. As heat transformers using LiBr − H_2O operate partially at sub-atmospheric pressures, it is likely that small residues of air may remain within the cycle, despite all efforts. Thus this unique final absorption mass fraction of water can be used as a design parameter after which it may be assumed that absorption has been completed.

A standard ordinary differential equation model was developed to predict the vertical displacement of such collapsing steam bubbles, approximating these as oblate spheriods. Probabilistic methods were used to include the random effects associated with the bubbles' semi-major axes and aspect ratios into this model, enabling an estimation of the predicted dispersion in final residence times and vertical displacements. The added mass force acting upon the bubbles was demonstrated to be the dominant force causing vertical translation, while the history force was negligible. The previously discussed importance of selecting the correct LiBr − H_2O solution temperature was reiterated once more in this analysis, as appropriately selecting this parameter was demonstrated to have the potential to cause up to fourfold reductions in the final mean bubble vertical displacement

(and hence absorber height). The vertical displacement dispersion observed in the experimental data, and as predicted by the model, indicates that the accurate prediction of bubble residence time is extremely difficult however. Variability of up to 100% was highlighted at a particular experimental setting, which would have a significant impact upon the design and operation of such a unit. The majority of this dispersion is due to uncertainty in the bubble size, while only marginally amplified by fluctuations in the bubble morphology. It should also be noted that this unpredictable behaviour has been demonstrated in this chapter using single steam bubbles collapsing in a concentrated $LiBr - H_2O$ solution. In reality however, this collapse would generally occur in a fully functioning bubble column in which interactive effects may begin to dominate, further amplifying this uncertainty.

Throughout this thesis it has been demonstrated that while triple absorption heat transformers have many thermodynamic benefits and may be used to great advantage in order to recycle waste heat energy, their current economic performance prevents them from becoming a widely-used commodity in industry. Several factors have been identified which may contribute to increasing their attractiveness, however the most fundamental of these is the price of energy. The return of natural gas prices to 2008/2009 levels would completely alter the economic outlook of heat transformers, potentially making them an very attractive investment option for companies. Reducing the capital cost of the cycle's components is also a significant factor and represents the only generally applicable solution which may be controlled by the designer. Future work in the area of heat transformers is for this reason advised to focus upon the use of more efficient unit operations and equipment designs which allow the same thermodynamic performance to be achieved but which are smaller in size, and hence lower in cost. This thesis has shown that the design of the most pivotal unit in the cycle, the absorber, may be potentially improved by using bubble columns. This research should be continued by conducting experimental tests using columns with interacting bubbles and different flow regimes, as these are the conditions likely to be encountered in reality in a full scale absorber. However even a relatively small change such as the replacement of shell and tube units with plate heat exchangers may enable triple absorption heat transformers to become a valuable asset for any company wishing to increase energy efficiency, and hence their financial bottom line, in the future.

References

Abrahamsson, K., Gidner, A., Jernqvist, Ã., 1995. Design and experimental performance evaluation of an absorption heat transformer with self-circulation. Heat Recovery Systems and CHP 15, 257–272.

Abrahamsson, K., Stenström, S., Aly, G., Jernqvist, Ã., 1997. Application of heat pump systems for energy conservation in paper drying. International Journal of Energy Research 21, 631–642.

Andberg, J.W., Vliet, G.C., 1983. Design Guidelines For Water-Lithium Bromide Absorbers. ASHRAE Transactions 89, 220–232.

Aristov, Y.I., 2012. Adsorptive transformation of heat: Principles of construction of adsorbents database. Applied Thermal Engineering 42, 18 – 24. Heat Powered Cycles Conference, 2009.

Arzoz, D., Rodriguez, P., Izquierdo, M., 2005. Experimental study on the adiabatic absorption of water vapor into LiBr-H2O solutions. Applied Thermal Engineering 25, 797 – 811.

Azbel, D., Kemp-Pritchard, P., 1981. Two-phase Flows in Chemical Engineering. Cambridge University Press.

Barragán, R.M., Arellano, V.M., Heard, C.L., Best, R., 1998. Experimental performance of ternary solutions in an absorption heat transformer. International Journal of Energy Research 22, 73–83.

Barragán, R.M., Arellano, V.M., Heard, C.L., Best, R., Holland, F.A., 1997. Experimental Performance of the System Water/Magnesium Chloride in a Heat Transformer. International Journal of Energy Research 21, 139–151.

Barragán, R.M., Heard, C.L., Arellano, V.M., Best, R., Holland, F.A., 1996. Experimental performance of the water/calcium chloride system in a heat transformer. International Journal of Energy Research 20, 651–661.

Barragán R., R.M., Arellano G., V.M., Heard, C.L., 1998. Performance study of a double-absorption water/calcium chloride heat transformer. International Journal of Energy Research 22, 791–803.

Best, R., Rivera, W., Cardoso, M., Romero, R., Holland, F., 1997. Modelling of single-stage and advanced absorption heat transformers operating with the water/carrol mixture. Applied Thermal Engineering 17, 1111 – 1122.

Bourouisa, M., Coronas, A., Romero, R., Siqueiros, J., 2004. Purification of seawater using absorption heat transformers with water-(LiBr+LiI+LiNO3+LiCl) and low temperature heat sources. Desalination 166, 209 – 214. Desalination Strategies in South Mediterranean Countries.

Cabin, R., Mitchell, R., 2000. To Bonferroni or not to Bonferroni: when and how are the questions. Bulletin of the Ecological Society of America 81, 246–248.

Campos, F., Lage, P., 2000a. Heat and mass transfer modeling during the formation and ascension of superheated bubbles. International Journal of Heat and Mass Transfer 43, 2883 – 2894.

Campos, F., Lage, P., 2000b. Simultaneous heat and mass transfer during the ascension of superheated bubbles. International Journal of Heat and Mass Transfer 43, 179 – 189.

Castro, J., Oliet, C., Rodríguez, I., Oliva, A., 2009. Comparison of the performance of falling film and bubble absorbers for air-cooled absorption systems. International Journal of Thermal Sciences 48, 1355–1366.

Cavallini, A., Del Col, D., Doretti, L., Matkovic, M., Rossetto, L., Zilio, C., Censi, G., 2006. Condensation in horizontal smooth tubes: A new heat transfer model for heat exchanger design. Heat Transfer Engineering 27, 31–38.

Chen, J., 1995. Optimal choice of the performance parameters of an absorption heat transformer. Heat Recovery Systems and CHP 15, 249 – 256.

Chen, J., 1997a. Equivalent combined cycle of an endoreversible absorption heat transformer and optimal analysis of primary performance parameters. Energy Conversion and Management 38, 705 – 712.

Chen, J., 1997b. Thermodynamic analysis of the performance of a solar absorption heat transformer at maximum coefficient of performance. International Journal of Energy Research 21, 975–984.

Chen, J., 1998. The coefficient of performance of a multi-temperature-level ab-

sorption heat transformer at maximum specific heating load. Journal of Physics D: Applied Physics 31, 3316.

Chuang, C.C., Sue, D.C., Lin, Y.T., 2004. Simulation and Performance Analysis of Lithium Bromide/Water for Absorption Heat Transformer Cycle Systems. ASHRAE Transactions 110, 409 – 416.

Clift, R., Grace, J., Weber, M., 1978. Bubbles, Drops, and Particles. Academic Press.

Colorado, D., Hernández, J., Hamzaoui, Y.E., Bassam, A., Siqueiros, J., Andaverde, J., 2011a. Error propagation on COP prediction by artificial neural network in a water purification system integrated to an absorption heat transformer. Renewable Energy 36, 1315 – 1322.

Colorado, D., Hernández, J., Rivera, W., Martínez, H., Juárez, D., 2011b. Optimal operation conditions for a single-stage heat transformer by means of an artificial neural network inverse. Applied Energy 88, 1281 – 1290.

Cortés, E., Rivera, W., 2010. Exergetic and exergoeconomic optimization of a cogeneration pulp and paper mill plant including the use of a heat transformer. Energy 35, 1289–1299.

Costa, A., Bakhtiari, B., Schuster, S., Paris, J., 2009. Integration of absorption heat pumps in a Kraft pulp process for enhanced energy efficiency. Energy 34, 254–260.

Şencan, A., Önder Kızılkan, Ç. Bezir, N., Kalogirou, S.A., 2007. Different methods for modeling absorption heat transformer powered by solar pond. Energy Conversion and Management 48, 724 – 735.

Darmana, D., Deen, N., Kuipers, J., 2005. Detailed modeling of hydrodynamics, mass transfer and chemical reactions in a bubble column using a discrete bubble model. Chemical Engineering Science 60, 3383 – 3404.

Dijkhuizen, W., van Sint Annaland, M., Kuipers, J., 2010. Numerical and experimental investigation of the lift force on single bubbles. Chemical Engineering Science 65, 1274 – 1287.

DIPPR, 2012. DIPPR Project 801 - Full Version. Design Institute for Physical Properties, Sponsored by AIChE.

Dong, F., 1993. On the identification of active contrasts in unreplicated fractional factorials. Statistica Sinica 3, 209–217.

Ekambara, K., Dhotre, M., 2010. CFD simulation of bubble column. Nuclear Engineering and Design 240, 963 – 969.

Escobar, R., Juárez, D., Siqueiros, J., Irles, C., Hernández, J., 2008. On-line COP estimation for waste energy recovery heat transformer by water purification process. Desalination 222, 666 – 672. European Desalination Society and Center for Research and Technology Hellas (CERTH), Sani Resort 22-25 April 2007, Halkidiki, Greece European Desalination Society and Center for Research and Technology Hellas (CERTH), Sani Resort.

Escobar, R., Uruchurtu, J., Juárez, D., Siqueiros, J., Hernández, J., 2009. On-line indirect measures estimation for the performance of an absorption heat transformer integrated to a water purification process. Measurement 42, 464 – 473.

Fartaj, S.A., 2004. Comparison of energy, exergy, and entropy balance methods for analysing double-stage absorption heat transformer cycles. International Journal of Energy Research 28, 1219–1230.

Florides, G., Kalogirou, S., Tassou, S., Wrobel, L., 2003. Design and construction of a LiBr-water absorption machine. Energy Conversion and Management 44, 2483 – 2508.

Genssle, A., Stephan, K., 2000. Analysis of the process characteristics of an absorption heat transformer with compact heat exchangers and the mixture TFE-E181. International Journal of Thermal Sciences 39, 30–38.

Ghajar, A.J., Tam, L.M., 1994. Heat transfer measurements and correlations in the transition region for a circular tube with three different inlet configurations. Experimental Thermal and Fluid Science 8, 79 – 90.

Göktun, S., Er, I.D., 2002. Performance analysis of an irreversible cascaded heat-transformer. Applied Energy 72, 529 – 539.

Gomri, R., 2009. Energy and exergy analyses of seawater desalination system integrated in a solar heat transformer. Desalination 249, 188 – 196.

Gomri, R., 2010. Thermal seawater desalination: Possibilities of using single effect and double effect absorption heat transformer systems. Desalination 253, 112 – 118.

Gränfors, A., Nilsson, B., Jernqvist, A., Aly, G., 1997. Dynamic simulation of an absorption heat transformer incorporated with an evaporation plant. Com-

puters & Chemical Engineering 21, Supplement, S715 – S720. Supplement to Computers and Chemical Engineering 6th International Symposium on Process Systems Engineering and 30th European Symposium on Computer Aided Process Engineering.

Guo, P., Sui, J., Han, W., Zheng, J., Jin, H., 2012. Energy and exergy analyses on the off-design performance of an absorption heat transformer. Applied Thermal Engineering 48, 506 – 514.

Hahn, T.A., 1970. Thermal Expansion of Copper from 20 to 800 K - Standard Reference Material 736. Journal of Applied Physics 41, 5096–5101.

Hendricks, T., Choate, W.T., 2006. Engineering Scoping Study of Thermoelectric Generator Systems for Industrial Waste Heat Recovery. Technical Report. Pacific Northwest National Laboratory (PNNL) and BCS, supported by the U.S. Department of Energy Office of Energy Efficiency and Renewable Energy, Industrial Technologies Program (ITP).

Hernández, J., Bassam, A., Siqueiros, J., Juárez-Romero, D., 2009a. Optimum operating conditions for a water purification process integrated to a heat transformer with energy recycling using neural network inverse. Renewable Energy 34, 1084 – 1091.

Hernández, J., Juárez-Romero, D., Morales, L., Siqueiros, J., 2008. COP prediction for the integration of a water purification process in a heat transformer: with and without energy recycling. Desalination 219, 66 – 80.

Hernández, J., Romero, R., Juárez, D., Escobar, R., Siqueiros, J., 2009b. A neural network approach and thermodynamic model of waste energy recovery in a heat transformer in a water purification process. Desalination 243, 273 – 285.

Hölzer, A., Sommerfeld, M., 2008. New simple correlation formula for the drag coefficient of non-spherical particles. Powder Technology 184, 361 – 365.

Horuz, I., Kurt, B., 2009. Single stage and double absorption heat transformers in an industrial application. International Journal of Energy Research 33, 787–798.

Horuz, I., Kurt, B., 2010. Absorption heat transformers and an industrial application. Renewable Energy 35, 2175 – 2181.

Huicochea, A., Rivera, W., Martínez, H., Siqueiros, J., Cadenas, E., 2013a.

Analysis of the behavior of an experimental absorption heat transformer for water purification for different mass flux rates in the generator. Applied Thermal Engineering 52, 38 – 45.

Huicochea, A., Romero, R., Rivera, W., Gutierrez-Urueta, G., Siqueiros, J., Pilatowsky, I., 2013b. A novel cogeneration system: A proton exchange membrane fuel cell coupled to a heat transformer. Applied Thermal Engineering 50, 1530 – 1535.

Huicochea, A., Siqueiros, J., 2010. Improved efficiency of energy use of a heat transformer using a water purification system. Desalination 257, 8 – 15.

Huicochea, A., Siqueiros, J., Romero, R.J., 2004. Portable water purification system integrated to a heat transformer. Desalination 165, 385–391.

Ibarra-Bahena, J., Romero, R., Velazquez-Avelar, L., Valdez-Morales, C., Galindo-Luna, Y., 2013. Evaluation of the thermodynamic effectiveness of a plate heat exchanger integrated into an experimental single stage heat transformer operating with Water/Carrol mixture. Experimental Thermal and Fluid Science 51, 257 – 263.

Ishida, M., Ji, J., 1999. Graphical exergy study on single stage absorption heat transformer. Applied Thermal Engineering 19, 1191–1206.

Ishida, M., Ji, J., 2000. Proposal of humid air turbine cycle incorporated with absorption heat transformer. International Journal of Energy Research 24, 977–987.

Islam, M.R., Wijeysundera, N., Ho, J., 2004. Simplified models for coupled heat and mass transfer in falling-film absorbers. International Journal of Heat and Mass Transfer 47, 395 – 406.

Ismail, I., 1995. Upgrading of heat through absorption heat transformers. International Journal of Refrigeration 18, 439 – 446.

Ji, J., Ishida, M., 1999. Behavior of a two-stage absorption heat transformer combining latent and sensible heat exchange modes. Applied Energy 62, 267–281.

Johnson, I., Choate, W.T., 2008. Waste Heat Recovery: Technologies and Opportunities in the U.S. Industry. Technical Report. BCS Incorporated supported by the U.S. Department of Energy Industrial Technologies Program.

Jouhara, H., Ajji, Z., Koudsi, Y., Ezzuddin, H., Mousa, N., 2013. Experimental

investigation of an inclined-condenser wickless heat pipe charged with water and an ethanol-water azeotropic mixture. Energy 61, 139 – 147.

Jouhara, H., Ezzuddin, H., 2013. Thermal performance characteristics of a wraparound loop heat pipe (WLHP) charged with R134A. Energy 61, 128 – 138.

Kang, Y.T., Nagano, T., Kashiwagi, T., 2002. Visualization of bubble behavior and bubble diameter correlation for NH3-H2O bubble absorption. International Journal of Refrigeration 25, 127 – 135.

Krishna, R., van Baten, J., 2003. Mass transfer in bubble columns. Catalysis Today 79-80, 67 – 75.

Kurem, E., Horuz, I., 2001. A comparison between ammonia-water and water-lithium bromide solutions in absorption heat transformers. International Communications in Heat and Mass Transfer 28, 427 – 438.

Lau, R., Lee, P.H.V., Chen, T., 2012. Mass transfer studies in shallow bubble column reactors. Chemical Engineering and Processing: Process Intensification 62, 18 – 25.

Lee, J.C., Lee, K.B., Chun, B.H., Lee, C.H., Ha, J.J., Kim, S.H., 2003. A study on numerical simulations and experiments for mass transfer in bubble mode absorber of ammonia and water. International Journal of Refrigeration 26, 551 – 558.

Lee, S.F., Sherif, S.A., 2000. Second law analysis of multi-stage lithium bromide/water absorption heat transformers. ASHRAE Transactions 106.

Lobo, V., 1993. Mutual diffusion coefficients in aqueous electrolyte solutions (technical report). Pure and applied chemistry 65, 2613–2640.

Ma, X., Chen, J., Li, S., Sha, Q., Liang, A., Li, W., Zhang, J., Zheng, G., Feng, Z., 2003. Application of absorption heat transformer to recover waste heat from a synthetic rubber plant. Applied Thermal Engineering 23, 797–806.

Magnaudet, J., Eames, I., 2000. The Motion of High-Reynolds-Number Bubbles in Inhomogeneous Flows. Annual Review of Fluid Mechanics 32, 659–708.

Martínez, H., Rivera, W., 2009. Energy and exergy analysis of a double absorption heat transformer operating with water lithium/bromide. International Journal of Energy Research 33, 662–674.

Medrano, M., Bourouis, M., Coronas, A., 2002. Absorption of water vapour in the falling film of water-lithium bromide inside a vertical tube at air-cooling thermal conditions. International Journal of Thermal Sciences 41, 891 – 898.

Merrill, T., Perez-Blanco, H., 1997. Combined heat and mass transfer during bubble absorption in binary solutions. International Journal of Heat and Mass Transfer 40, 589 – 603.

Meza, M., Márquez-Nolasco, A., Huicochea, A., Juárez-Romero, D., Siqueiros, J., 2014. Experimental study of an absorption heat transformer with heat recycling to the generator. Experimental Thermal and Fluid Science 53, 171 – 178.

Miller, W., Keyhani, M., 2001. The correlation of simultaneous heat and mass transfer experimental data for aqueous lithium bromide vertical falling film absorption. Journal of Solar Energy Engineering, Transactions of the ASME 123, 30–42.

Moore, D., 1965. The velocity of rise of distorted gas bubbles in a liquid of small viscosity. Journal of Fluid Mechanics 23, 749–766.

Mostofizadeh, C., Kulick, C., 1998. Use of a new type of heat transformer in process industry. Applied Thermal Engineering 18, 857 – 874.

NASDAQ Stock Exchange, ., 2014.

Oak Ridge Laboratory, ., 2011. Biomass Energy Handbook. Technical Report. U.S. Depertment of Energy.

Odar, F., Hamilton, W.S., 1964. Forces on a sphere accelerating in a viscous fluid. Journal of Fluid Mechanics 18, 302–314.

Palacios, E., Izquierdo, M., Lizarte, R., Marcos, J., 2009. Lithium bromide absorption machines: Pressure drop and mass transfer in solutions conical sheets. Energy Conversion and Management 50, 1802 – 1809.

Parham, K., Yari, M., Atikol, U., 2013. Alternative absorption heat transformer configurations integrated with water desalination system. Desalination 328, 74 – 82.

Pátek, J., Klomfar, J., 2006. Solid-liquid phase equilibrium in the systems of LiBr-H2O and LiCl-H2O. Fluid Phase Equilibria 250, 138–149.

Qin, X., Chen, L., Sun, F., 2008. Performance of real absorption heat-transformer

with a generalized heat transfer law. Applied Thermal Engineering 28, 767 – 776.

Qin, X., Chen, L., Sun, F., Wu, C., 2004a. An absorption heat-transformer and its optimal performance. Applied Energy 78, 329 – 346.

Qin, X., Chen, L., Sun, F., Wu, C., 2004b. Optimal Performance of an Endoreversible Four-Heat-Reservoir Absorption Heat-Transformer. Open Systems & Information Dynamics 11, 147–159.

Reyes, R.M.B., Gómez, V.M.A., García-Gutiérrez, A., 2010. Performance modelling of single and double absorption heat transformers. Current Applied Physics 10, S244 – S248. The Proceeding of the International Renewable Energy Conference and Exhibition 2008 (RE2008) The Proceeding of the International Renewable Energy Conference and Exhibition 2008 (RE2008).

Rivera, W., 2000. Experimental evaluation of a single-stage heat transformer used to increase solar pond's temperature. Solar Energy 69, 369–376.

Rivera, W., Best, R., Hernández, J., Heard, C., Holland, F., 1994. Thermodynamic study of advanced absorption heat transformers-II. Double absorption configurations. Heat Recovery Systems and CHP 14, 185 – 193.

Rivera, W., Cardoso, M., Romero, R., 2001. Single-stage and advanced absorption heat transformers operating with lithium bromide mixtures used to increase solar pond's temperature. Solar Energy Materials and Solar Cells 70, 321 – 333. Cancun 2000.

Rivera, W., Cerezo, J., 2005. Experimental study of the use of additives in the performance of a single-stage heat transformer operating with water-lithium bromide. International Journal of Energy Research 29, 121–130.

Rivera, W., Cerezo, J., Martínez, H., 2010a. Energy and exergy analysis of an experimental single-stage heat transformer operating with the water/lithium bromide mixture. International Journal of Energy Research 34, 1121–1131.

Rivera, W., Cerezo, J., Rivero, R., Cervantes, J., Best, R., 2003. Single stage and double absorption heat transformers used to recover energy in a distillation column of butane and pentane. International Journal of Energy Research 27, 1279–1292.

Rivera, W., Huicochea, A., Martínez, H., Siqueiros, J., Juárez, D., Cadenas, E.,

2011a. Exergy analysis of an experimental heat transformer for water purification. Energy 36, 320–327.

Rivera, W., Martínez, H., Cerezo, J., Romero, R., Cardoso, M., 2011b. Exergy analysis of an experimental single-stage heat transformer operating with single water/lithium bromide and using additives (1-octanol and 2-ethyl-1-hexanol). Applied Thermal Engineering 31, 3526 – 3532.

Rivera, W., Romero, R., 1998. Thermodynamic design data for absorption heat transformers. Part seven: operating on an aqueous ternary hydroxide. Applied Thermal Engineering 18, 147 – 156.

Rivera, W., Romero, R., 2000. Evaluation of a heat transformer powered by a solar pond. Solar Energy Materials and Solar Cells 63, 413 – 422.

Rivera, W., Romero, R., Best, R., Heard, C., 1999. Experimental evaluation of a single-stage heat transformer operating with the water/Carrol mixture. Energy 24, 317 – 326.

Rivera, W., Romero, R., Cardoso, M., Aguillón, J., Best, R., 2002. Theoretical and experimental comparison of the performance of a single-stage heat transformer operating with water/lithium bromide and water/Carrol. International Journal of Energy Research 26, 747–762.

Rivera, W., Siqueiros, J., Martínez, H., Huicochea, A., 2010b. Exergy analysis of a heat transformer for water purification increasing heat source temperature. Applied Thermal Engineering 30, 2088 – 2095.

Roghair, I., Lau, Y., Deen, N., Slagter, H., Baltussen, M., Annaland, M.V.S., Kuipers, J., 2011. On the drag force of bubbles in bubble swarms at intermediate and high Reynolds numbers. Chemical Engineering Science 66, 3204 – 3211. 10th International Conference on Gas-Liquid and Gas-Liquid-Solid Reactor Engineering.

Romero, R., Rivera, W., Pilatowsky, I., Best, R., 2001. Comparison of the modeling of a solar absorption system for simultaneous cooling and heating operating with an aqueous ternary hydroxide and with water/lithium bromide. Solar Energy Materials and Solar Cells 70, 301 – 308. Cancun 2000.

Romero, R., Siqueiros, J., Huicochea, A., 2007. Increase of COP for heat transformer in water purification systems. Part II - Without increasing heat source temperature. Applied Thermal Engineering 27, 1054 – 1061.

Romero, R.J., Martínez, A.R., Silva, S., Cerezo, J., Rivera, W., 2011. Comparison of double stage heat transformer with double absorption heat transformer operating with Carrol - Water for industrial waste heat recovery. Chemical Engineering Transactions 25, 129–134.

Romero, R.J., Rodríguez-Martínez, A., 2008. Optimal water purification using low grade waste heat in an absorption heat transformer. Desalination 220, 506 – 513. European Desalination Society and Center for Research and Technology Hellas (CERTH), Sani Resort 22-25 April 2007, Halkidiki, Greece European Desalination Society and Center for Research and Technology Hellas (CERTH), Sani Resort.

Romero, R.J., Silva-Sotelo, S., Cerezo, J., 2010. First double stage heat transformer (DSHT) in latinamerica. Chemical Engineering Transactions 19, 149–155.

Rostami, M., Ardeshir, A., Ahmadi, G., Thomas, P.J., 2006. Can the history force be neglected for the motion of particles at high subcritical Reynolds Number range? International Journal of Engineering 19, 23–34.

Scott, M., Jernqvist, Ã., Aly, G., 1999a. Experimental and theoretical study of an open multi-compartment absorption heat transformer for different steam temperatures. Part III: Application to process industry. Applied Thermal Engineering 19, 431–448.

Scott, M., Jernqvist, A., Olsson, J., Aly, G., 1999b. Experimental and theoretical study of an open multi-compartment absorption heat transformer for different steam temperatures. Part I: hydrodynamic and heat transfer characteristics. Applied Thermal Engineering 19, 279 – 298.

Scott, M., Jernqvist, A., Olsson, J., Aly, G., 1999c. Experimental and theoretical study of an open multi-compartment absorption heat transformer for different steam temperatures Part II: process modelling and simulation. Applied Thermal Engineering 19, 409 – 430.

Sekar, S., Saravanan, R., 2011. Experimental studies on absorption heat transformer coupled distillation system. Desalination 274, 292 – 301.

Shah, M., 1982. Chart Correlation For Saturated Boiling Heat Transfer: Equations and Further Study. ASHRAE Transactions 88, 185–196.

Shi, C., Chen, Q., Jen, T.C., Yang, W., 2010. Heat transfer performance of

lithium bromide solution in falling film generator. International Journal of Heat and Mass Transfer 53, 3372–3376.

Shi, L., Yin, J., Wang, X., Zhu, M.S., 2001. Study on a new ejection-absorption heat transformer. Applied Energy 68, 161–171.

Shiming, X., Yanli, L., Lisong, Z., 2001. Performance research of self regenerated absorption heat transformer cycle using TFE-NMP as working fluids. International Journal of Refrigeration 24, 510 – 518.

Silva, M.K., d'Ávila, M.A., Mori, M., 2012. Study of the interfacial forces and turbulence models in a bubble column. Computers & Chemical Engineering 44, 34 – 44.

Sinnott, R., 2005. Coulson and Richardson's Chemical Engineering Volume 6 - Chemical Engineering Design (4th Edition). Elsevier.

Siqueiros, J., Romero, R.J., 2007. Increase of COP for heat transformer in water purification systems. Part 1 - Increasing heat source temperature. Applied Thermal Engineering 27, 1043–1053.

Smith, R., 2005. Chemical process design and integration. Wiley, Chichester, England.

Sözen, A., 2004. Effect of irreversibilities on performance of an absorption heat transformer used to increase solar pond's temperature. Renewable Energy 29, 501–515.

Sözen, A., Arcaklioğlu, E., 2007. Exergy analysis of an ejector-absorption heat transformer using artificial neural network approach. Applied Thermal Engineering 27, 481–491.

Sözen, A., Arcaklioğlu, E., Özalp, M., Yücesu, S., 2005. Performance parameters of an ejector-absorption heat transformer. Applied Energy 80, 273 – 289.

Sözen, A., Yücesu, H.S., 2007. Performance improvement of absorption heat transformer. Renewable Energy 32, 267–284.

Srikhirin, P., Aphornratana, S., Chungpaibulpatana, S., 2001. A review of absorption refrigeration technologies. Renewable and Sustainable Energy Reviews 5, 343 – 372.

Stankus, S., Khairulin, R., Gruzdev, V., Verba, O., 2007. The density of aqueous

solutions of lithium bromide at high temperatures and concentrations. High Temperature 45, 429–431.

Stephan, K., Schmitt, M., Hebecker, D., Bergmann, T., 1997. Dynamics of a heat transformer working with the mixture NaOH-H2O. International Journal of Refrigeration 20, 483 – 495.

Sun, F., Qin, X., Chen, L., Wu, C., 2005. Optimization between heating load and entropy-production rate for endoreversible absorption heat-transformers. Applied Energy 81, 434 – 448.

Taborek, J., 1983. Shell-and-tube heat exchangers: single-phase flow.. volume 3 : Thermal and Hydraulic Design of Heat Exchangers, Dusseldorf, Fed. Rep. Germany, VDI-Verlag GmbH, 1.

Talbi, M., Agnew, B., 2000. Exergy analysis: an absorption refrigerator using lithium bromide and water as the working fluids. Applied Thermal Engineering 20, 619 – 630.

U.S. Energy Information Administration, ., 2014. Annual Energy Outlook 2014 Early Release Overview. Technical Report. U.S. Depertment of Energy.

Wang, C.C., Chang, Y.J., Hsieh, Y.C., Lin, Y.T., 1996. Sensible heat and friction characteristics of plate fin-and-tube heat exchangers having plane fins. International Journal of Refrigeration 19, 223 – 230.

Wang, T., Wang, J., 2007. Numerical simulations of gas-liquid mass transfer in bubble columns with a CFD-PBM coupled model. Chemical Engineering Science 62, 7107 – 7118. 8th International Conference on Gas-Liquid and Gas-Liquid-Solid Reactor Engineering.

Wang, X., Shi, L., Yin, J., Zhu, M.S., 2002. A two-stage heat transformer with H2O/LiBr for the first stage and 2,2,2-trifluoroethanol(TFE)/N-methy1-2-pyrrolidone (NMP) for the second stage. Applied Energy 71, 235 – 249.

Warnakulasuriya, F., Worek, W., 2008. Drop formation of swirl-jet nozzles with high viscous solution in vacuum-new absorbent in spray absorption refrigeration. International Journal of Heat and Mass Transfer 51, 3362 – 3368.

Wu, S., Chen, J., 2005. Parametric optimum design of an irreversible heat-transformer based on the thermo-economic approach. Applied Energy 80, 349 – 365.

Yin, J., Shi, L., Zhu, M.S., Han, L.Z., 2000. Performance analysis of an absorption

heat transformer with different working fluid combinations. Applied Energy 67, 281–292.

Yuan, Z., Herold, K.E., 2005. Thermodynamic properties of aqueous lithium bromide using a multiproperty free energy correlation. HVAC and R Research 11, 377–393.

Zebbar, D., Kherris, S., Zebbar, S., Mostefa, K., 2012. Thermodynamic optimization of an absorption heat transformer. International Journal of Refrigeration 35, 1393 – 1401.

Zhang, J., Fan, L.S., 2003. On the rise velocity of an interactive bubble in liquids. Chemical Engineering Journal 92, 169 – 176.

Zhang, K., Liu, Z., Li, Y., Li, Q., Zhang, J., Liu, H., 2014a. The improved CO2 capture system with heat recovery based on absorption heat transformer and flash evaporator. Applied Thermal Engineering 62, 500 – 506.

Zhang, X., Hu, D., 2012. Performance analysis of the single-stage absorption heat transformer using a new working pair composed of ionic liquid and water. Applied Thermal Engineering 37, 129 – 135.

Zhang, X., Hu, D., Li, Z., 2014b. Performance analysis on a new multi-effect distillation combined with an open absorption heat transformer driven by waste heat. Applied Thermal Engineering 62, 239 – 244.

Zhao, Z., Ma, Y., Chen, J., 2003a. Thermodynamic performance of a new type of double absorption heat transformer. Applied Thermal Engineering 23, 2407 – 2414.

Zhao, Z., Zhang, X., Ma, X., 2005. Thermodynamic performance of a double-effect absorption heat-transformer using TFE/E181 as the working fluid. Applied Energy 82, 107 – 116.

Zhao, Z., Zhou, F., Zhang, X., Li, S., 2003b. The thermodynamic performance of a new solution cycle in double absorption heat transformer using water/lithium bromide as the working fluids. International Journal of Refrigeration 26, 315 – 320.

Zhuo, C., Machielsen, C., 1996. Performance of high-temperature absorption heat transformers using Alkitrate as the working pair. Applied Thermal Engineering 16, 255 – 262.

Appendices

Appendix A

Mathematical Function Details

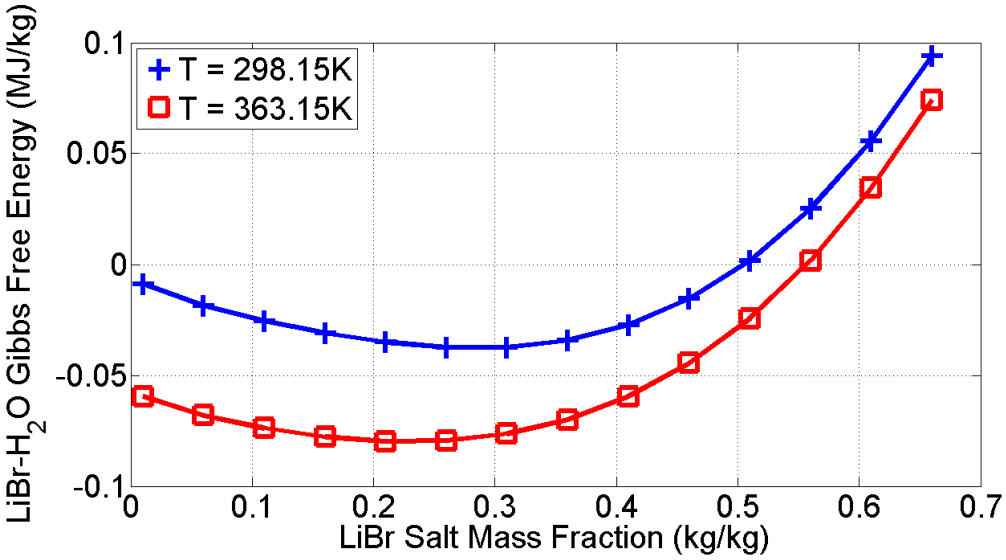


Figure A.1: Specific Gibbs free energy of the LiBr − H_2O solution at various different salt concentrations and temepratures at atmospheric pressure (101325Pa).

A.1 Water-Lithium Bromide Solution Properties

A.1.1 Gibbs Free Energy

In Chapter 2, the physical properties of the LiBr − H_2O solution are calculated from the Gibbs free energy of the solution. The correlation published by Yuan and Herold (2005) is used to quantify this Gibbs free energy throughout the thesis. Their correlation is presented in equation A.1, while its parameters are listed in Tables A.1 and A.2.

$$\begin{aligned} gb \; &= \left(A_0 + A_1 x + A_2 x^2 + A_3 x^3 + A_4 x^{1.1}\right) \\ &+T\left(B_0 + B_1 x + B_2 x^2 + B_3 x^3 + B_4 x^{1.1}\right) \\ &+T^2\left(C_0 + C_1 x + C_2 x^2 + C_3 x^3 + C_4 x^{1.1}\right) \\ &+T^3\left(D_0 + D_1 x + D_2 x^2 + D_3 x^3 + D_4 x^{1.1}\right) \\ &+T^4\left(E_0 + E_1 x\right) + \frac{F_0 + F_1 x}{T - T_0} \\ &+P\left(V_0 + V_1 x + V_2 x^2 + V_3 T + V_4 x T + V_5 x^2 T + V_6 T^2 + V_7 x T^2\right) \\ &+\ln T\left(L_0 + L_1 x + L_2 x^2 + L_3 x^3 + L_4 x^{1.1}\right) \\ &+T\ln T\left(M_0 + M_1 x + M_2 x^2 + M_3 x^3 + M_4 x^{1.1}\right) \end{aligned} \tag{A.1}$$

Nomenclature

B_c	Baffle Cut Percentage (percentage of baffle window height relative to shell diameter)
C_{bh}	Empirical factor equal to 1.25
c_p	Specific heat capacity ($W/(m^2K)$)
D_{ab}	Mass diffusivity of water in $LiBr - H_2O$ solution (m^2/s)
D_s	Diameter of the shell (m)
D_t	Diameter of a tube (m)
D_{ctl}	Center line tube limit (diameter of the tube bundle using the center line of the outside tubes as the outer limit) (m)
F_{sbp}	Ratio of bypass to cross flow area
F_w	Fraction of the baffle cross sectional area occupied by the window
gb	Specific Gibbs Energy (J/kg)
J_B	Bundle bypass correction factor
J_c	Baffle cut correction factor
J_L	Baffle leakage correction factor
J_R	Laminar flow correction factor
J_S	Unequal baffle spacing correction factor
L_{bb}	Distance between the inner shell wall and the outer tube bundle (m)
L_{bc}	Spacing between central baffles (m)
L_{bi}	Spacing between baffles at the inlet (m)
L_{bo}	Spacing between baffles at the outlet (m)
L_{pl}	Width of the bypass lane between tubes (m)
L_{pp}	Horizontal distance between tubes (m)
L_{sb}	Distance between the inner shell wall and the baffle (m)
L_{tb}	Tube to baffle clearance (m)
L_{tp}	Tube pitch (m)
m_{vel}	Mass velocity (the mass flowrate per unit area, $kg/(m^2s)$)
Mr_{LiBr}	Molecular Mass of lithium bromide (0.0868 mol/kg)
N_b	Number of baffle compartments in the heat exchanger
N_c	Total number of tubes rows crossed by the flow in the entire heat exchanger
N_{ss}	Number of sealing strips
N_{tt}	Total number of tubes
N_{tcc}	Number of tube rows crossed between baffle tips in one baffle section
N_{tcw}	Number of tube rows crossed in the window area
r_{ss}	Ratio of the number of sealing strips to the number of tube rows crossed between baffle tips in one baffle section
S_b	Bundle bypass area (m^2)
S_m	Cross flow area at the bundle centerline (m^2)
S_{sb}	Shell to baffle leakage area (m^2)
S_{tb}	Tube to baffle hole leakage area (m^2)
T	Temperature (K)
T_o	Gibbs free energy reference temperature (273.15K)
x	Lithium Bromide mass Fraction (kg/kg)

Nomenclature continued

Dimensionless Numbers

Pr	Prandtl Number = $c_p\mu/k$
Re	Reynolds Number = $\rho v D/\mu$

Greek Symbols

α	Heat transfer coefficient (W/(m^{2}K))
θ_{ctl}	Angle of the baffle cut relative to the centerline of the heat exchanger and the centerline of the outer tubes in the tube bundle
θ_{ds}	Angle of the baffle cut relative to the centerline of the heat exchanger and the outer shell diameter
μ	Viscosity (Ns/m^2)
ρ	Density (kg/m^3)

	0	1	2	3	4
A	5.5062×10^{3}	5.2132×10^{2}	7.7749	-4.5752×10^{-2}	-5.7929×10^{2}
B	1.4527×10^{2}	-4.9848×10^{-1}	8.8369×10^{-2}	-4.8710×10^{-4}	-2.9052
C	2.6484×10^{-2}	-2.3110×10^{-3}	7.5597×10^{-6}	-3.7639×10^{-8}	1.1762×10^{-3}
D	-8.5265×10^{-6}	1.3202×10^{-6}	2.7920×10^{-11}	0	-8.5115×10^{-7}
E	-3.8404×10^{-11}	2.6255×10^{-11}	0	0	0
F	-5.1599×10^{1}	1.1146	0	0	0
L	-2.1834×10^{3}	-1.2670×10^{2}	-2.3646	1.3894×10^{-2}	1.5834×10^{2}
M	-2.2671×10^{1}	2.9838×10^{-1}	-1.2594×10^{-2}	6.8496×10^{-5}	2.7680×10^{-1}
V	1.1767×10^{-3}	-1.0225×10^{-5}	-1.6957×10^{-8}	-1.4972×10^{-6}	2.5382×10^{-8}

Table A.1: Parameters used in the Gibbs free energy correlation used in this thesis (Yuan and Herold, 2005)

	5	6	7
V	5.8158×10^{-11}	3.0580×10^{-9}	-5.1296×10^{-11}

Table A.2: Parameters used in the Gibbs free energy correlation used in this thesis (Yuan and Herold, 2005)

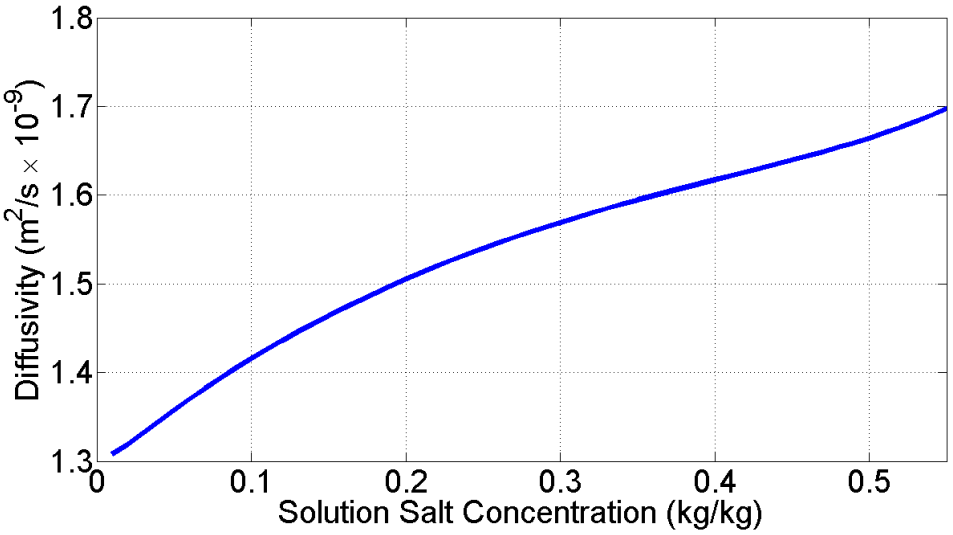


Figure A.2: Mass diffusivity of water in a lithium bromide solution as a function of salt concentration

A.1.2 Diffusivity

The diffusivity of water molecules through the $LiBr - H_2O$ solution is being modelled in this thesis based upon the correlation suggested by Lobo (1993) presented in equations A.2 and A.3.

$$C = \frac{x}{Mr_{LiBr}} \rho_{LiBr} \times 10^{-3} \tag{A.2}$$

$$D_{ab} = \left(a_0 + a_1 C^{\frac{1}{2}} + a_2 C + a_3 C^{\frac{3}{2}} + a_4 C^2 \right) \times 10^{-9} \tag{A.3}$$

A.2 Heat Transfer Coefficients

A.2.1 Shell Side Heat Transfer Coefficient

As discussed in Section 2.4.1, the single fluid shell side heat transfer coefficient being used in this thesis is based upon the correlation developed by Taborek (1983). This correlation calculates an ideal heat transfer coefficient in the shell side, and then applies correction factors to this figure to account for flows across baffle cuts (J_C), baffle leakage flows (J_L), unequal baffle spacings (J_R), flow over

the tube bundle (J_B), laminar flow (J_S) and viscosity variations ($J\mu$) as shown in equations A.4 and A.5.

$$\alpha_{ideal} = j_i m_{vel} c_p Pr^{-2/3} \tag{A.4}$$

$$\alpha = J_C J_L J_B J_R J_S J_\mu \alpha_{ideal} \tag{A.5}$$

The heat transfer factor j_i in equation A.4 is a function of the fluid's Reynolds number and the physical design of the heat exchanger. It is calculated using equations A.6 and A.7 where a_1, a_2, a_3 and a_4 are all empirical factors given in Table A.3.

$$j_i = a_1 \left(\frac{1.33}{L_{tp}/D_t} \right)^a Re^{a_2} \tag{A.6}$$

$$a = \frac{a_3}{1 + 0.14 Re^{a_4}} \tag{A.7}$$

The baffle cut correction factor J_c accounts for the non-ideality of flow through the baffle window and is calculated using equations A.8 to A.13.

$$J_c = 0.55 + 0.72\,(1 - 2F_w) \tag{A.8}$$

$$F_w = \frac{\theta_{ctl}}{360} - \frac{\sin\theta_{ctl}}{2\pi} \tag{A.9}$$

$$\theta_{ctl} = 2\cos^{-1}\left\{ \frac{D_s}{D_{ctl}} \left[1 - 2\left(\frac{B_c}{100} \right) \right] \right\} \tag{A.10}$$

$$B_c = \left(\frac{\text{BaffleWindowHeight}}{D_s} \right) 100 \tag{A.11}$$

$$D_{ctl} = D_s - L_{bb} - D_t \tag{A.12}$$

Tube Layout	Re	a_1	a_2	a_3	a_4
30 °	$10^5 - 10^4$	0.321	-0.388	1.450	0.519
	$10^4 - 10^3$	0.321	-0.388		
	$10^3 - 10^2$	0.593	-0.477		
	$10^2 - 10^1$	1.360	-0.657		
	<10	1.400	-0.667		
45 °	$10^5 - 10^4$	0.370	-0.396	1.930	0.500
	$10^4 - 10^3$	0.370	-0.396		
	$10^3 - 10^2$	0.730	-0.500		
	$10^2 - 10^1$	0.498	-0.656		
	<10	1.550	-0.667		
90 °	$10^5 - 10^4$	0.370	-0.395	1.187	0.370
	$10^4 - 10^3$	0.107	-0.266		
	$10^3 - 10^2$	0.408	-0.460		
	$10^2 - 10^1$	0.900	-0.631		
	<10	0.970	-0.667		

Table A.3: Empirical Factors required for the calculation of the ideal shell side heat transfer coefficient in equations A.6 and A.7

$$\begin{array}{r|l} D_s < 0.3 & L_{bb} = 9.5 \times 10^{-3} m \\ 0.3 < D_s < 1 & L_{bb} = 12.7 \times 10^{-3} m \\ D_s < 1 & L_{bb} = 15.9 \times 10^{-3} m \end{array} \tag{A.13}$$

The baffle leakage correction factor (J_L) accounts for the small amount of fluid which flows through the baffle tubeholes and around the edge of the baffle (i.e.: not through the baffle window). It is calculated using equations A.14 to A.20.

$$J_L = 0.44\,(1 - r_s) + [1 - 0.44\,(1 - r_s)] \exp\left[-2.2 r_{lm}\right] \tag{A.14}$$

$$r_s = \frac{S_{sb}}{S_{sb} + S_{tb}} \tag{A.15}$$

$$r_{lm} = \frac{S_{sb} + S_{tb}}{S_m} \tag{A.16}$$

$$S_{sb} = 0.00436 D_s L_{sb} (360 - \theta_{ds}) \tag{A.17}$$

$$\theta_{ds} = 2\cos^{-1}\left[1 - 2\left(\frac{B_c}{100}\right)\right] \tag{A.18}$$

$$S_{tb} = \left\{\frac{\pi}{4}\left[(D_t + L_{tb})^2 - D_t^2\right]\right\} N_{tt} (1 - F_w) \tag{A.19}$$

$$S_m = L_{bc}\left[L_{bb} + \frac{D_{ctl}}{L_{tp}}(L_{tp} - D_t)\right] \tag{A.20}$$

The bundle bypass correction factor (J_B) describes the non-ideality associated with fluid which flows parallel to the tube bundle instead of perpendicularly through it, and it is calculated using equations A.21 to A.25.

$$J_B = \exp\left[-C_{bh} F_{sbp}\left(1 - \sqrt{[2r_{ss}]}\right)\right] \tag{A.21}$$

$$F_{sbp} = \frac{S_b}{S_m} \tag{A.22}$$

$$S_b = L_{bc}[D_s - D_{otl} + L_{pl}] \tag{A.23}$$

$$r_{ss} = \frac{N_{ss}}{N_{tcc}} \tag{A.24}$$

$$N_{tcc} = \frac{D_s}{L_{pp}}\left[1 - 2\left(\frac{B_c}{100}\right)\right] \tag{A.25}$$

Heat transfer is generally reduced in laminar flow conditions (in this case if Re<100). If the Reynolds number is less than 20, then equations A.26 to A.28 may be used to estimate the corresponding correction factor (J_R).

$$J_R = \left(\frac{10}{N_c}\right)^{0.18} \tag{A.26}$$

$$N_c = (N_{tcc} + N_{tcw})(N_b + 1) \tag{A.27}$$

$$N_{tcw} = \frac{0.8}{L_{pp}} \left[D_s \left(\frac{B_c}{100} \right) - \frac{D_s - D_{ctl}}{2} \right] \tag{A.28}$$

If the Reynolds number is greater than 20 but less than 100, then equation A.29 is used instead.

$$J_R = \left(\frac{10}{N_c} \right)^{0.18} + \left(\frac{20 - Re}{80} \right) \left[\left(\frac{10}{N_c} \right)^{0.18} - 1 \right] \tag{A.29}$$

Any difference between the spacing of internal and inlet/outlet baffles is accounted for using equation A.30, the unequal baffle spacing correction factor (J_s), where n = 0.6 for turbulent flow and n = 1/3 for laminar flow.

$$J_s = \frac{(N_b - 1) + (L_{bi}/L_{bc})^{1-n} + (L_{bo}/L_{bc})^{1-n}}{(N_b - 1) + (L_{bi}/L_{bc}) + (L_{bo}/L_{bc})} \tag{A.30}$$

The wall viscosity correction factor (J_μ) is a correction due to differences in the fluid properties of the bulk fluid and the fluid at the wall and is given by equation A.31.

$$J_\mu = \left(\frac{\mu}{\mu_{wall}} \right)^{0.14} \tag{A.31}$$